2015

Diamond microdosimetry for radioprotection applications in space

Jeremy A. Davis
University of Wollongong

UNIVERSITY OF WOLLONGONG

DIAMOND MICRODOSIMETRY FOR RADIOPROTECTION APPLICATIONS IN SPACE

A Dissertation Submitted in Fulfilment of
the Requirements for the Award of the Degree of

Doctor of Philosophy

from

UNIVERSITY OF WOLLONGONG

by

Jeremy A. Davis

B.Sc. Physics (Honours Class 1)
B.A. Philosophy
Graduate Diploma of Education
Graduate Certificate of Research Commercialisation

School of Engineering Physics
Faculty of Engineering

Doctorate of Philosophy

CERTIFICATION

I, Jeremy A. Davis, declare that this thesis, submitted in fulfilment of the requirements for the award of Doctor of Philosophy, in the School of Engineering Physics, Faculty of Engineering, University of Wollongong, is wholly my own work unless otherwise referenced or acknowledged. The document has not been submitted for qualifications at any other academic institution.

(Signature Required)

Jeremy A. Davis
2015 Doctorate of Philosophy

My family and friends

Table of Contents

List of Tables

List of Figures

List of Abbreviations

ABA Active Brazing Alloy

ACR Anomalous Cosmic Rays

ANSTO Australian Nuclear Science and Technology Organization

ARS Acute Radiation Syndrome

BC Buried Contact

BID Boron Implanted Diamond

CCD Charge Collection Distance

CCE Charge Collection Efficiency

CCE Charge Collection Efficiency

CMRP Centre for Medical Radiation Physics

CREME96 Cosmic Ray Effects on Micro-Electronics Code 1996

CSV Cylindrical Sensitive Volume

CVD Chemical Vapour Deposition

DIL Dual-In-Line package

DLR Dose Legal Record

DRIE Deep Reactive Ion Etching

FIB Focussed Ion Beam

GCR Galactic Cosmic Rays

GEANT4 GEometry ANd Tracking toolkit 4

GoF Goodness-of-Fit

GPS General Particle Source

HIM Heavy Ion Microprobe

HPHT High Pressure High Temperature

IBIC Ion Beam Induced Current

ICRP International Commission on Radiological Protection

KS Kolmogorov-Smirnov

LET Linear energy transfer

LT Laser-milled Trench

MARC MicroAnalytical Research Centre

MC Monte Carlo

MCN Melbourne Centre for Nano-fabrication

MIM Metal-Insulator-Metal

NSBRI National Space Biomedical Research Institute

PDMS Polydimethylsiloxane

RBE Relative Biological Effectiveness

RID Radiation Induced Damage

RPP Rectangular Parallelepiped

SEE Single Event Effects

SPE Solar Particle Events

SRH Shockley-Read-Hall

STIM Scanning Transmission Ion Microscopy

SV Sensitive Volume

TCAD Technology Computer Aided Design

TEM Transmission Electron Microscopy

TEPC Tissue Equivalent Proportional Counter

UHECR Ultra High Energy Cosmic Rays

DIAMOND MICRODOSIMETRY FOR RADIOPROTECTION APPLICATIONS IN SPACE

Jeremy A. Davis

A Thesis for

School of Engineering Physics
University of Wollongong

ABSTRACT

The harsh space radiation environment, imposes a significant risk, to both biological and non-biological matter. Radiation Induced Damage (RID), depends upon the type and energy of radiation and the material properties of the interacting medium. The similarities between microelectronics and biological cells in relation to RID then, are such that a common methodology of measuring radiation dose might be used. Microdosimetry, being a technique that allows for the measurement of stochastic energy deposition distributions within micron size sensitive volume (SV), is a methodology well suited to act as dose monitoring system for biological and non-biological matter.

A number of restrictions are placed upon device operation within the space radiation environment, that must be addressed when considering the viability of a detector. The cost of deployment, necessitates that the size, weight and power usage of the device be minimal. Spatial resolution, tissue equivalence and radiation hardness, especially for long term biological applications are concerned, are also vital. Solid state microdosimetry is well suited to address these issues and requirements, given the appropriate selection of materials such as diamond, which is both tissue equivalent and radiation hard.

A variety of different device structures based upon different fabrication technologies were developed and investigated with respect to applicability to microdosimetry. The behaviour of each device, was studied using both experimental and simulation based techniques. Experimental characterisation was performed to determine the electrical and charge collection properties of each device and validate charge confinement to the desired SV region. Simulation studies, to support experimental results, utilised two different simulations package suites; Geant4 and Sentaurus TCAD. Geant4 was used to investigate the effect of contact thickness upon energy deposition in addition to determining a tissue equivalence correction, to convert the energy deposition response in diamond to that in water. TCAD was used to model device structures and characterising the electric field structures and response to heavy ion strikes. TCAD modelling enabled a pre-fabrication assessment tool for device design and optimisation.

The results presented, demonstrate the viability of diamond along with a variety of different fabrication techniques, employed to produce structures, for solid state microdosimetry. Provided certain recommendations are followed, this work will certainly lead to the eventual realisation and commercialisation of diamond based devices for microdosimetric applications in space.

KEYWORDS: Microdosimetry, Diamond, Space and Radioprotection.

Acknowledgements

"*If I have seen further than others, it is by standing upon the shoulders of giants*".

-Isaac Newton

It is important to note that this work could not have been completed, were it not for the collaboration and support of my friends, family and colleagues. First and foremost, I would like to thank my supervisors Prof. Anatoly Rosenfeld and Dr. Susanna Guatelli, without whom, this project and my own involvement, would have never occurred. Prof. Rosenfeld who inspired, encouraged and drove my development within the field of semiconductor research. Dr. Susanna Guatelli (CMRP) for her tireless support, and long hours of assistance in writing and debugging code is greatly appreciated. Most of all, I would like to acknowledge the patience and understanding she showed in her role as both a supervisor and mentor.

Next, I would like to acknowledge and thank Assoc. Prof. Michael Lerch, Dr. Marco Petasecca and Dr. Dean Cutajar for the many useful discussions and their insight into my work, but most importantly their humour. Next, Dr. Dale Prokopovich, whose operation of the ANTARES heavy ion microprobe and discussions of semiconductor characterisation methods was a significant contribution to this work. Dr. Michael Weaver and Dr. Carson Drummond whose guidance and assistance in Matlab was crucial in the analysis of experimental and simulation based results. Karen Ford (CMRP), Sonny Spargo and Donna Wright, for organising domestic/international travel and accommodation for experiments and conferences. To my colleagues at Melbourne University, Dr. Kumar Ganesan, Dr. Andrew Alves, Dr. Arman Ahnood, Dr. Alastair Stacey and Prof. David Jamieson. The access to labs and materials, in addition to their intimate knowledge of diamond and fabrication processes was vital.

Lastly, I would like to thank my mother, Jenny, my brother, Jonno and my sister Julia for putting up with me, which was needless to say, no mean feat. Finally my grandparents Dr. Suzanne Davis and Dr. Wesley Davis, who inspired my love of science.

List of Publications

First author publications:

1. J. A. Davis, K. Ganesan, A. D. C. Alves, S. Guatelli, M. Petasecca, J. Liv- ingstone, M. L. F. Lerch, D. A. Prokopovich, M. I. Reinhard, R. N. Siegele, S. Prawer, D. N. Jamieson, Z. Kuncic, V. L. Pisacane, J. F. Dicello, J. Ziegler, M. Zaider, A. B. Rosenfeld, "Characterisation of a novel diamond-based microdosimeter prototype for radioprotection applications in space environments", IEEE Trans. on. Nucl. Sci., 59(6), 3110 - 3116, 2012.

2. J. A. Davis, S. Guatelli, M. Petasecca, M. L. F. Lerch, M. I. Reinhard, M. Zaider, J. Ziegler, A. B. Rosenfeld, "Tissue Equivalence Study of a Novel Diamond-Based Microdosimeter for Galactic Cosmic Rays and Solar Particle Events," IEEE Trans. on. Nucl. Sci., 2014

3. J. A. Davis, K. Ganesan, A. D. C. Alves, D. A. Prokopovich, S. Guatelli, M. Petasecca, M. L. F. Lerch, D. N. Jamieson, and A. B. Rosenfeld "Characterization of an Alternative Diamond Based Microdosimeter Prototype", IEEE Trans. on. Nucl. Sci., 61(6), 2014

Pending publications:

1. J. A. Davis, K. Ganesan, D. A. Prokopovich, M. Petasecca, D. N. Jamieson, and A. B. Rosenfeld "A Buried Lateral Contact Structure for Diamond Based Microdosimetry", IEEE Trans. on. Nucl. Sci., 2015 (estimated date of publication)

List of Conference Presentations

Oral presentation:

1. 16th International Conference on Solid State Dosimetry, Sydney, Australia, September 19-24, 2010.
2. Engineering and the Physical Sciences in Medicine Conference, Darwin, Australia, August 14-18, 2011.
3. 11th Australian Space Science Conference, Canberra, Australia, September 26-29, 2011.
4. 1st Geant4 Australian School and User Workshop, Wollongong, Australia, April 11-16, 2011.
5. IEEE Nuclear and Space Radiation Effects Conference, Miami, USA, July 16-20, 2012.
6. 2nd Geant4 Australian School and Monte Carlo Workshop, Wollongong, Australia, April 19-24, 2013.
7. Australian Institute of Physics Congress, Sydney, Australia, 2014.
8. AFAD Conference, Melbourne, Australia, 2014.

Poster presentation:

1. 16th International Conference on Solid State Dosimetry, Sydney, Australia, September 19-24, 2010.
2. IEEE Nuclear Science Symposium and Medical Imaging Conference, Valencia, Spain, October 23-29, 2011.
3. IEEE Nuclear Science Symposium and Medical Imaging Conference, Anaheim, USA, October 29 - November 3, 2012.
4. Australian Institute of Physics Congress, Sydney, Australia, 2014.
5. IEEE Combined Nuclear and Space Radiation Effects Conference & Radiation Effects on Components and Systems, Paris, France, July 16-20, 2014.

Part I

Space, Diamond and Microdosimetry

Chapter 1

Introduction

1.1 Motivation

Radiation, be it terrestrial or extraterrestrial can have adverse effects upon biological and non-biological matter. For living organisms, interactions with ionising radiation can result in the corruption or death of healthy cellular activity. Cell death ordinarily becomes significant only if many cells are killed since most body organs contain many more cells than are needed to maintain the normal function of the organ[1]. More worrisome than cell death, is the corruption of healthy cells. This can result in abnormal cell function, increased/decreased rate of cell division and life span and, due to the process of cellular mitosis, these effects can be passed on to succeeding cell generations. Cancer is just one of the biological problems associated with increased exposure to harmful ionising radiation, i.e. radiation dose, other issues are: Acute radiation syndrome (ARS), skin damage, cataract, sterility (temporal or permanent), leukaemia, hereditary effects in offspring and even death. Radiation is also a cause of concern for electronics. Single event effects (SEE) occur when high energy particles interfere with on-board computer systems in spacecraft/aircraft. One result is the change of data, perhaps from a 0 to a 1 or vice versa affecting function and/or causing a loss of data[2].

Microdosimetry, has been a subject of study at the Centre for Medical Radiation Physics (CMRP) for more than twenty years. Microdosimetry is concerned with the measurement of lineal energy; being the stochastic energy deposition along a chord length within micron size sensitive volumes (i.e., lineal energy (y) = energy deposition (ε) / mean chord length (l)). Accurate knowledge of the lineal energy is important as it can be used to determine the dose equivalent (H)[3] [4] [5].

$$H = D \int Q(y) y^2 f(y) d(logy) \tag{1.1}$$

where:

- D is the absorbed dose.
- Q(y) is the quality factor describing the radio-biological effectiveness.
- f(y) is the distribution of lineal energy events (y).

The tissue equivalent proportional counter ((TEPC)) is considered to be the standard for experimental microdosimetry. The TEPC is able to simulate a single micron size sensitive volume (SV) through the use of a low pressure, tissue equivalent gas. The advantages of the TEPC, however, are also the cause of its drawbacks, which include but are not limited to: large physical size (low spatial resolution), wall effects and inherent inability to simulate more than one isolated biological cell[6].

Whether the issue for concern is biological or electronic, the risk due to radiation is increased with exposure to harsh radiation fields such as those which dominate at high altitudes and beyond the Earth's atmosphere. For astronauts and those who work within the aviation industry, the health risks associated with radiation are a clear and present danger. The solution to preventing such harmful effects will lie in our ability to successfully employ protective devices that are able to detect and shield from radiation.

Dose monitoring technologies have three main requirements to fulfil in order to be eligible for use in the field, which are:

- Accurately monitor astronaut radiation exposures.
- Provide warning of dangerous changes in radiation environment.
- Document radiation exposure history.

Given the similarities between radiation induced damage on a biological scale and for that in microelectronics (i.e., SEE), microdosimeters are well suited to study both as well as act as dose monitoring and early warning for system. The development of solid state microdosimetry has addressed these issues and requirements. Solid state microdosimeters, whether they are based upon silicon or diamond, represent a very real solution to the necessity for a dose monitoring device. This technology offers a significant advantage over traditional methods, i.e., the TEPC.

There are also a number of requirements that these device should meet in order to be viable for applications in space, of which a small subset are :

- Radiation hardness.
- Tissue equivalence.

1.2 Objectives and Scope

The overall aim of this thesis is to examine the use of diamond as a new material for use in microdosimetric applications. This will be approached with the following objectives:

- Examine various fabrication techniques for microdosimetric applications.
- Experimentally characterise and evaluate alternative diamond based radiation detectors.

- Address the tissue equivalence of diamond for hadrons.
- Model diamond as a unique material within TCAD
- Optimise detector design using TCAD simulations via an examination of the electric field profiling of various diamond based devices.

1.3 Thesis Outline

This thesis aims to verify the use of diamond as a substitute for silicon, for microdosimetric applications in aviation and space radiation environments. Whilst Diamond has been used before within the field of dosimetry, until now its use in microdosimetry has been non-existent thus making this work unique. The structure of this work has been given in the Table of Contents and has been expanded here from Chapter 2 onwards, as follows:
A literature review is presented in Chapter 2, focussing upon space/aviation radiation fields, microdosimetry and the properties of diamond within the scope of microdosimetric applications.
Chapters 3, 4 and 5 present a summary of the methodology related to the technical aspects of the three main components of this thesis. Chapter 3 focussed upon the technologies,techniques and methods used to fabricate the various devices. Chapter 4 deals with the theory and practical operation of methods used to experimentally characterise the electrical and charge collection properties of the devices developed. Finally Chapter 5 gives a brief introduction to the two simulation packages used in this work, i.e., GEANT4 and TCAD.
Chapters 6, 7 and 8 are devoted to the experimental characterisation of three alternative diamond based microdosimeter alternatives. In Chapter 6, the first device developed is discussed. This device makes use of boron implantation to create electrically isolated structures connected by common electrodes to form an array. The work presented in this chapter was published in IEEE Transactions on Nuclear Science in 2012[7]. Chapter 7, presents the sec-

ond alternative structure, featuring laser milled trenches (LT) and a metal-insulator-metal design. The results associated with the experimental characterisation of this device were published in IEEE Transactions on Nuclear Science in 2014[8]. The last of the three design alternatives characterised is presented in Chapter 8. This device utilised a buried contact (BC) structure in order to confine charge laterally between the buried contacts. This work is at the time of submission, unpublished.

Chapters 9 and 10 are focussed upon the current status of next generation devices, aimed at addressing the shortcomings of their predecessors. Two of the three previous devices were selected for further development, which are the LT and BC devices. Multiple design variations of the LT device, were considered in this work, based upon the use of thin, single crystal (intrinsic) diamond or a thin layer of intrinsic diamond upon a thick base layer of extrinsic (boron doped) diamond. The level of complexity from a fabrication point of view, from the 1st generation LT device to the two alternative 2nd generation designs was significant. Whilst the 2nd generation LT device is as yet unfinished, a test structure fabricated upon thick (500 μm) diamond was completed with initial electrical characterisation presented. The 2nd generation BC device was fabricated upon the same sample of layered electronic grade diamond upon boron doped diamond. The fabrication of this device was completed successfully, but was unable to be tested due to incomplete status of the alternative structures being fabricated upon the same layered diamond sample. A third design, based upon modifications of the BC devices and utilising boron doping technology was also selected. This design was tasked with the production of a SV structure better suited for microdosimetry. Using BC technologies, a cylindrical sensitive volume (CSV) was designed and developed. This device also fabricated upon the layered diamond sample discussed previously, has yet to be experimentally characterised though at the time of submission.

Chapters 11 and 12 are concerned with the Geant4 based investigation to determine the effect upon charge collection efficiency with respect to varied thickness of overlaying contact

material and the correction factor required to convert the energy deposition for protons and alpha particles within a diamond volume to water for the purpose of confirming the tissue equivalence of diamond, respectively. This tissue equivalence study was published in IEEE Transactions on Nuclear Science in 2014[9].

Chapters 13 through 17 deal with the Sentaurus TCAD simulations which model each of the device geometries along with variations for optimisation considerations. Chapter 13 deals with the modelling and initial validation of the material "diamond" which is user defined by necessity. Chapters 14, 15, 16 and 17 deal with the boron implanted diamond (BID), laser milled trench (LT), buried contacts (BC) and cylindrical sensitive volume (CSV) device designs, respectively. The electric field structures and response to heavy ion strikes was modelled for each device design.

Chapter 18 presents, the overall conclusions of the thesis, summarising the concluding remarks and recommendations for future work contained within each chapter. This work is the culmination of theoretical and experimental studies. Multiple generations of diamond microdosimeter prototypes have been characterised utilising a variety of experimental techniques including electrical and charge collection characterisation. In addition, particular aspects specific to the function and accuracy of a diamond detector have been investigated using Monte Carlo (MC) and electrostatic driven simulation packages.

Chapter 2

Literature Review

This chapter delivers a background upon dosimetry and radiation fields within space and avionics. Additionally, microdosimetry is introduced and discussed in the context of solid state radiation detectors. Lastly a review of work in the field of diamond based dosimetry is provided.

2.1 Space Radiation Environments

In 1958, following the discovery of the radiation belts surrounding the Earth, Ernie Ray, a protege of Van Allen, for whom the "Van Allen" radiation belts were named, is quoted to have said "*My god, space is radioactive!*". The extent and complexity of the space radiation environment is greater than Ernie Ray or Van Allen could ever have predicted. The space radiation environment is composed of a variety of particles including all of the naturally occurring nuclei, from protons (atomic number Z=1) to uranium (Z=92). These particles originate from almost every imaginable source including, but not limited to: planetary magnetosphere's, the Sun, our own Milky Way Galaxy and even more powerful and as yet, still unidentified extragalactic objects[10]. These numerous sources combine to produce particle spectra with energies extending over twenty orders of magnitude[11]. Most of these nuclei

are fully stripped of electrons, but others are ions which arrive at Earth with a distribution of charge states characteristic of their origin. The intensity, composition and spectrum of all of these species also varies with time, location and arrival direction[10].
The space radiation environment is perilous to mankind's current and future endeavours beyond earth's frontier. The ionising radiation of space is not only hazardous to the electrical components used in satellites, shuttles and space habitats, but also to the astronauts themselves. However, this well known impact of radiation upon astronauts is well known, though not completely understood. The basic mechanism for radiation induced biological damage is illustrated in Fig. 2.1. Radiation can cause cells to mutate, spreading corrupted genes to successive cell generations and resulting in abnormal cellular function i.e. cancer. Neglecting a non-effect, the best case scenario is often cell death, with even this being a serious cause for concern should it affect vital organic tissue[1].

Research programs developed to address such problems typically are designed to target one or more of the following aspects of this problem:

- Understanding the biological effects of the types of radiation present in space.
- Designing adequate shielding to protect astronauts/electronics from this radiation environment.
- Designing radiation detectors to serve as online monitoring system.

Whilst each of these represents a significant concern for astronauts, this thesis is aimed at the third aspect; the development of appropriate detector systems for online dose monitoring in space radiation environments.

2.1.1 Galactic Cosmic Rays

Galactic Cosmic Rays (GCR) are stable charged particles and nuclei with lifetimes greater than 10×10^6 years, originating from astrophysical sources of both galactic and extra-

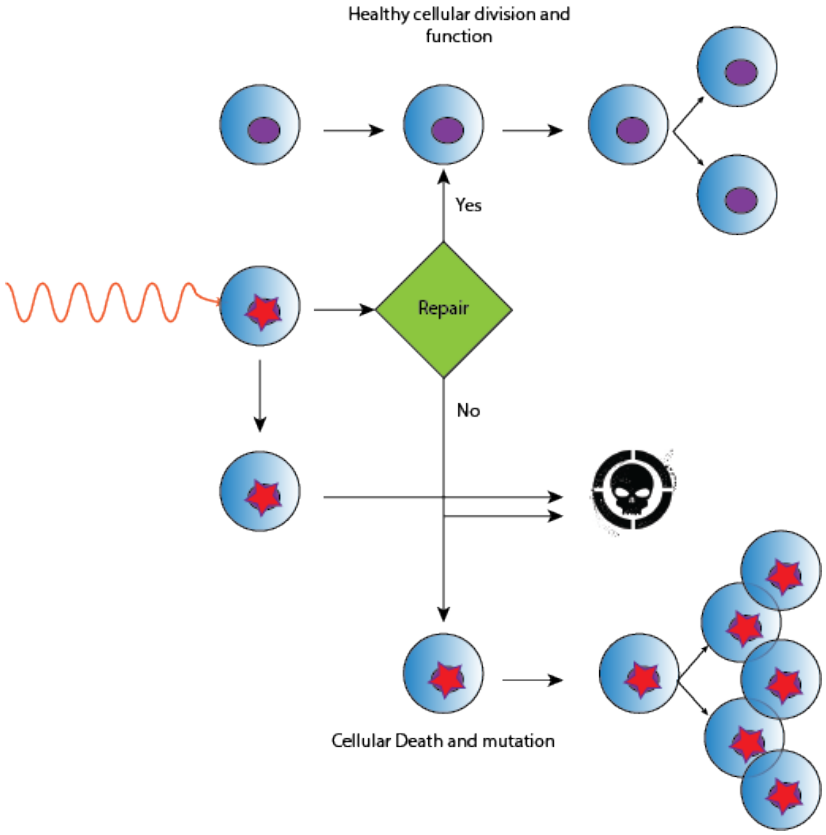

Figure 2.1: Flow chart depicting the response of a biological cell interacting with ionising radiation. If the cell repair is possible, then the cell will follow the same path as that of a cell which has not been exposed. If repair isn't possible, then either cell death or mutation will follow.

galactic origin[12]. GCR may be further distinguished as being either primary or secondary. Primary GCRs are typically the result of nuclei synthesis, the by-products of stellar fusion, and so it is that only a distinct subset of elements of the periodic table are produced in this cycle. Steller fusion is the result of gravity overcoming the strong nuclear force and forcing lighter elements like hydrogen to come together and form helium with a release of energy. Each stage of this cycle is associated with an expansion and contraction of the star in order to force heavier and heavier elements to fuse until iron has been synthesised and all avenues of fusion become closed. This cycle is ended upon the production of iron as it takes additional energy in order the synthesise elements of higher elemental value. Gravity is no longer able to exert enough pressure to continue the fusion cycle and the strong nuclear

force becomes dominant resulting in a violent implosion/explosion called a supernovae. A supernovae is essentially the death of a star. In these final moments, these violent death thralls spew forth vast amounts of particles and charged nuclei, accelerated to high energies outward into space[13].

Given an understanding of nucleosynthesis, primary GCRs are defined to be electrons, protons, and helium, as well as heavy nuclei such as; carbon, oxygen, and iron. The spectral fluence for GCR protons and alphas as given by (CREME96)[10] is presented in Fig. 2.2. The relative contribution to the GCR environment by particle is subject to variation[14]. Limiting the discussion here to protons and heavy charged nuclei, the composition of GCR particles is approximately 85 % hydrogen (atomic number Z = 1), and about 15 % helium (Z = 2). Secondary GCR on the other hand are the result of interactions between primary GCR and interstellar gas. Nuclei which are not abundant end-products of stellar nucleosynthesis, such as lithium, beryllium, and boron are produced in this manner[13] [12].

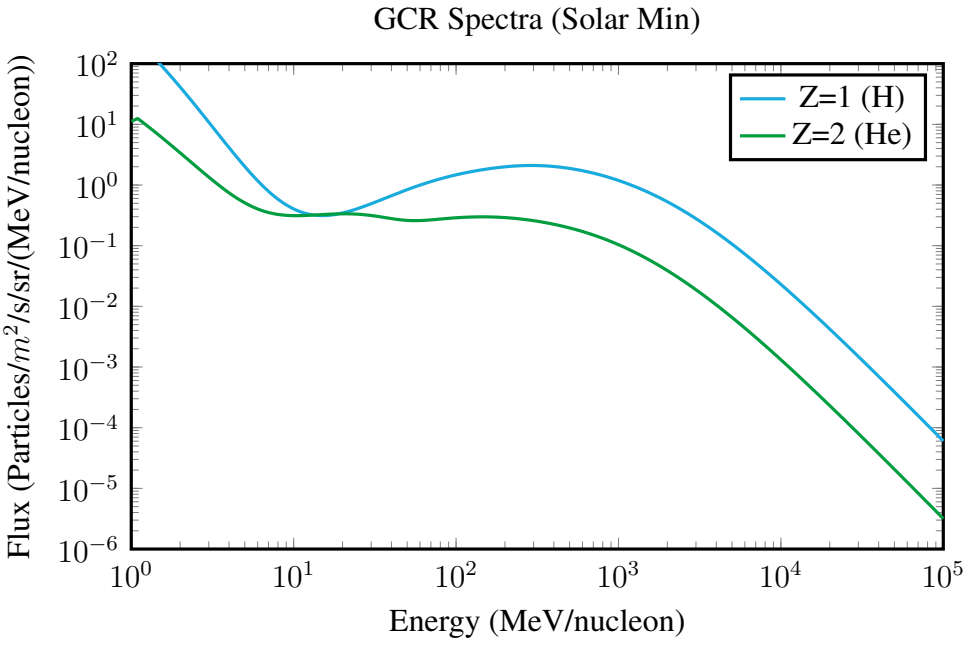

Figure 2.2: GCR Protons and Alpha: CREME96[10]

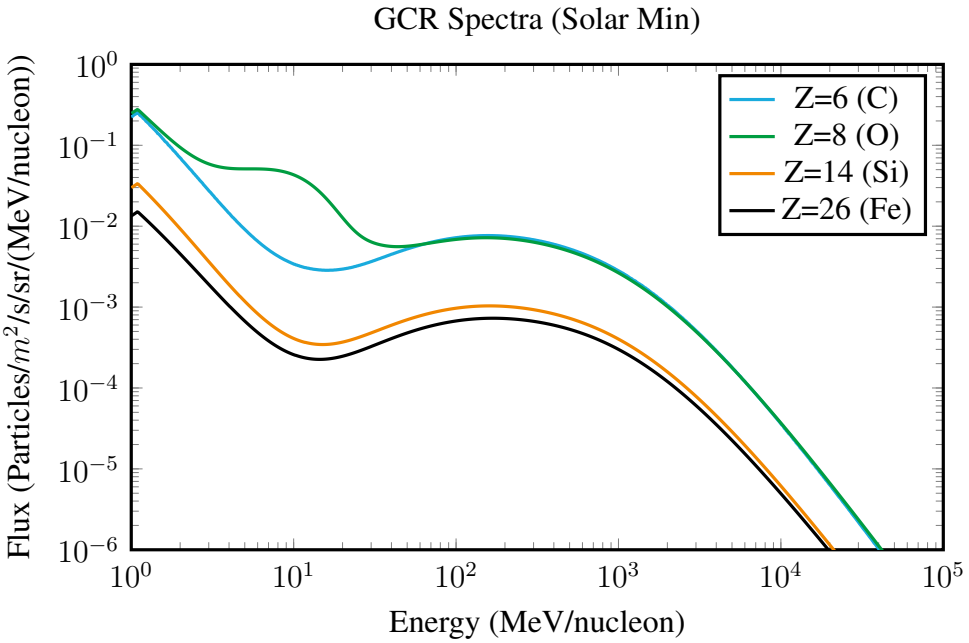

Figure 2.3: GCR Heavy Ions: CREME96[10]

Galactic Cosmic Rays (GCR) have been shown to exhibit a periodicity in the variation of intensity of approximately 11 years, thus showing a significant anti-correlation between solar activity and the flux of GCRs particularly those of lower energy[15]. This is known as solar "modulation", whereby the solar wind will actively affect GCR flux and energy in the inner solar system through deceleration and scattering[16][17][12]. An energy dependence upon the reduction in GCR intensity is evident particularly at lower GCR energies. Low energy GCR are more susceptible to deflection/scattering i.e., solar modulation, than their higher energy counterparts due to interplanetary magnetic fields associated with the solar wind[14]. These low energy components are also more likely to be deflected by the geomagnetic field, which they must penetrate to reach the top of the atmosphere. Thus the intensity of any component of the cosmic radiation in the GeV range depends both on the location and time. Depending upon the energy and angle of incidence, there is an additional probability of becoming trapped within the geomagnetic field. These trapped particles will then travel in helical paths along the geomagnetic field lines coming into contact with the atmosphere

at the magnetic poles and bringing about auroras.

Two additional components of GCR may be further distinguished, which are: ultra high energy cosmic rays (UHECR) and anomalous cosmic rays (ACR). The UHECR component of GCR is extremely small ($\approx 1\ \mathrm{particle\,km^{-2}\,yr^{-1}}$) with energies exceeding 10×10^{19} eV[18]. Not much is known about UHECR, but they are thought to be result of exotic galactic and extra galactic objects. The creation of ACRs occur when neutral interstellar gas becomes ionised upon entering the heliopause[19]. After becoming charged the particle or ion is now readily affected by the Sun's magnetic field which carries them back toward the solar wind termination shock. The ions will repeatedly undergo collisions until they have enough energy to escape from the shock and become ACRs. ACRs are thought to represent a sample of the very local interstellar medium. They are not thought to have experienced such violent processes as GCRs, and are typically only partially ionised and possessing of lower energy. The low energy of ACRs limit the penetration probability within habitable regions of spacecraft or the likelihood of biological damage. Thus ACRs within a dosimetry viewpoint are not considered to be highly important[20].

2.1.2 Solar Particle Events

The effect of solar activity upon the modulation of GCR has already been discussed in Section 2.1.1. The role of solar activity however is not limited to such. Solar Particle Events (SPE) refer to the emission of energetic charged particles during extreme solar events such as solar flares or coronal mass ejections (CME). The lifespan for such events is generally small; usually only hours, but there are events that have been known to last for days. SPEs primarily produce large fluxes of protons, however electrons and heavier nuclei with Z>1 may also comprise the SPE spectra, though with a significantly smaller contribution. SPEs have been known to have energies ranging from the keV to GeV range[21]. Whilst SPEs do not have the energy or contribution of heavy nuclei that is typical of GCR, they are often

considered to be potentially more dangerous, due to the greater potential fluence particularly in the event of severe solar storms.

As it stands, no current model can accurately predict SPE. Due to the unpredictable nature of SPEs, they present a significant concern for manned missions and for on-board electronics. Smaller SPEs may occur more frequently but are of less concern due the reduced flux of high energy particles that are able to penetrate an EVA spacesuit or shielding upon spacecraft making it unlikely that there will be a significant risk to crew[14]. No two SPEs are excactly the same, as each SPE is characterised by a distinct temporal and spectral energy signature. The worst case scenario is a hypothetical SPE based upon empirical evidence of past events and is thought to represent a realistic description of the energy fluence spectrum of a SPE of life threatening proportions. Fig 2.4 presents what the likely spectral fluence for protons and alpha particles based upon this worst case scenario,[10].

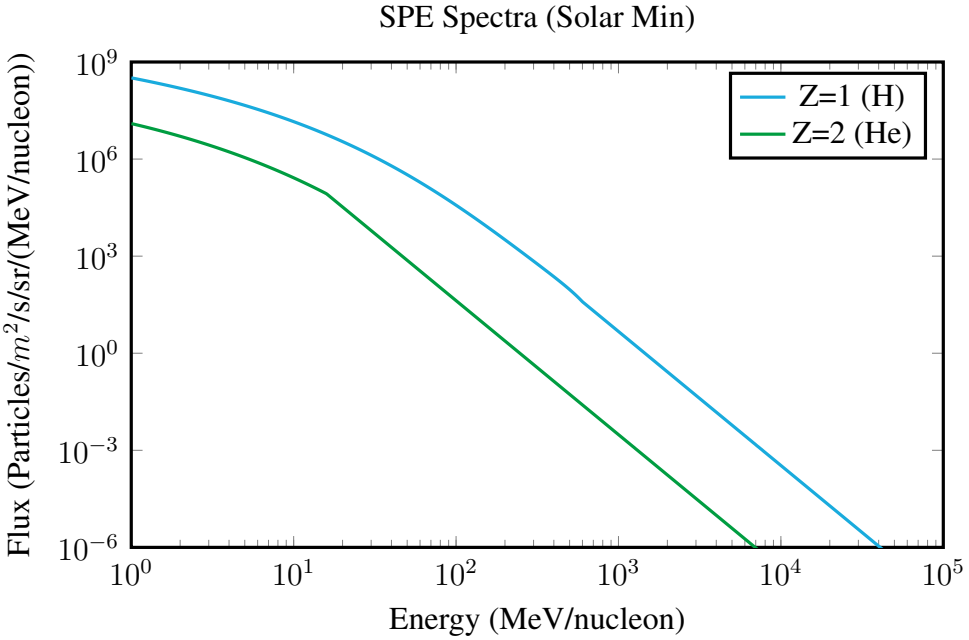

Figure 2.4: SPE Protons and Alpha: CREME96[10]

2.1.3 Avionics Radiation Environments

Radiation exposure for aircraft personnel, whilst less than that of manned missions in space, is still greater than that of people terrestrially bound. The duration and frequency of exposure, particularly for commercial flights, poses a significant risk over time increasing the probability of deterministic effects. Unlike trips to interplanetary space, aircraft personnel are afforded the protection of the geomagnetic field. However, due to the typical altitudes of domestic and commercial flight patterns, there is a decreased absorbing layer of atmosphere to attenuate harmful radiations. Given that exposure is typically due to GCR, radiation levels at aviation altitudes are highly predictable, with the exception of very rare giant solar flares. The hadron (neutrons and protons) component of aviation radiation contributes more than fifty percent to the total dose either through direct or indirect ionisation[22]. In addition, the atmosphere at the altitude (11-14 km) of aircraft is a 'breeding ground' for the production (see Fig. 2.5) of secondary particles (cascade showers) due to the interactions of GCR and SPE within the upper atmosphere. These secondary particles are frequently high Linear Energy Transfer (LET) particles and therefore of significant risk[22].

2.2 Microdosimetry

Dosimetry is a method of detecting harmful radiation and quantifying its effect within in tissue. More particularly, dosimetry is concerned with the interaction of ionising radiation on a biological scale in matter. Microdosimetry, which considers the energy deposition upon a micron scale is a natural extension of dosimetry in that radiation effects are largely determined by energy distributions in microscopic structures. Microdosimetry is a technique that allows accurate measurement of dose equivalent in any mixed radiation field, on a cellular level (1-5 μm)[23]. It is desirable to quantify radiation effects and dose on this scale in that

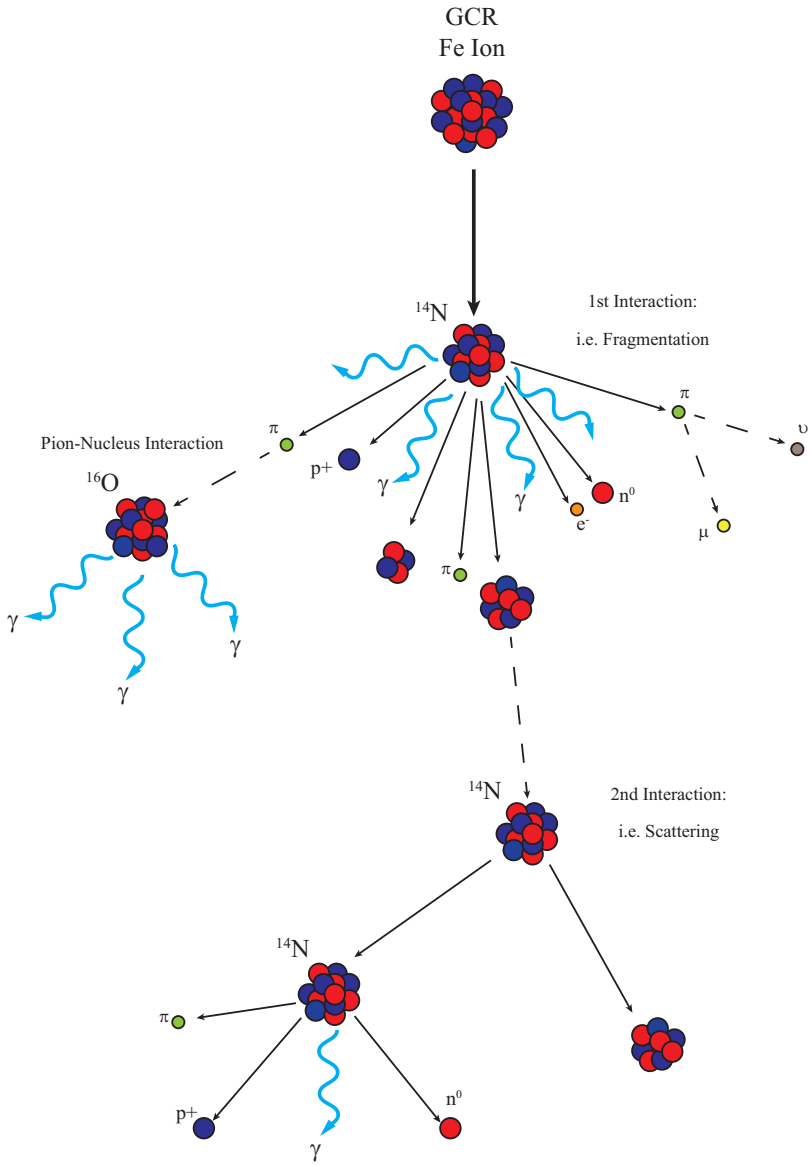

Figure 2.5: Particle cascades in the upper atmosphere and their role in the aviation radiation field.

radiobiological effects of ionising radiation upon a cell nucleus, a principle target for radiation injury can be directly obtained.

Conventional microdosimetry utilised a device known as a tissue equivalent proportional counter (TEPC). The TEPC features a spherical chamber filled with a tissue equivalent gas (low pressure) and electrodes to collect charge following radiation induced ionisation events. The TEPC is the standard for experimental microdosimetry, and allows for the modelling of

biological cell. It is not without limitations however. The TEPC requires a large operating bias in order to function correctly. Its large size imply poor spatial resolution and limit its application in areas where size and weight are an issue i.e. in space. The major drawback though, is that it can only ever model a single isolated cell. It is for these reasons, then that solid state devices are the logical next step with regards to microdosimetry[6].

2.2.1 Solid State Microdosimetry

Solid state microdosimetry has been under investigation for more than a decade at CMRP as a possible alternative to tissue equivalent gas counters for microdosimetric measurements in medical physics and radiation protection[24]. Applications of the technology include but are not limited to radiation protection for: personnel in space, aviation altitudes, charged particle therapies and at nuclear facilities. The technology can also be applied to determine radiation effects on microelectronics in space and aviation applications. Whilst solid state dosimeters may differ in terms of materials, geometries and methods of fabrication; the basic functionality remains unchanged. The method by which microdosimeters function, is outlined in brief in the following sections.

2.2.1.1 Signal Formation

As ionising radiation passes through a semiconducting material (i.e. Diamond), it interacts in the target medium, depositing energy. Electrons can become liberated with sufficient energy, resulting in free charge carriers or electron/hole pairs. For diamond, the energy required to generate electron/hole pairs is ε_C = 13 eV, and is independent upon the energy and type of incident radiation. Under normal conditions, these charge carriers will diffuse into the medium, with diffusion depending upon the charge concentration gradient (Diffusion Current) and carrier mobilities/lifetimes. The carrier mobilities of diamond are among the highest recorded for known materials with μ_e = 2200 $\mathrm{cm^2\,V^{-1}\,s}$ and μ_h = 1600 $\mathrm{cm^2\,V^{-1}\,s}$

indicating fast signal collection. Detector systems utilise an electric field through the use of an applied bias, so that electron/hole pairs migrate to their respective electrodes. This movement of charge carriers induces a small current pulse (drift current) within the detector system.

The current measured by the detector system is thus determined by the generation of charge carriers within the active region or sensitive volume of the detector and therefore proportional to the energy deposited by the incident radiation. Given the ultra short time frame of such current pulses (i.e. nanoseconds), such detector systems allow for real time monitoring of energy deposition, essential for applications where radiation personnel may be at risk from a variable radiation environment such as that encountered in space.

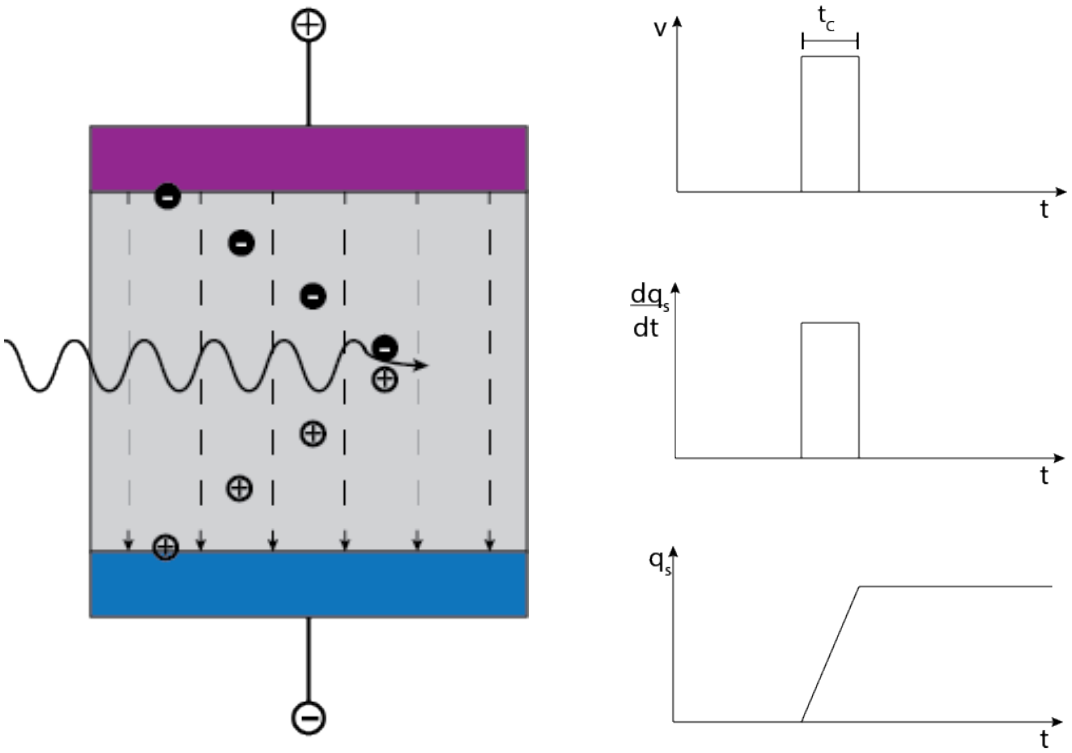

(a) Metal-Insulator-Metal detector structure. (b) Signal production

Figure 2.6: Ionising radiation (wavy line) incident upon radiation detector generates electron/hole pairs, which migrate under influence of applied electric field (dashed lines). Charge migration induces mirror charges of equal magnitude within electrodes.

2.2.1.2 Signal Processing

The current measured within such detector systems is typically quite small and requires appropriate processing in order to be useful for microdosimetry. The signal processing system utilised in detector systems, typically consists of three main components; a pre-amplifier (pre-amp), linear amplifier (shaping amp) and a Single or Multi Channel Analyser (SCA or MCA). It is worth noting that most modern systems, also include a method of digitising signal data through the use of an Analogue to Digital Converter (ADC).
The role of the first component, the pre-amp is necessitated by the small signal produced by detector systems. The pre-amp not only acts as an interface between the detector and subsequent components of the signal processing system, but also provides a means of increasing the signal, ideally, with minimal effect upon the signal to noise ratio. The shaping amp is the second component of the signal processing system, amplifies and transforms the output from the pre-amp into a form that might be utilised more easily, i.e. Gaussian. Following the appropriate transformation of the signal, they can be sorted into a histogram or spectrum of events, using the third component of the signal processing system, the MCA. The MCA can sort signals on an event by event basis, providing pertinent information pertaining to each signal, which may include energy and/or time of arrival. The ADC, while not necessary is a desirable component to include in signal processing systems. It allows the conversion of analogue data from the MCA into digital data. Digital data inherently allows for greater flexibility in the context of data processing, along with compatibility with modern systems.

A more complete and detailed explanation of the signal processing system, in the context of the experimental aspects of this work is provided in Chapter 8.2.

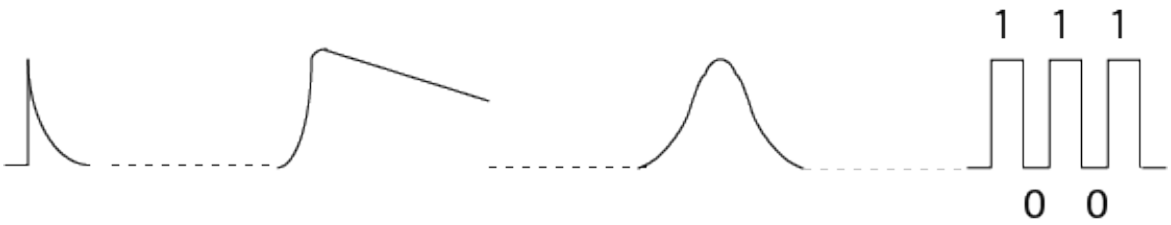

Figure 2.7: Simplified diagram depicting the signal processing chain, depicting the output from various components such as: a) Detector b) Pre-amplifier output. c) Shaping Amplifier d) ADC

2.2.1.3 Microdosimetric Evaluation

Once the signal has been processed and stored, it can be passed through to a purpose made program, developed at CMRP to convert the digital signal into a microdosimetric spectra. This program utilises the microdosimetric method outline in Section 2.2.2.5. It can be used with both experimental and simulation derived data, see Fig 2.8. The GUI features a calibration mode (see Fig. 2.9), that can determine calibration factors or use those already known to properly calibrate the raw data before it is converted into a microdosimetric spectrum, see Fig. 2.10.

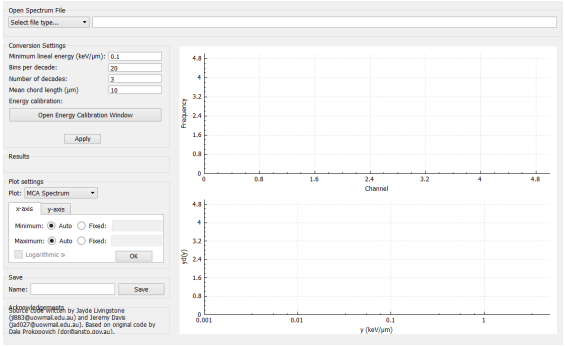

(a) Load, manipulate and save data.

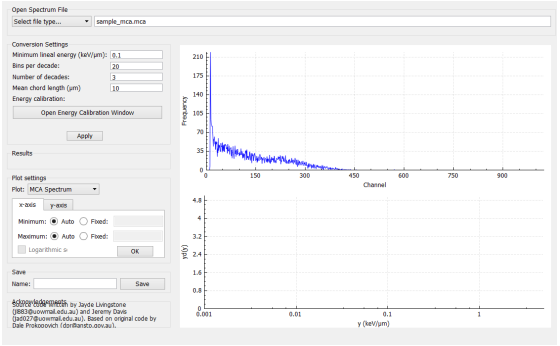

(b) Example: Experimental data loaded.

Figure 2.8: Microdosimetry GUI- Screen 1 & 2

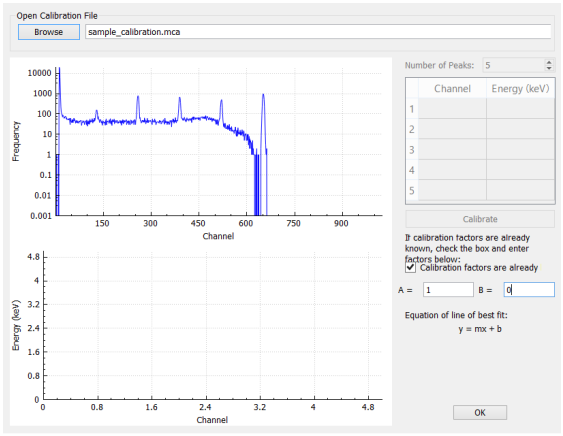

(a) Calibration mode 1: If the calibration factors A and b, are already known.

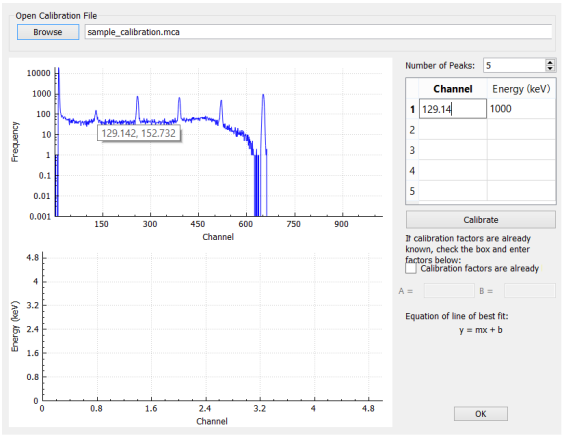

(b) Calibration mode 2: Determination of calibration factors (A & b) are unknown,

Figure 2.9: Microdosimetry GUI- Screen 3 & 4: Calibration factors can be calculated by recoding the channel number associated with a series of experimentally calibrated pulses which correspond to increments of the primary particle energy (keV). Calibration factors are then determined by plotting a straight line, with slope (A) and y-intercept (b).

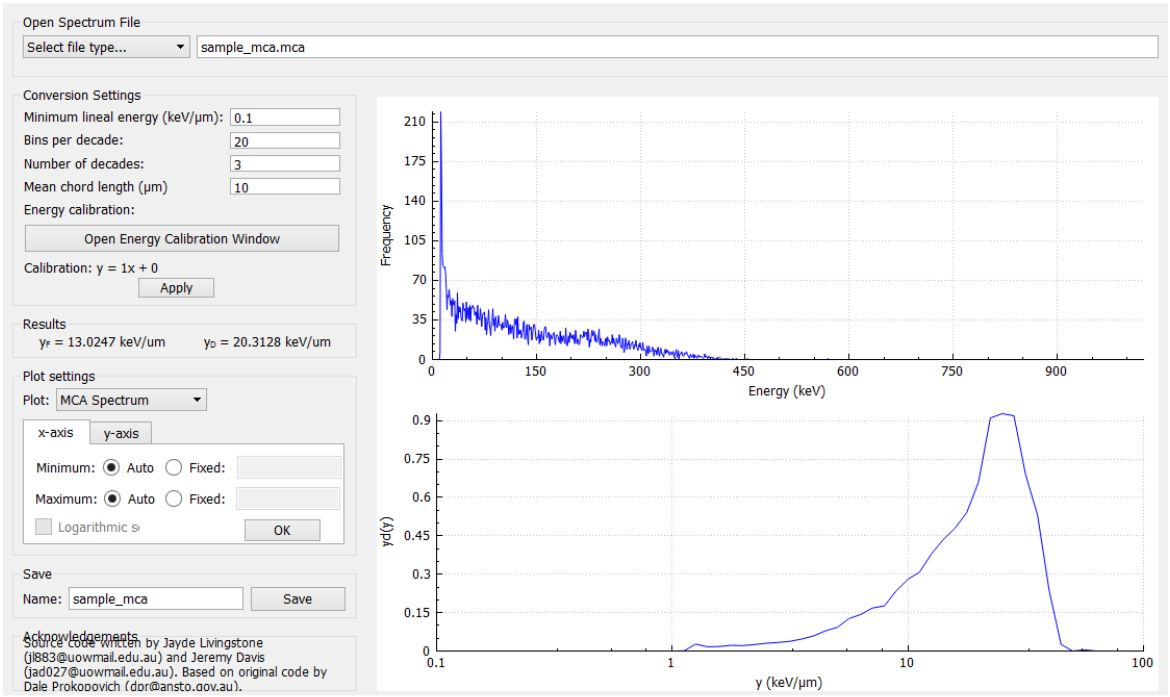

Figure 2.10: The GUI uses the microdosimetric method and converts the calibrated experimental data into a microdosimetric spectrum of lineal energy distribution. A logarithmic scale is used to illustrate the large variance of LET due the varied components of the mixed radiation field.

2.2.2 Key Terms

The key terms related to dosimetry and microdosimetry are outlined in the following sections.

2.2.2.1 Dose

Key to an understanding of dosimetry is the definition of dose. Dose is the term given when the exposure of a sample to harmful radiations is quantified. It is the fundamental dosimetric quantity in radiation protection and provides a measure of the energy (E) deposited within a medium of mass (M). It is an all-inclusive quantity that can be used for any ionizing radiation and any absorbing medium. Dose is given by:

$$D = \frac{E}{M} \tag{2.1}$$

and is given in units of joules/kilogram ($\mathrm{J\,kg^{-1}}$) or equivalently gray (Gy).

2.2.2.2 Relative Biological Effectiveness

However, since it is possible for the same absorbed dose to result from radiation types with different energy distributions more information is needed. The Relative Biological Effectiveness (RBE) is a measure that is increasingly becoming the standard in determining biological effects. RBE has been defined in order to determine the capability of radiation to kill cells provided a reference radiation, or in other words how the radiation corresponds to cell survival.

RBE may be determined by the ratio of absorbed dose of incident radiation D_A and the absorbed dose of the aforementioned reference radiation D_R. RBE may be expressed as:

$$RBE = \frac{D_R}{D_A} \tag{2.2}$$

Radiation Type and Energy	**Weighting Factor (W_R)**
Photons (X-ray & γ)	1
Electrons, positrons and muons	1
Neutrons	
< 10 keV	5
10 keV to 100 keV	10
$>$ 100 keV to 2 MeV	20
$>$ 2 MeV to 20 MeV	10
$>$ 20 MeV	5
Protons (E $>$ 2 MeV)	2-5
Alpha, Fissile products & HZE	20

Table 2.1: Radiation Weighting Factors

2.2.2.3 Dose Equivalent and Effective Dose

Dose Equivalent Sum of contributions of dose to tissue from different radiation types, each multiplied by the radiation weighting factor (W_R). A radiation weighting factor is an estimate of the effectiveness per unit dose of the given radiation relative a to low-LET standard.

$$H_T = \sum_R W_R D_{T,R} \tag{2.3}$$

Effective Dose Sum of equivalent doses to organs and tissues exposed, each multiplied by the appropriate tissue weighting factor (W_T)

$$E = \sum_T W_T H_T \tag{2.4}$$

Tissue Type	Weighting Factor (W_T)
Gonads	0.20
Red Bone Marrow	0.12
Colon	0.12
Lung	0.12
Stomach	0.12
Bladder	0.05
Breast	0.05
Liver	0.05
Esophagus	0.05
Thyroid	0.05
Skin	0.01
Bone Surface	0.01
Remainder	0.05

Table 2.2: Tissue Weighting Factors

2.2.2.4 Exposure history

It is a requirement for radiation workers; including but not limited to those working within the medical, aviation and space industries to maintain a detailed radiation exposure history. Astronauts, who are classified as radiation workers, are required to monitor daily dose in order to stay within career limits based upon NCRP Report 98, "Guidance on Radiation Received in Space Activities" (July, 1989)[25]. The maximum exposure limits for astronauts by gender and age are presented in Table 2.3 and the maximum exposure specific to individual organs of astronauts compared with civilians is presented in Table 2.4[26]. Short term (Monthly and Annual) exposure limits have been included in Table 2.4 in order to limit any of the physiological effects common in short term radiation exposures. The career limits have been selected to maintain mortality risks due to cancer, of less than 3%.

Career Exposure Limits for NASA Astronauts by Age and Gender

Age (years)	25	35	45	55
Male	1.5 Sv	2.5 Sv	3.25 Sv	4 Sv
Female	1 Sv	1.75 Sv	2.5 Sv	3 Sv

Table 2.3: Career Exposure Limits for NASA Astronauts by Age and Gender

Radiation Penetration & Exposure Limits for Astronauts/General Public

	Exposure Interval	Blood Forming Organs (5 cm depth)	Eyes (0.3 cm depth)	Skin (0.01 cm depth)
Astronaut	Monthly	0.25 Sv	1 Sv	1.5 Sv
	Annual	0.5 Sv	2 Sv	3 Sv
	Career	1-4 Sv	4 Sv	6 Sv
Civilian	Annual	0.001 Sv	0.015 Sv	0.05 Sv

Table 2.4: Exposure Limits for NASA Astronauts versus Civilian

2.2.2.5 Microdosimetric Method

The microdosimetric approach[3] involves the stochastic measurement of energy deposition (ϵ), upon an event by event basis. The method is dependent upon an accurate and well defined sensitive volume, comparable to that of a biological cell. From the SV dimensions, i.e., the volume (V) and surface area (A_s); the mean chord length ($<l>$) can be determined. According to Cauchy the mean chord length of convex volumes,[27] is given by Equation 2.5.

$$\langle l \rangle = \frac{4V}{A_s} \tag{2.5}$$

Lineal energy (y) is concerned with the energy deposition in a single event and is given as the quotient of the energy deposition (ϵ) and the mean chord length ($<l>$) of the sensitive volume, see Equation 2.6. *Lineal energy (y)* is typically given in units of $\mathrm{keV}\,\mu\mathrm{m}^{-1}$.

$$y = \frac{\epsilon}{\langle l \rangle} \tag{2.6}$$

An event within the context of microdosimetry is the result of charge particles traversing the sensitive volume region, interacting with the target medium and depositing energy. Microdosimetry has an advantage over other methods in that dose equivalent measurements can be made in any mixed radiation field, without a-priori knowledge of field composition. Microdosimetry is limited in that incident particles are 'crossers' and not 'stoppers', i.e. do not come to rest within the SV.

Due to the stochastic nature of ionising radiation interactions in matter, the *lineal energy (y)* is subject to a probability density distribution, f(y). This probabilistic nature, necessitates the use of the frequency mean lineal energy, y_F (Equation 2.7), which in turn can be used to calculate the dose mean lineal energy, y_D (Equation 2.8).

$$y_F = \int_0^\infty y f\,(y)\,dy = \frac{\int_0^\infty y^2 f\,(y)\,dy}{\int_0^\infty y f\,(y)\,dy} \tag{2.7}$$

$$y_D = \frac{1}{y_F}\int_0^\infty y^2 f\,(y)\,dy = \int_0^\infty y d(y) dy \tag{2.8}$$

The dose distribution d(y) is the total dose to the sensitive volume occurring from lineal energies in the region [y: y + dy]. The dose distribution relationship simply reflects the fact that higher lineal energies deposit a higher dose.

$$d(y) = \frac{y f(y)}{y_F} = \frac{y f(y)}{\int_0^\infty y f(y) dy} \tag{2.9}$$

A general feature of most microdosimetric distributions derives from the probability

that the lineal energy, y, and its distribution f(y), span several orders of magnitude. It is thus standard practice to use a logarithmic representation when representing microdosimetric distributions. The y Vs d(y) distribution gives the fraction of total absorbed dose in the interval [y:y+dy]. By definition the distribution d(y) is normalized to unit y:

$$\int_0^\infty d(y)dy = 1 \tag{2.10}$$

and so microdosimetric distributions will typically be plotted as yd(y) Vs. log y.

2.2.3 Applied Dosimetry

The previous sections have provided a brief summary of the radiation environments of space and high altitude avionics. These radiation environments represent an appreciable risk, making radiation detection and measurements a necessity. Section 2.2.3.1, describes the requirements for dosimetric applications in Space environments, likewise a similar study is made of avionic dosimeters in Section 2.2.3.2. With regards to any real world application, a radiation dosimeter must exhibit the following characteristics[28]:

- *Accuracy and precision* : The dosimeter must reliably be able to reproduce accurate measurements under similar conditions.
- *Linearity with dose* : Dosimeter measurement should be proportional to the absorbed dose.
- *Dose rate independence* : Dosimeter measurement should be independent of the dose rate (with/without the appropriate corrections)
- *Energy response and tissue equivalence* : Dosimeter response is known to generally depend upon the energy of the ionising radiation. It also means that dosimeters are required to be constructed from tissue equivalent materials; those characterised with absorption and scattering properties due to radiation similar to biological tissue.

- *Spatial resolution and physical size* : A high spatial resolution should be possible following the Bragg-Gray theory.

- *Dynamic response* : The dosimeter response should be fast and reproducible. This means the device should be characterised by fast rise/decay times during and after exposure.

- *Long term stability of response* : The dosimeter should ideally have a response that is stable during irradiation and also independent of both time and storage conditions before and after irradiation. The device should also be independent of any accumulated dose from successive irradiations.

2.2.3.1 Dosimetry in Space

Since the beginning of space exploration, both manned and unmanned, active and passive dosimeters have been used to measure radiation exposure of astronauts and onboard electronic components[29]. The primary objectives for Space Radiation Dosimetry is to:

1. Accurately monitor astronaut radiation exposures in order to provide warning upon exceeding exposure limits.

2. Monitor radiation environment, providing warning for potentially hazardous radiation environment changes.

3. Document radiation exposure history.

Dosimetry for radioprotection applications in space is clearly distinguishable from standard terrestrial applications by the particular demands and constraints specific to such a task[20]. Space bound dosimeters, must in no way compromise crew safety either in their use or potential failure. This implies limitations upon the materials used in construction,

both in terms of mechanical properties but also in terms of biological risk in case of breakdown, i.e. outgassing of toxic and noxious substances[20]. Financially suitable dosimeters are limited by mass/size, power consumption and material cost and robustness. Detectors must be hardy and robust enough to be able to withstand long term exposure to the harsh radiation fields of space without an appreciable effect upon measurement accuracy, without need of repair due to the probable unavailability of spare parts.

As discussed in section 2.1, the radiation environment of space is complex, with a variety of particles both charged and uncharged spanning a wide range of energies. In addition, depending upon location, time and as yet more unknown variables, the radiation field is subject to large variations in terms of particle flux and energy. Thusly this unique and varying radiation environment requires a device with a large and dynamic range of sensitivities in terms of particle flux, energy, resolution etc. It is desirable to have good charge, energy and LET resolution so as to apply the appropriate quality factors based upon particle type[20] [30].

Since no one detector can possible satisfy these requirements, it is standard practice to include different types of detectors both passive and active, on-board spacecraft. The requirement of widespread dosimetry lends itself to the use of passive detection methods that are small, economical, and can operate without major demands upon the limited supply of electricity during space missions[6]. Passive detectors are limited in that they provide no immediate knowledge of radiation exposure and dose. Instead they are used primarily as a means of documenting exposure, providing a dose legal record (DLR). Active dosimeters whilst generally larger and with higher power consumption, have many benefits over their passive counterparts. The capability of time based dose rate resolution and real time dosimetry provides the ability to distinguish and characterise the dose contribution from varying sources and alert spacecraft personnel to major solar particle events[6]. Since the inclusion of multiple devices leads to financial difficulties and mission concerns in terms of mass and power consumption, the goal is to develop a device capable of meeting as many

of the requirements of space dosimetry as possible.

2.2.3.2 Dosimetry in Avionics

An increased interest has arisen over the years regarding the prolonged radiation exposure of airline crew and frequent flyers. It was recommended by the International Commission on Radiological Protection (ICRP) in 1990 that airline crew be recognised within the same subset as terrestrially based radiation exposure occupations due to exposure to GCR and secondaries produced within the atmosphere and materials which comprise the aircraft[31] [32]. This has sparked interest in on-board dosimetry systems to calculate radiation dose.

Doses on board aircraft are generally predictable, with the rare exceptions of the extremely intense and high energy solar particle events. Thus, it is possible to make calculations of effective dose per unit time as a function of geographic location, altitude and solar cycle phase, for the assumed field geometry (taken as isotropic). Such calculations however can be problematic and require validation, and do not take into account SPE. For this reason, it is recommended that on-board dosimetry systems be in place to monitor dose equivalent in real time and provide accurate dose history.

It is recommended that instruments for dose measurements on board aircraft determine the operational quantity, ambient dose equivalent, H*(10). Instruments sensitive to neutrons as well as to low-LET radiations are required. Some instruments, such as tissue equivalent proportional counters (TEPC), silicon semiconductor LET spectrometers and recombination ionization chambers[33], are capable of measuring both high and low-LET dose components, as well as the approximate LET distribution or mean LET,[34] [30]. It should be noted that the aviation industry at present has no laws to restrict business travellers completing equivalent number of hours per year in flight as airline crew. Some such flights may also include time at altitudes almost as high as that at which supersonic Concorde flights were known to travel. The risk for passengers on these flights is greater however given that this mode of travel is

Route	Duration (Round trip)	Dose (μGy)
Los Angeles to Paris	11.1 hrs	48
Chicago to Paris	8.3 hrs	36
New York to Paris	7.4 hrs	31
New York to London	7.0 hrs	29
Los Angeles to New York	5.2 hrs	19
Sydney to Acapulco	17.4 hrs	44

Table 2.5: Calculated dose due to cosmic ray at altitude 11 km (36000 ft)

sub-sonic and thus time in air is high. Additional restrictions have been recommended for the occupational exposure of pregnant women, where the levels of protection required for the embryo have been further defined[31] [35].

2.2.4 SOI Microdosimetry

Silicon-On-Insulator microdosimetry refers to the layered use of single crystal silicon and insulating material, typically SiO_2 to create a solid state microdosimeter, with SV regions to be created in the initial silicon layer. SOI devices represent a significant advancement over previous silicon bulk devices in that:

1. Decreased parisitic capacitance
2. Decreased leakage currents
3. Decreased sensitive volume size
4. Increased radiation hardness

Silicon-On-Insulator (SOI) microdosimetry has been under development at the Centre for Medical Radiation Physics (CMRP)[24] [36]. Silicon based microdosimeters offer compact

size, low voltage operation and low cost. Being a solid state device also means durability, as well as causing the redundancy of a tissue equivalent gas, such as that used in the tissue equivalent proportional counter (TEPC). Since the beginning of SOI microdosimetry, a number of advances have taken place resulting in successive generations, with each being an improvement upon the last.

2.2.4.1 1st Generation SOI microdosimeter

The 1st generation SOI microdosimeter served well as a proof of concept. This device showed the applicability of SOI technology for use in microdosimetric applications. The 1st generation SOI microdosimeters consists of a 2D planar diode array of rectangular parallelepiped (RPP) SV structures (30 x 30 μm^2) fabricated upon 2, 5 and 10 μm thick p-type silicon. The array consists of 4800 diodes in close proximity and connected in parallel for single SV read out, each with a junction size of 10x10 μm^2.The device structure is illustrated in Fig. 2.11. The charge collection properties of the device were characterised in terms of its use in proton/neutron therapy and space and aviation based radio-protection applications[36] ,[37],[38],[24] [39]. The Charge Collection Efficiency (CCE) of the device was shown to be dependent upon ion strike position due to the less than ideal electric field structure within the planar RPP SV. Charge confinement and therefore SV definition was also an issue, with charge diffusion from outside of the 'SV' regions observed.

2.2.4.2 2nd Generation SOI microdosimeter

The motivation behind the 2nd generation SOI microdosimeter was to address the limitations of its predecessor. To that end, multiple variations were designed, fabricated and tested. The 2nd generation microdosimeter can be divided into two subcategories; the Mesa (3D SV) and the 2D planar array. Each type shares a common feature however, that of a cylindrical SV structure. The cylindrical SV represents an improvement upon the 1st generation SOI

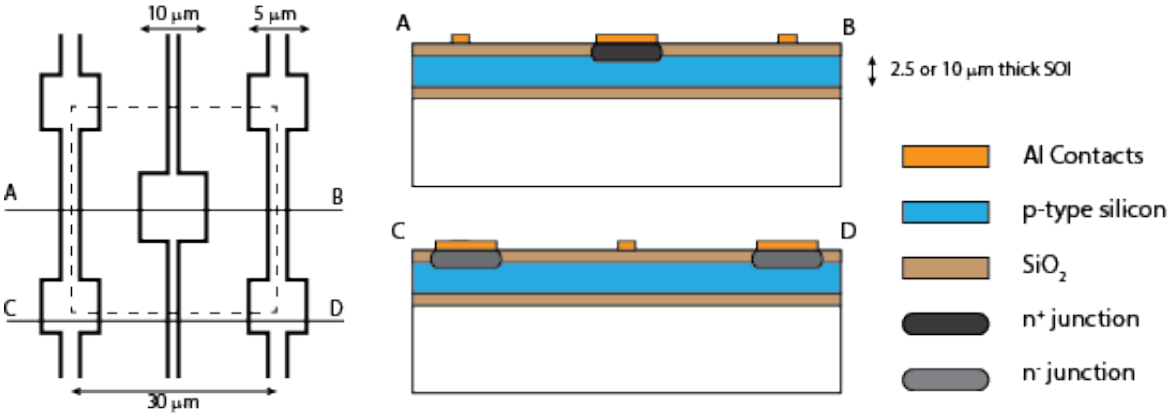

Figure 2.11: Left: A schematic of an SOI Microdosimeter unit cell (dashed square). The dotted lines show the position of the profile cuts on the right. Right: A profile cut (top) though the central n+ region of the unit cell and a profile cut (bottom) though the shared p+ contacts of a unit cell[36].

in terms of chord length variance as compared to that produced by the RPP previously discussed. The cylindrical SV also produces a radial electric field distribution with uniformity that improves upon CCE.

The 'Mesa' SOI, features elevated (mesa) structures fabricated upon a buried oxide. The Mesa structure design combined with the insulating oxide layer acts to physically isolate SVs, thereby limiting charge diffusion between adjacent structures. Two types of mesa structures were fabricated within a SOI layer (2 µm thick), with the first and second designs having a radial width of 2 and 10 µm respectively, see Fig. 2.12a[40]. This device suffered from two main drawbacks. Firstly, results derived from charge collection studies with the mesa device revealed the collection of laterally diffused charge from outside the SV, indicating a lack of confinement and a resultant poor SV definition. Problems incurred during the fabrication, i.e., the evaporation of aluminium contacts, led to a low yield in functioning devices.

The 2D planar array utilises a cylindrical p-i-n diode structure as illustrated in Fig. 2.12b on 2 and 10 µm thick SOI and surrounded by concentric n+ guard rings, to reduce the lateral diffusion which marred the performance of the mesa SOI device. Multiple versions of

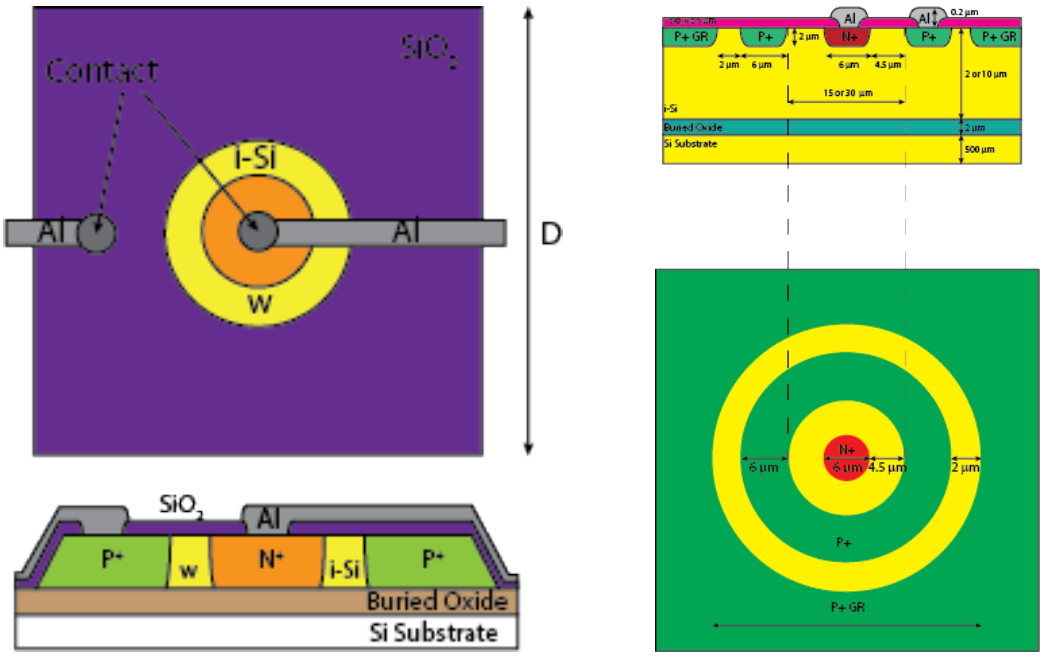

(a) 2nd Generation mesa SOI Microdosimeter[40].

(b) 2nd generation planar SOI microdosimeter[41].

Figure 2.12: 2nd Generation SOI Microdosimeter

this device were fabricated, with the key difference being whether the guard ring is made to surround individual volumes (Defined annular Guard Ring a.k.a DGR) or set so as to separate rows of volumes (Guard Ring Everywhere, a.k.a GRE). Unlike the mesa SOI device, each version of the planar SOI had a constant radial width of 4.5 µm. The planar structure improved upon its mesa counterpart by having well defined cylindrical SV, as observed through charge collection studies, though with some loss in charge collection at boundaries. For the scanned region of interest, most devices were observed to be functioning correctly and adjacent SVs were shown to be fully isolated (i.e., no cross-talk), indicating a higher yield rate of functional SVs and the ability to read out a full array in parallel[41].

2.2.4.3 3rd Generation SOI microdosimeter

The last of the SOI microdosimeter devices that will be discussed in this literature review is the 3rd generation SOI device. The 3rd generation, large area SOI microdosimeters were

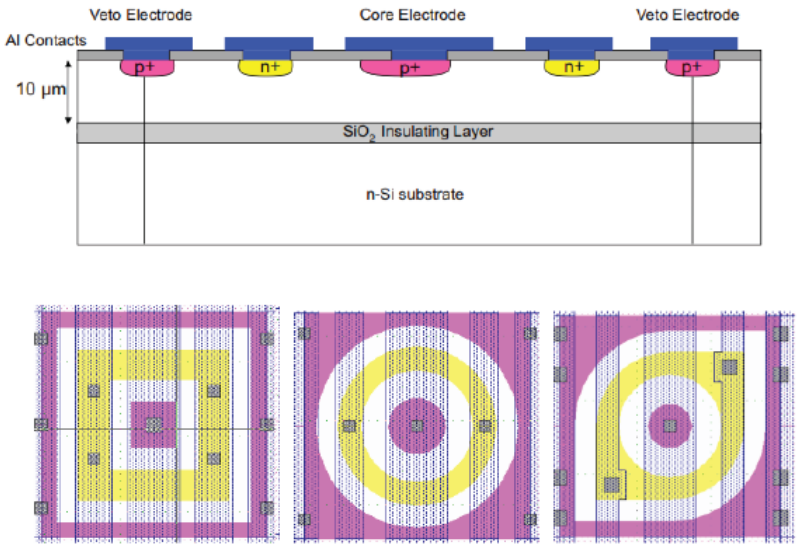

Figure 2.13: Cross-sectional view of the 3rd generation SOI microdosimeter[43].

fabricated upon n-type SOI wafers as opposed to the p-type SOI used in previous generations[42]. Like the 2nd generation device, guard rings were incorporated to reduce charge collection from outside the sensitive volume resulting from diffusion and capacitive coupling. Four different device structures were created utilising RPP (6 and 10 µm width), cylindrical (10 µm diameter) and Rhom-cylindrical SV (6 µm diameter) structures, as shown in Fig. 2.13[43]. The device did however show lack of confinement in terms of diffusion of charge from regions outside the SV and capacitance-resistive charge sharing between adjacent sensitive volumes, resulting in poor definition of the SV.

2.2.4.4 Current Developments in SOI microdosimetry

Recent advancements in fabrication techniques look promising in taking the device to the next step; from the research regime to a commercially viable product. This latest device, utilised etching techniques to isolate sensitive volumes by removing substrate and intermediate silicon material to create 3D structures (mushrooms). The fabrication process simplified can be expressed in a few key points. Firstly, using Deep Reactive Ion Etching (DRIE), holes are 'drilled' into the Si wafer and subsequently filled with polysilicon. A gaseous based dop-

ing technique is used to doped silicon in the regions of interest. DRIE is used again to etch away silicon in the regions surrounding SVs. These voids are then filled with PMMA, acting as a tissue equivalent 'filler' material. DRIE is used for a third time to etch away the silicon substrate from the back, effectively thinning the silicon material and reducing probability of lateral diffusion from surrounding silicon regions. These new SOI devices can then be operated at full depletion, under a low applied bias and have been shown to feature a spatial resolution of approximately 2 μm [44] [45]. It should be noted that this device mentioned is not a microdosimeter, however the fabrication techniques used, appear to be promising in terms of application for microdosimetry.

2.2.4.5 Overview

SOI microdosimeters are a promising technology. The current status, along with advancements in the field, making it likely that SOI microdosimetry will become a viable commercial technology. Currently, research driven SOI microdosimeter technologies developed at CMRP, are producing devices with high yield arrays of sensitive volumes on the cellular scale with high charge collection efficiency. However, silicon based devices, regardless of application, suffer from a lack of radiation hardness and tissue equivalence. For the harsh radiation environments imposed by space and high energy physics applications, diamond is being considered as an alternative to silicon based devices, due to its superior radiation hardness and tissue equivalence.

2.3 Diamond Radiation Detectors

2.3.1 Diamond Structure

Carbon (Z=6) may be found to exist in nature in two different forms/allotrope's: graphite and diamond. Graphite is typically the more stable allotrope under normal conditions, whereas

diamond requires an extended period of time within a high pressure environment to form. Diamonds may be produced synthetically or found naturally occurring. Natural Diamonds are formed within high pressure, high temperature environments over millions of years. Natural diamonds, being a product of nature are highly variable in terms of properties, size, quality and consistency. Natural diamonds often contain impurities which can cause structural and electronic defects. These defects must be considered when selecting materials for use in detectors.

Natural diamonds may be classified by the type and amount of impurities present, with the various categories listed below[46]:

- **Type Ia** diamond contains up to 0.1 % nitrogen impurity and is the most common type of natural diamond.
- **Type Ib** diamond also features nitrogen impurities, but at smaller amounts and are typically present in dispersed substitutional form.
- **Type IIa** diamond is effectively free of nitrogen. These diamonds have improved optical and thermal properties. Synthetic diamond, including the electronic grade synthetic diamond used in this thesis, is of this type. These diamonds are typically synthetic due to their being very rare in nature.
- **Type IIb** diamond is also very pure and contains small amount of boron impurities giving it p-type semiconducting properties.

The electronic configuration of an isolated C atom is $1s^2 2s^2 2p^2$. In order to create the covalent bonds common to diamond, the s orbital mixes with the three p orbitals to form sp^3 hybridization. The four valence electrons are thus equally distributed among the sp^3 orbitals, while each orbital points to one of the four corners of a tetrahedron. The tetrahedral structure, together with the highly directed charge density, give strength and stability to the bonds. Consequently, all the bonds in diamond are of the same length (1.54 Å), with the

same bond angle (109.47 °). Diamond owes its superior radiation hardness to the high cohesive energy related to each bond (3.62 eV/bond), necessitating high energies to displace atoms from its site within the diamond crystalline lattice.

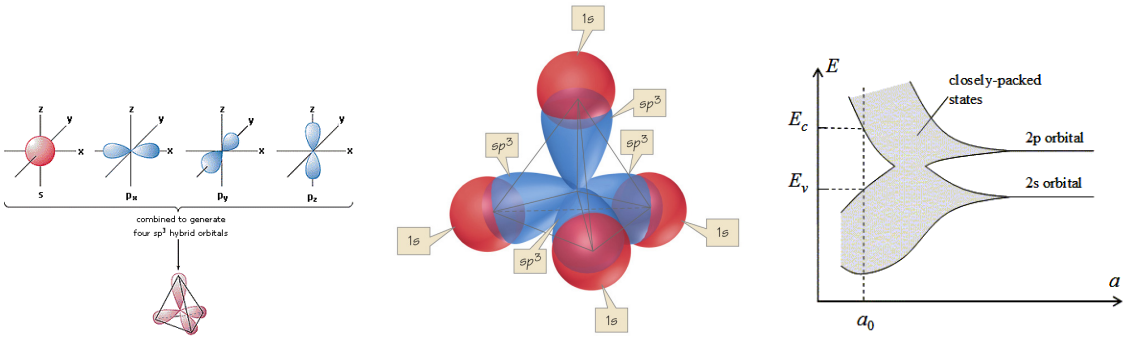

(a) Hybridization (b) Tetrahedral structure (c) Band Diagram

Figure 2.14: Formation of Diamond

As more C atoms come together, there is an overlap of the electron wave functions occupying adjacent atoms. This leads to a splitting of the energy levels consistent with the Pauli exclusion principle. The splitting results in an energy band containing 2N states in the 2s band and 6N states in the 2p band, where N is the number of atoms in the crystal. A further reduction of the lattice constant causes the 2s and 2p energy bands to merge and split again into two bands containing 4N states each. At zero Kelvin, the lower/valence band (E_v) is completely filled with electrons and the upper/conduction band (E_c) is empty, making diamond an insulator or wide band gap semiconductor.

2.3.2 Diamond Properties for Detector application

In terms of the relevant properties (Table 2.6) for radiation detectors, diamond is superior to silicon and other commonly used semiconductor materials in many respects for use in space radiation environments.

Property	Value	Units	Detector Implications
Average atomic number (Z)	6		Tissue equivalence
Density	3.52	$\mathrm{g\,cm^{-3}}$	
Thermal conductivity	20.0	$\mathrm{W\,cm^{-1}\,K^{-1}}$	Heat dissipation
Debye temperature	2200	K	
Electron mobility	2200	$\mathrm{cm^2\,V^{-1}\,s^{-1}}$	Fast signal
Hole mobility	1600	$\mathrm{cm^2\,V^{-1}\,s^{-1}}$	Fast signal
Carrier lifetime	≈ 2000	ns	Full Charge Collection
Relative dielectric constant ϵ	5.7		Low capacitance
Saturation velocity	2.7×10^7	$\mathrm{cm\,s^{-1}}$	
Breakdown field	1.5×10^7	$\mathrm{V\,cm^{-1}}$	
Energy to create e-h pair E_{eh}	13	eV	Low signal
Mean MIP ionization q_p	36	e $\mu\mathrm{m^{-1}}$	
Bandgap	5.45	eV	High T operation
Radiation length χ_0	12.0	cm	Low background
Lattice constant	3.567	Å	
Resistivity	10^{13} - 10^{16}	$\Omega\,\mathrm{cm^{-1}}$	

Table 2.6: Diamond properties and their relation to detector applications[47].

2.3.2.1 Detector Signal

The large band-gap of diamond (5.5 eV) gives a low probability of thermally excited charge carriers crossing the band gap, resulting in low leakage currents and low noise making diamond detectors well suited for high temperature operation[48][49]. A diamond based detector may be considered as a solid state ionisation chamber, can be biased to produce a large internal electric field without the need to engineer a reverse diode to get extra field into the material.

Charge carriers created by the interaction of ionising radiation drift in the presence of an electric field, producing a changing electrical conductance that is measured. Measurements

of this type, have been performed in diamond by numerous groups over the last several decades with some notable pioneers[50] [51] [52]. Diamond detectors are even noted for use as a neutron spectrometer with some distinct advantages over silicon based alternatives[53]. The small dielectric constant (5.6) means devices with small capacitance and low noise operation. However, the amount of energy to create electron-hole pair in diamond (13 eV) compared with silicon (3.6 eV) results in a comparative decrease in sensitivity and an energy resolution of $(13/3.6)^2$ 13 times less[54]. An energy resolution of 82 keV for diamond has been reported for alpha spectroscopy[55]. The suitability of diamond for dosimetry has been shown in several studies[56] [57] [58] [59]. Diamond dosimeters have been shown to have a stable linear response with absorbed dose, a relatively small LET dependence and an independence upon the particle species measured[58].

2.3.2.2 Tissue Equivalence

Given the strong dependence upon the atomic number of a material (Z) that many photonic interactions with matter have, it is generally accepted that tissue equivalence of materials with respect to photons can be achieved by matching of the atomic number. Diamond's low atomic number, $Z_{Diamond}$=6, implies tissue equivalence for photons given its proximity to that of the mean atomic number of soft tissue (Z_{Tissue}=7.42).

Water (Z_{Water} = 6.6) is a commonly used reference material, to compare materials, to determine tissue equivalence. For X-rays, the mass attenuation (Fig. 2.15) and mass energy absorption coefficients (Fig. 2.16) for diamond/water are relatively constant, showing negligible energy dependence, when compared with that of silicon/water. Likewise, with the electron, proton and alpha stopping power ratio (see Fig. 2.17, 2.18 and 2.19)[60]. It is shown that given a suitable correction factor, diamond may also be considered as tissue equivalent for protons and alpha particles typical of GCR and SPE (see Chapter 12)[9]. Carbon also has a similar neutron cross section tissue making it applicable within neutron fields.

The tissue equivalence of diamond make diamond an ideal candidate for use in dosimetric applications. Diamond dosimeters in 'online mode' have been shown to outperform ionisation chambers in terms of sensitivity by several orders of magnitude[61]. The suitability of diamond in dosimetry has been supported from various authors across the literature[62] [63] [64] [65]. The chemical inertness and mechanical robustness also make diamond particularly promising for in-vivo dosimetric applications[66].

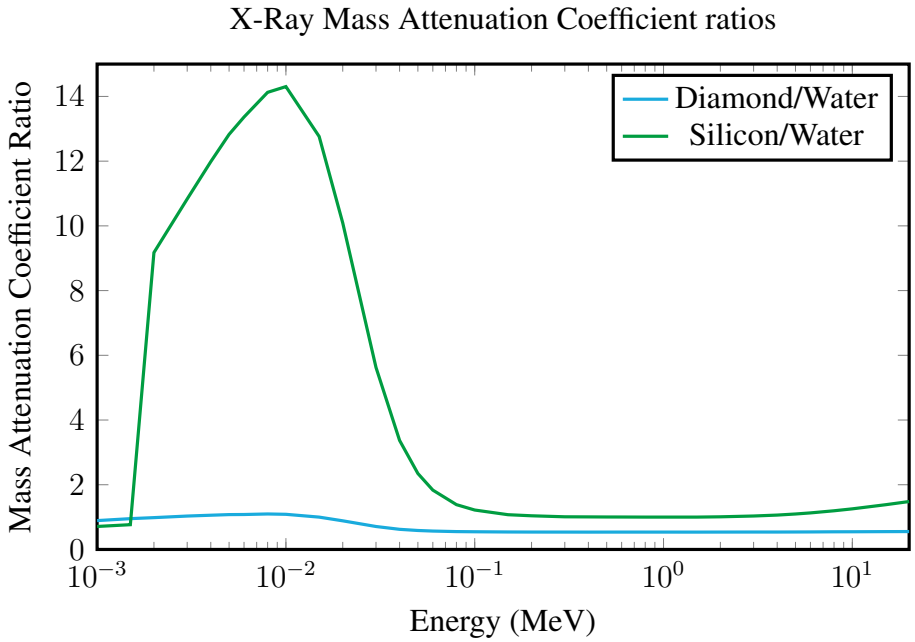

Figure 2.15: NIST X-Ray Mass Attenuation Coefficient ratios[60]

2.3.2.3 Radiation Hardness

Complex and severe radiation environments necessitate a device with a long operational lifespan in terms of its ability to withstand radiation damage. The strong covalent bonds, large band-gap and small neutron transmutation cross section make diamond a radiation hard material able to meet this need[67] [68] [69] [70] [71]. While the relative sensitivity of diamond ensures that silicon will never be fully replaced; the superior radiation hardness qualifies its choice to supersede silicon in severe radiation environments such as: low earth orbit mis-

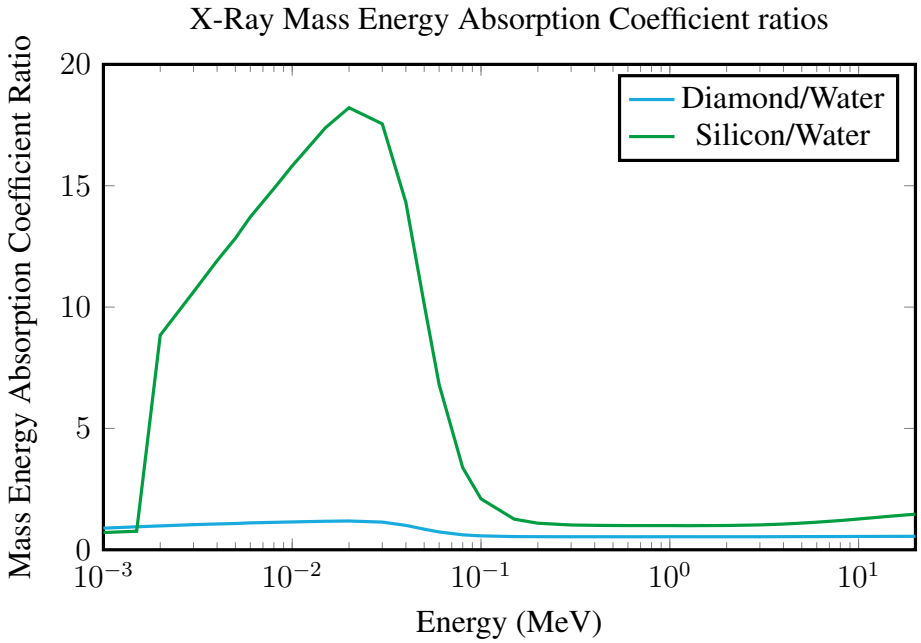

Figure 2.16: NIST X-Ray Mass Energy Absorption Coefficient ratios[60]

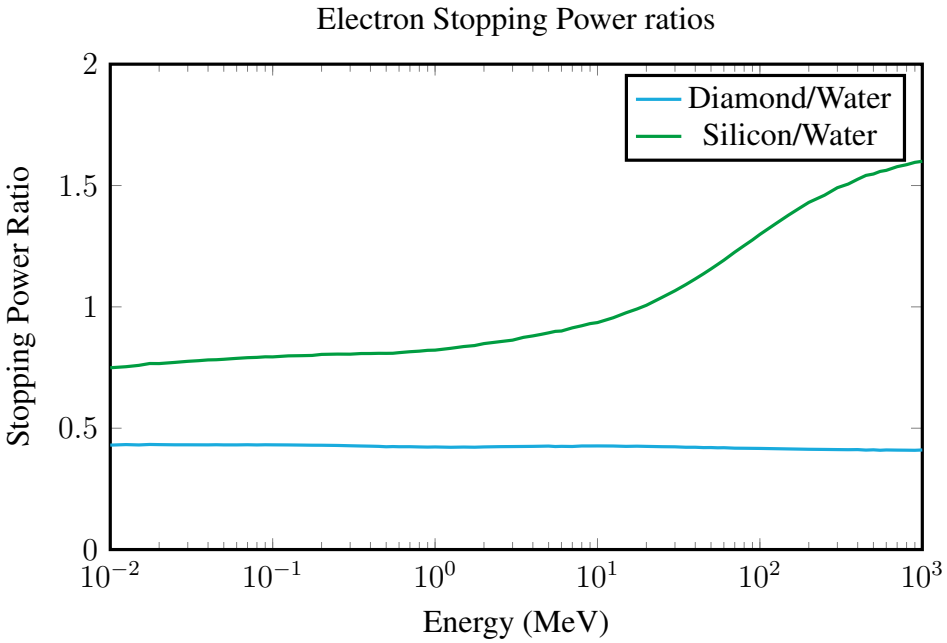

Figure 2.17: NIST Electron Stopping Power ratios[60]

sions, aviation[72] and for use in high energy physics experiments[20][73][63].

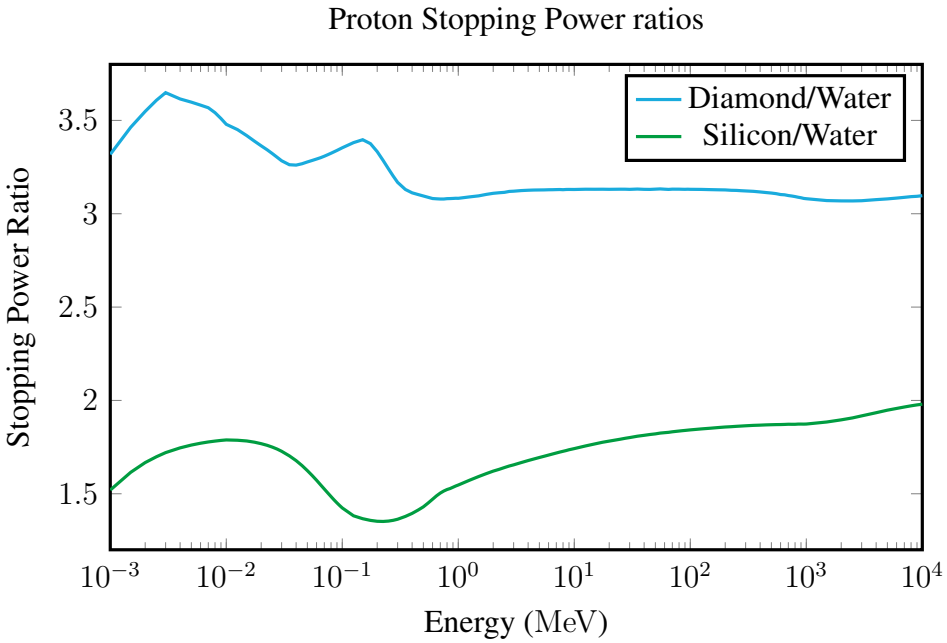

Figure 2.18: NIST Proton Stopping Power ratios[60]

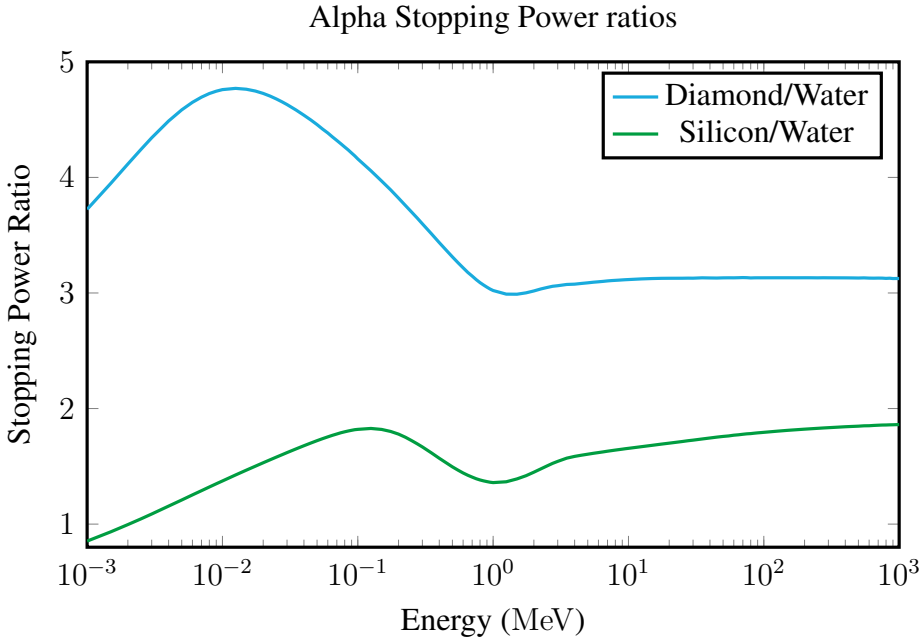

Figure 2.19: NIST Alpha Stopping Power ratios[60]

2.3.2.4 Micromachining

For measuring small fields the sensitive volumes (SV) reported vary between as low as 0.48 mm^3 [59] up to and exceeding 1.4 mm^3 and 6.4 mm^3 [56],[58]. In each of these cases, the SV size is due to the sample availability or from controlled limitations imposed during the diamond growth process itself rather than by any post-growth fabrication means. The limitations upon SV size imposed by the microdosimetric method require a method to create micron sized isolated SVs. Recent reports on generating device SVs have used ion implantation[7], laser milling[8], microstructures using sacrificial silicon moulds[74], bottom-up engineering[75] or angled etching[76] and have shown progress in creating small structures confined either electrically or physically. The physical manipulation of SV size in diamond by lithographic definition of the metal contact pads has been performed by W. Adam, *et al*,. 1999[77] (with a minimum width of 50 $\mu\mathrm{m}$) in a polycrystalline diamond where the CCD is in the same order as the contact pad spacing. However, for metal contacts patterned on single crystal diamond where the CCD is very much greater than 50 $\mu\mathrm{m}$ it is unclear how the charge sharing between pixels will affect the detector's spatial resolution.

2.3.3 Synthetic Diamond

Diamond has been investigated for use in radiation detection for decades, due to its many desirable qualities (see Table 2.6). Initially investigation was centred solely upon natural diamond[50]. Such research was hampered by the lack of consistency in material quality and composition. The emergence of synthetic diamond has seen a resurgence in diamond based research, due to the improved quality of diamond on offer. Whilst an improvement over its naturally formed counterparts, initial work with synthetic samples, still suffered from inability to produce diamond with Nitrogen concentration consistently $\leq$ 10 parts per million (ppm)[52]. Improvements in the Chemical Vapour Deposition (CVD) fabrication process has led to polycrystaline (PC) diamond with improved carrier mobilities[78] and increased

charge collection distances (CCD) 50 μm[79] and 150 μm[77]. As the development of the CVD fabrication process continued, high purity single crystal diamond was introduced. A reduction in charge trapping sites coincided with the removal of grain boundaries that typify polycrystalline diamond, which in turn led to improved carrier mobilities[80]. Single crystal diamond was shown to outperform the polycrystalline diamond by 2-3 orders of magnitude in terms of $\mu\tau$ products (mobility-lifetime), i.e. CCD[81].

The charge collection efficiency (CCE) of a device is the ratio of the collected charge, (Q_M), to the charge produced, (Q_0). It has been reported that a CCE of almost 100% can be achieved with high purity single crystal CVD diamond with an electric field of >0.3 $V\,\mu m^{-1}$ [82] [83]. CCD is defined as the mean distance, with which an electron and hole can separate, and can be expressed as the product of the electric field strength, E, with the sum of the electron and hole mobility, μ, and lifetime, τ product. It can also be directly inferred from the CCE given the detector thickness (d), i.e. if the CCE is 100% then the CCD must be greater than the detector thickness. The CCD of CVD diamond has been shown to be dependent upon the strength of the applied electric field, and the quality of the sample material itself. In one study the CCE was shown to drop off to 0% at 100 μm[83] whilst another study reported a CCD of approximately 500 μm under an external electric field with strength $1\ V\,\mu m^{-1}$ for scCVD diamond amounting to the thickness of the diamond providing full CCE[84].

Synthetic diamond, either single or polycrystalline, can be produced with large surface areas (mm^2) and at consistently high purity with few defects. Whilst a variety of grades of diamond are on offer (i.e. optical, electronic), this work shall deal primarily with high purity single crystal diamond with typical nitrogen content in the order of parts per billion (ppb), purchased from Element6[1] and Diamond Delaware Knives Inc.[2] or grown at the Melbourne Centre for Nano-fabrication (MCN).

[1] Element Six Ltd, Kings Ride Park, Ascot, SL5 8BP, UK- http://www.e6.com/

[2] Diamond Delaware Knives Inc, 3825 Lancaster Pike Wilmington, DE 19805 U.S.A - http://www.ddk.com/

2.3.3.1 Diamond Defects

Defects can appear in different forms in diamond crystal such as:

- Point defect: The two main types of point defects are Schottky and Frenkle defects and refers, respectively, to the singular vacancy or misplacement to an interstitial site of an atom within the lattice structure.

- Line defects: refer to misalignment of of the crystal lattice, usually caused by edge or screw dislocations, which refer to extra planes present orthogonal to crystal growth or appearing at the surface, respectively.

- Planar defects: refer to stacking faults in addition to faults due to the presence of grain boundaries. Stacking faults occur when an additional yet smaller plane of crystalline atoms occur between the normal much larger crystal planes. Grain boundaries, which are problems specifically for polycrystalline diamond, appear at the interface between two distinct crystals having different crystallographic orientations. The results being a line of defects along the boundary interface separating the two crystalline lattices

Defects in the material can give rise to charge trapping and produce a fixed space charge. Two phenomena have been shown to occur due the occurrence of fixed space charge and are as follows:

- **Polarization**, effects occur with the partial or non-uniform filling of charge traps due to the interaction of ionising radiation with diamond. The resultant space charge creates an internal electric field to oppose that of the externally applied field. This results in decreased field strength throughout the bulk material and a subsequent loss in signal and charge collection efficiency.

- **Priming** effects occur with a more complete filling of charge traps. Complete occupation of charge traps, leads to improved charge collection via decreased free trap density and a corresponding increase in carrier lifetime.

Polarisation and priming effects are stable at room temperature given that charge traps are typically located in the band gap, some as deep as 1 eV and thus naturally restrict trap filling from thermally excited charge carriers. Deep charge traps may be depopulated however, provided the input of enough energy to thermally excite carriers. De-trapping may also be achieved via illumination of the sample with light having energy less than that of the bandgap. It is common practice to pre-expose lower quality diamonds to UV light in order to improve the long-term charge collection properties of a device.

The goal in the production of electronic grade single crystal diamond is to minimise any and all impurities to obtain pure intrinsic diamond. Common impurities in CVD growth are Nitrogen (a substitutional impurity), and is introduced into the crystal lattice unintentionally. These impurities may be the product of the CVD process itself or an externally introduced contaminant (i.e. from poor vacuum). Substitutional impurities are those which replace carbon atoms at lattice sites within the crystal structure and can, depending upon concentration, have an undesirable and unanticipated effect upon the electronic properties of the diamond material. Dangling bonds (unsatisfied valence condition) commonly form around impurity sites and depending upon concentration can drastically alter electrical properties.

In some applications however, impurities or dopants are introduced purposefully to fulfil a desired role, i.e., changing electrical characteristics etc. Common intentionally introduced dopants include: Li, B, S and P and can be done during the CVD process or post growth, using ion beam implantation. The characteristics of diamond are readily susceptible to changes in the concentration of impurities, and thus great care and foresight must be given to the CVD process and any inclusion of impurity atom, intentional or otherwise to ensure optimal quality of the diamond.

Part II

Methods

Chapter 3

Fabrication

The diamond based radiation detectors in this thesis have been produced as part of a joint collaboration between the Centre for Medical Radiation Physics at the University of Wollongong and the MicroAnalytical Research Centre (MARC) at the University of Melbourne. This chapter has been written with the purpose of providing the technical details of the fabrication process for each detector constructed.

3.1 Chemical Vapour Deposited Diamond

The diamond used in this work is high purity electronic grade type IIa single crystal chemical vapour deposited diamond (scCVD) and has been purchased from Element6[1] and Delaware Diamond Knives Inc[2]. The wafer size of the purchased samples is typically around 4x4 mm^2 with thickness between 30 and 500 $\mu\mathrm{m}$. Additionally, detector grade diamond was also grown as part of this work upon a wafer of boron doped diamond.

The synthesis of CVD diamond is a low pressure process, that takes place typically between 1 and 200 Torr. The process is conceptually simple, requiring a target substrate, energy and

[1]Element Six Ltd, Kings Ride Park, Ascot, SL5 8BP, U.K- http://www.e6.com/

[2]Diamond Delaware Knives Inc, 3825 Lancaster Pike Wilmington, DE 19805, U.S.A - http://www.ddk.com/

two reagents; a carbon containing precursor gas (typically a hydrocarbon like methane) and pure hydrogen gas.

$$\mathrm{CH_4} \xrightarrow{\text{Activation}} \mathrm{C_{Diamond}} + \mathrm{H_2}$$

The hydrocarbon and hydrogen gas are energised to create a plasma of free hydrogen radicals and hydrocarbons. The energy required to generate atomic hydrogen radicals can be produced by microwaves, radio frequency, laser induction, hot filament etc, see Fig. 3.1

$$\mathrm{H_2} \longrightarrow 2\,\mathrm{H^+}$$
$$\mathrm{CH_4} + \mathrm{H^+} \longrightarrow \mathrm{CH_3} + \mathrm{H_2}$$
$$\mathrm{CH_3} + \mathrm{H^+} \longrightarrow \mathrm{CH_2} + \mathrm{H_2}$$
$$\mathrm{CH_2} + \mathrm{H^+} \longrightarrow \mathrm{CH} + \mathrm{H_2}$$
$$\mathrm{CH} + \mathrm{H^+} \longrightarrow \mathrm{C} + \mathrm{H_2}$$

As the hydrocarbon and hydrogen radicals, react according to the chemical equations above, sp^2 and sp^3 bonds are formed, creating a layer of carbon upon the target substrate. Under normal conditions, the graphitic sp^2 bond is more stable than the diamond like sp^3 bond counterpart.

Hydrogen in the form of a reactive free radical, is the key behind the CVD process for diamond synthesis. Whilst atomic hydrogen will react with both sp^2 and sp^3 carbon bonds, reactions with sp^2 bonds are more likely/preferential. Therefore, despite the fact that sp^2 bonds are thermodynamically more likely to form, the continual suppression sp^2 bonds through reactions with atomic hydrogen results in a net growth of sp^3-bonded carbon, or diamond[85]. Growth conditions and substrate will determine the quality and crystalline structure of diamond produced.

The formation of single crystal diamond requires a diamond based substrate as a forming layer or seed, with subsequent growth forming layer by layer, adopting the crystalline nature of preceding layers. Once a sample of suitable size has been formed, a significant amount

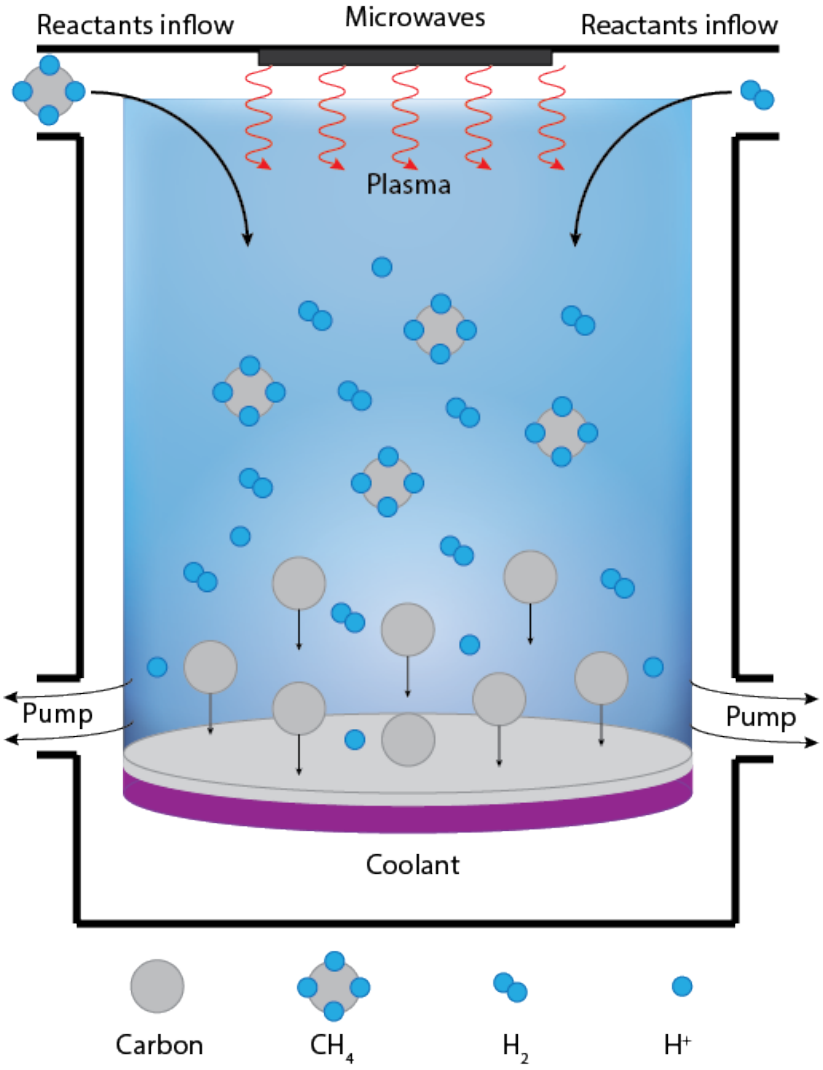

Figure 3.1: Diagram of the CVD reactor used to produce synthetic diamond. Microwaves produce hydrogen radicals which react with hydrocarbons, with the deposition of carbon upon the base substrate.

of post-growth processing is required in order to produce sample material of use. These processes may include, but are not limited to the removal of any remaining sp^2 bonded carbon and hydrogen contaminants and the mechanical polishing and cutting for required sample size. Post-processing is a time consuming process and requires significant time and expertise. The superior qualities that make diamond ideal for many applications, i.e., its hardness, also make it a demanding material to work.

3.2 Ion implantation

Ion implantation is a technique that can alter the physical and electronic properties of a material through the directed embedding of ions. This technique is best suited to semiconductors where a small concentration of impurity/dopant atoms can have a large impact upon the materials electronic qualities. Ion implantation of 2 MeV stripped boron ions accelerated by the MARC 5U NEC Pelletron Accelerator (see Fig. 3.3) was performed upon high purity single crystal CVD diamond. The implantation of boron was utilised to create a radiation damaged patterned region in diamond in the 1st generation device, essentially creating P-Type diamond.

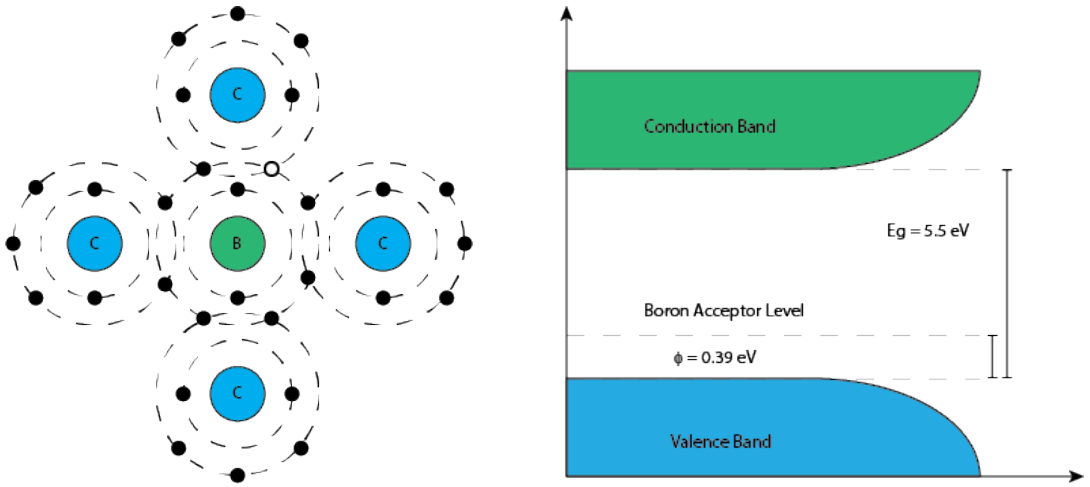

(a) Boron Substitution (b) Boron Acceptor levels

Figure 3.2: Extrinsic P-type Diamond through boron implantation.

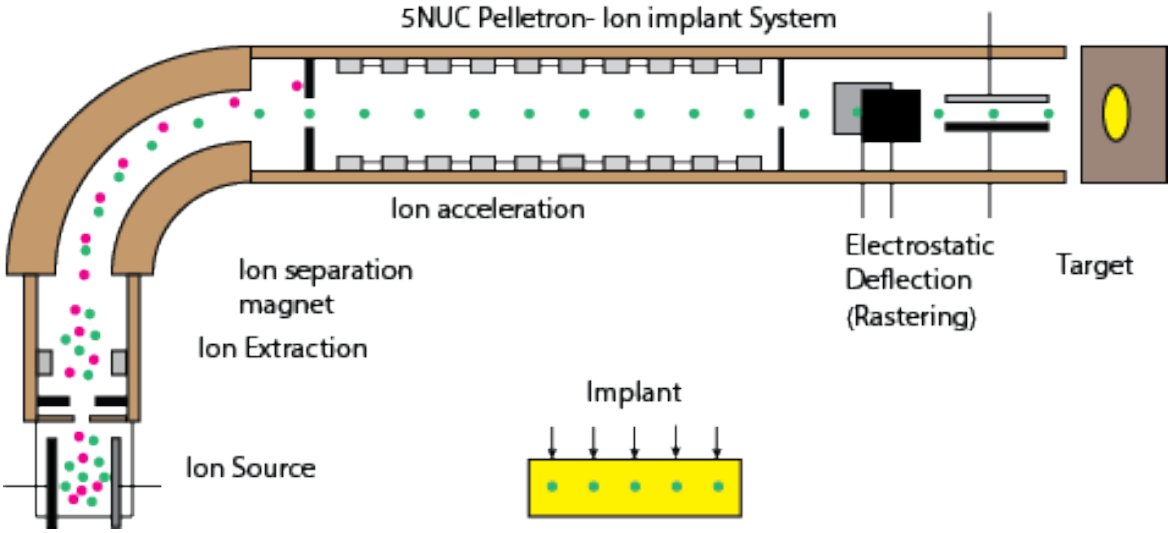

Figure 3.3: Schematic of an ion implantation system, with particles originating within the ion source (left) and directed upon the target (right)

3.3 Sample preparation and cleaning

Throughout the fabrication cycle, the sample material should be cleaned to remove any unwanted contaminants, biological or otherwise. A number of methods are available to meet this end. Solvents used for cleaning are acetone, methanol, ethanol and isopropanol with purity greater or equal to 99.5%,

3.3.1 Sonication

Sonication is a non destructive technique used in the cleaning process. Dust particulates and other undesirable contaminants are removed in this process through ultra sonic agitation. Sound with frequencies greater than 20 kHz is applied using an ultrasonic bath or sonicator. The sample is placed within a volumetric flask filled with acetone solvent (99.5% purity) and placed upon the stainless steel basket of the sonicator which is immersed within water. As the sound waves pass through the system, particles vibrate with the experienced pressure wave cycle resulting in a process known as cavitation, where the formation and subsequent

collapse of microscopic bubbles or cavities causing mixing, molecular disruption and the breaking of particulate clumps.

3.3.2 Acid Etching

One of the primary purposes of Acid etching for this project was the removal of graphite; a by-product left over from the laser milling method (see Section 3.5.1). An acidic solution is made using a mixture of sodium nitrate ($NaNO_3$) and sulphuric acid (H_2SO_4) using a 0.5g:2-5ml mix. The acid solution and sample are added to a round-bottomed flask, which is placed within a sand bath situated upon a hot plate and supported by a retort stand. The process takes place at approximately 225 $^{\circ}\mathrm{C}$ for a period of 60 min.

3.3.3 Plasma cleaning

Oxygen plasma cleaning was performed in a Diener FEMTO LF with a 40kHz, 50W generator. The sample/detector is placed within the sealed plasma chamber with process gas (25% oxygen:75% argon) pumped in. Plasma is created by use of high frequency voltages causing the gas molecules to become highly excited until an ionised state is reached. Oxygen based, gas phase plasma is an electrically neutral mixture of electrons, ions, radicals, photons, recombination products and neutral particles[86]. As excited particles de-excite to lower energy states, they release their energy in discrete bundles of energy equal to the difference in energy of the two states, i.e photons. For argon, this corresponds the production of photons with typical wavelengths in the UV range of λ = 309 and 336 nm. This provides the plasma cleaning process with a light blue "glow". The wavelength of emitted light can be useful in breaking chemical bonds. The reactive radical species are capable of chemical work where the ionized atom and molecular species are capable of physical work through sputtering[86].

3.4 Microscopy

A number of microscopy methods were used throughout the fabrication process as a means of quality assurance in terms of the methods being employed. The various microscopy tests employed, allowed for the measurement of important spatial features produced throughout the various stages of the fabrication process.

3.4.1 Optical Microscopy

Optical microscopy was performed on a Leica DM2700 M upright compound microscope and a Leica EX5 stereomicroscope. An attached measurement grid allowed for micron scale measurements to be performed with one interval/gradient equal to 1 μm at 100x optical zoom. This tool was useful for measuring the depth of laser cuts along the side of diamond substrates during the laser optimisation process (see Section 3.5.1.3).

3.4.2 Optical Profiling

Optical profilometry is a non-contact means of profiling samples. Optical profilers are interference microscopes which are used to measure height variations on surfaces with great precision using the wavelength of light as the ruler. Optical interference profiling is a well-established method of obtaining accurate surface measurements. The primary mode in which the Bruker Contour GT-K 3D optical profilometer was put to use in this work was vertical scanning interferometry. This technique was used to measure key features, specifically trench depth following laser milling. Optical profilometry was used as a preliminary form of quality assurance to assess each stage of the fabrication process, ensuring that the process was unencumbered by fault. Monochromatic green light was used at 5x and 20x magnification in the vertical scanning interferometry mode. The vertical resolution was 0.120 μm. Phase stimulated interferometry was also used in this work to examine surface

roughness following polishing routines.

3.4.3 Cathodoluminescent Microscopy

Cathodoluminscent (CL) microscopy utilises an evacuated cathode tube gun to bombard a sample with electrons, with the energy dependent upon the applied potential. This microscopy method takes advantage of electron interactions within the sample material, namely luminescence, to examine the composition and texture of the sample. An optical examination of these properties can be enabled by using optical microscopy in conjunction with cathodoluminesence.

3.5 Micro-Machining processes

3.5.1 Laser machining of Diamond

The superior hardness and chemical inertness of diamond are advantages for many applications, yet provide a significant challenge in terms of engineering, in order to be useful. Mechanical processes are time consuming and are useful only upon a macroscopic scale. By contrast, laser processing, provides a non-contact means of manipulating the spatial dimensions of diamond material by optical and thermal processes with the required precision at microscopic scale.

3.5.1.1 Equipment

All of the LASER milling recorded in this thesis, was performed upon an Oxford laser Alpha Series / Ultra-compact Micromachining System [3]. The LASER source was a diode-pumped, solid state Nd:YAG system of 532 nm wavelength. The system produced pulse durations

[3] Oxford Lasers, 8 Moorbrook Park, Didcot, Oxon, UK, OX11 7HP- http://www.oxfordlasers.com/laser-micromachining/laser-micromachining-systems/

between 5 - 100 ns (15 ns at 5 kHz) with a repetition rate of 10 - 50,000 Hz, and a power of 2.5 W at 6 kHz.

The workstation was a Class 1 enclosure containing a computer CNC stage, exhaust line and optional inert gas shower. The CNC stage was a servo motor driven ball-screw XYZ CNC stage holding the workpieces with a resolution of 0.1 $\mu\mathrm{m}$ and accuracy of $\pm$ 2 $\mu\mathrm{m}$. The control software (g-code) was custom written by the user and interfaced the CNC stage with the LASER source.

3.5.1.2 Machining Process

The concept of LASER milling is simple. The LASER is used to ablate a small amount of material and then is scanned across the surface to produce the desired feature.

The effectiveness at which LASER ablation can remove target materials is dependent upon the material's optical properties and the wavelength of the LASER. Diamond, having poor absorption qualities is a difficult material for Laser ablation. The operating parameters must be optimised to the quality of the diamond in order to produce accurate micron sized structures.

Due to the poor absorption of diamond, an absorbing layer such as gold may be applied to the surface to promote LASER ablation. The LASER will ablate the absorbing layer and in doing so the surface of the underlying diamond will be converted to graphite allowing efficient absorption. Sequentially, the graphite is ablated and a new layer of diamond is converted. This process is continued until the desired spatial feature has been produced. As sequential layers are ablated the CNC stage steps down in the vertical plane in user defined increments to ensure the focus is always optimised.

3.5.1.3 Laser Optimisation

The parameters for Laserablation must be carefully selected in order to produce the desired feature. First and foremost is the selection of an appropriate wavelength with minimum absorption length, to ensure highly localised energy deposition for rapid and confined ablation. The second parameter is that of pulse duration and repetition rate. It is important to select a short pulse duration with repetition rate high enough to provide maximal peak power and minimise thermal conduction to the surrounding regions. Appropriate selection of time and rate will increase the efficiency of ablation rate and localisation. The fourth parameter is the beam quality, which may be described and quantified in terms of brightness (energy), focusability and homogeneity. Beam quality is perhaps the most important consideration in terms of laser machining. The uniformity and beam spot size according to the focusability will allow for beam energy to be efficiently delivered to the target ablation region, without which, will result in a larger than desired ablation region with increased sloping in the side-walls of the ablated region. A balance of operating conditions is crucial in order to produce features of fine detail at the required depth. A mismatch in these parameters may result in the production of coarse features with an undesirable ablation depth. Parameters are optimised in preliminary testing and fine tuned in order to produce reliable and consistent results. Typical operating parameters have been included in Table 3.1.

Operating parameters for laser ablation

Paramater	Wavelength (nm)	Frequency (Hz)	Power (%)	Sweep time (s)	Depth (μm)
Value	532	5000	10	0.05	15

Table 3.1: Typical operating parameters of Oxford alpha series laser used in this work. Power has been referred as a percentage of total available power output of the system. The depth of laser ablation in scCVD diamond with a 200 nm absorbing layer (gold) has been given.

3.5.2 Focussed Ion Beam Milling

Focussed ion beam (FIB) milling was used to remove diamond from a desired region with improved spatial resolution as compared with pulsed laser milling. This method was used in the 1st generation diamond microdosimeter to create a milled region which could later be filled with gold Active Braze Alloy (ABA) to create a contact connection with the buried boron mesh created through ion implantation as described previously in Section 3.2.

3.5.3 Polishing

Various polishing methods were employed in the fabrication process to either remove unwanted diamond material (substrate thinning) or to lap overlying metal or epoxy layers to be level with the diamond surface. This is done so as to remove any height based discrepancies upon the surfaces of buried contact structures and the surrounding diamond material.

Automated: The Rotopol system[4] was used to polish back surface layers of metal contacts applied during the brazing process (see Section 3.6.1). A force of 40 N was applied during the procedure. The polishing plates used was made of steel with layers of nano-diamond paste and was rotated at a constant rate. The plate was continually cleaned throughout the procedure to remove braze by-products. In addition, de-ionised water was used to cool the polishing plate to limit thermal conduction to brazing metals.

Manual: Various grades of sandpaper were used to manually polish brazing metal and epoxy resin. Tissue paper was used in the final stages as it provided less coarseness than the finest commercial grade sandpaper.

[4]Struers Rotopol system, 27 Mayneview Street, Milton, QLD 4064, Aus- http://www.struers.com.au/

3.6 Metallisation

In order for diamond to be applicable as a radiation detector, a means of signal collection is required which necessitates connection to an electrical circuit. Metal-diamond contacts, either Ohmic or Schottky, are therefore inherently necessary in order to create any type of detector technology. The underlying principle behind the formation of Ohmic metal-diamond contacts is the appropriate matching of work function of the contact metal to that of diamond ($\phi \approx 5$ eV)[87]. Carbide forming metals like titanium (ϕ = 4.33 eV) and Tantalum (ϕ = 4.22 $\pm$ 0.06 eV) are used often in such applications, having closely matching work function and providing good adhesion with the diamond surface[87]. The typical requirements of such contacts are metallurgical stability at elevated temperatures and good adhesion[88]. Additionally, contact metals are chosen specifically to avoid injection of charge carriers into the diamond bulk material given an applied bias balanced with providing efficient charge collection. Given that one metal may not be sufficient to meet all requirements, it is often common practice to use layered metallisation schemes in order to take advantage of the different properties of each. An example is the selection of Ti(50 nm)/Ni(50 nm)/Au(20 nm) scheme used in the indium bump bonding process (see Chapter 9). In this scheme, three different metals are selected in order to meet the requirements of adhesions and metallurgic stability. The titanium is selected for its well known adhesion to diamond surfaces, whereas nickel is selected as it bonds well with indium. A thin gold or platinum layer is applied after nickel in order to prevent oxidisation of the nickel surface. It is clear that great care must be given in the selection of metals to be used for metal-diamond contacts.

For the purpose of microdosimetry however, an additional requirement is applied to the selection of metals, which is to satisfy tissue equivalent requirements. For this purpose, aluminium, having a relatively low atomic number (Al (Z) = 13) is selected as part of this work.

The standard requirements for metal-diamond contacts are:

- low contact resistivity (for ohmic/nonrectifying contacts);
- good adhesion;
- high thermal stability;
- high corrosion resistance;
- bondable top-layer; and
- suitable for micro-patterning

Two different methods of metallisation were used in this work, brazing and evaporation via photolithography. Both methods are described in the following sections.

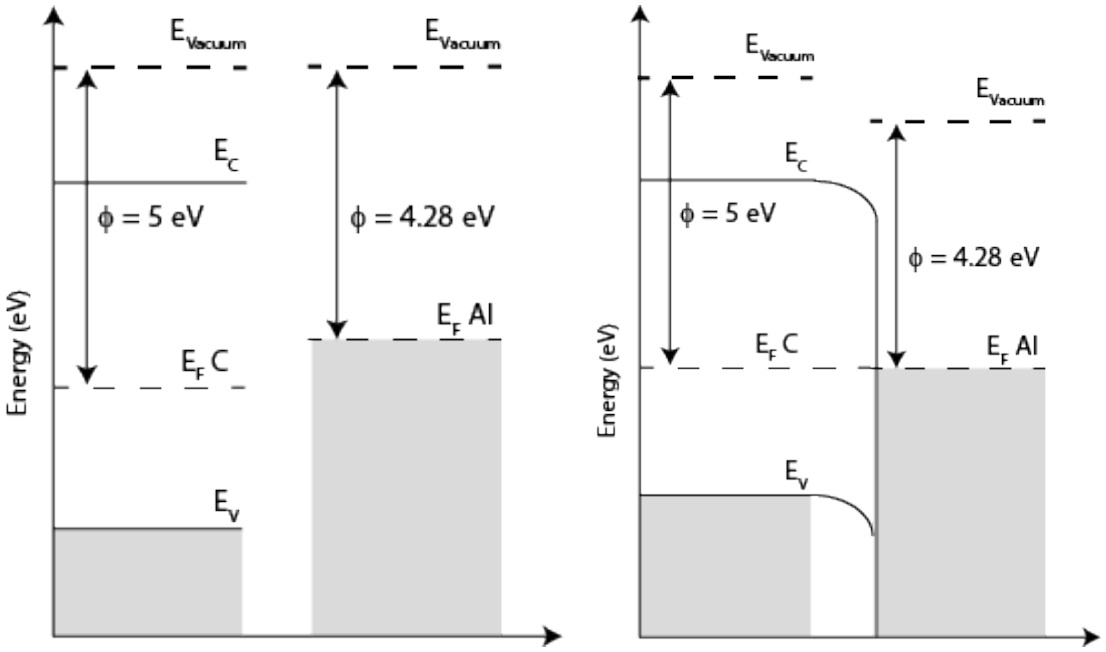

(a) Before (b) After

Figure 3.4: Work function diagrams at the Insulator (diamond) / Metal (Aluminium) interface before (Fig. 3.4a) and after (Fig. 3.4b) contact. As the two materials form an interface, in order for the fermi levels to align, the conduction and valence bands bend, as illustrated.

3.6.1 Active Brazing Alloys

Active Brazing Alloys (ABA) are commercially available materials that provide an alternative means of bonding metals to a desired surface. Brazing typically takes place at temperatures greater than 450 $^{\circ}\mathrm{C}$. Active braze alloys contain an active element, usually Titanium which allows for wet application to a sample material. Forming gas (4.14% H2, balance Ar) was used during brazing to exclude oxygen. Silver and gold ABA were chosen in this work as they create good ohmic contacts with diamond.

3.6.1.1 Brazing

Two different methods of brazing were used throughout this work to braze/set the metals, which are listed.

- **Quartz tube furnace** with maximum operating temperature of 1100 $^{\circ}\mathrm{C}$ was used for brazing and curing of liquid glass. Forming gas flowed through the quartz tube after an evacuation step to provide an inert, oxygen-removing atmosphere. The achievable vacuum was on the order of 10^{-2} mbar, so a positive pressure of forming gas was used to control the atmosphere.

  Brazing samples were held in a quartz boat which remained in the tube during furnace ramp up. The boat could be moved in and out of the hot zone while under controlled atmosphere, as it was attached to a magnet on the end of a long quartz stem.

- **Electron Beam Evaporator** was also used as it provides a low vacuum environment for metals to be brazed over long duration.

3.6.2 Photolithography

Photolithography is the process of transferring geometric shapes from a mask to the surface of a diamond wafer. Photolithography is a binary pattern transfer, in that a pattern is ei-

ther transferred or it isn't. The fine detail and thickness of contact shapes created through lithography depend upon the materials, deposition rates and dispersion of light during UV exposure. The complete list of steps involved in the photolithographic process are mask design/creation, wafer cleaning; photoresist application; soft baking; mask alignment; exposure and development; and hard-baking. These steps are outlined in the following sections, except wafer cleaning given its previous coverage in Section 3.3.

3.6.2.1 Shadow Mask

Masks are designed using KLayout; a free-ware program that allows for the production of simple designs with output in standard dxf file format. This format systems allows for compatibility with equipment used to manufacture masks. The design is etched onto photosensitive chromium backed glass to the effect that the desired patterns are visible as regions without a chromium layer. An alternative method to produce shadow masks was also implemented due to time constraints. Laser ablation was used to produce the desired designs upon chromium coated glass by using the co-ordinate output, from the aforementioned .dxf file in the appropriate g-coding script. Using the contact exposure method outlined in Section 3.6.2.3. Whilst this method inherently involves more steps, all of these processes could be performed in house at the University of Melbourne.

3.6.2.2 Photoresist application

The photoresist is a liquid chemical that allows for the transfer of patterns from one surface to another utilising its well known sensitivity to UV radiation. The standard method for application is 'Spin Coating', which utilises high speed centrifugal motion to produce a uniformly thin layer of photoresist on the wafer surface. Depending upon the need (i.e., contact thickness), different resist thickness's are required. The resist thickness depends upon the spinner rotational speed and the photoresist material. The wafer is held in place by vacuum

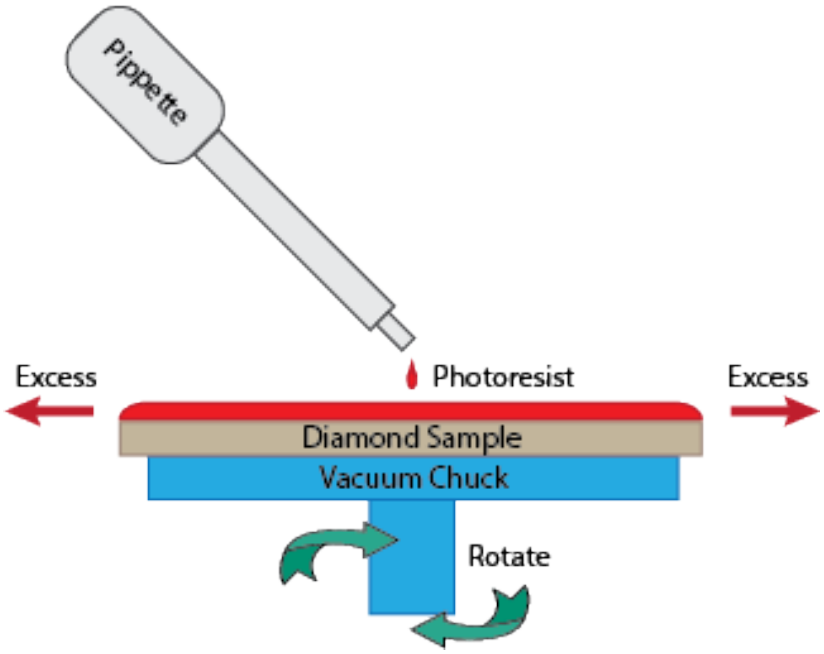

Figure 3.5: Depiction of the process of photoresist application and spinning.

upon the chuck of the spinner and then, depending upon the recipe parameters, subjected to a spins up to between 2000-6000 rpm for approximately 15-60 s see Fig. 3.5. Two different spin recipes were using in this work in order to produce two different thickness's of photoresist, which will then correlate to different thickness's of evaporated metal.

The spinning process following photoresist dispersion, is an incremental process of three stages, where speed is stepped with time according to a recipe. During this process, it is common for spin artefacts to be produced, which may affect the uniformity of the photoresist layer as a result. In this work, the most commonly observed artifact was spin edge beading, being an increased thickness of photoresist. A non-uniform thickness in the photoresist layer will affect further steps in the photolithography process, therefore a technique to resolve this affect was utilised. This method involved embedding the sample within a Polydimethylsiloxane (PDMS) construct providing a artificially lengthened top surface. The effect of this technique is not to eliminate edge beading, rather it is to translate the effect of edge beading outwards until it no longer affects the target sample, see Fig. 3.6. The last

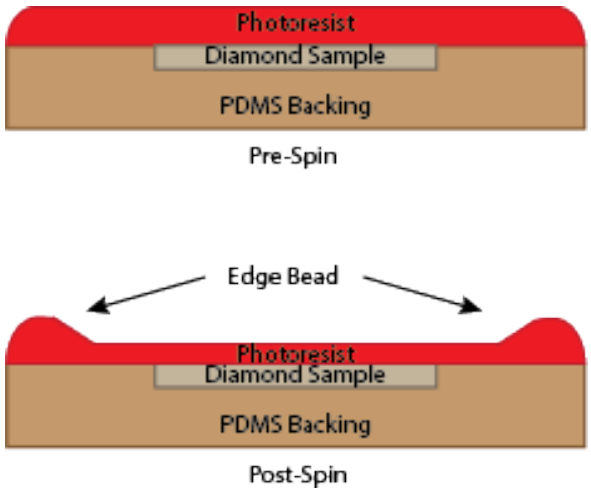

Figure 3.6: Depiction of the process used in this work to avoid edge bead effect through the use of PDMS construct

step in this section is to cure/set the photoresist which requires the sample and resist to be 'baked' upon a hot plate at 100-110 °C for 60 s.

3.6.2.3 Mask Aligner, expose and development

The next stage in the photolithography process is the alignment, exposure and development of the sample. The Neutronix Quintel Q4000[5] is used to align predefined markers upon both the shadow mask and the sample. Multiple cross hairs at various locations upon the sample surface are used to ensure the best agreement is reached. Once suitable alignment has been made, the two surfaces are brought into contact and held in place. The set-up is then exposed to UV light (λ = 350 nm) for a period of 10-30 s. Given a positive photoresist, patterns are created in the regions exposed. The exposure to UV light decomposes a development inhibitor in the photoresist, such that when the sample is then developed in a specific solution (AZ 400K), the solution used will dissolve photoresist only in exposed regions. The entire process is either carried out in a dark room or with UV filtered lights to minimise extraneous UV light sources. Once the developer solution has been applied (typically 30-90 s), the sample is rinsed with deionised water and dried in pure nitrogen gas. The sample then

[5]Neutronix Quintel, 385 Woodview Ave,200 Morgan Hill, Ca 95037, U.S.A- http://neutronixinc.com/

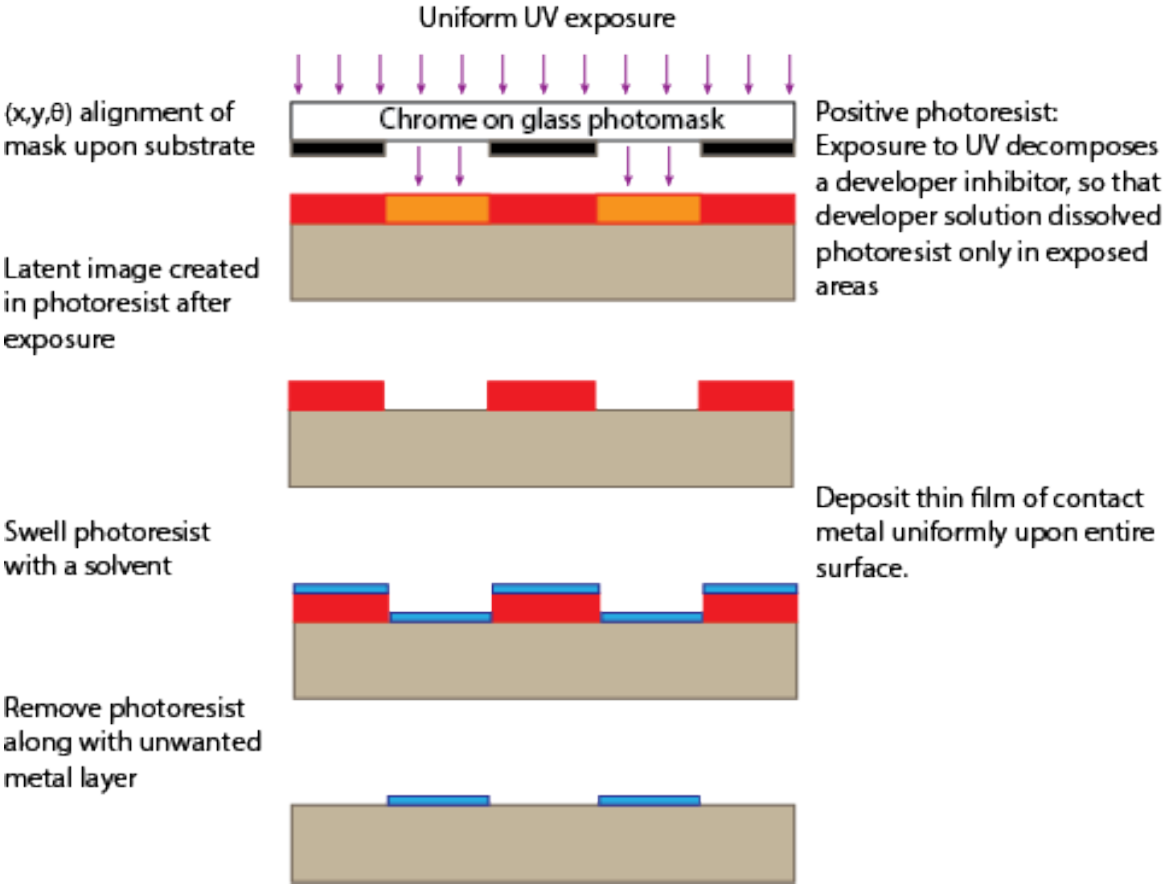

Figure 3.7: Photolithographic process for contact metallisation

undergoes a post-bake to stabilise and harden the developed photoresist and remove any traces of the developer solution.

The Neutronix Quintel Q4000-6 UV front side mask aligner, has a flexible size vacuum chuck system capable of handling wafers up to sizes of 2" with sub-micron feature resolution. It is capable of handling both contact, non-contact and proximity based exposure modalities depending upon user needs for both thin and thick photoresist.

3.6.2.4 Electron Beam Evaporator

Given that photolithography is used in this work to produce patterned electrical contacts upon diamond surfaces, the next stage involves controlled metal deposition processing using the photoresist as a masking film. Electron beam evaporation of Aluminium, gold, plat-

inum, chromium and nickel metal layers was performed in a Thermionics VE-180 Coating System[6], with a 3 kW electron gun and ultimate vacuum on the order of 1 x 10-7 mbar.
The Lesker 75 model[7] Indium evaporator was used to evaporate Indium bumps through a shadow mask upon two separate wafers. This was done, so as to allow for the process of bump bonding to take place. Bump bonding in this case, is where respective Indium bumps upon the two separate diamond surfaces can be bonded together to form a connection between separate diamond wafers.
Pure metals used for evaporation were obtained from Kurt J. Lesker, Australia. These comprised 99.99% purity titanium pellets, 99.9% purity gold pellets, 99.9% purity nickel pellets and 99.99% purity indium pellets.

3.6.2.5 Stripping/Lift-off

The final stage in the photolithography/evaporation process is lift-off. In this process, unwanted metal situated on top of the photoresist is removed as is the underlying resist layer. This is achieved by means of sonification in acetone and then plasma cleaning as described in Section 3.3.1 and 3.3.3.

[6]Thermionics, 1842 Sabre Street Hayward, California 94545, U.S.A- http://www.thermionics.com/
[7]Kurt J. Lesker, 39 Allegheny Square Glassport, PA 15045, U.S.A -https://www.lesker.com

Chapter 4

Experimental Detector Characterisation Techniques

A standard set of experimental techniques have been used to characterise all of the diamond detector technology discussed in this thesis. This chapter is dedicated to discuss these techniques in detail in order to provide the basis for which experimental results will be discussed.

4.1 Electrical Characterisation

Electrical characterisation is the first testing of new devices performed, following fabrication. The first and foremost aim, is to ensure device functionality, thereby providing quality assurance of the fabrication process used to realise the device. Secondly, devices are characterised to ensure that the electrical characteristics of the device are appropriate for the desired application.

4.1.1 Current-Voltage (I-V) Characterisation

Current Voltage (I-V) measurements are performed on all devices as a preliminary means of detector characterisation to ensure the integrity of each device. IV measurements are used

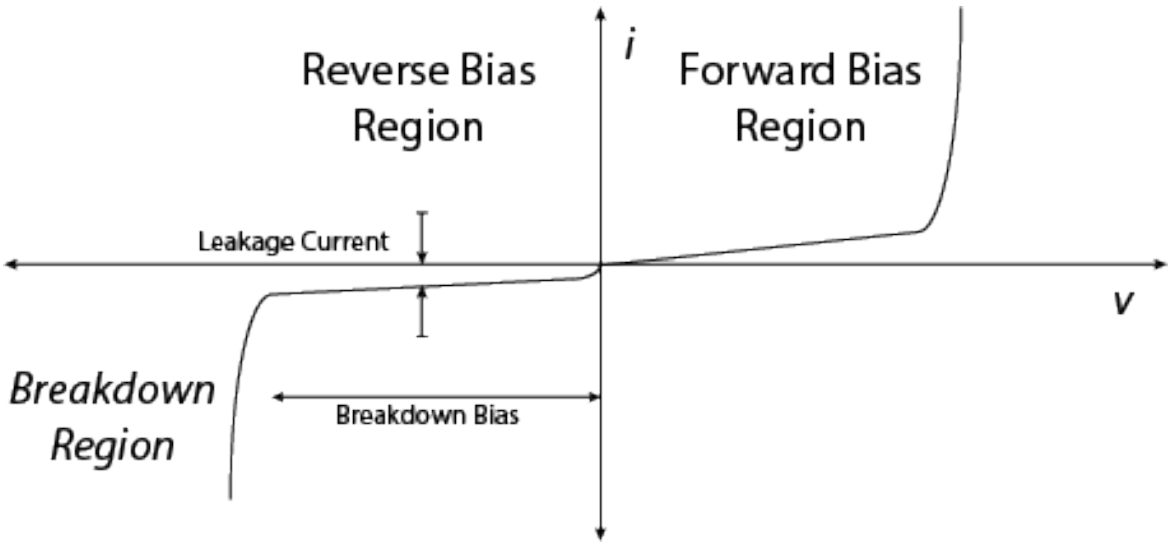

Figure 4.1: Current-Voltage (I-V) curve of a diode.

to produce I-V characteristic curves, which serve as a visual illustration tool to determine and understand the basic parameters of a component or device.

This work utilises diamond (electrical insulator), sandwiched between two metals, effectively creating a Metal-Insulator-Metal (MIM) diode. The I-V curve corresponding to MIM diodes is dependent upon the choice of metals on either side of the insulator material, a.k.a diamond. It should be noted at this point that the choice of metals used to create electrical contacts is dependent on the matching of work functions between metal and diamond. An asymmetric I-V curve is the result of having metal/insulator interfaces, with different barrier heights on either side, and would lead to some measure of rectification. The barrier height (ϕ_B) value is defined in Equation 4.1, where ϕ is the work function of the metal and χ, the electron affinity of the insulator.

$$\phi_B = \Phi_M - \chi \tag{4.1}$$

Diamond, being an electrical insulator, is a material where all electrons are bound within the valence band and separated from the conduction band by a large band gap (5.5 eV). The

electrical properties of diamond are largely determined by its large band-gap. The size of the bandgap prohibits the thermal conduction of electrons at room temperature (limiting leakage current) and is what gives intrinsic diamond such a high resistivity in the region of $10^{42}\ \Omega\,\mathrm{cm}$, see equation 4.2. The high resistivity means that intrinsic diamond can act as a radiation detector without the need for a dopant/impurity atoms.

$$I_T = CT^{3/2}exp(-E_g/2kT) = \sqrt{n_V n_C}exp(-E_g/2kT) \tag{4.2}$$

where:

- C = Proportionality constant characteristic of the material
- T = Change in temperature
- Eg = Band-gap
- k = Boltzmann constant

Since the majority of charge carriers do not flow freely therefore, it is necessary to provide energy or a driving potential in order for bulk diamond to conduct. When diamond is stimulated by an applied bias, the electrons can acquire the energy required to become free and conduct. Breakdown occurs when the applied bias is too high, leading to an exponential increase in the current flow. The breakdown voltage or bias is another important parameter given that it defines the operating parameters for which a device may be effectively and safely used. The breakdown voltage for a device may be determined by Equation 4.3 and the breakdown field for diamond is $10^{6-7}\ \mathrm{V\,cm^{-1}}$.

$$V_{BV} = \frac{\epsilon_r E_C^2}{2qN_d} \tag{4.3}$$

Charged mobile carriers contribute to current flow via diffusion and drift mechanisms. The drift velocity of electrons and holes (see Equation 4.4 and 4.5) is dependent upon the

magnitude of the electric field, but can and will saturate (saturation velocity) at higher electric fields. Operation at high drift velocities is desirable in that the carrier collection time can be minimised and an improvement in charge collection efficiency can be obtained.

$$\nu_h = \mu_h E \tag{4.4}$$

$$\nu_e = \mu_e E \tag{4.5}$$

The leakage current ($I_{Leakage}$) of a radiation detector is independent of radiation, but rather a product of the material conductivity. The high resistivity of diamond ensures that the leakage current of diamond based radiation detectors to be typically quite low. It is desirable for detectors to have a small leakage current to limit noise, thus making leakage current an important consideration in the development of radiation detectors. Given the relatively large mean ionisation energy for diamond (13 eV), it is important to limit leakage current and therefore noise to ensure an optimal signal to noise ratio to maintain the viability of diamond for use as a radiation detector. The leakage current of a device may be determined through analysis of I-V characteristics. The leakage current along with the total resistance of the circuit (R_{Total}) has the effect of limiting the true bias applied across the detector (V_{Det}), as shown in Equation 4.10. A high leakage current will reduce the bias applied across the detector region, effectively decreasing the electric field strength, slowing drift mechanisms and thus hampering charge collection. The derivation for such is shown below, with the first step being an examination of the voltage drop across the detector, which may be determine from Ohms law by:

$$V_{Det} = I \times R_{Det} \tag{4.6}$$

Where R_{Det} is the quotient of V_{Bias} and $I_{Leakage}$ and may be determined from mea-

surements taken to produce an I-V curve (Equation 4.8). Since the current measured depends upon not just the resistance of the detector, but of the entire circuit (i.e. $R_{Total} = R_{Set-up} + R_{Det}$), then we have:

$$I = \frac{V_{Bias}}{R_{Total}} \tag{4.7}$$

$$V_{Det} = I \times \frac{V_{Bias}}{I_{Leakage}} = \frac{V_{Bias}}{R_{Total}} \times \frac{V_{Bias}}{I_{Leakage}} \tag{4.8}$$

$$V_{Det} = \frac{(V_{Bias})^2}{I_{Leakage}(R_{Set-up} + R_{Det})} = \frac{(V_{Bias})^2}{I_{Leakage}(R_{Set-up}) + I_{Leakage}(\frac{V_{Bias}}{I_{Leakage}})} \tag{4.9}$$

$$V_{Det} = \frac{(V_{Bias})^2}{I_{Leakage}R_{Set-up} + V_{Bias}} \tag{4.10}$$

Measurements were performed at the detector lab at the Australian Nuclear Science and Technology Organisation (ANSTO) using a Keithley 237 High Voltage Measurement Unit. The hardware used is controlled by dedicated computer software (Metrics V2.1). A limit of 100 μA was placed upon the measurement procedure to prohibit current overload. Voltage steps are followed by 3 second delay to allow current to stabilise before measurements are taken. All measurements were taken at room temperature, which was not explicitly regulated and is thus considered to be typically 25 $\pm$ 3 °C.

4.1.2 Capacitance-Voltage (CV) Characterisation

Capacitance-voltage (C-V) characterisation of devices is another important technique utilised in the preliminary testing of a device performance. C-V measurements provide insight into the electrical noise specific to the detector. The capacitance (C) of a device can be deter-

mined by the ratio of the charge (Q) and the operating bias (V) as given by:

$$C_{Det} = \frac{Q}{V_{Det}} \tag{4.11}$$

$$Q = \int I \, dt \tag{4.12}$$

$$V_{Det} = \frac{1}{C_{Det}} \int I \, dt \tag{4.13}$$

In terms of operation, this translates to a ratio of the signal (Q) received by the charge-sensitive pre-amplifier and the input voltage (V) to the pre-amplifier, with the result (C) being the sum of the detector capacitance (unknown) and amplifier capacitance (known). Typically detectors with low capacitance are considered desirable, given the dependence of signal-to-noise ratio upon capacitance. A constant capacitance over a bias range indicates full depletion operation. Intrinsic diamond, being a natural insulator can for all practical purposes be considered as fully depleted unless it is otherwise doped.

All C-V measurements were performed upon a Boonton capacitance meter (Model 7200) controlled by a PC via an IEEE-488 interface at ANSTO. The system is calibrated prior to testing without the device connected to cancel out capacitance contributions inherent in the experimental set-up. The Boonton 7200 provides fast characterisation of components at 1 MHz, and has a resolution of 0.01 pF with a measurement error of 0.5%. It utilises two phase sensitive detectors to perform simultaneous measurements of the device resistance under a known bias and frequency, in order to produce a capacitance value in pF.

4.2 Charge Collection Characterisation

4.2.1 Signal Processing

The majority of radiation detectors require a combination of signal processing electronics and software so that information, i.e. energy and time, pertaining to ionisation interactions can be properly extracted and represented. In this section, the signal processing electronics used is described in detail.

4.2.1.1 Pre-Amplifier

Following an ionisation event, a small current is induced by the collection of charge at electrodes through a combination of drift and diffusions mechanisms under the presence of an electric field. The signal is passed to the pre-amplifier whose primary function, is to extract and transform/increase the small signal collected into something that is more readily measurable, with minimal degradation of the signal-to-noise ratio. There are essentially two different types of pre-amps, which are :

1. Voltage-sensitive
2. Charge-sensitive

This thesis utilises the Amptek A250; a charge sensitive pre-amplifier, see Fig. 4.2. The low noise, fast rise time (2.5 ns) and high sensitivity (C_f = pF) make it an ideal choice for use in Charge Collection Characterisation of solid state detectors. A charge sensitive pre-amplifier is able to deliver information upon the quantity of charge and the time of occurrence of an event concurrently. A feedback capacitor C_F between the input and output stores the charge from the detector. For charge sensitive pre-amps, the output voltage V_{out} is proportional to the input charge Q_{Det}. The charge is integrated over a feedback capacitor to avoid any sensitivity of the gain with respect to changes in detector capacitance during

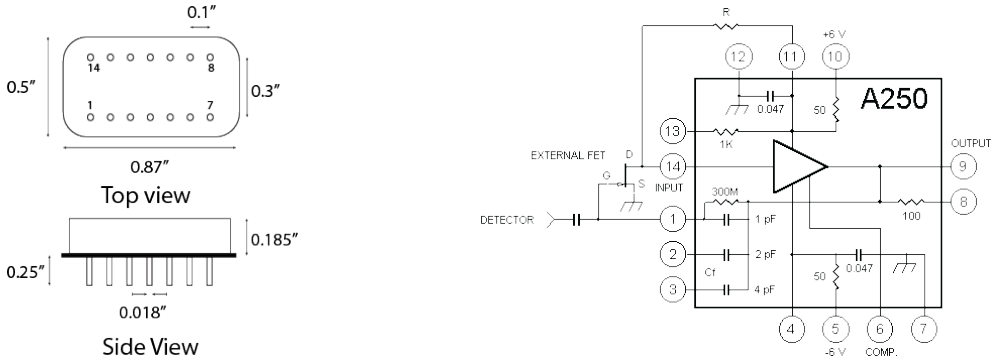

(a) Structure (b) Schematic

Figure 4.2: Amptek A250

ionisation events, and ideally will give a rise time of the output pulse equal to that of the detector current pulse width.

Without the inclusion of a feedback resistor in parallel with the feedback capacitor, V_{Out} will increase until the preamplifier reaches its maximum output. The feedback resistor, provides a means of 'resetting' the pre-amp, by selectively modifying the decay time (Eq. 4.15) of the pulse. The inclusion of R_F introduces a significant component of noise within the system, one that albeit decreases with increasing resistance. Increasing the resistance corresponds to an increased pulse tail length. The long tail makes digitizing the pulse heights impractical, because pulses will often ride on top of the long tail of one or perhaps several preceding pulses before the output voltage has returned to its baseline. Due to this pile up of events, signal pulses are first routed through a shaping amplifier before digitization.

Given that the number of charge carriers created by an ionisation event is proportional to energy deposited, then so long as the decay time constant, is sufficiently large with respect to the duration of the input pulse, then once appropriately processed, can be used to make dose equivalent measurements. The output voltage V_{Out} from the pre-amplifier and decay time constant τ_F, is given respectively by Eq 4.14 and 4.15, where Q_{Det} is the charge collected during an ionisation event and C_F and R_F are the feedback capacitor and resistor

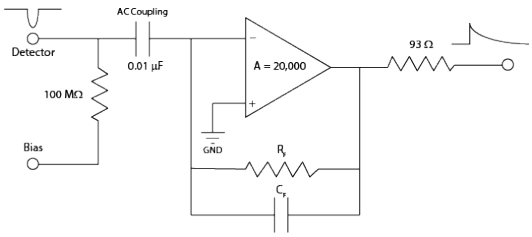

(a) Simplified version of pre-amp

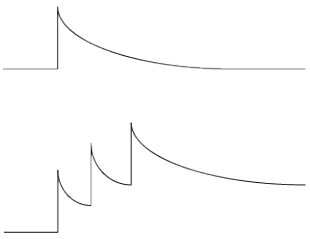

(b) Pulse pile up

Figure 4.3: Amptek A250

respectively.

$$V_{Out} = \frac{Q_{Det}}{C_F} = \frac{\int^t i_{Det} d\tau}{C_F} \tag{4.14}$$

$$\tau_F = R_F C_F \tag{4.15}$$

4.2.1.2 Linear (Shaping) Amplifier

In radiation detection measurements, there are two types of signal pulses: logic and linear. Logic pulses are signal pulses at their most basic and carry information only by their presence or absence. Logic pulses in the context of radiation measurements are only useful in confirming the presence of radiation, but provide no further information. Linear pulses on the other hand carry information particular to the event through its amplitude and shape. Linear signal pulse processing is the more useful of the two for the application of microdosimetry.

The detector signal, now having undergone initial amplification is passed from the preamplifier to the linear ('shaping') amplifier, where further signal amplification (from the mV to V range) and pulse shaping is undergone. The shaping amplifier converts the signal pulse (see Fig. 4.3b) into a Gaussian pulse, a symmetric bell shaped curve. Signal shaping has the effect of increasing the decay time of the signal pulsing, providing a means to reach

a baseline more rapidly. This allows for higher count rates and noise filtering, decreasing the effects of signal pile-up (overlap between successive pulses) and potentially revealing signals that were previously buried/hidden in noise.
The most important parameter to be considered at this stage is the shaping time, which is defined as one standard deviation of the Gaussian pulse. An appropriate selection of the shaping time must be delicately balanced so as to:

1. Minimise electronic noise
2. long enough to collect all the charge from the detector
3. short enough to accommodate the expected counting rate

Pole/Zero cancellation- The long decay time of the input pulse creates a small overshoot in the shape of the output pulse unless a pole/zero correction is utilized

4.2.1.3 Multi Channel Analyser

A Multi Channel Analyser (MCA) analyses and sorts voltage pulses into a histogram or spectrum of events containing information pertaining to pulse-height, which depending upon the application may relate to energy or time of arrival. The MCA makes use of a multiple "channels" equally spaced, with each channel having its unique threshold, allowing for the determination of pulse energy by measuring time above threshold. Once the information has been appropriately binned into a histogram, the spectrum can be stored, displayed and analysed.

4.2.1.4 Pulse Discriminator

Pulse discriminator provides a means to discard pulses that do not satisfy user criteria, i.e. when the input signal falls under an adjustable threshold value. Pulse discriminators typically come in two types; integral and differential. An integral discriminator, rejects pulses

below a certain energy by use of an logic circuit, by having only pulses above a set threshold able to trigger a logic pulse output, allowing for low energy pulses or noise to be ignored. A differential discriminator utilised a second threshold so as to only allow output pulses that fall between the lower and upper threshold values.

4.2.1.5 Analogue to Digital Converter

An Analogue to Digital Converter (ADC) as the name implies, converts a variable analogue signal to a multilevel digital signal, with minimal degradation of the signal information.

4.2.1.6 Pulse Generator

A pulse generator is used to generate rectangular (voltage) pulses, with pulse frequency, amplitude, width and delay all user controlled. Pulse generators allow for the production of pulses, with widths (duration) ranging from minutes down to under 1 picosecond. More-sophisticated pulse generators may allow control over the rise time and fall time of the pulses. The pulse generator is used in this work to calibrate the system, by producing a pulse with amplitude equal to that of the peak of known energy within some spectra associated with radiation field induced energy deposition in a detector.

4.2.2 Ion Beam Induced Charge (IBIC) Collection Characterisation

Ion Beam Induced Charge (IBIC) microscopy/spectroscopy is an analytical technique that exploits the interaction of heavy ion beams, focused down to a micrometer scale, with matter to investigate the electronic properties of devices. Ion Beam Induced Charge (IBIC) collection experiments were carried out at the Microanalytical Research Centre (MARC), University of Melbourne, Australia and at the Australian Nuclear Science and Technology Organization (ANSTO). The work presented in this thesis, however was all performed at ANSTO, with the system described in detail in Section 4.2.2.1.

Regardless of the system used, the method is the same. IBIC is a method whereby charge is induced through the use of incident monoenergetic ions, raster scanned across a device or sample. Charge collection is measured using a spectroscopy system, which is calibrated to energy deposition ΔE, upon an event by event basis (see Section 4.2.2.2) and is measured in co-incidence with x and y coordinates of the beam. Median energy maps can be produced through an appropriate manipulation of these data triplets (x,y, ΔE) to allow for analysis of charge collection characteristics across a desired scan region of a sample.

The amount of energy deposited within the microdosimeter for each ion traversal, was measured with a standard charge sensitive pre-amplifier (Ortec142a), shaping amplifier and multi-channel analyzer (MCA) in coincidence with digitized voltage signals of the beam position, x and y for each event in ΔE.

Matlab was used to produce median energy maps of IBIC measurements. A median energy map is a 512x512 pixel map, with each pixel containing information pertaining to the median energy of charge collected. In order to eliminate dark pixels, the map resolution can be down sampled to 256 x 256 pixels, by taking the median of 4 pulse heights. The data is then upsampled back to a 512 x 512 map using cubic splining to retain initial pixel numbers and then passed through a median filter to further reduce noise. This form of data manipulation (down-sampling/up-sampling) was only used in Chapter 7. These pixels can be spatially resolved using the method described in Section 4.2.2.3.

A similar technique, though much less refined is alpha spectroscopy, which allows for an examination of charge collection properties of a detector before more rigorous testing is performed, such as IBIC. An analysis of the charge collection characteristics of the device with respect to a known field allows for the verification of detector functionality. This experiment involves an alpha emitter of moderate activity (i.e. Americium-241 alpha-gamma source, see Fig. 4.4) placed in close proximity to a detector under an applied bias within a vacuum chamber. Alpha spectroscopy is performed upon all devices before IBIC is under-

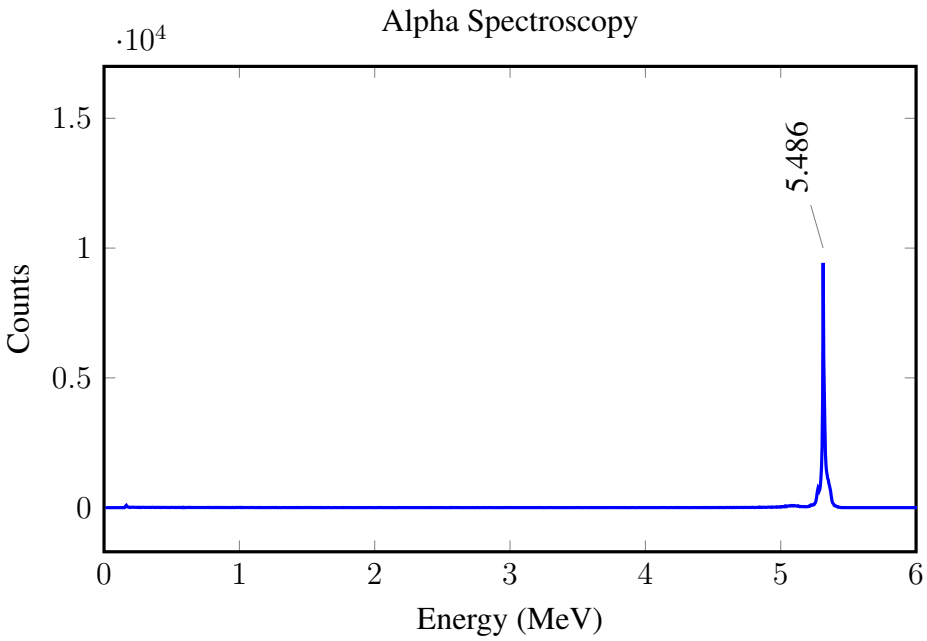

Figure 4.4: Alpha Spectroscopy of Silicon PIN diode. The major energy peak of an Am241 alpha source at 5.486 MeV as labelled.

taken.

4.2.2.1 ANSTO Facility

Most of the IBIC results presented in this thesis are derived from work carried out upon the high energy heavy ion microprobe beam line of the Australian National Tandem for Applied RESearch (ANTARES) accelerator, which is a 10 MV tandem van de Graaf accelerator.

The ANTARES accelerator is capable of producing a broad range of elements spanning much of the periodic table. It is equipped with two sputter ion sources (α-tross and 860 Caesium ion sources) and a charge exchange RF ion source. The results presented in this thesis are for the majority derived from protons and alpha particles, though heavier species such as beryllium and carbon ions have also been used.

The α-tross ion source is used to produce protons and α particles. A RF field is used to ionise

hydrogen or helium gas. The positively charged ions are extracted and acquire a negative charge as they are passed through rubidium vapour. Since the ion source is operated below ground potential, the negative beam is accelerated out of the source and is available for injection into the Van de Graaff accelerator. The negatively charged ions are pre-accelerated to keV energies before being passed to the tandem accelerator where they will be accelerated to the desired energy.

A system of magnets (electrostatic steering plates) and lenses are used to steer and focus the beam, with beam symmetry being monitored at designated beam profile monitors. A Faraday cup and a beam viewer are located after the object slits and before the collimating slits. These are used to optimise and align the beam.

Following the focussing of the keV ion beam, the negatively charged ions are accelerated towards the positive terminal of the Van De Graaf accelerater and passed through a stripping gas (i.e. argon, nitrogen or Sulphur Hexafluoride) or stripper foil, which removes most if not all the electrons. The now positively charged ions are accelerated back and away from the terminal. The belt charging system used in the ANTARES beamline was upgraded to a pelletron system in 1996, which provided improved terminal voltage stability of less than 1 kV at 8 MV[89]. Pelletrons differ from Van De Graaf accelerators in terms of the charging system used. Pelletron chains are made of metal pellets connected by insulating nylon links and are charged by an induction scheme that does not use rubbing contacts or corona discharges. The Pelletron is a superior charging system and offers several advantages for high voltage generation including:

- Excellent voltage stability.
- No spark damage, intrinsically protected.
- High efficiency.
- Isolation from line voltage ripple.

- No electronic diagnostic equipment required.
- Virtually insensitive to moisture.
- Long life (over 50,000 hours reported).
- Simple and reliable.

The name 'Tandem' arises from this two stage process of acceleration, i.e., acceleration before and after stripping. The final energy of the ions after acceleration is dependent upon the terminal voltage (V) and the charge state (q), so that

$$E_{Ion} = V(q+1)e \tag{4.16}$$

where e is electronic charge. Thus the terminal voltage required to produce a 3 MeV proton would be approximately 1.5 MV. In principle, the final kinetic energy is a little bit higher since the negative ions have already been pre-accelerated.

Upon leaving the accelerator, the high energy ion beam is analysed and switched by a 30° deflection magnet. The deflection is sufficient to isolate ions by energy and charge states, as well as neighbouring ions[89]. The selected ions are deflected and steered to the entrance of the heavy ion microprobe (HIMP) beamline. The beamline is then focused by the HIMP lens system, which consists of a magnetic quadrupole lens which have been reported to focus beams up to 166 $\mathrm{MeV\,u^{-1}}$.

Following ion selection and focus, the ion beam enters the microprobe, passing through a set of 'pre-slits'. These are adjustable apertures that allow the operator to limit the current impinging upon object slits which follow immediately after upon the beam line. A second faraday cup in addition to a beam viewer allow for measurement and alignment of the beam. The beam may be further optimised by an additional set, preceding the collimating slits. Finally the collimating slits, beam scanning system and quadrupole system provide the operator a means to control spot size. The target chamber is evacuated by a turbo-molecular

pump and is equipped with a video camera and an x-y-z manipulator for target alignment. The beam scanning system scans ion beams with a maximum scan area of 300x300 μm^2. The data was collected using a MicroDAS data acquisition system from MARC at Melbourne University, which also provided the control of the scanning ion beam.

4.2.2.2 Energy Calibration

The process used to calibrate the energy for charge collection measurements in diamond is the same for alpha spectroscopy and IBIC experiments. This energy calibration method relies upon an assumption that the charge collected is proportional to energy deposition. This technique relies upon a comparison of the charge collection characteristics of a known device to an unknown diamond device, to calibrate the energy deposition within the unknown diamond device.

A 300 μm Hamamatsu S3590-09 PIN diode with an active area of 1 cm^2 mounted upon ceramic carrier, is used to calibrate an Ortec Model 448 precision pulse generator with respect to some known radiation field, whether it is the main 5.486 MeV alpha peak of the Am-241 spectra or alternatively the peak in ion beam spectra. The pulser is calibrated for each perspective gain setting and pre-amplifier/circuitry board combination used throughout experimentation. With appropriate adjustments to the pulser, a range of pulses corresponding to calibrated energies incrementally stepped are passed through the silicon planar diode in order to determine a relationship between channel number and collected charge energy. A line of best fit (y=mx+b) or calibration curve where the gradient (m) of the line is and the y-intercept is the offset is produced for each bias, gain setting and pre-amplifier/circuitry board combination. Once the system has been calibrated to silicon, it can be recalibrated for diamond using the ratio of electron-hole pair formation in silicon (3.6 eV) and diamond (13 eV)[90],[7],[8].

The calibration process relies upon some basic assumptions. Firstly that the dominant en-

ergy (5.48 MeV) of the Am-241 alpha source will come to rest within the detector material, and that the resulting signal is due to 100 % charge collection. Providing that alpha particles cross the detector region orthogonally, and that the range of 5.48 MeV alpha particles is approximately 27.91 $\mu\mathrm{m}$ in silicon 13.57 $\mu\mathrm{m}$ in diamond, this is a reasonable assumption to make. Secondly, when calibrating with respect to diamond, an ionisation energy of 13 eV based upon the relevant literature[90] is assumed in addition to the aforementioned 100 % charge collection.

4.2.2.3 Spatial Calibration

Spatial calibration is performed for IBIC measurements allowing for the production of spatially resolved median energy maps. Spatial calibration is performed by means of scanning transmission ion microscopy (STIM) . This is essentially, a silicon planar diode (B-series charged particle detector from ORTEC) with copper grid with 1000 lines per inch equating to a pitch of 25.4 $\mu\mathrm{m}$. The MCA spectrum and median energy map corresponding to one such measurement is presented in Fig. 4.5 and 4.6. A double peak is present within the MCA spectra, due to the attenuation of the beryllium ions passing through the copper grid. The results presented here, refer to the spatial calibration measurements undertaken for the BID detector presented in Chapter 6. Given the known dimensions of the STIM grid, along with scan size, pixels can be calibrated in terms of distance. Using this calibration, along with the ratio of scan size from STIM image to IBIC median energy map, spatially resolved median energy maps can be produced. This calibration technique using STIM, is carried out for each ion/energy used in IBIC measurements.

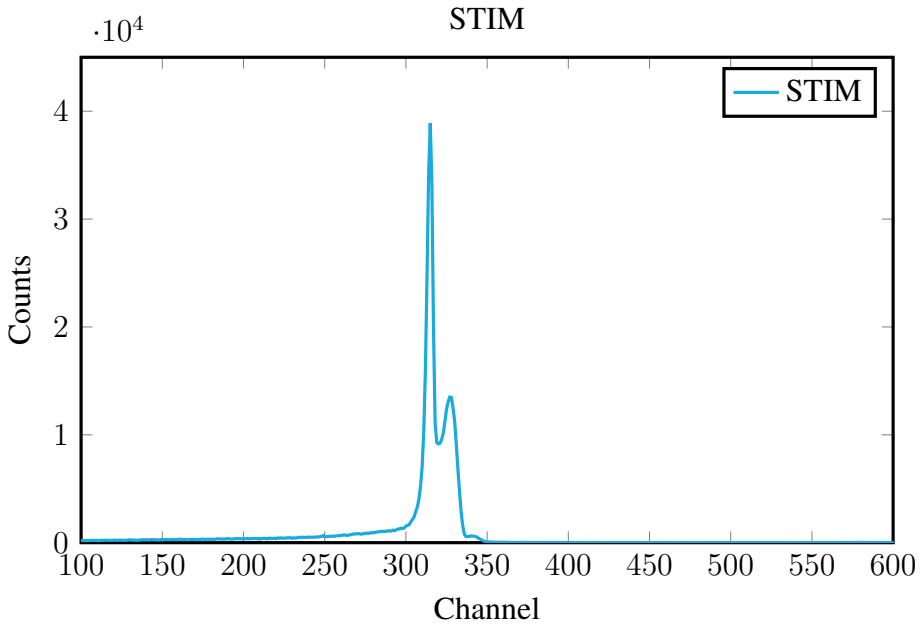

Figure 4.5: A MCA spectrum generated by 5.9 MeV beryllium ions directed onto a silicon detector. The two peaks are due to the energy loss in of the particles passing through the copper of the grid or unimpeded through the grid spaces.

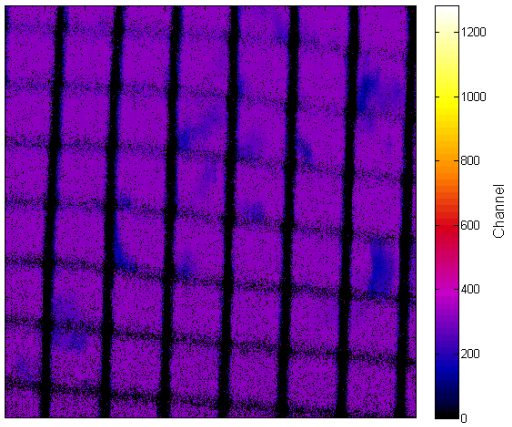

Figure 4.6: Scanning Transmission Ion Spectroscopy (STIM) measurement of a 25.4 µm pitch copper grid. This 1x scan amplifier measurement was used to spatially calibrate the IBIC images and determine the spot resolution. The image is 177.8 µm in width.

Chapter 5

Theoretical Methods

5.1 Geant4: Monte Carlo Simulations

The GEometry ANd Tracking toolkit (GEANT4) is a Monte Carlo code used to simulate the interactions of particles with matter[91]. Monte Carlo is a method used to obtain numerical solutions to problems that are too complicated to be solved analytically. The method is used to solve a problem by generating suitable random numbers and observing that fraction of the numbers obeying some property or properties. The use of Monte Carlo method to solve radiation physics problems allows a user to create and run experiments in a low cost, risk free environment that would otherwise be both expensive and time consuming. It provides a basis that can justify the benefit of new concepts, pre-implementation.

Geant4 is a powerful, robust, flexible and extensible simulation toolkit; it adopts the Object-Oriented C++ programming and follows an iterative-incremental software process. Geant4 is constantly going through development to refine its functionality and through different testing phases to quantify its reliability and accuracy. Geant4 is free and open source. The areas of application of Geant4 include but is not limited to High Energy Physics, nuclear and accelerator physics, as well as studies in medical and space science.

The Geant4 toolkit includes all aspects of the simulation process. Users are able to write

their own C++ program or can use/edit pre-defined examples which cover a range of different application from medical physics to high energy physics. Using the Geant4 classes, users are given the capability to model the experimental environment, through materials and geometries, the particles and physical interactions/processes to be considered and the generation of event data and the visualization of the detector and particle trajectories. Care must be taken in the development stage to ensure the validity of the simulation, however this must be balanced with time and computing power required/available. From the time in which this thesis was started until its completion, Geant4 has gone through a number of version upgrades, from Geant4 9.3 to Geant4 10.0.

The physics component of Geant4 handles electromagnetic, hadronic interactions, radioactive decay, and transportation etc [92] [93] [94].

The electromagnetic physics package governs the interactions of charged particles and photons with matter. There are three alternative packages: Geant4 DNA, Low Energy ($\geq$ 250 eV) and the Standard Package (1 keV- 10 PeV).

The hadronic physics component governs processes such as elastic and inelastic scattering, capture, fission and at rest processes of hadrons. The Package offers a wide set of complementary and alternative physics models, specific to the type of particle or to the energy range of validity.

Users are given the capability to define 'cuts', which define the particle production threshold. Essentially this prohibits the production of secondary particles below the cut value and instead deposits energy locally. To fix a cut properly means to reach a satisfying compromise between the accuracy of the results deriving from the simulation and the CPU performance.

5.2 Sentaurus TCAD

A commercially available Technology Computer Aided Design (TCAD) simulation package by Sentaurus, was utilised in this work to perform static and dynamic device simula-

tions upon the various diamond based detectors investigated in this thesis[95]. This software package allows for the properties and behaviour of semiconductor devices to be described through the technique of finite element analysis. This technique functions by using the initial conditions specified by the user and then solves the electrostatic potential (Poisson's equation) and charge continuity equations for each mesh element until solutions converge. The Poisson equation relates the total space-charge ρ to the divergence of the electric field $\vec{E}$, where ε_s is the semiconductor permittivity, N = N_D^+ - N_A^- is the electrically active net impurity concentration, q is the electric charge, and n and p are the electron and hole carrier densities[96].

$$\varepsilon_s \nabla . \vec{E} = -\varepsilon_s \nabla^2 \psi = \rho = q(p - n - N) = q(p - n - N_D^+ + N_A^-) \tag{5.1}$$

where the electrostatic potential ψ is defined via:

$$\vec{E} = -\nabla \psi \tag{5.2}$$

The continuity equations for electrons and holes are given by Equations 5.3 and 5.4, where G incorporates generation phenomena, such as impact ionization or carrier generation by external radiation and R describes recombination processes.

$$\frac{\partial n}{\partial t} = \frac{1}{q} \nabla . \vec{J_n} + (G - R) \tag{5.3}$$

$$\frac{\partial p}{\partial t} = -\frac{1}{q} \nabla . \vec{J_p} + (G - R) \tag{5.4}$$

The current equations for electrons and holes are given by Equations 5.5 and 5.6, where μ_p and μ_n are the electron and hole mobility and D_p and D_n are the corresponding diffusion

coefficients.

$$\vec{J_p} = q\mu_p\vec{E} + qD_p\nabla p \tag{5.5}$$

$$\vec{J_n} = q\mu_n\vec{E} + qD_n\nabla n \tag{5.6}$$

The simulation suite was used to study the physics of charge transport within the various detectors fabricated in this work as well as those still within the conceptual phase. The benefit being that devices may be optimised during the pre-fabrication stage, saving valuable time and money. Using static case simulations, allows for the determination of leakage currents, intrinsic resistance of the detector and electric field profiles due to defined geometries at an applied bias. Sentaurus Device or DESSIS, also offers dynamic case capabilities allowing for the study or alpha particles and heavy ion interactions and the corresponding generation and transport of charge carriers. The Sentaurus software package features a number of tool-sets, including; the Sentaurus Structure Editor, Sentaurus Device, Inspect and Tecplot that allow the user full control in device modelling, simulating parameters and simulation output.

Part III

Experimental Characterisation of Current Device Prototypes

Chapter 6

Boron Implanted Diamond (BID) Detector

6.1 Introduction

The boron implanted diamond (BID) detector is the first prototype in a series of alternative diamond based microdosimeters produced as part of a collaboration between the Centre for Medical Radiation Physics and the University of Melbourne. The key motivation behind this device concept was to create an electrically isolated SV array that could be the basis behind true diamond based microdosimetry. The purpose of the work presented in this chapter is to establish and assess the functionality of new fabrication techniques in diamond in relation to microdosimetry. This work involves a combination of experimental and computer based techniques to evaluate this new technology. The work presented in this chapter has in part been published in IEEE Transactions on Nuclear Science[7]. This research was supported by Australian Research Council Discovery Grant ID 1096600 and partially by grant from National Space Biomedical Research Institute (NSBRI), USA.

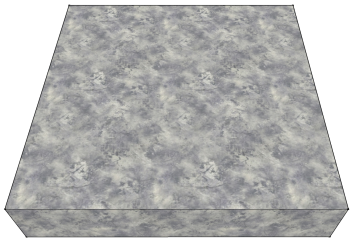

(a) Electronic grade scCVD Diamond

(b) TEM grid (sketch) used in the fabrication process

Figure 6.1: Start of the fabrication process to develop the BID device.

6.2 Fabrication

The goal of this work was to test the feasibility of patterned radiation damage through single ion implantation as a means of creating an electrically connected SV array in diamond crystal bulk for use in microdosimetry. Electronic grade (type IIb) diamond sourced from Element Six was selected for this work[97]. Electronic grade refer to the ultra high purity quality of the diamond, with typical nitrogen impurities in the range of parts per billion (ppb). The dimensions of the selected diamond used in this work is 3.5 x 3.5 x 0.5 mm^3.

The first step in the fabrication process was sample preparation. The sample undergoes a rigorous cleaning process designed to remove any unwanted contaminants on the diamond surface. Following sample preparation, a Transmission Electron Microscopy (TEM) grid with pitch 100 $\mu\mathrm{m}$, is mounted upon the diamond surface (see Fig. 6.2a) and 4 $\mu\mathrm{m}$ of Aluminium is evaporated using an electron beam evaporator (see Fig. 6.2b). The TEM grid is removed leaving a 4 $\mu\mathrm{m}$ Aluminium mask upon the diamond surface (see Fig. 6.3a). A 2 MeV Boron beam, with fluence 1 x 10×10^{15} B cm^{-2} is raster scanned across the diamond surface to the effect that boron is implanted into the diamond bulk in regions with an absent aluminium surface area. The result is a TEM grid patterned radiation damaged region, effectively creating a buried conducting electrode structure at a 1.38 $\mu\mathrm{m}$ depth (see Fig. 6.3b). After ion implantation, annealing treatment was performed at 1425 $^\circ$ for 15 minutes in vacuum.

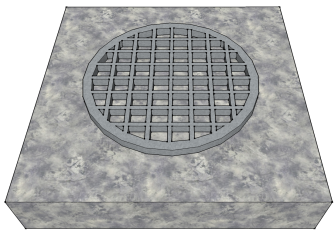

(a) A TEM grid with pitch 100 μm is placed on a diamond substrate.

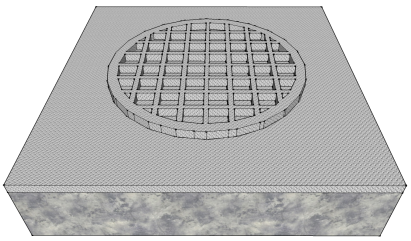

(b) 4 μm Al was evaporated on top of the diamond surface including the TEM grid.

Figure 6.2

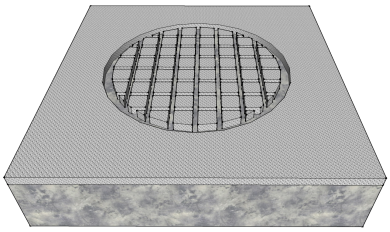

(a) This sketch shows the Aluminium remaining following the removal of the TEM grid.

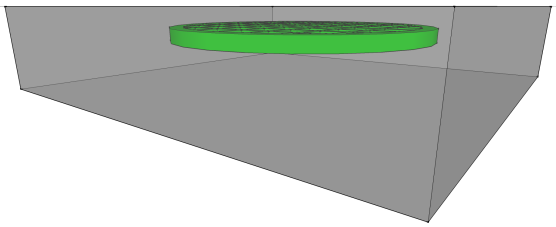

(b) Boron implanted diamond in regions without aluminium over-layer creating mesh structure.

Figure 6.3: 2 MeV Boron at room temperature is raster scanned across the diamond surface. The result is a buried boron grid structure embedded within the diamond due to the pre-existing layer of aluminium on the diamond substrate. Following boron implantation, the aluminium layer is removed.

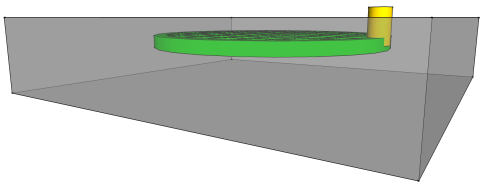

(a) FIB milling and Gold ABA contact (yellow)

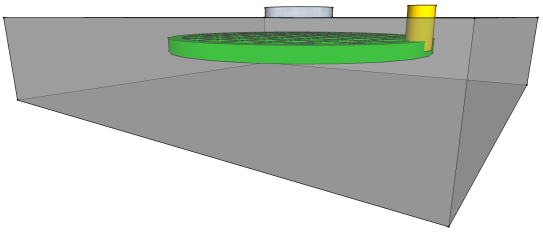

(b) The final BID detector structure.

Figure 6.4: Focussed Ion Beam (FIB) milling is used to create a trench to reach the buried boron implanted region (green). The trench is then filled with gold to create an accessible back contact with the buried boron gird (yellow). A front contact pad is visible on top of the diamond surface (grey), which may be either Aluminium or Gold/Chromium, deposited through e-beam evaporation.

Focussed Ion Beam (FIB) milling is used to trench down to the conducting boron implanted region. The FIB milled trench is then filled with a gold/titanium Active Brazing alloy (ABA) which is thermally evaporated at 800 $^{\circ}$ under vacuum. The gold/titanium filled trench allows for a conductive path to connect to the buried boron contact, thereby creating a back contact, (see Fig. 6.4a). A front contact was realised by evaporating a 500 nm circular Aluminium pad which covers a large region of the diamond surface (see Fig. 6.4b). This was done by utilising the photolithography process outlined previously. Additional groups of Chromium/Gold (100x200 $\mu\mathrm{m}^2$) contacts in a circular configuration were realised upon the diamond surface, which are represented as dark rectangles in Fig. 6.5b. Material selection for front electrodes must satisfy a balance between the desirable mechanical/electronic properties and technical limitations. The technical limitations in terms of metal selections is most commonly a reference to the creation of mechanically stable metal/diamond interface. As discussed in Section 3.6, Titanium is often used being a carbide forming metal and thus allowing for the production of good metal/diamond contacts, whereas gold and aluminium have been selected for electrical conductivity and microdosimetric considerations, respectively. The front contacts (Aluminium), for example was selected for its relatively low atomic number (Z=14), in an effort to maintain the overall tissue equivalence of the device. During characterisation, ions entering the diamond SV after passing through front contacts will have higher LET as compared with those ions which travel directly into the diamond bulk. This change in stopping power of ions passing through the front contacts must be considered as it will produce a corresponding change in the resultant microdosimetric spectra.
The finished device was mounted upon a Dual-In-Line (DIL) package using silver paste, and wirebonding to desired contacts and the DIL package were made as evident in Fig. 6.5a. Two bonded wires (20 and 22) can be seen in contact with the aluminium pad and two bonded wires (24 and 26) connected to deposited Cr/Au pads on top of the device. A square has been drawn in Fig. 6.5a, over the aluminium pad, to show the scan region used

in IBIC experiment. A Gold contact (9) connects to the buried boron mesh as on a Fig 6.4b. Contact numbers refer to the pin out configuration on the DIL package. A cathodoluminescence image of the diamond microdosimeter is presented in Fig. 6.5b. Due to the difference in materials, the cathodoluminescence technique is clearly able to differentiate the different regions of interest in the device. The dark grey squares represent pure intrinsic diamond (SV's) whilst the regions in between represent the boron implanted diamond grid.

This fabrication method allows for the production of multiple well defined SVs with approximate dimensions 150 x 150 x 1.38 μm^3. Whilst the size of the SV regions is not representative of true microdosimetric volumes, they do allow for testing of the fabrication concept. The thin diamond layer (1.38 μm) and high electric field, means that charge can be collected quickly before it can become trapped in defect centres typical for e-h transport in diamond. The final result being that such a design represents a solid state version of the 2D gas wire ionization chamber where boron implanted mesh is similar to wire anodes.

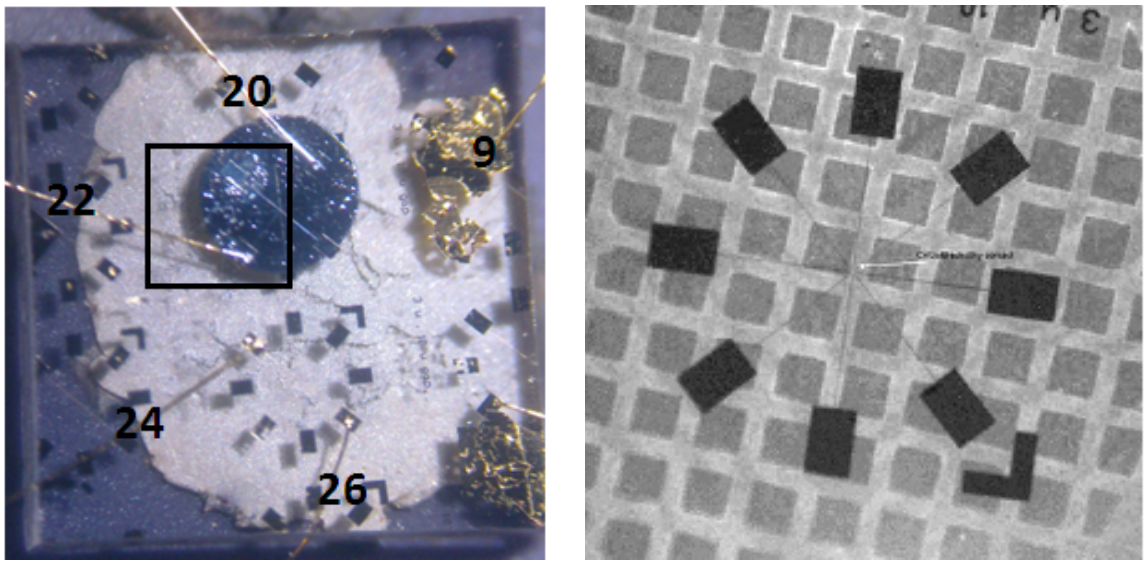

(a) Optical image. (b) Cathodoluminescence image.

Figure 6.5: Optical (left) and cathodoluminescent (right) image of the BID microdosimeter. The different contact configurations are visible in the optical image and the boron implanted regions evident in the cathodoluminescent image.

6.3 Electrical Characteristics

I-V characteristics of the diamond microdosimeter were measured using conventional current-voltage (IV) testing with a Keithley 6517A electrometer at room temperature. Measurements were performed using the common back contact, pin 9 and front Al electrode connected to pin 20. This back contact being a gold pad, implanted using the FIB method mentioned previously. I-V measurements were taken in the range of -15<V<15. A bias was applied to pin 9 and ramped in 0.5 V increments. Pin 20, 24 and 26 were connected to a virtual ground corresponding to an input of electrometer. A $1\mathrm{s}$ delay between each step was implemented in order to allow measured currents to stabilise. This method utilised a current threshold (1 $\mu\mathrm{A}$) to ensure device and equipment were not overloaded. I-V measurements were undertaken before and after exposure to UV light (see Fig. 6.6) to examine whether there was an appreciable effect due to "priming". After the initial testing of the device, UV light was made incident for three hours upon the device and the electrical characteristics were retested. I-V measurements were taken after an hour and also after a week. Fig. 6.7, 6.8 and 6.9 shows the results from IV measurements. The results presented show I-V characteristics before, 1 hour and 1 week after UV priming.

The IV characteristics can be explained by the selection of metals used for electrical contacts. The use of gold ABAs provide an ohmic back contact due to the carbide forming titanium present within ABAs, whilst the use of aluminium and chromium/gold contacts on top of the diamond produce schottkey contacts. Thus, the IV characteristics presented in Fig. 6.7, 6.8 and 6.9 do present some rectifying behaviour under a negatively applied bias. The capacitance was found to be constant (pF range) and therefore independent of the applied bias within the range tested ($0 \leqq \mathrm{V} \leqq 20$) as expected. Electrical characterization proved that the device behaves similarly to the solid state ionization chamber in contrast to SOI p-n junction based microdosimeter. The results show that the effect of UV priming is negligible, which can be seen in the stability of the I-V response over time (before and after

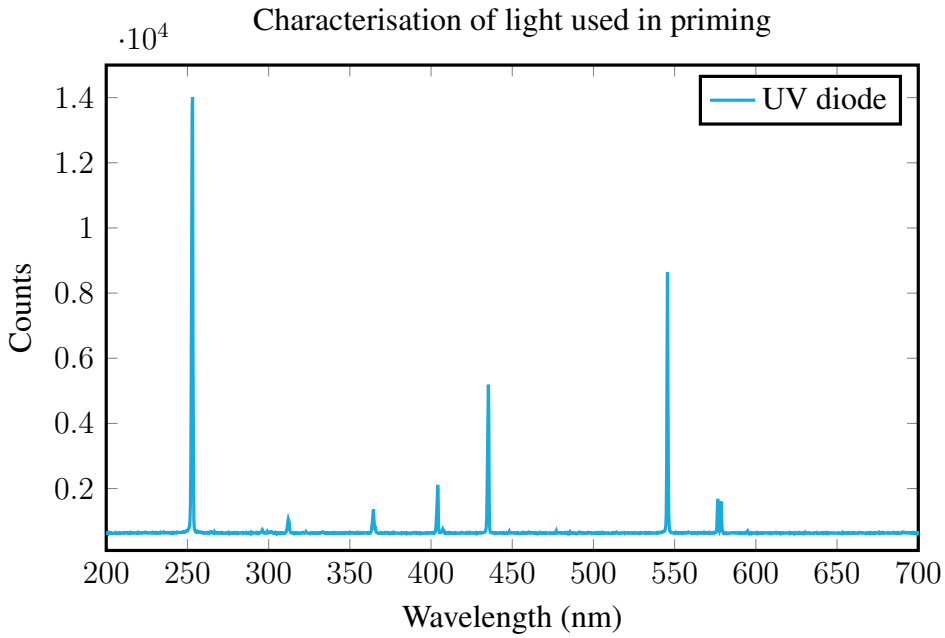

Figure 6.6: Characterisation of the blue/UV led light used to 'prime' diamond samples. A strong peak is evident at $\lambda = 250$ nm

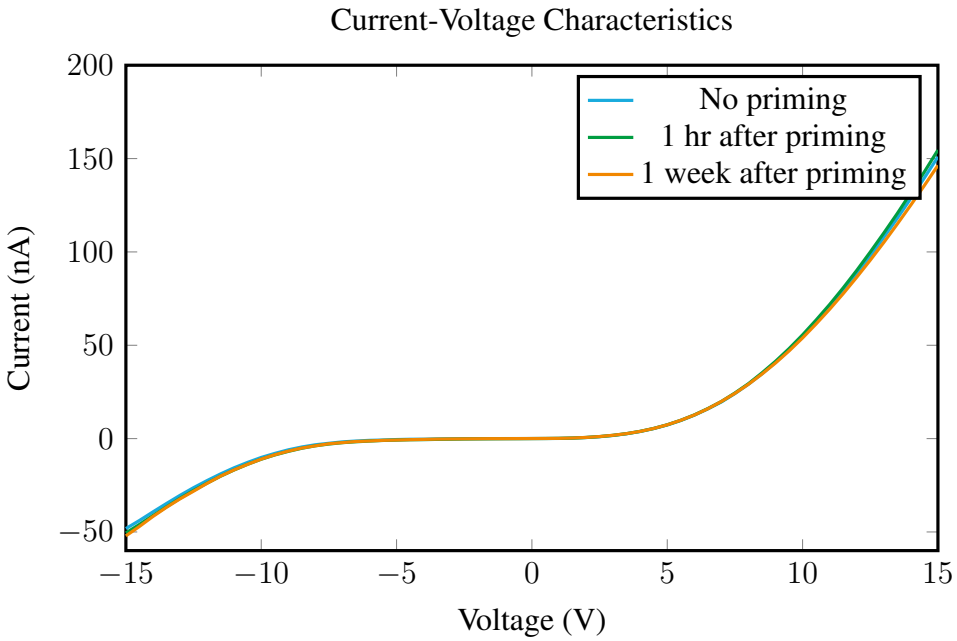

Figure 6.7: This plot shows the IV characteristics for the BID device. The bias is applied between the Al contacts (top: pin 20) and the buried boron grid with connecting gold contact (back: pin 9).

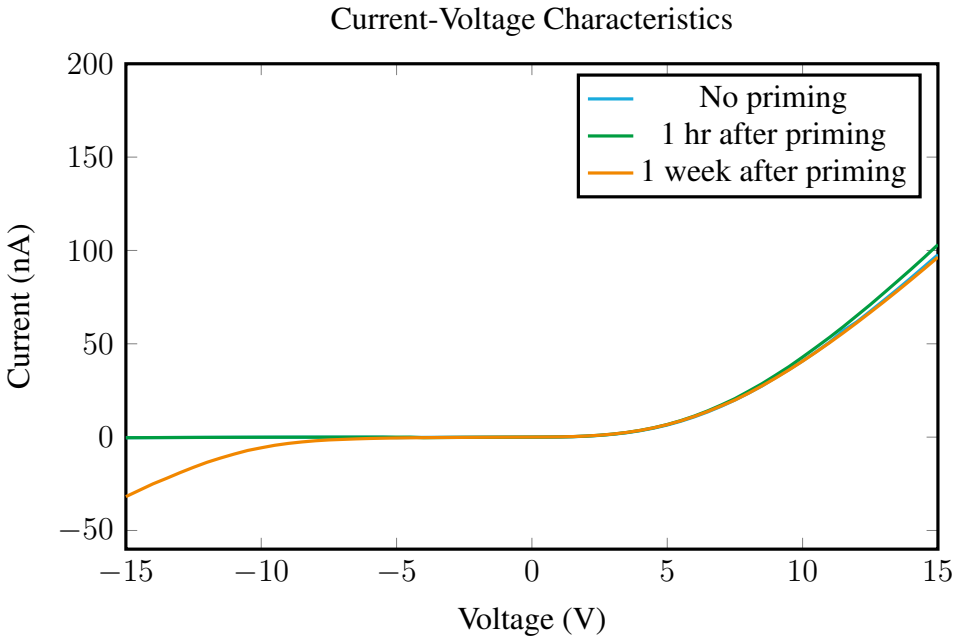

Figure 6.8: This plot shows the IV characteristics for the BID device. The bias is applied between the Cr/Au contacts (top: pin 24) and the buried boron grid with connecting gold contact (back: pin 9).

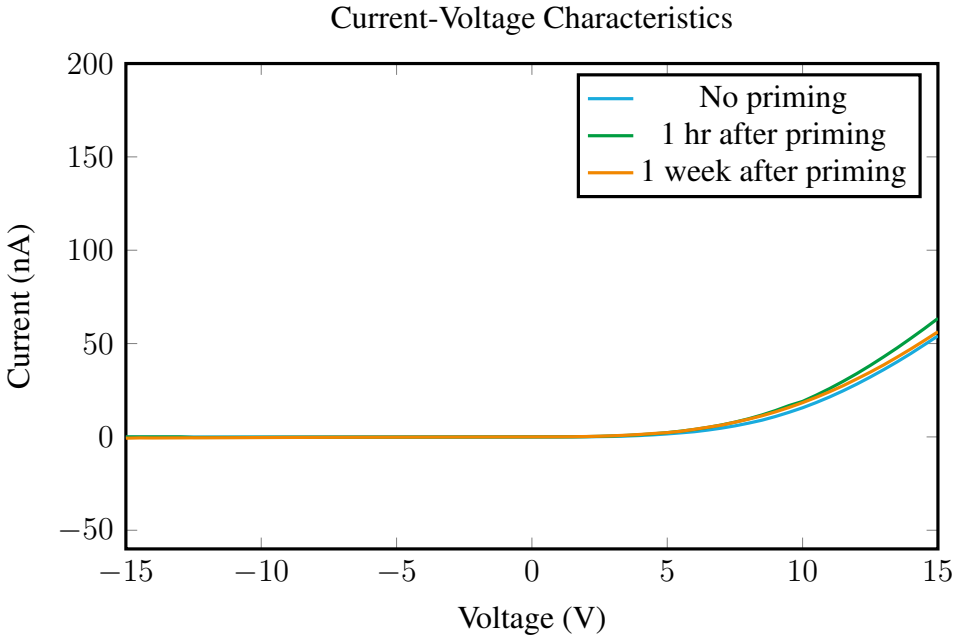

Figure 6.9: This plot shows the IV characteristics for the BIDn device. The bias is applied between the Cr/Au contacts (top: pin 26) and the buried boron grid with connecting gold contact (back: pin 9).

priming).

6.4 IBIC Experiment

An important requirement of a microdosimeter is an accurately defined and well characterised charge collection volume. It is also important from a quality assurance point of view to assess the new microfabrication technique used to realise the 3D SVs. In order to test these properties, an Ion Beam Induced Current (IBIC) study of the devices was undertaken on the Heavy Ion Microprobe (HIM) beam line on the ANTARES accelerator at the Australian Nuclear Science and Technology Organization (ANSTO). The purpose of this study was to ascertain the spatially resolved charge collection characteristics of the device. I-V characteristics of the device were measured to select bias for charge collection studies and effect of UV priming on them. The IBIC experiment was performed using a 5.9 MeV monoenergetic beam of beryllium fully stripped ions, focused to a spot size of approximately 1 $\mu\mathrm{m}$. The ion beam was normally incident on the microdosimeter device biased at 20 V and raster scanned across the device. The beam flux was maintained at 100 $\pm$ 10 ions s^{-1} throughout all experiments. The amount of energy deposited within the microdosimeter for each ion traversal, was measured with a standard charge sensitive preamplifier, shaping amplifier and multi-channel analyser (MCA) in coincidence with digitized voltage signals of the beam position, x and y for each event in ΔE. Data triplets (x,y, ΔE) were saved and stored. Analysis software was then used to generate IBIC imaging maps displaying a median energy map showing a spatially resolved image of the median amount of collected charge. The charge collection was investigated in different regions under the Al front electrode. The final calibration factor for diamond taking into account the e-h production energy is E = 0.4816 keV/Channel with an offset of -91keV.

6.4.1 Results: Charge collection study

Detailed charge collection was investigated in a region close to the edge of Al front electrode. The results presented in this section (see Fig. 6.11 - 6.12) are associated with 5.9 MeV Be^{4+} ions being rastered scanned across the diamond device in roughly the area marked out by the black square (0.7 x 0.7 mm^2) in Fig. 6.5a. The median energy map corresponding to this result (Fig. 6.12), shows clearly defined regions of charge collection 132 x 132 $\mu\mathrm{m}^2$ of the same shape and approximate size of the TEM grid voids (125 x 125 $\mu\mathrm{m}^2$) used in the fabrication process. The increased size of the charge collection regions or sensitive volume could be explained by straggling of the boron ions used in implantation or inaccuracies in the spatial calibration used in this experiment. The absence of charge collection between pixels is due to strong radiation damage from boron implantation as clearly observed. An inspection of the median energy map (Fig. 6.12), indicate a variance in the charge collection behaviour underneath the aluminium contact pad. Pixels underneath the middle of the aluminium pad have demonstrated a reasonable uniform charge collection, whereas enhancement of the collected charge in pixels is observed closer to the edge of Aluminium electrode. This increase in charge collection may be explained by an increased thickness of aluminium or the presence of an underlying Cr/Au contact beneath the aluminium pad at the edge of the contact which can be supported by the following images. The effect of increasing thickness's of aluminium has been a subject of investigation in Chapter 11.1. Another explanation could involve the increasing electric field strength caused by the geometry of the contact edges. A TCAD study will be designed to investigate this affect.

A 5.9 MeV Be^{4+} ion passing through 0.5 $\mu\mathrm{m}$ aluminium into diamond, will have a theoretical energy deposition of 1973 keV at 1.38 $\mu\mathrm{m}$[98]. Be^{4+} ions incident directly upon the diamond surface will have a theoretical energy deposition of 1891 keV at the same depth. Using the calibration factor determined previously, the maximum charge collection observed underneath the aluminium pad, during the experiment was approximately 565 keV.

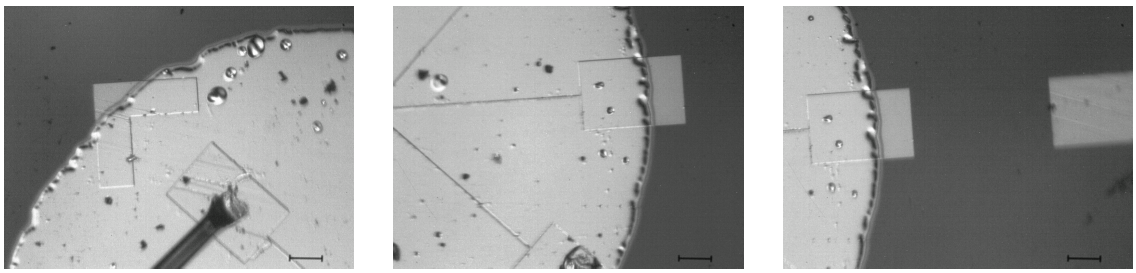

(a) Rotation 1 (b) Rotation 2 (c) Rotation 3

Figure 6.10: Optically magnified image of the top aluminium electrode of the BID device. Three different images are presented to provide a complete but enhanced perspective of the contact edges.

An estimate of the charge collection efficiency of this device can be made by comparing the ratio of the experimental energy deposition (565 keV) to the theoretical energy deposition of a 5.9 MeV Be^{4+} ion at 1.38 $\mu\mathrm{m}$ depth in diamond, with (1973 keV) and without (1891 keV) ions passing through an aluminium contact layer. The maximum Charge Collection Efficiency (CCE) of the diamond detector is approximately 29 and 30%, with and without a 0.5 $\mu\mathrm{m}$ aluminium contact atop the diamond.

In order to better illustrate the changing charge collection occurring beneath the aluminium contact pad, the MCA spectra has been divided into three distinct regions; I, II and III, as shown in Fig. 6.11. Each of these regions have been chosen specifically to detail peaks within the charge collection spectra of Fig. 6.11. The MCA spectra and corresponding median energy map depicting charge collection, for each region are presented in Fig. 6.13, 6.14, 6.13, 6.16, 6.15, 6.18 and 6.17.

Region I is user-defined by the Channels domain $250 : 450$, so as to include the first dominant peak within the MCA spectra presented in Fig. 6.11. This domain corresponds to an energy range of 30 - 126 keV with the peak situated at approximately 78 keV, giving a 4 % CCE. Region I accounts for the more uniform charge collection occurring in SVs closer to the centre of the aluminium contact pad, whereas for SVs at close proximity to the edge of the Aluminium contact, the energy deposition is pushed to the periphery of SV

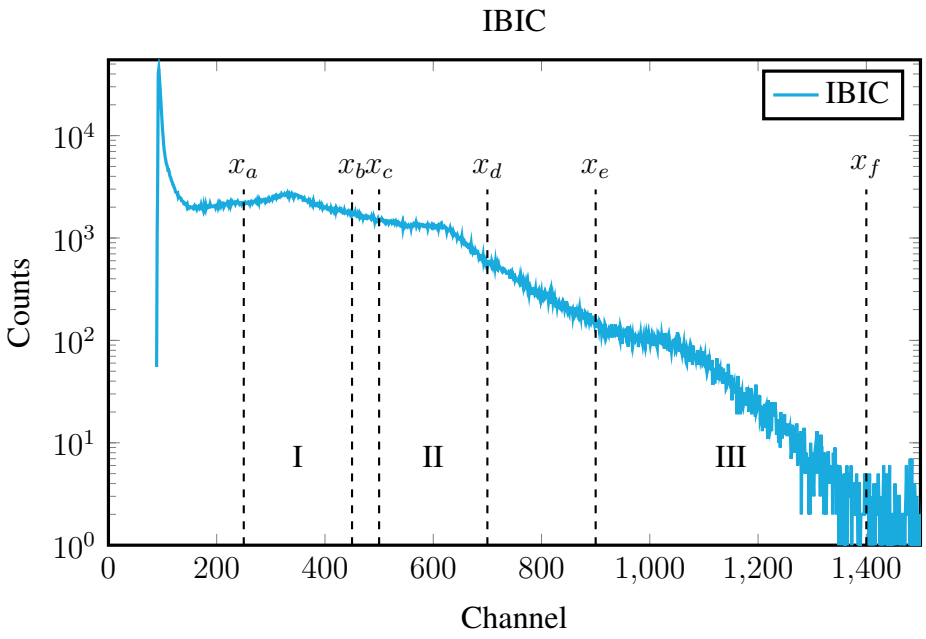

Figure 6.11: MCA spectrum generated by 5.9 MeV beryllium ions. The counts on the right hand side of the spectrum are those corresponding to the non-uniform charge collection in the IBIC map in Fig. 6.12.

pixels. The median energy map for region I is indicative of a non-uniform electric field distribution produced between the aluminium electrode and the buried boron mesh, with increasing strength towards the contact edges.

Region II is user-defined by the channel domain 500 : 700, so as to include the second prominent peak within the MCA spectra presented in Fig. 6.11. This domain corresponds to an energy range of 150 - 246 keV with the peak situated at approximately 194 keV, giving a 10 % CCE. Region II events appear to be confined towards the edge of the aluminium contact pad, again supporting the idea of increased field strength at the edge of the electrode or that of a thicker overlayer of aluminium and/or chromium/gold contact, see Fig. 6.10.

Region III is user-defined by the Channels domain 900 : 1500, so as to include the second prominent peak within the MCA spectra presented in Fig. 6.11. This domain corresponds to an energy range of 342-585 keV with the upper threshold of the region giving a 30 % CCE. The events unique to region III events are doubly confined to the SVs created by the

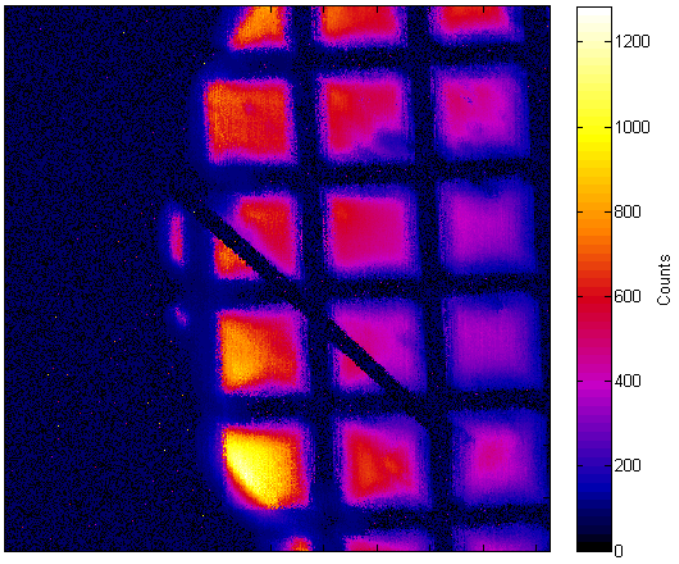

Figure 6.12: Charge collection mapping of the device. These results come from charge collection towards the edge of the aluminium pad. Charge is collected only from beneath the aluminium pad. The image is 711 µm in the x and y dimensions.

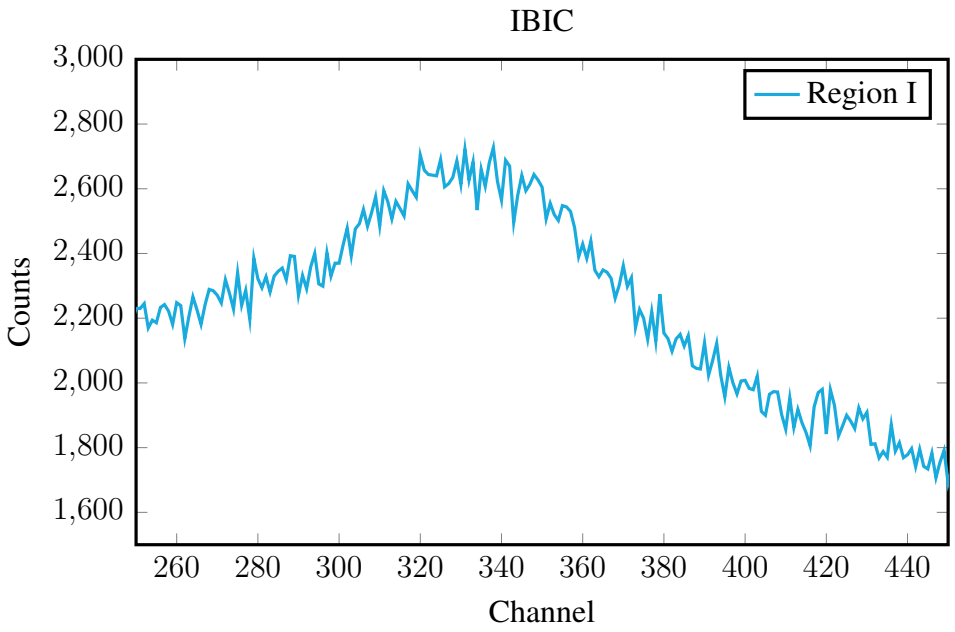

Figure 6.13: MCA spectrum for Region I

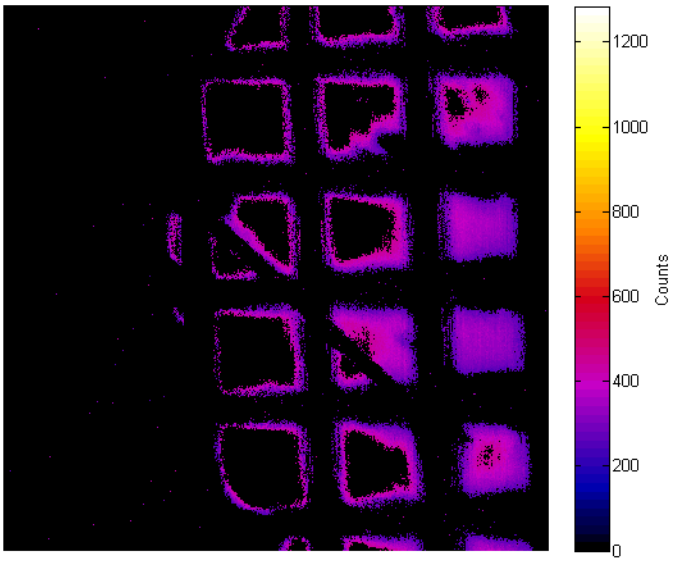

Figure 6.14: Charge collection mapping of the device. These are the same results as from Fig. 6.12, but the counts have been restricted energy window 30-126 keV. The most uniform charge collection occurs away from the contact pad edge.

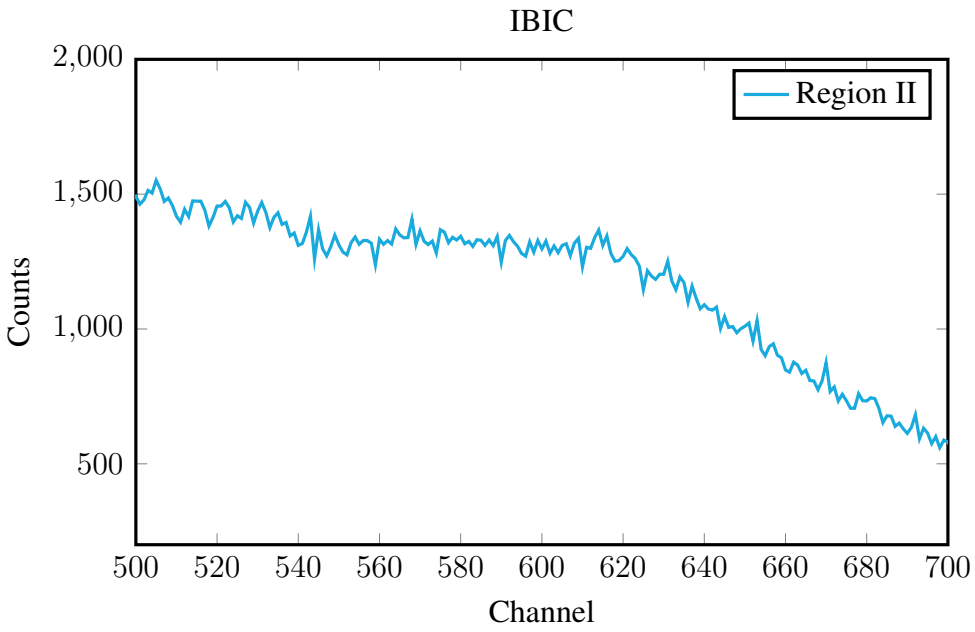

Figure 6.15: MCA spectrum for Region II

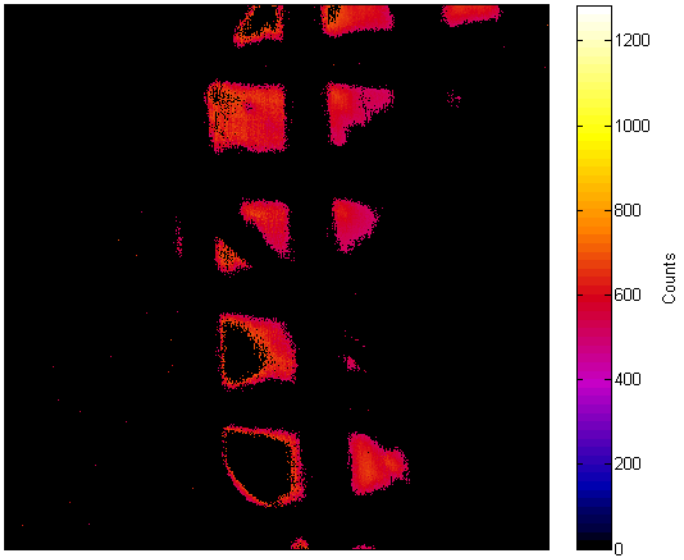

Figure 6.16: Charge collection mapping of the device. These are the same results as from Fig. 6.12, but the counts have been restricted for energy window 150-246 keV corresponding to the second 'peak' in Fig. 6.11. This figure shows regions of higher charge collection occur toward the edge of the contact pads.

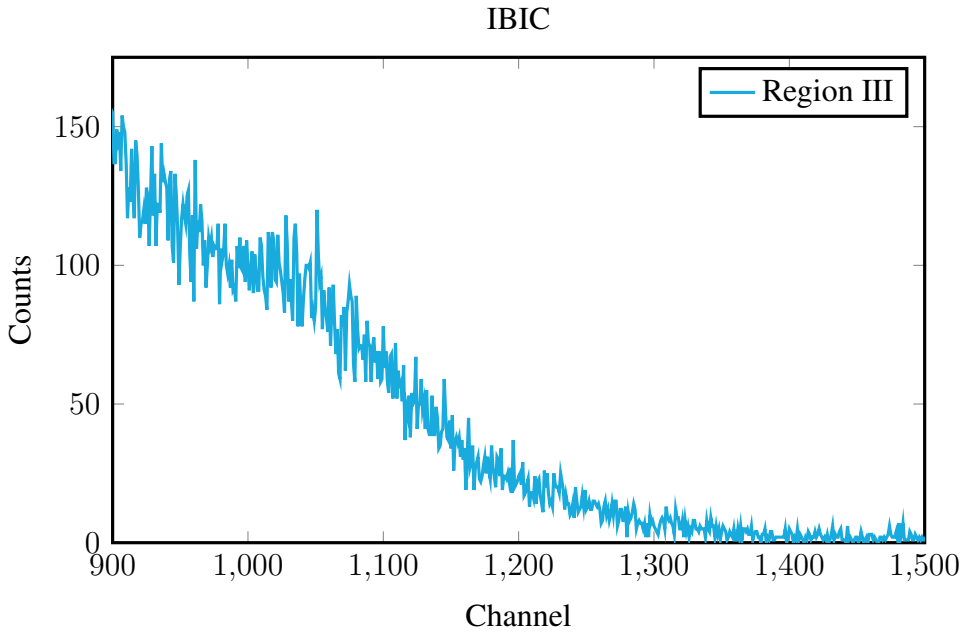

Figure 6.17: MCA spectrum for Region III

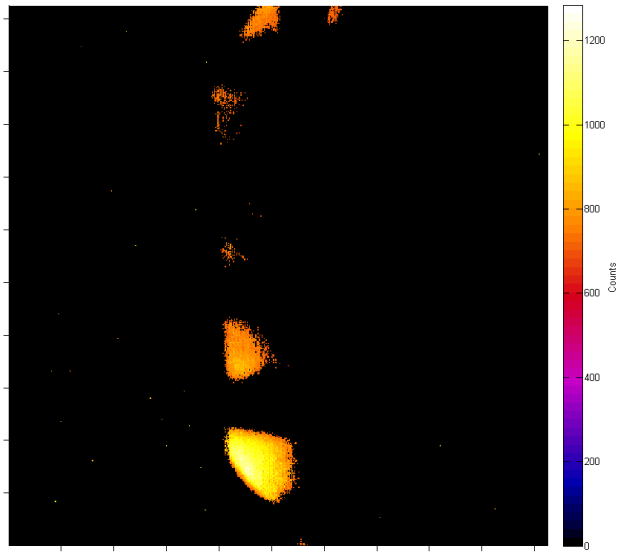

Figure 6.18: Charge collection mapping of the device. These are the same results as from Fig. 6.12, but the counts have been restricted to energy window 342-585 keV corresponding to the third 'peak' in Fig. 6.11.

buried boron mesh as well as the edge of the aluminium contact pad. Like with the previous two regions, a distinct 'line' of zero charge collection cutting diagonally across the median energy map is evident. From Fig. 6.5a, it is clear that this lack of charge collection is due to the presence of gold wire used in wire-bonding. The gold wire bonding is of sufficient thickness (25 $\mu\mathrm{m}$) that beryllium ions are stopped.

6.5 Discussion and Conclusion

A original method for creating isolated sensitive volume structures in diamond for the purpose of microdosimetry was examined in this work. Ion implantation using 2 MeV B^{5+} was used to create a buried conductive structure i.e. an electrode, within detector grade CVD diamond from Element6. Focussed Ion Beam (FIB) milling and gold electroplating was used to connect to the boron mesh and create a common 'back' contact, whilst aluminium and chromium/gold contacts were evaporated using photolithography, onto the surface to create

the 'front' contacts. The Ion Beam Induced Current experiments performed as part of this work, demonstrate that the use of ion implantation to create a buried electrode structure in detector grade CVD diamond has led to the production of well defined, 3D sensitive volumes.

The advantage of this technology is in the relative simplicity of design, requiring only a limited number of steps in the fabrication process, leading to the a decreased potential for faults. The large aluminium contact pad allows for simple connection to be made with a large number array of sensitive volumes simultaneously. The method of metallisation used in the fabrication method, has resulted in electrical contacts that are both hardy/durable and for the most part, perform reliably.

Whilst, this technology did allow for the production of well defined, electrically isolated SV structures, it was not without its disadvantages. The device failed to achieve full charge collection efficiency, possibly due to the very ion implantation used to create the device. It is possible that room temperature annealing can lead to changing of the geometry of the sensitive volume and also should be investigated. Given that radiation induced signal is already much lower in diamond detectors than in their silicon counterparts, this failure to achieve full CCE is at present a major drawback for this technology. In future work, it shall be investigated whether or not the near four times less charge induced for the same deposited energy in comparison with silicon will significantly compromise the dynamic range of the detected lineal energies of low LET ions.

Low, but uniform charge collection was achieved for the majority of SV structures underneath the aluminium contact pad. However, a gradual increase in the charge collection efficiency was observed towards the edges of aluminium contact pad. The two most likely candidates to provide explanation to this deviation in charge collection is an increased thickness of contact material and the increasing electric field strength due to the geometry of the circular contact pad. The effect of contact thickness is explored in Chapter 11.1. The sec-

ond hypothesis will require a detailed modelling of the electric field structure of the device using TCAD and will be the subject of future studies. Such a study may also be useful in optimising the structure to achieve higher charge collection efficiencies. This study will also include theoretical counterpoint to the experimental characterisation carried out in this work by exploring the theoretical CCE of a 5.9 MeV Be^{4+} ions in the modelled structure.

A novel diamond microdosimeter prototype has been created using ion implantation (2 MeV B^{5+}). The device was experimentally characterised in terms its charge collection properties. The results are promising in that they indicate the viability of using ion implantation as a means of creating isolated wall-less sensitive volumes through patterned radiation damage. Future generations of this design will require a more appropriate mask or grid to be used in the fabrication process in order realise true microdosimetric volumes. Lastly a means of increasing the low performance in terms of CCE is required for such a device to be made commercially viable and competitive.

Chapter 7

Laser milled Trench (LT) Detector

7.1 Introduction

The low charge collection efficiency associated with the boron implantation of the first generation BID microdosimeter prototype was a key motivator in the development of the LT device. To overcome this disadvantage, an alternative method of creating isolated sensitive volume regions was investigated. This method of laser ablation was investigated for its capability in producing physical isolated SVs, is described in this chapter.

The LT device, like the BID device was produced as part of a collaboration between the Centre for Medical Radiation Physics and the University of Melbourne. The purpose of the work presented in this chapter, is to establish and assess the functionality of new fabrication techniques in diamond in relation to microdosimetry through the experimental characterisation of prototype devices. The work presented in this chapter has in part been published in IEEE Transactions on Nuclear Science[8].

7.2 Fabrication

A sample of scCVD diamond of ultra high purity (electronic grade), with dimensions 4.72 x 4.72 mm^2 and 500 $\mu\mathrm{m}$ was obtained from Element6[97]. Prior to the fabrication process, the sample (see Fig. 7.1a) underwent initial sample cleaning and preparation. This involved the immersion into an acetone bath within an sonicator (see Section 17.2), following by isopropanol rinse, water rinse and drying within pure nitrogen gas. Sample cleaning was followed by the evaporation of gold, using e-beam evaporator, to act as an absorption layer for laser ablation (see Fig. 7.1b). This absorbing layer is required as diamond is transparent for particular wavelengths (λ = 532 nm) used by the Oxford Laser-Alpha series equipment. For more information on the process of laser ablation with diamond, see Section 3.5.1.

Following the evaporation of a gold absorption layer, a nano second pulsed laser, generated by the aforementioned Oxford Laser-Alpha series, was used to mill trenches in the diamond substrate 20 $\mu\mathrm{m}$ wide and 20 $\mu\mathrm{m}$ deep. Two patterns of laser milled trenches were created in this work. The first is a two by two grid, evident in the top right hand corner of Fig. 7.2a. The second pattern is a twenty by twenty grid, evident in the bottom right hand corner of Fig. 7.2a. It should be noted that the pattern shown in this sketch is not to scale and is used only to illustrate the concept to the reader.

Whilst the gold is removed in the regions where laser ablation is used, the majority of the gold absorption layer remains. In addition, graphitic by-products of the laser ablation of diamond is present within the trenched regions. In order to remove any metallic/conductive materials from the diamond, the sample underwent an acid bath ($NaNO_3$ & H_2SO_4) for 60 min at approximately 225 $^{\circ}\mathrm{C}$. Upon the culmination of the acid bath process, the sample was again cleaned using the same process listed above.

The entire sample is then coated with a hard setting epoxy (EpoFix) such that the laser milled 'trenches' are filled. The recommended ratio of resin to hardener (25:3) is used in this work. The ratio used is important as it will determine setting time as well as the effectiveness of

the epoxy to 'wet' the diamond surface and thus the ability to flow and fill the trenched regions. The epoxy is left to cure for 24 h within a desiccator. The desiccator provides a seal-able enclosure that reduces the humidity and allows the resin to properly set within a manageable time-frame. Once the resin is 'set', the surface of the sample is lapped to remove any remaining epoxy from the diamond surface such that the diamond pixels are revealed, without affecting or removing the epoxy from the trenches.

The next step in the fabrication process is the evaporation of electrical contacts on the back and top side of the diamond substrate. The E-beam evaporator is used to create a common back contact of 20 nm titanium and 150 nm of gold through an evaporation mask. The same process is used to create the aluminium contacts on the top side of the diamond substrate, where 200 nm of aluminium is evaporated through a purpose made evaporation mask. Next, the diamond device is attached to a DIL package/carrier using a silver paste, which was spread along the bottom side of the DIL package cavity. Lastly, gold ball point wire-bonding is used to create an electrical connection between each contact and the DIL package, with the back contact being connected via the silver paste mentioned previously.

The end result of the fabrication process is four distinct and separate 'devices' or rather groups of devices. Device 1, labelled as D1 in Fig. 7.3 is scCVD diamond contacted from the top with Al contact pad with surface area $\approx$ 1.4 x 1.4 mm^2. Device 2, labelled as D2 in Fig. 7.3 features four separately connected Al contact pads with surface area of 606 x 606 $\mu\mathrm{m}^2$. Device 3, labelled as D3 in Fig. 7.3 is a 2 x 2 pixel array with pixel size of 985 x 985 $\mu\mathrm{m}^2$. The pixel area is defined by laser milled trenches described previously. Device 3 has four contacts of the same dimensions as device two, situated within each pixel. Devices 2 and 3 are identical with the exception of the presence of laser milled trenched in between adjacent contact pads as in device 3. The fourth device, D4, again evident in Fig. 7.3 was not used in this work due to problems encountered during the fabrication process which resulted in the top/front contacts being damaged, leaving the device unusable.

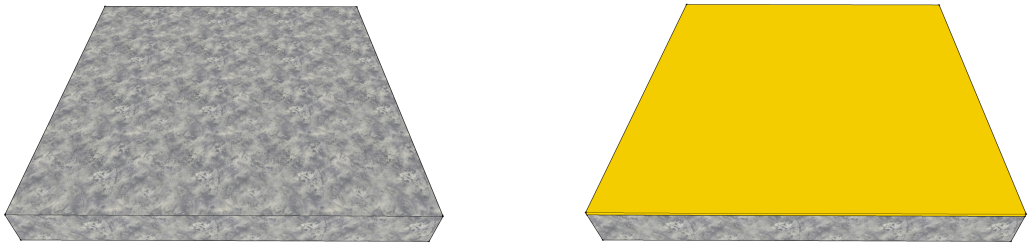

(a) Sample preparation. (b) Evaporation of gold.

Figure 7.1: The first step of the fabrication process is sample preparation (left). The diamond is cleaned using high purity solvents (Acetone C_3H_6O and Isopropanol C_3H_8O) and then rinsed with water and dried in pure N_2 gas. A gold (Yellow) absorption layer is evaporated upon the diamond surface to allow for laser ablation in successive steps (right).

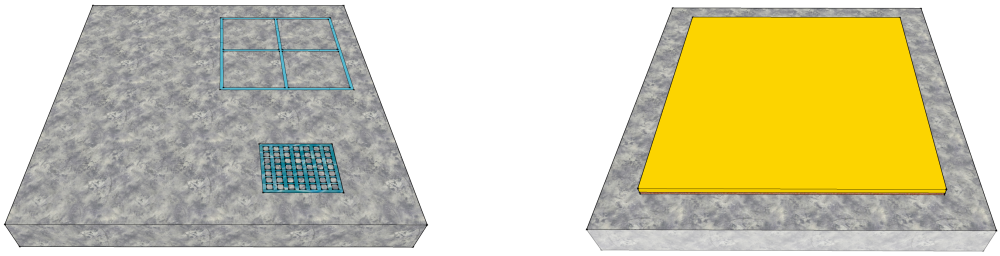

(a) Laser milled trenches & fill with EpoFix (b) Common back contact of Ti/Au.

Figure 7.2: Laser milled trenches filled with EpoFix (blue), corresponding to D3 (top right) and D4 (bottom right). The trenches are 20 μm wide and 20 μm deep. A common contact of Ti (20 nm) and Au (150 nm) is evaporated onto the back side of the diamond substrate.

7.3 Electrical Characteristics

The electrical characteristics of the LT diamond microdosimeter prototype were tested using a Keithley 6517A electrometer. All measurements utilised a common back contact as detailed in the fabrication section. This common back contact of titanium and gold was connected to a virtual ground corresponding to an input of electrometer. I-V measurements were taken in the range of -400<V<400, with bias applied to the front contacts individually and ramped in 5V increments. A time delay of 2s was utilised to allow measured currents to stabilise after each step in applied bias. Lastly, a current threshold (1 μA) was used as a current limiter.

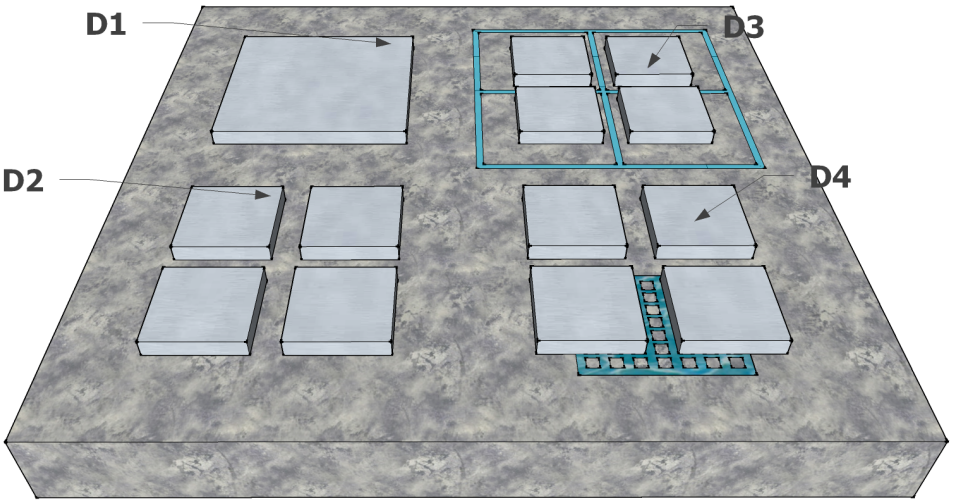

Figure 7.3: Aluminium contacts are evaporated onto the top side of the diamond surface through a mask. Four separate 'devices', labelled D1 through D4 are presented here.

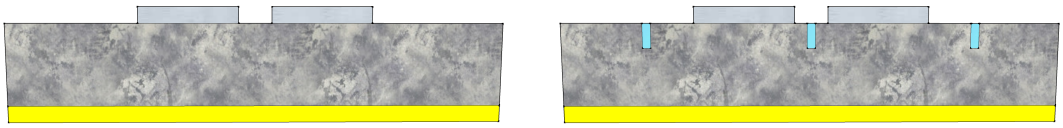

(a) D2 (b) D3

Figure 7.4: Cross sectional viewpoint of D2 and D3. The epoxy filled trenches are in blue for D3 and the top aluminium contacts in grey and the bottom titanium/gold contacts in yellow acting as a common contact for all devices.

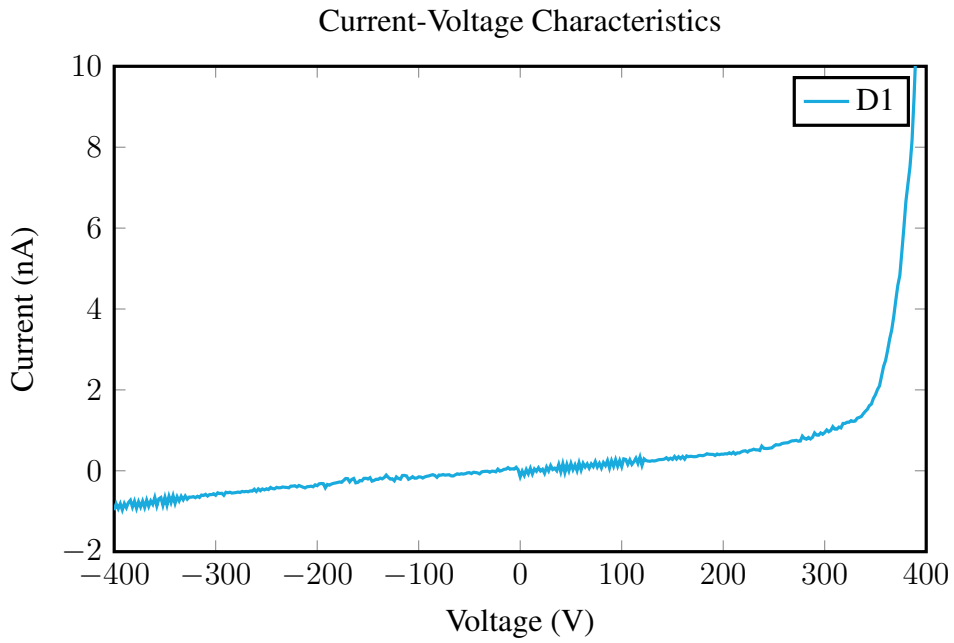

Figure 7.5: IV characteristics of the 1st generation LT device (D1)

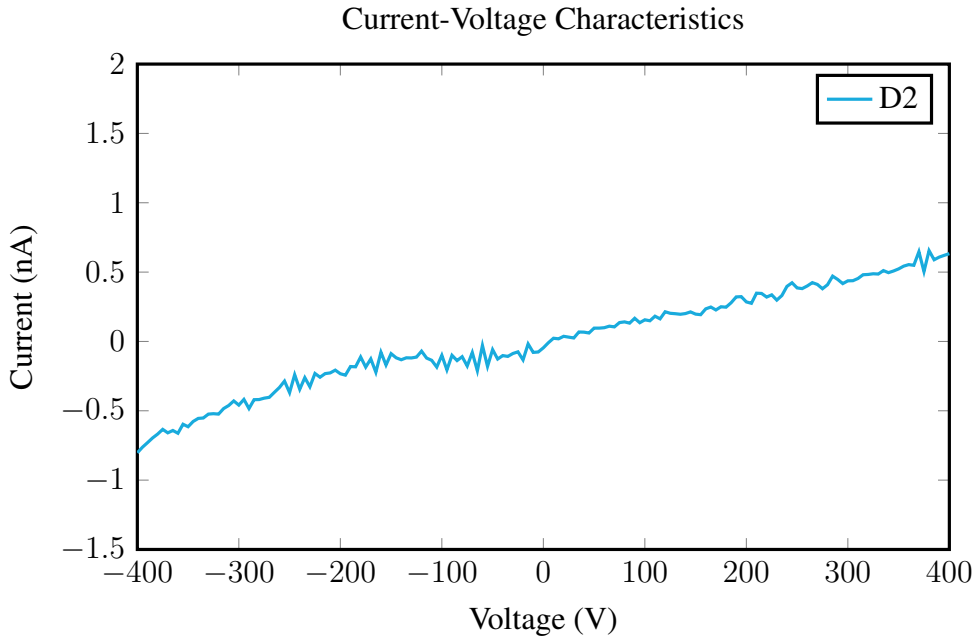

Figure 7.6: IV characteristics of the 1st generation LT device (D2)

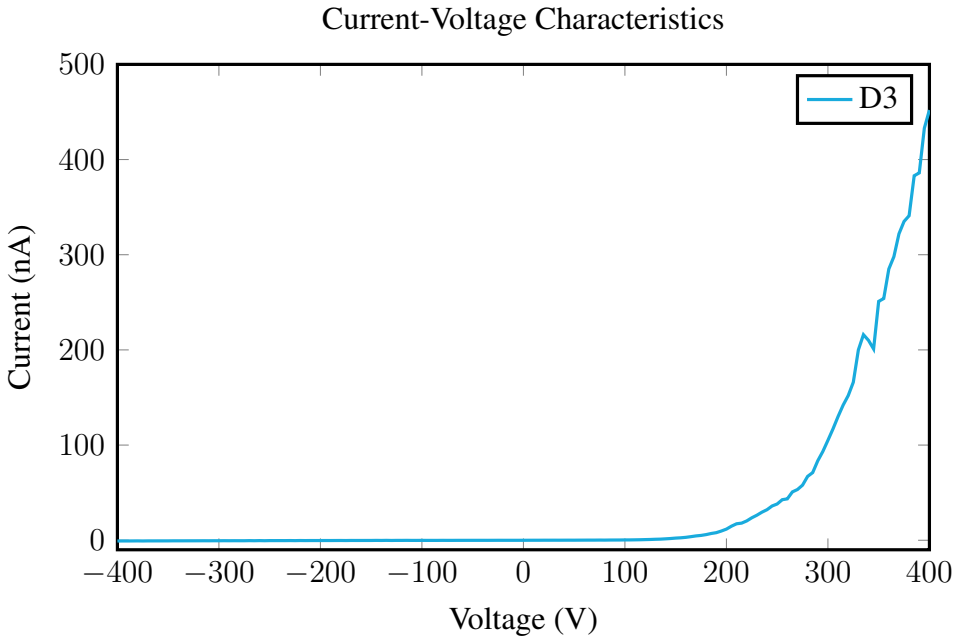

Figure 7.7: IV characteristics of the 1st generation LT device (D3)

7.4 Charge Collection Study

An important requirement of a microdosimeter is an accurately defined and well characterised charge collection volume. It is also important from a quality assurance point of view to assess the micro-fabrication technique used to realise physically isolated SVs. Additionally, the sample quality of the material itself in terms of charge collection characteristics should also be investigated.

The purpose of this study was to ascertain the effect of laser milling upon charge sharing between devices as a means of creating a pixelated diamond based radiation detector potentially leading towards microdosimetric sized sensitive volumes. In order to test these properties, an Ion Beam Induced Charge Collection (IBIC) study of the devices was undertaken upon the Heavy Ion Microprobe (HIM) beam line on the ANTARES accelerator at the Australian Nuclear Science and Technology Organization (ANSTO). The beam was focused to a spot size less than 10 μm and raster scanned normally incident across the device.

The back contact was connected to a virtual ground with the top contact under an applied bias. The signal from the biased contact was sent through to the charge sensitive pre-amplifier. Detailed charge collection was investigated in regions underneath and around aluminium electrodes on top of the diamond device. The MCA spectra and corresponding charge collection median energy maps are presented.

Stripped hydrogen and helium ions were chosen for study in this work. The energy of ions selected, was determined by range based considerations. The respective range of 1.5 MeV H^+, 5.5 MeV He^{2+} and 6.5 MeV He^{2+} in diamond is 15.05 $\mu\mathrm{m}$, 13.62 $\mu\mathrm{m}$ and 18.09 $\mu\mathrm{m}$, giving a range less than the depth of the laser milled trenches[99]. At normal incidence, the range in diamond of 12 MeV He^{2+} is 47.95 $\mu\mathrm{m}$, i.e. ion range greater than trench depth. This range can be effectively reduced by manipulating the angular incidence of the ion beam to reduce the projected range in diamond. An angular dependence study of the charge collection was performed by changing the angle of incidence of the ion beam from 0-60 $^\circ$, reducing the effective range in diamond from 48 to 24.1 $\mu\mathrm{m}$ at 60 $^\circ$. The approximate scan region for each ion and energy is presented in Fig. 7.8a - 7.9b.

The device was found to experience polarisation behaviour during extended multi-sweep runs. Different techniques as a means to avoid this issue were investigated. It was found that resetting the bias between runs provided an effective means of limiting polarisation. Following this bias reset, devices were retested under the same conditions with results added together in order to increase statistics to a usable degree.

7.4.1 1.5 MeV H^+

Part 1 of this study utilised 1.5 MeV H^+ ions with scan regions used, shown in Fig. 7.8a. The primary aim of this study was to ensure diamond quality in terms of charge collection and to provide preliminary assessment of the micro-fabrication technique used on this device. The ion species and energy was chosen such that the range of the incident particle was

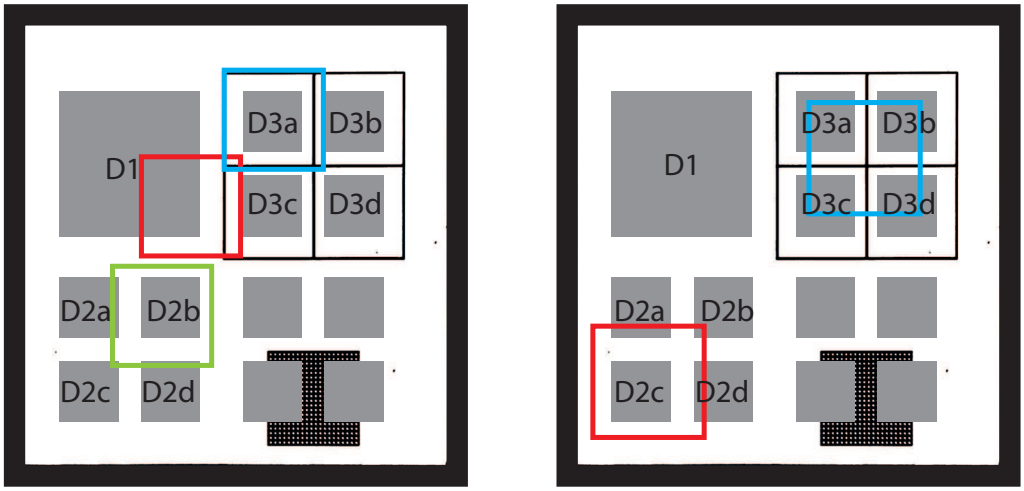

(a) 1.5 MeV H^+ (b) 5.5 MeV He^{2+}

Figure 7.8: Scan regions of the diamond device used in IBIC measurement with 1.5 MeV H^+ and 5.5 MeV He^{2+}

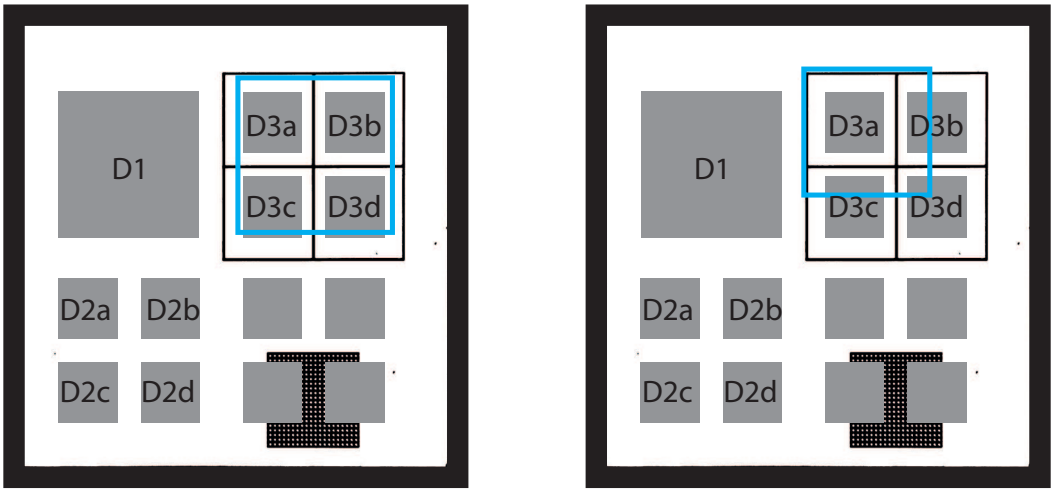

(a) 6.51 MeV He^{2+} (b) 12.01 MeV He^{2+}

Figure 7.9: Scan regions of the diamond device used in IBIC measurement with 6.51 and 12.01 MeV He^{2+}

less than that of the laser milled trench depth. 1.5 MeV H^+ have a range of 15.05 µm in diamond[99]. It should be noted that ions which travel through the contact pad will have an energy loss of approximately 7 keV and a thusly reduced range within the diamond substrate beneath. Three of the devices were tested in this study. Each device was biased at a variety of different biases with range -300≤V≤300.

IBIC measurements were undertaken with device 1, labelled D1 in Fig. 7.8a under an applied bias of 300 V. The MCA spectra and median energy map corresponding to these measurements are presented in Fig. 7.10a and 7.10b. As indicated in Fig. 7.8a, the scan encompassed the "bottom left" corner of D1 as well as the trenches of D3. This can be seen in the median energy map in Fig. 7.10b where distinct features of contact pad for D1, gold wire bonding for D3 and trenches are readily apparent. The maximum CCE for device 1, associated with the sharp peak in Fig. 7.10a is approximately 96%. This value of CCE is uniform underneath the contact pad and diminishes with distance away from the contact pad according to the strength of the applied electric field. This diminishing charge collection is different when comparing CC taken below D1 and CC to the right of D1 in Fig. 7.10b due to the presence of laser milled trenches.

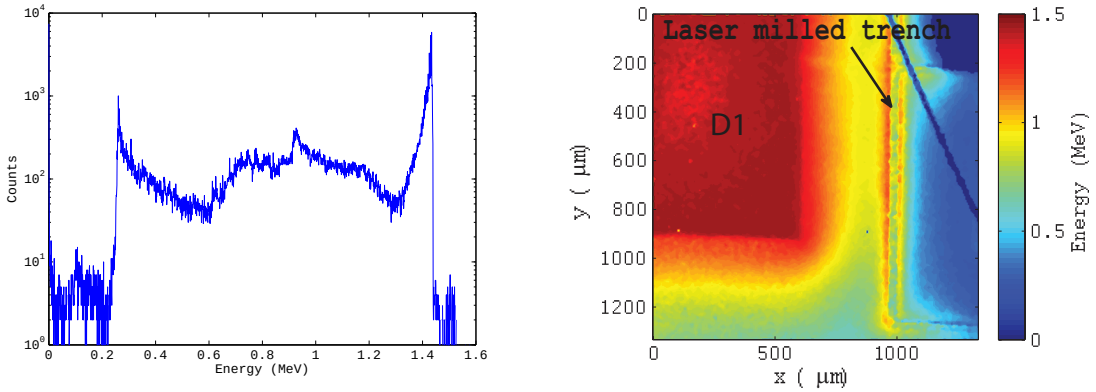

(a) MCA spectrum.

(b) Median energy map.

Figure 7.10: MCA spectrum and corresonding median energy map, generated by 1.5 MeV protons. The sharp peak at 1.43 MeV is associated with the charge collection underneath the aluminium pad in device 1 (D1). Scan is situated over D1 as represented by the red square in Fig. 7.8a.

‘ IBIC measurements were undertaken with device 2, labelled D2 in Fig. 7.8a under an applied bias of -300 V. The MCA spectra and median energy map corresponding to these measurements are presented in Fig. 7.11a and 7.11b. The maximum CCE for device 2 is approximately 90% as evident in Fig. 7.11a and labelled as point A in Fig. 7.11b. At point

B in Fig. 7.11b, which is approximately 630 µm away from point A, the CCE has dropped from 90% to 75%. The CCE is at a maximum underneath the contact pad and only diminishes slightly with distance.

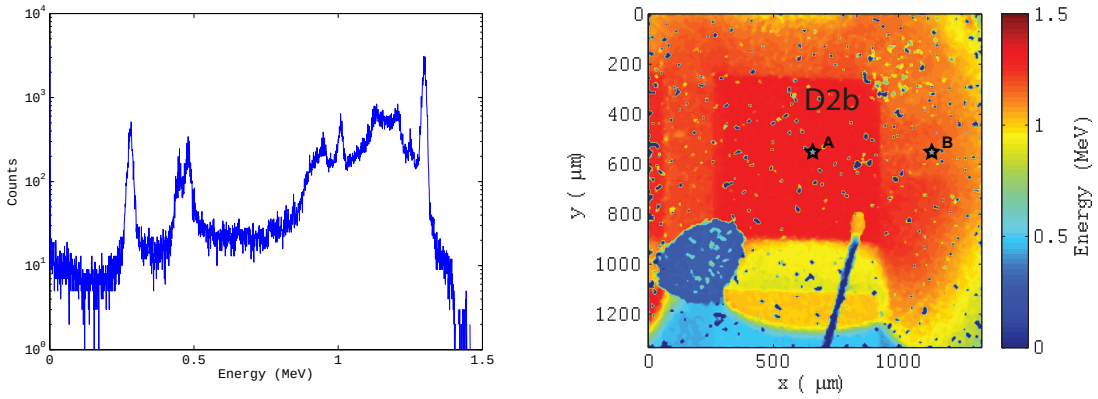

(a) MCA spectrum.

(b) Median energy map.

Figure 7.11: MCA spectrum and median energy map, generated by 1.5 MeV hydrogen ions. The sharp peak at 1.3 MeV is associated with the charge collection underneath the aluminium pad in device 2. Scan is situated over device 2 as represented by the green square in Fig. 7.8a.

IBIC measurements were undertaken with device 3, labelled D3 in Fig. 7.8a under an applied bias of 300 V. The MCA spectra and median energy map corresponding to these measurements are presented in Fig. 7.12a and 7.12b. The maximum CCE for device 3 is approximately 95% as evident in Fig. 7.12a and labelled as point A in Fig. 7.12b. The behaviour underneath the contact pad is consistent with previous results. The median energy map shows a lateral confinement of CC within the boundaries of the laser milled trenches.

According to the CCE profiles taken across the median energy map of D3a for 1.5 MeV H^+ ions, there is an approximate 40% drop in the CCE from inside to outside of the trenches region marked as B (CCE = 76%) and C (CCE = 33%) respectively in Fig. 7.12b and Fig. 7.13a. Given that the charge carriers generated outside the trenched region are generated at less than the depth of the trench, there is a markedly decreased probability of charge collection due to change in permittivity of the epoxy filled trenches.

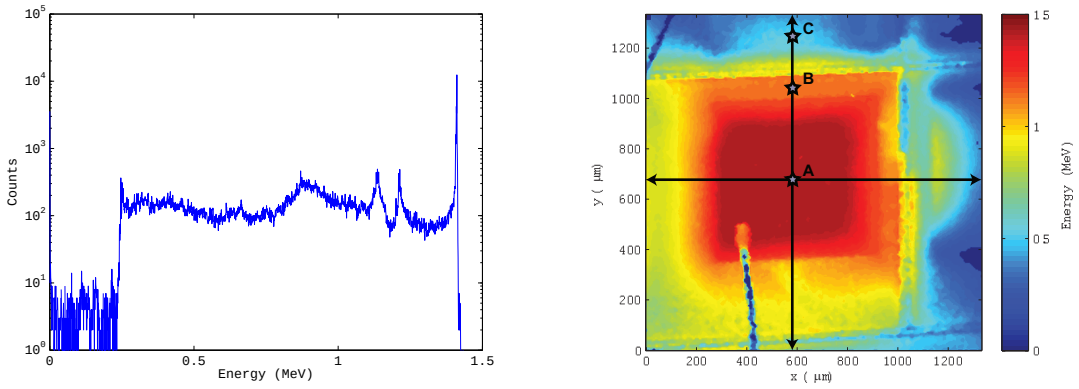

(a) MCA spectrum. (b) Median energy map.

Figure 7.12: MCA spectrum generated by 1.5 MeV hydrogen ions. The sharp peak 1.4 MeV is associated with the charge collection underneath the aluminium pad in device 3 (D3). Scan is situated over D3 as represented by the blue square in Fig. 7.8a.

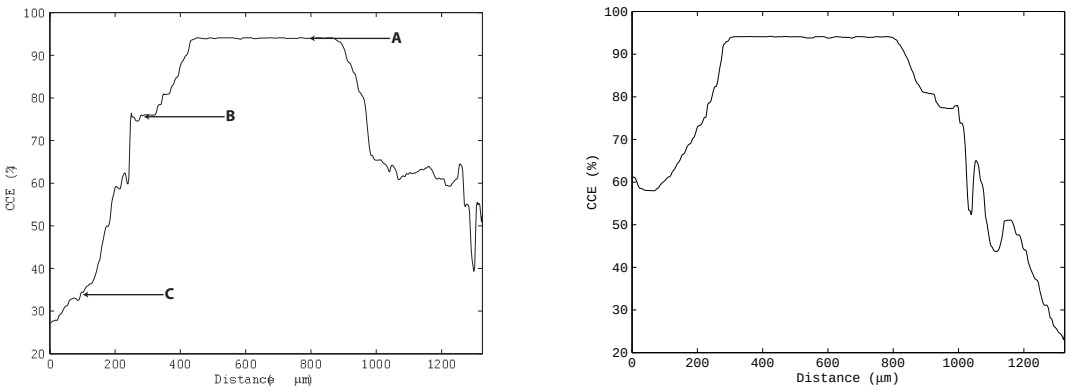

(a) CCE profile of D3a taken at x = 585 µm (b) CCE profile of D3a taken at y = 716 µm

Figure 7.13: CCE profile of D3a taken at x = 585 µm and y = 716 µm, generated by 1.5 MeV protons, as illustrated by the vertical and horizontal arrows in Fig. 7.12b.

A comparison of the drop in CCE over distance for devices 2 and 3 can be made by comparing the CCE at point A and B in Fig. 7.11b and points A and C in Fig. 7.12b. In both cases, point A is positioned for charge collection occurring underneath the contact pad where CCE is at a maximum. The second point is chosen to be at distance approximately 630 µm away from the first. For device 2, there is an approximate 25% drop in CCE from point A to point B. For device 3, this drop in CCE from A to C is increased to 62% due to the presence of the laser milled trenches.

7.4.2 5.5 MeV He^{2+}

An additional investigation using 5.5 MeV He^{2+} ions was undertaken. In this study, devices 2 and 3 are investigated and compared directly. Again, the ion and energy was selected specifically such that the range of the particle (13.62 $\mu\mathrm{m}$) is less than that of the trench depth. A dual channel spectroscopy 'stick' was used in this study with each channel having an identical set-up in terms of the components aforementioned. This setup allows for components to be biased and collected separately and simultaneously. In this study, MCA spectra and median energy maps are generated, collecting from one contact under an applied bias on channel 1. In addition, the three adjacent contacts are connected to channel 2 under an applied bias equal to that of channel 1. This is done to simulate the charge collection characteristics of the detector as near as possible to the operational mode of a microdosimeter.

IBIC measurements were undertaken with device 2, labelled D2 a) in Fig. 7.8b under an applied bias of 150 V on channel 1 with the adjacent pads D2 b-d), were biased at 150 V on channel 2. The MCA spectra and median energy map corresponding to these measurements are presented in Fig. 7.14a and 7.14b. As with part 1 of this study, the CCE of D2 was again close to 100%.

Fig. 7.14b is a median energy map corresponding to scans taken over Device 2a). The adjacent pads of device 2 biased on channel 2 are located in Fig. 7.14b below, to the right and diagonally opposite the contact pad visible. This result shows the charge collection to be confined by the surrounding electric fields of the adjacent contact pads (D2a, D2b and D2d).

IBIC measurements were undertaken with device 3, labelled D3 c) in Fig. 7.8b under an applied bias of 150 V on channel 1 with the adjacent pads D3 a,b and d) were biased at 150 V on channel 2. The MCA spectra and median energy map corresponding to these measurements are presented in Fig. 7.15a and 7.15b. As with part 1 of this study, the CCE of D3 was again close to 100%.

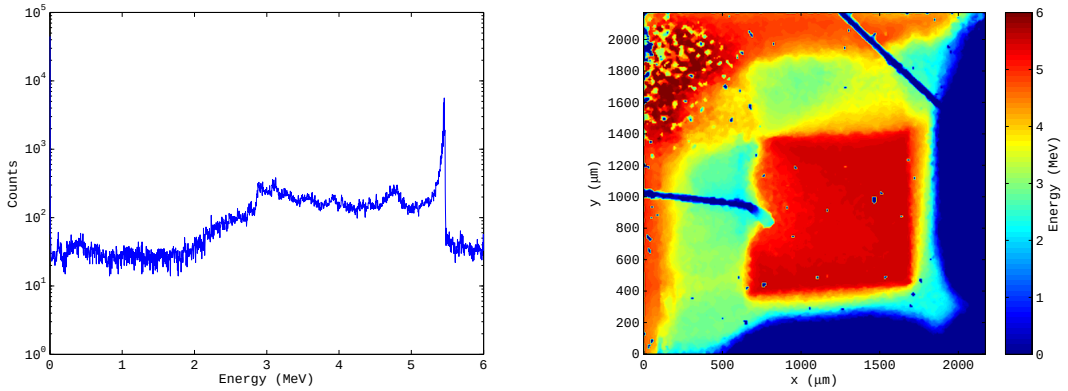

(a) MCA spectrum

(b) Median energy map

Figure 7.14: MCA spectrum and median energy map, generated by 5.5 MeV helium ions. The sharp peak on the right is associated with the charge collection underneath the aluminium pad in device 2 (D2). Scan is situated over D2. D2 is under an applied bias of 150 V on channel 1. The adjacent pads are connected to channel 2 under an applied bias of 150 V.

Fig. 7.15b is a median energy map corresponding to scans taken over Device 3c). The adjacent pads of device 3 biased on channel 2 are located in Fig. 7.15b above, to the right and diagonally opposite the contact pad visible. This result shows the charge collection to be confined by the surrounding electric fields of the adjacent contact pads (D3b, D3c and D3d). In contrast with the previous result in Fig. 7.11b, a much more defined charge collection region is evident with device 3 due to the presence of the microfabricated laser milled trenches.

7.4.3 6.51 MeV He^{2+}

In this study, the ion species and energy was chosen, such that the range of the incident particle was close to that of the laser milled trench depth (20 µm). 6.51 MeV He^{2+} ions have a range of 18.09 µm in diamond[99]. It should be noted that ions which travel through the contact pad will have an energy loss of approximately 27 keV.

Fig. 7.16b and 7.17b are the median energy maps of D3a at 200 V and 50 V respectively as labelled in Fig. 7.9a. The corresponding MCA spectra are presented in Fig. 7.16a and 7.17a.

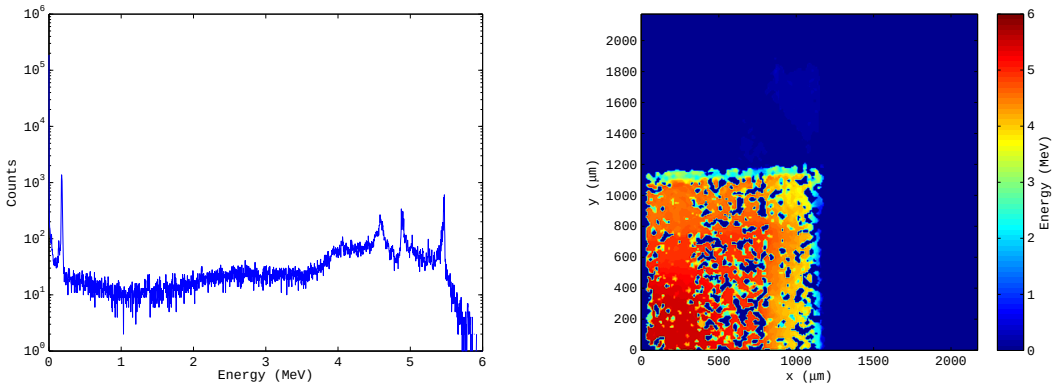

(a) MCA spectrum

(b) Median energy map

Figure 7.15: MCA spectrum and median energy map, generated by 5.5 MeV helium ions. The sharp peak on the right is associated with the charge collection underneath the aluminium pad in device 3. Scan is situated over device 3. Device 3 is under an applied bias of 150 V on channel 1. The adjacent pads are connected to channel 2 under an applied bias of 150 V.

In both cases, the main peak lays at $\approx$ 6.4 MeV equating to a charge collection efficiency (CCE) of $\approx$ 98 %, accounting for charge collection taking place directly underneath the biased contact pad. The charge collection is reduced outside of the desired region showing good charge collection confinement. This confinement is enhanced in the case of Fig. 7.17b due to the manipulation of the electric field strength via the applied bias, thus indicating the capability to optimise charge collection for specific SV sizes.

This is evident in the comparison of the CCE profiles for 6.51 MeV He^{2+} ions under an applied bias of 200 V and 50 V, provided in Fig. 7.16b and 7.17b. The contrast in lateral CCC is readily evident in Fig 7.18 which depicts the charge collection profiles as measured along the y-axis for Fig. 7.16b and 7.17b. The CCC is shown to result from the trench presence as well as the magnitude of the applied bias and hence the strength of the electric field.

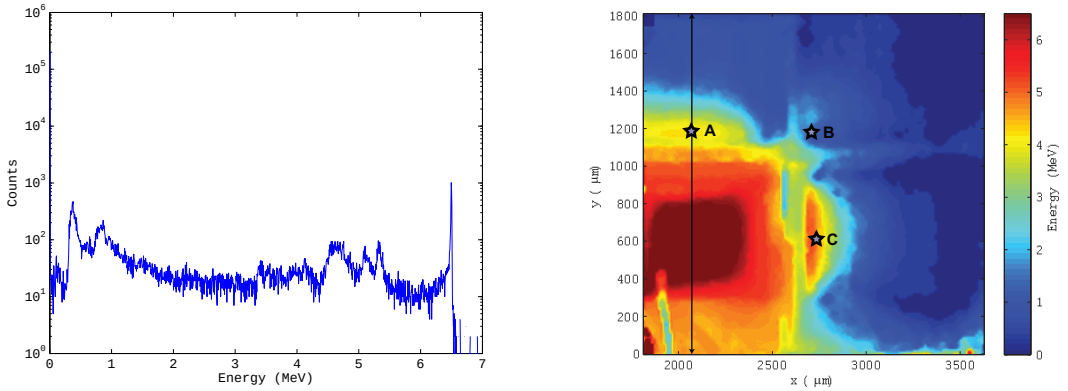

(a) MCA spectra (b) Median energy map

Figure 7.16: MCA spectra and median energy map of Device 3. D3 a) is biased at 200 V on channel 1. The arrow represents the cross section at which the line profile in Fig. 7.18 is generated. The stars are used as reference points to charge collection sites in the second study.

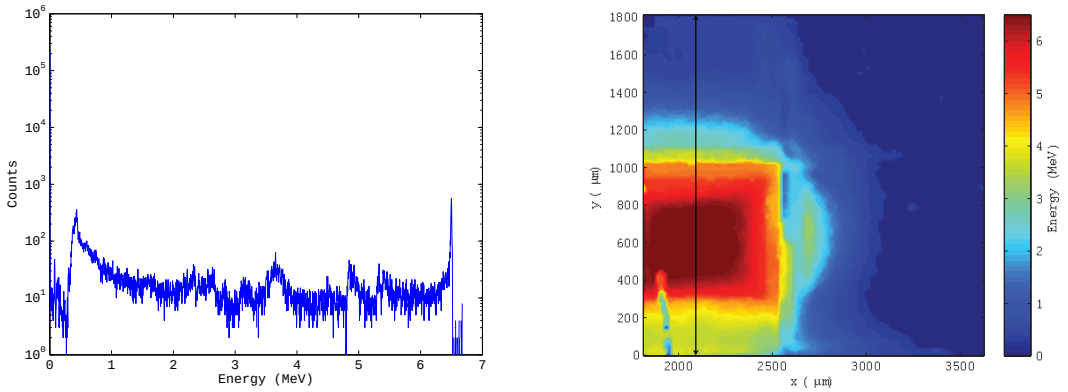

(a) MCA spectra (b) Median energy map

Figure 7.17: MCA spectra and median energy map of Device 3, generated by 6.5 MeV alphas. D3 a) is biased at 50 V on channel 1. The arrow represents the cross section at which the line profile in Fig. 7.18 is generated.

7.4.4 12.01 MeV He^{2+}

This study utilised 12.01 MeV He^{2+} ions incident upon device 3. The energy used in this study was chosen such that the range of the incident particle was greater than that of the laser milled trench depth of 20 µm. 12.01 MeV He^{2+} ions have a range of 47.95 µm in diamond[99]. It should be noted that ions which travel through the contact pad will have an

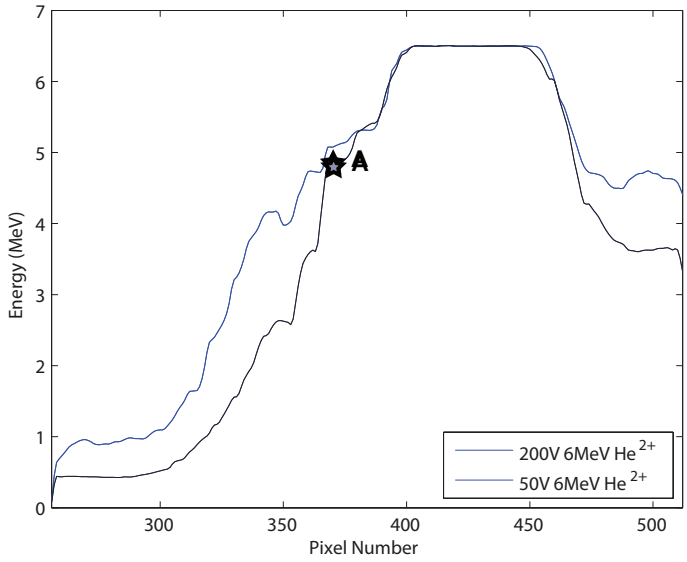

Figure 7.18: CCE profiles of D3c for 6.51 MeV He^{2+}+ ions under an applied bias of 200 V and 50 V

energy loss of approximately 18 keV.

Fig. 7.19a and 7.19b are the MCA spectra and median energy maps of D3a at 200 V as labelled in Fig. 7.9b. The main peak in Fig. 7.19a lays at $\approx$ 11.7 MeV equating to a charge collection efficiency (CCE) of $\approx$ 97 %, accounting for charge collection taking place directly underneath the biased contact pad evident in Fig. 7.19b. Whilst some charge collection confinement is apparent, it is not as readily apparent as in the case of the study with 6.51 MeV He^{2+} ions. Charge sharing in adjacent pixels is occurring at an increased magnitude. A comparison of the charge collection in adjacent pixels has been made for 6.51 MeV and 12.01 MeV He^{2+} ions. Like with the previous study, 100% CCE is present underneath the biased contact, with diminishing CCE in the surrounding regions.

In Fig. 7.16b and 7.19b, three points labelled A, B and C have been marked. These points have been selected as they are within the same approximate position of the Device 3 for each median energy map presented. In Fig. 7.16b, the points A, B and C correspond to a CCE of approximately 63, 20 and 70% respectively. For Fig. 7.19b the same points correspond

to CCE of 69, 49 and 76 %. For each point chosen there is increased charge collection occurring in the case of the 12.01 MeV He^{2+} ions when compared with the 6.51 MeV He^{2+} ions case.

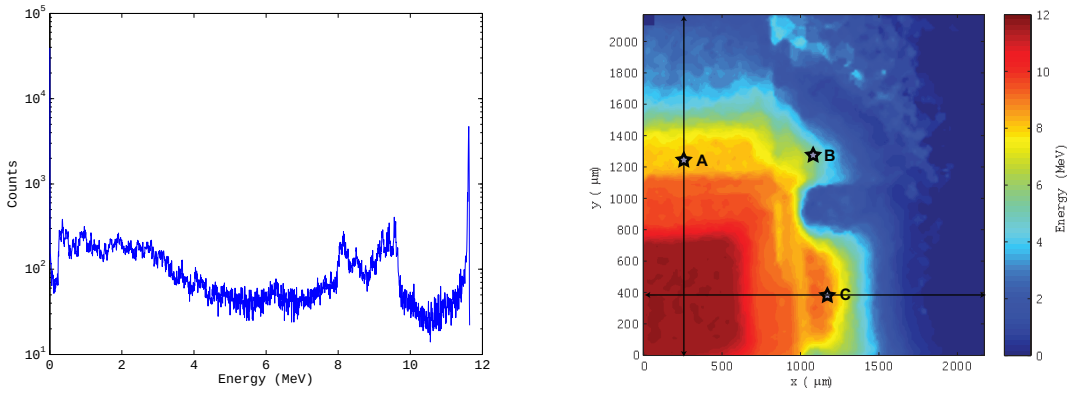

(a) MCA spectra

(b) Median energy map

Figure 7.19: MCA spectra and median energy map of Device 3. D3 a) is biased at 200 V on channel 1. The arrow represents the cross section at which the line profile in Fig. 4 is generated.

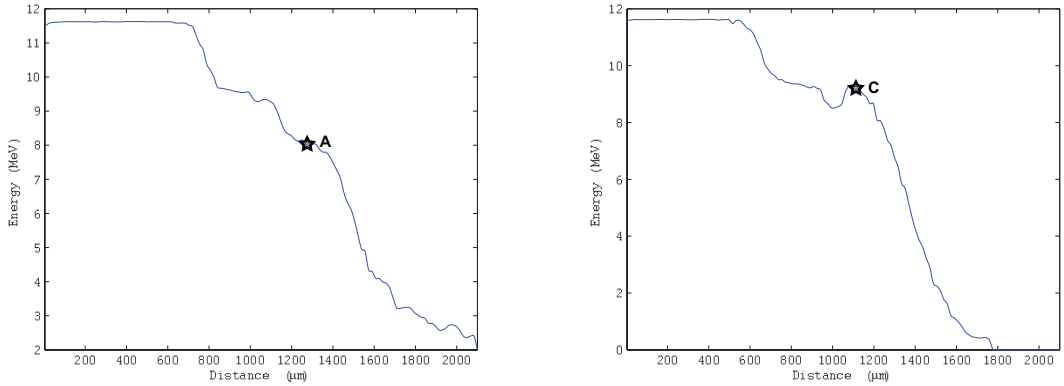

(a) CCE profiles (x) of 1st Gen LT device (D3)

(b) CCE profiles (y) of 1st Gen LT device (D3)

Figure 7.20: CCE profiles (x & y) of D3a for 12.01 MeV He^{2+} ions under an applied bias of 200 V. The profile is taken at a fixed value upon the x & y axis.

7.4.5 Angular Dependence

The IBIC study was continued with devices 2 and 3 under an applied bias of 250 V, with an emphasis upon angular dependence. 12.01 MeV He^{2+} were made incident upon the device at 0°, 30°, 45° and 60°. The effect of this is to change the effective vertical range or penetrative depth of the helium ions from 48.1 μm to: 41.7 μm, 34 μm and 24.1 μm[99]. Thus, the manipulation of the incident angle can allow for further examination of the effectiveness of the laser milled trenches in laterally confining charge collection to specific region or pixel.
In this section, the median energy maps corresponding to each incident angle for each device are presented. In addition, CCE profiles taken through the middle of the contacted region are also included. The median energy maps and CCE profiles in this section have not undergone the same spatial calibration used in previous sections and have instead been presented in terms of 'pixel number'.
The results presented, agree with previous results with 6.51 and 12.01 MeV He^{2+} ions incident upon the devices orthonormally. An examination of the charge collection profiles of each device as the incident angle is increased does not show any significant change from the results when the angle of incidence is orthonormal.
Fig. 7.21b, 7.22b, 7.22b and 7.24b presents the median energy map of D3a at each of the incident angle of 0° through to 60°. An associated contraction of the median energy map on the x-axis, but not the y-axis, occurs with increasing incident angle. For this reason, the median energy maps presented in terms of pixel number rather than distance.
Fig. 7.25 presents the CCE profiles taken along the centre of the contact pad shown in the median energy maps for each angle tested. The CCE profiles are taken using a fixed coordinate on the x-axis. This choice has been made as it allows for the best comparison of CCE profiles. The charge collection can be seen to drop off at a sharper rate with increasing angle and therefore a more shallow range, implying an increased effect due to the presence of laser milled trenches.

In each of the median energy maps presented in this section, regions of zero charge collection or 'cold' regions are visible. Enhanced charge collection can be observed surrounding these 'cold' regions and also with the MCA spectra in Fig. 7.21a, 7.22a 7.23a and 7.24a. These 'cold' regions and enhanced charge collection were not observed within any of the other results.

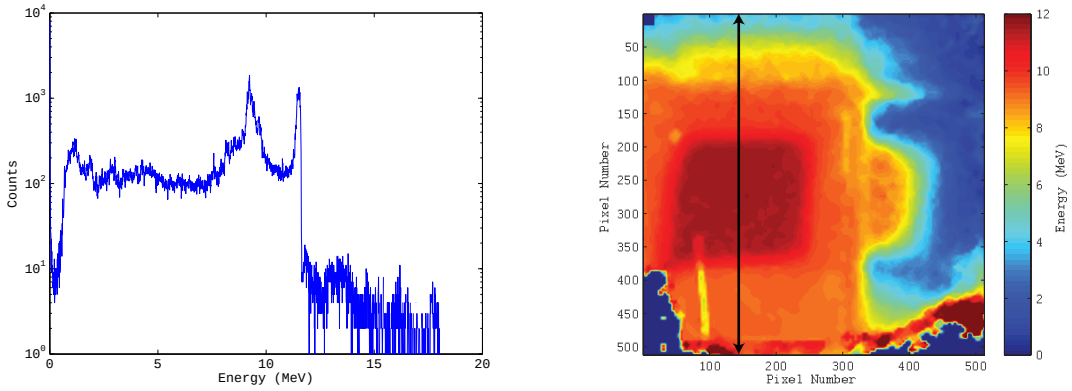

(a) MCA spectra. (b) Median energy map.

Figure 7.21: MCA spectra and median energy map of Device 3. D3a) is biased at 200 V on channel 1 with an incident angle of 0°. The arrow represents the cross section at which the line profiles in Fig. 7.25 is generated.

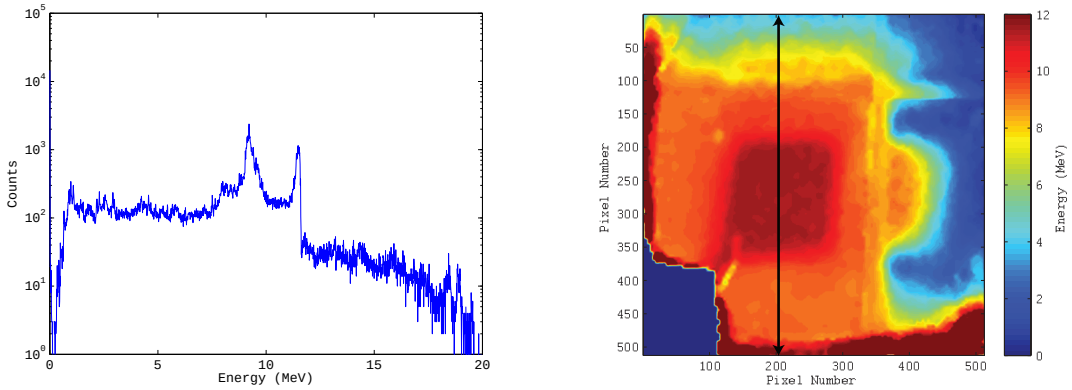

(a) MCA spectra. (b) Median energy map

Figure 7.22: MCA spectra and median energy map of Device 3. D3a) is biased at 200 V on channel 1 with an incident angle of 30°. The arrow represents the cross section at which the line profiles in Fig. 7.25 is generated.

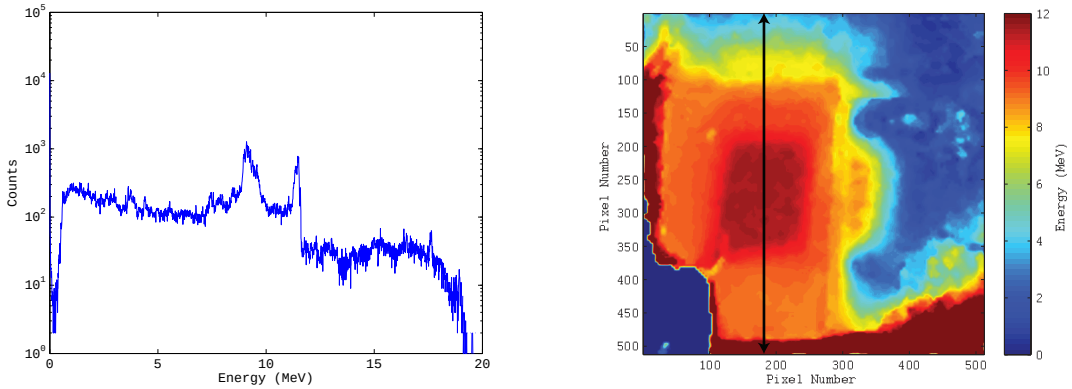

(a) MCA spectra. (b) Median energy map.

Figure 7.23: MCA spectra and median energy map of Device 3. D3a) is biased at 200 V on channel 1 with an incident angle of 45°. The arrow represents the cross section at which the line profiles in Fig. 7.25 is generated.

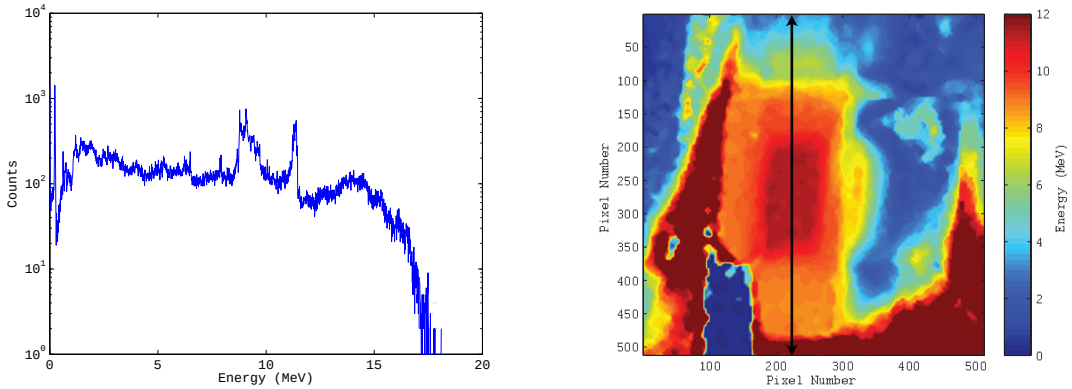

(a) MCA spectra. (b) Median energy map.

Figure 7.24: MCA spectra and median energy map of Device 3. D3a) is biased at 200 V on channel 1 with an incident angle of 60°. The arrow represents the cross section at which the line profiles in Fig. 7.25 is generated.

7.5 Conclusion

Four separate and distinct devices were fabricated upon a high purity, single crystal synthetic diamond from Element 6. Each device was based upon deposited front (Al) and back (Ti/Au) planar metal contacts and connected by gold wire bonds. The device was irradiated with 1.5 MeV protons and 5.5, 6.51 and 12.01 MeV He^{2+} ions. The particles with energy

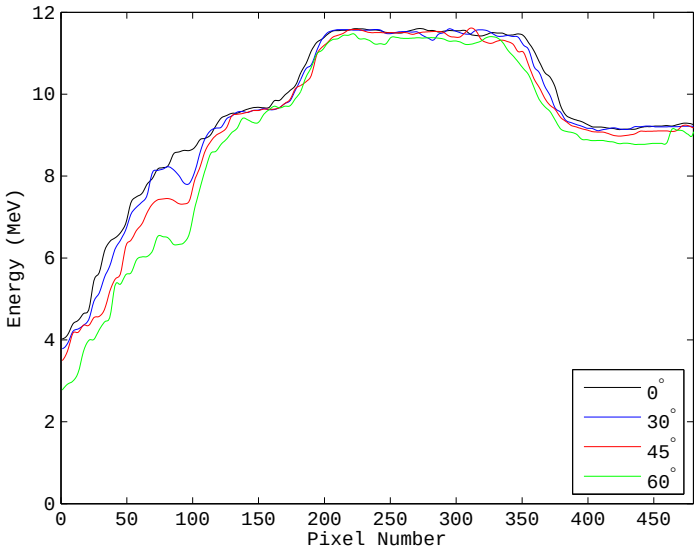

Figure 7.25: CCE profiles of D3a 12.01 MeV He^{2+} ions under an applied bias of 200 V at 0° (black), 30° (blue), 45° (red) and 60° (green).

used have been chosen as they are well within the energies spanned by Galactic Cosmic Rays (GCR), which span from the $\mathrm{MeV\,u^{-1}}$ to $\mathrm{GeV\,u^{-1}}$ range and, thus, can be considered as representative of a component of the space radiation environment[10].

These initial results verify the high quality of the diamond sample and demonstrate the effective simplicity of the Metal-Insulator- Metal (MIM) detector design. The devices have demonstrated charge signal amplitudes matching the theoretical value, i.e. approximately 100% charge collection efficiency (CCE). The Ion Beam Induced Current (IBIC) experiments showed that the technique of pulsed laser milling is capable of creating physically isolated sensitive volumes (SV), leading to reduced effect of charge sharing between adjacent pixels. Charge collection confinement (CCC) was shown to be affected by particle energy and angle of incidence, i.e. penetration depth. In addition it was shown that the CCC could be further improved/optimised though appropriate adjustment of the electric field strength. Lastly, it was shown that a combination of the fabricated laser milled trenches and surrounding electric fields when the device is in 'operation' mode results in a well defined and laterally confined charge collection region.

7.6 Discussion

The results of the IBIC experiment with 1.5 MeV H^+ and 5.5, 6.51 and 12.01 MeV He^{2+} ions show that the device performed as expected. The results for each device presented demonstrate the high quality of the sample provided by Element 6. An analysis of the results using Ramo's theorem[100], has shown charge collection distances (CCD) of the order of mm, to be observed[101]:

$$CCD = d * CCE \tag{7.1}$$

where d refers to the thickness of the detector (500 $\mu\mathrm{m}$).

Polarisation effects not previously observed within alternative Si based devices have been observed. A method to limit such effects was implemented in this work, however, further investigation into the mechanisms causing this effect is required and will be addressed in future work. In Section 7.4.5, enhanced charge collection was observed throughout the results shown. This enhanced charge collection is likely due to the delayed and cumulative collection of charge from outlying regions, distant from the contact pad. This enhanced charge collection should disappear in future designs where SV size is restricted to a smaller volume.

The slight difference between the maximum CCE of device 1 (96%) and device 2 (90%) for 1.5 MeV H^+ ions, may be attributed to the applied bias polarity and the different physical attributes of dominant charge carriers (see Table 2.6). A CCE of almost 100% was seen underneath the aluminium contact pad for each device regardless of the bias polarity, ion species or energy.

The presence of the trenches, in addition to the contact size and location relative to the pixel centre, results in a complex electric field structure. The increased charge collection surrounding the sides of the contact pad in closest proximity to the trenches may be explained by the increasing electric field strength due to the fabrication process (i.e. trench presence and contact location). This provides an explanation for the non-uniformity of the charge

collection surrounding the aluminium contact pad within device 3 in Fig. 7.12b. To correct and optimise the electric field structure, contact pads should be placed centrally, and the contact pad area should be increased to encompass the entirety of the pixel. This will help improve the uniformity of the electric field structure within the pixel and, thus, improve localised pixel charge collection. Furthermore, a mirrored top/back contact arrangement will be adopted in order to best ensure accurate and well defined sensitive volumes that are key to microdosimetry. These improvements, likely should limit the observed decrease in charge collection confinement with increasing particle penetration depth that hampered this device. In addition to the aforementioned improvements, future devices will incorporate true microdosimetric volumes by utilising small pixel areas ($\approx$ 10 x 10 $\mu\mathrm{m}^2$) upon a diamond wafer with thickness close to that of the trench depth ($\approx$ 30 $\mu\mathrm{m}$).

Chapter 8

Buried Contacts (BC) Detector

8.1 Introduction

In the last two chapters, the 1st Generation BID and LT microdosimeter prototypes were explored, with results confirming the performance of each device to varying degrees of success. Ion implantation was successfully utilised in the BID device to create isolated sensitive volumes, however, this device was limited by poor charge collection efficiency and non-uniformity of top layer electrical contacts. Laser ablation, used in the LT device, was shown to provide a viable means of creating isolated sensitive volumes without the loss of charge collection efficiency. However, the isolation of charge collection in this device was found to be dependent upon the range of the particle, with respect to that of the laser milled trench. The sensitive volume size, due to the nature of top/bottom or longitudinal electrical contact configuration used was also inherently dependent upon the thickness of the diamond substrate.

The 3rd alternative diamond based microdosimeter prototype was produced to profit from the advantages of laser ablation aforementioned, but to also overcome the dependence on substrate thickness. This device utilises a buried contact (BC) structure in close proximity to confine charge collection to a desired SV region. Sensitive volume size can be easily

restricted through the dimensions of the buried contact. SV dimensions can be further optimised through bias control and the proximity of charge confining, laser milled trenches. This lateral contact structure is advantageous in that it allows for the production of truly microdosimetric sized SVs without the need for a thin diamond substrate. A charge collection study of the device and an assessment of the technology is presented in this work.

8.2 Fabrication

To test this concept of a buried lateral contact structure, nine devices labelled D1 through D9 in Fig. 8.1 were fabricated upon ultra high purity type IIa single crystal diamond, originally sourced from Element 6[97], with dimensions 4.5 x 2 x 0.5 mm^3. The diamond used was recycled from the previous LT prototype[8] and thus has a history of radiation exposure. Features of the previous detector (laser milled trenches) are evident in Fig. 8.1. These features are present upon the backside of the diamond sample and are visible due to the transparency of the sample.

Prior to the fabrication treatments specific to the BC device, all remnants (metallic/-conductive materials) of previous work which might interfere, were removed. The sample underwent acid etching by submersing in an acid bath ($NaNO_3$ & H_2SO_4) for 60 min at approximately 225 $^{\circ}\mathrm{C}$. Upon the culmination of the acid bath process, the sample underwent initial sample cleaning and preparation. This involved an acetone bath within an sonicator, following by isopropanol rinse, water rinse and drying within pure nitrogen gas. Sample cleaning was followed by the evaporation of gold, using e-beam evaporator, to act as an absorption layer for laser ablation. This absorbing layer is required as diamond is transparent for the particular wavelengths (λ = 532 nm) used by the Oxford Laser-Alpha series equipment. For more information on the process of laser ablation with diamond, see Section 3.5.1.

Using an oxford alpha series laser, milled rectangular prisms 80 $\mu\mathrm{m}$ wide, 60 $\mu\mathrm{m}$ long and

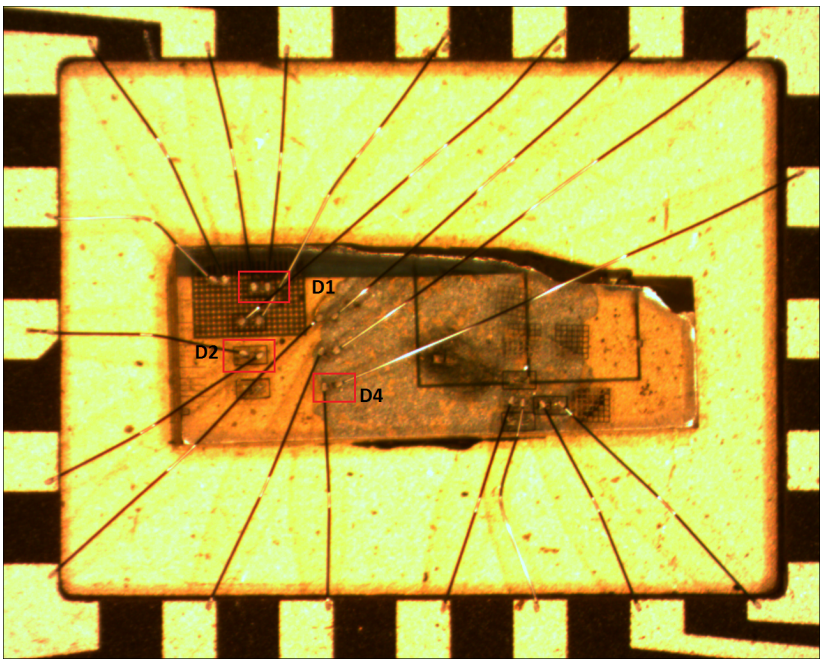

Figure 8.1: Optical microscope image of the Buried Lateral Contact Structure for Diamond Based Microdosimetry with devices D1, D2 and D4 labelled and presented within red squares.

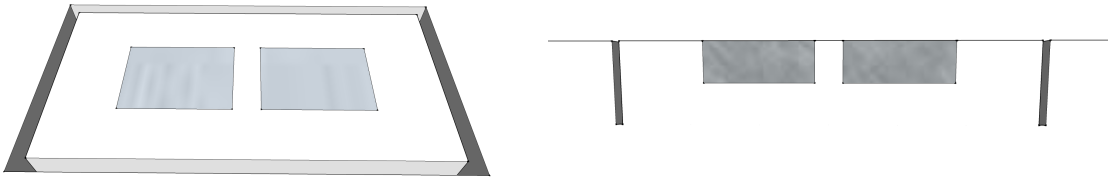

(a) Tilted birds eye viewpoint. (b) Cross section viewpoint.

Figure 8.2: 3D representation of the Buried Lateral Contact Structure.

30 µm deep were created upon the diamond surface. These milled prisms were made in pairs, separated by 10, 20 and 30 µm. The size of the prisms comes from a compromise between the goal of creating true microdosimetric sized volumes and the testing of a new fabrication method. Given that each contact was to be wire bonded, a significant surface area of at least 50x50 μm^2 was required. Multiple sets of the device structure were fabricated to provide security, in case of the failure of one or more devices.

The set of paired laser milled prisms were then filled with silver active brazing alloy and

heated to 800 ° under vacuum, using an evaporation beam chamber to set the braze. Following the application of a brazing metal the diamond was polished to remove silver from the surface without removing silver from the laser milled prisms. An optical profilometry was carried out to determined the difference in height between the diamond surface and the silver filled trenches. Using vertical stimulated interferometry a difference of 0.3 μm was found to exist between the two regions. A thin layer of silver was purposefully left upon the diamond surface as an absorbing layer for the next set of laser milling. Laser milled trenches were milled around selected device structures to create a box with a length of 300 μm and width of 160 μm. The depth of the trench was approximately 60 μm and width of 5 μm. These laser milled trenches surrounding the device were left empty. The sample was then re-polished to remove any existing silver braze upon the surface of the diamond and subjected to plasma cleaning prior to gold wire bonding. The diamond sample was then mounted upon a DIL package with each contact separately wire bonded. In this work, only three of the nine available wire bonded devices shown in Fig. 8.1 are utilised. The devices that are used in this study are listed in **bold** in Table 8.1.

Device	Electrode Separation	Boundary trench
D1	**10** μm	**Yes**
D2	**20** μm	**Yes**
D3	30 μm	Yes
D4	**10** μm	**No**
D5	20 μm	No
D6	30 μm	No

Table 8.1: Information pertaining to the individual differences of the fabricated devices. Devices in bold have been characterised and are presented in Section 8.4.1 and 8.4.2.

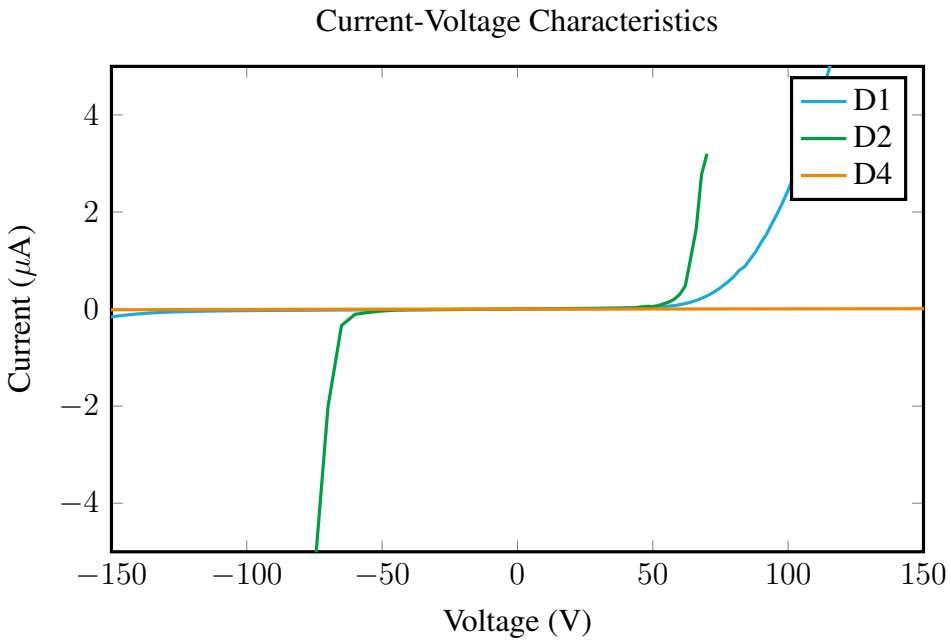

Figure 8.3: IV characteristics of BC devices. IV curves for three devices, D1, D2 and D4 are shown.

8.3 Electrical Characterisation

The electrical characteristics of the BC diamond microdosimeter prototype were tested using a Keithley 6517A electrometer. For each pair of buried contacts corresponding to an individual device, one contact was connected to a virtual ground corresponding to an input of electrometer whilst the other was biased in 1 V increments, with measurements taken over a bias range of at least-50<V<50. A time delay of 2s was utilised to allow measured currents to stabilise after each step in applied bias. Lastly, a current threshold (1 μA) was used as a current limiter. The IV curves for each device present different electrical behaviour in terms of breakdown etc. The IV curves provide enough information to show that use of these devices within 0.5 to 2 $\mathrm{V\,\mu m^{-1}}$ range corresponding to a bias range -60<V<60.

8.4 Charge collection characterisation

A feasibility study was undertaken to ascertain the effectiveness of a lateral buried contact design for microdosimetric purposes. This study used ion induced charge collection measurements (IBIC) undertaken upon the heavy ion microprobe (HIM) beam line of the ANTARES 10 MV tandem accelerator at the Australian Nuclear Science and Technology Organisation (ANSTO).

The IBIC study was performed using 5.5 and 12 MeV He^{2+} ions, with energy chosen such that particle range in diamond was well within the SV (13.62 $\mu\mathrm{m}$) and beyond the SV region (47.88 $\mu\mathrm{m}$)[99]. The ions, normally incident with respect to the diamond surface, were raster scanned across the device. The study was performed over a number of biases to determine optimal running conditions and to ascertain any charge collection (CC) dependence upon electric field strength.

8.4.1 Charge collection study: 5.5 MeV He^{2+}

The first IBIC study was performed using 5.5 MeV He^{2+} ions, having a range in diamond and silver of 13.62 and 11.67 $\mu\mathrm{m}$[99]. The ions, normally incident with respect to the diamond surface, were raster scanned across the device. Results were selected from two of the devices (D1 & D4) characterised to be presented in this section.

The first device presented here, (D4) has an electrode separation of 10 $\mu\mathrm{m}$. The bias conditions of the results presented here are for 10 V translating to an electric field strengths of 1 $\mathrm{V}\,\mu\mathrm{m}^{-1}$. Fig. 8.4a and 8.4b are the median energy maps of D4 under a bias of 10 V respectively and the corresponding MCA spectra.

Upon observation of the MCA spectra (Fig. 8.4b) for D4, only one peak in the charge collection spectra is evident. This peak is situated at $\approx$ 5.4 MeV corresponding to 98 % charge collection efficiency (CCE) and is associated with charge collection between the two electrodes. The rest of the charge collection spectra portrays a broad continuum charge

collection characteristics as is typical of diminishing electric field with distance.

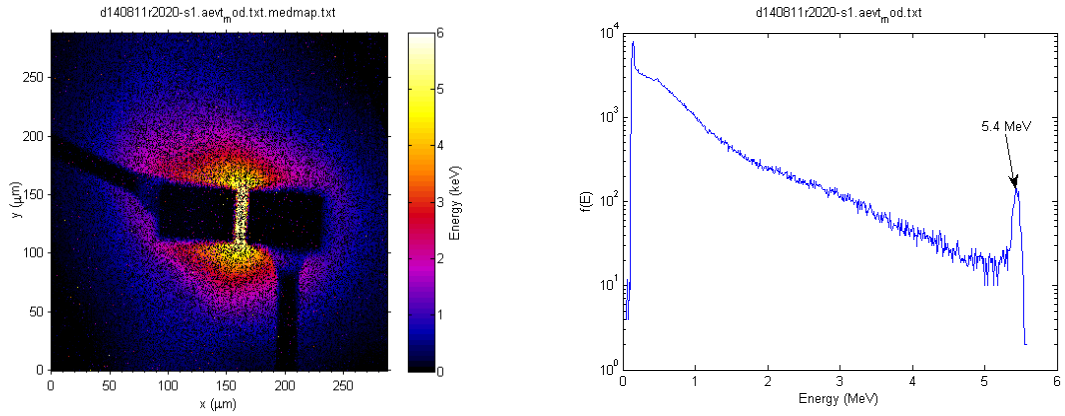

(a) Median energy map.

(b) MCA spectrum

Figure 8.4: Median energy map and MCA spectrum generated by 5.5 MeV He^{2+} ions. The sharp peak at 5.4 MeV is associated with the charge collection between the adjacent electrodes. Scan is situated over D4, which is under an applied bias of 10 V.

The second device presented here, (D2) has an electrode separation of 20 $\mu\mathrm{m}$ and features a boundary trench, surrounding the entirety of the device. Fig. 8.5a and 8.5b are the median energy maps of D2 under a bias of 20 V and the corresponding MCA spectra.
An analysis of the MCA spectra (Fig. 8.5b) shows two main peaks in the energies of charge collected. Peak 1 is positioned at $\approx$ 5.3 MeV corresponding to 96 % charge collection efficiency (CCE)and is associated with charge collection between the two electrodes, where the electric field strength is at its highest (1 $\mathrm{V}\,\mu\mathrm{m}^{-1}$). Peak 2 is positioned at $\approx$ 2.1 MeV corresponding to 38 % charge collection efficiency (CCE) and represents charge collection bounded by the surrounding trench. Charge collection outside of this trenched region drops off rapidly.

8.4.2 Charge collection study: 12 MeV He^{2+}

In this section, the charge collection properties of two devices (D1 & D4) were characterised with respect to 12 MeV He^{2+} ions. The two devices chosen to be presented both have an

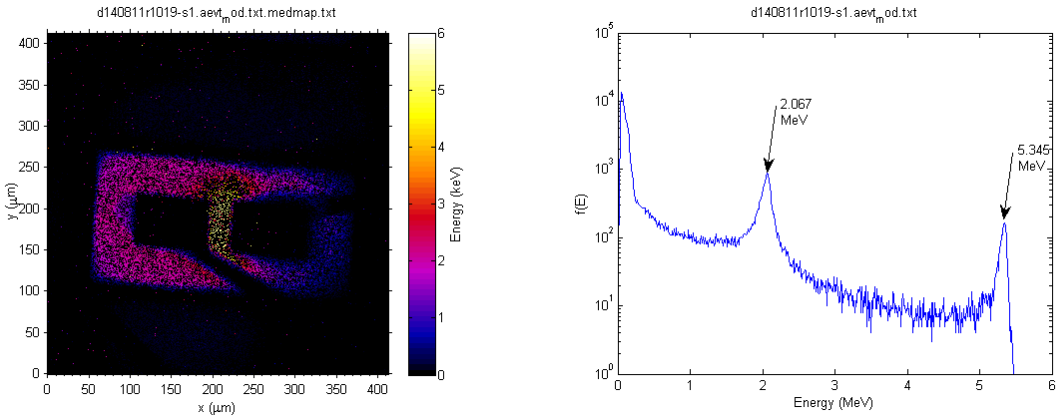

(a) Median energy map.

(b) MCA spectrum.

Figure 8.5: Median energy map and MCA spectrum generated by 5.5 MeV He^{2+} ions. The sharp peak at 5.3 MeV is associated with the charge collection between the adjacent electrodes. Scan is situated over D2, which is under an applied bias of 20 V.

electrode separation of 10 $\mu\mathrm{m}$ and as with the previous section, the two devices chosen are with a boundary trench (D1) and without (D4). The particles chosen in this study (12 MeV He^{2+}) having a range in diamond and silver of 47.88 and 36.64 $\mu\mathrm{m}$, respectively[99]. Ions travelling through the silver electrodes have a markedly reduced end of range compared with counterpart ions travelling only through diamond. While these ions have a range greater than that of the hypothetical SV size, the range is still less than that of the depth of the boundary trench (60 $\mu\mathrm{m}$) that surrounds some of the devices characterised in this paper.

The first device (D4) as described previously in Section 8.4.1 has an electrode separation of 10 $\mu\mathrm{m}$ and does not feature a boundary trench. The device was biased at 10 V and the scan size was reduced so as to more closely examine the charge collection within the electrode separation region. Reducing the scan size has the effect of changing the effective area upon which the beam is scanned. Given that the beam conditions are unchanged, leads to an increased flux which will improve statistics in a short time. The median energy map and MCA spectra corresponding to this are presented in Fig. 8.6a and 8.6b. A peak in the MCA spectra 8.6b at 12 MeV equating to 100 % charge collection demonstrate the effectiveness of charge collection between the two electrodes. The median energy map

demonstrates charge collection taking place underneath the electrodes, due to the extended range of primary particle in this experiment. Charge collection underneath the electrodes is associated with the emergence of broad peaks at 2.9 MeV in the MCA spectra in Fig. 8.6b (24 % CCE). The change/loss in charge collection efficiency underneath the electrodes with distance away from the electrode separation provides another indication of the role of the lateral electric field structure in charge collection behaviour of this device. The result combined with that previously shown, whilst confirming the excellent charge collection within the region between the two electrodes demonstrates that more work is required in confining the electric field laterally and longitudinally.

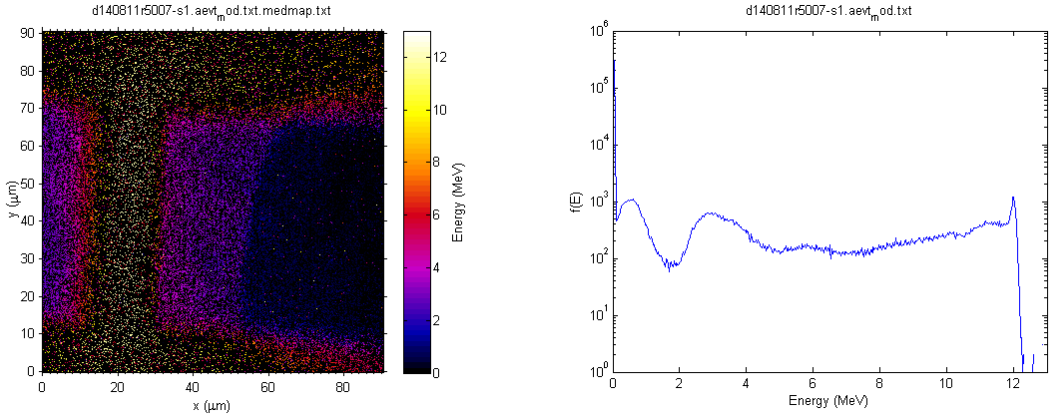

(a) Median energy map.

(b) MCA spectrum.

Figure 8.6: Median energy map and MCA spectrum of BC diamond detector for 12 MeV alphas. The Scan is situated over D4 which has an electrode separation on 10 $\mu\mathrm{m}$, which is under an applied bias of 10 V giving a maximum electric field strength of 0.5 $\mathrm{V}\,\mu\mathrm{m}^{-1}$.

To examine the effect of electrical field strength upon the charge collection properties, a bias of 5, 10 and 20 V was applied. The median energy maps for each respective bias is presented here in Fig. 8.7a, 8.8a and 8.9a as well as the corresponding MCA spectra, Fig. 8.7b, 8.8b and 8.9b.

As expected, the charge collection characteristics of D1 for 12 MeV He^{2+} ions are similar to those produced with the lower energy counterparts (5.5 MeV He^{2+}) with D2, though with a few notable differences. There is less confinement within the lower energy regime in

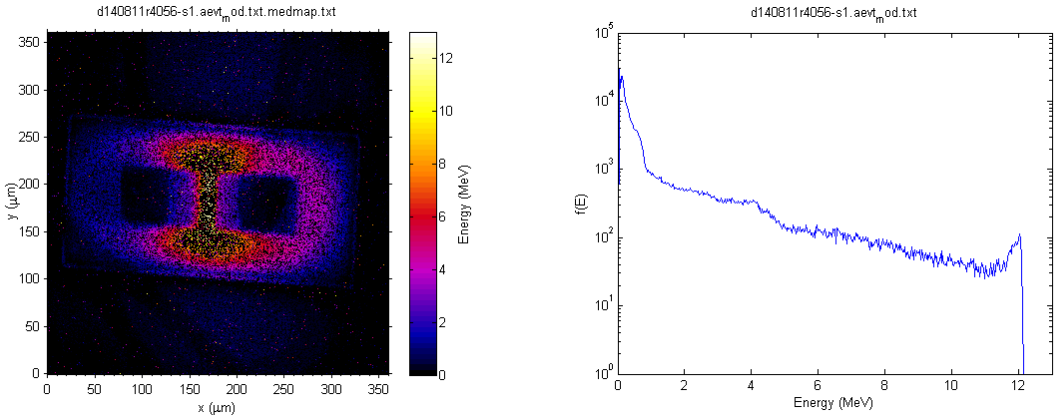

(a) Median energy map. (b) MCA spectrum.

Figure 8.7: Median energy map and MCA spectrum of BC diamond detector generated for 12 MeV He^{2+} ions. The Scan is situated over D1 which has an electrode separation on 10 µm, which is under an applied bias of 5 V, giving a maximum electric field strength of 0.5 V µm^{-1}.

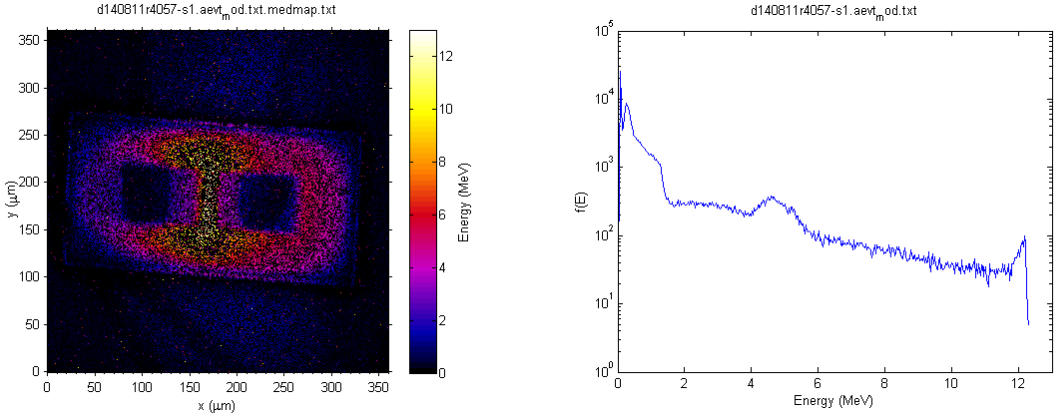

(a) Median energy map. (b) MCA spectrum.

Figure 8.8: Median energy map and MCA spectrum of BC diamond detector, generated by 12 MeV He^{2+} ions. The Scan is situated over D1 which has an electrode separation on 10 µm, which is under an applied bias of 10 V giving a maximum electric field strength of 1 V µm^{-1}.

Fig. 8.7a compared with 8.5a. In Fig. 8.7a, a region of charge collection surrounding the boundary trenched device with CCE $\leq$ 15% is evident. The diffusion length of charge carriers in diamond along with the strength of the electric field allow for the partial collection of charge outside the boundary region for ions of equivalent range. Additionally charge is now being collected from underneath the electrodes, whereas in the previous section this was not

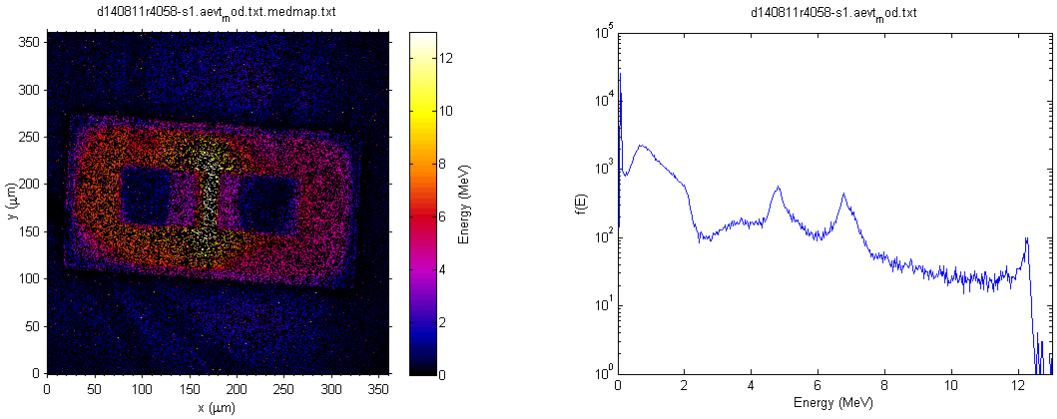

(a) Median energy map

(b) MCA spectrum

Figure 8.9: Median energy map and MCA spectrum of BC diamond detector, generated by 12 MeV He^{2+} ions. The Scan is situated over D1 which has an electrode separation on 10 µm, which is under an applied bias of 20 V giving a maximum electric field strength of 2 V µm^{-1}.

a contributing factor.

While there is no appreciable increase in the magnitude of the CCE (15 %) outside the trenched region, there is an increase in the area of this collection region with increasing bias. Furthermore, the increased electric field strength within the bounded region results in an increased charge collection. An analysis of the MCA spectra in Fig. 8.7b, 8.8b and 8.9b shows distinct peaks arising. There is an enhancement in the charge collection with increased bias leading to a shift in peak position. The main peak resulting from charge collection between the two electrodes is positioned at 12.03, 12.17 and 12.22 MeV for a bias of 5, 10 and 20 V. A second peak can be distinguished from the spectrum in Fig. 8.7b, laying at 4.1 MeV arising from charge collection within the bounded region. This peak shifts to 4.5 MeV in Fig. 8.8b and 4.8 MeV in Fig. 8.9b. A third peak is clearly apparent in Fig. 8.9b at 6.7 MeV.

8.5 Conclusion and Discussion

A new method of fabricating diamond microdosimeters has been investigated. Laser ablation of diamond, in conjunction with silver brazing metal was used to create a buried lateral contact structure in high purity electronic grade type IIa single crystal synthetic diamond from Element 6[97]. A number of devices were created upon the same wafer with two main differences to distinguish them from one another. The first identifying factor was the electrode separation which was set to be 10, 20 and 30 μm. The second difference was the presence of boundary trench surrounding the device, with the purpose of containing and restricting charge collection to within the bounded area.

A charge collection study of the new detector was performed with 5.5 and 12 MeV He^{2+} ions, in order to ascertain the effectiveness of this new design. The results of the study show excellent charge collection properties (100 % CCE), indicative of the high quality of the material produced from Element 6 and consistent with previous research[8]. These charge collection properties occurred within each device tested, in the desired region between the two electrodes. The presence of a boundary trench showed a comparatively improved confinement of charge collection within the bounded region demonstrating a significant reduction in the CCE from inside to outside the trenched region. Given that microdosimetry is fully dependent upon an accurately defined micron sized sensitive volume where charge collection is wholly contained, further improvements are a necessity if buried lateral contacts are to be useful for diamond based microdosimetry.

The major improvement required would be with respect to the volume definition i.e., the region from which charge is collected. This would require a method of decreasing laterally and longitudinally the region of charge collection. One method would be the decrease the size of the bounded region by increasing the proximity of the trenches to the buried contacts. This can be further improved by increasing the trench width and depth to prevent charge from migrating from outside the bounded region. The next method to improve upon

volume definition is through the size of the buried contacts themselves. According to the size and location of the contacts used in this device, the minimum size of the SV is by definition 30x60xD μm^3, where D is the contact separation equal to either 10, 20 or 30 μm. Finally charge collection from underneath electrodes needs to be limited, which might be achieved through a combination of substrate thinning and/or bias control.

This device is further investigated through the use of dedicated TCAD studies in Chapter 16.

Part IV

Future Detectors: Concept to Reality

Chapter 9

2nd Generation LT Detector

The 2nd Generation LT microdosimeter prototype is conceptually identical to the 1st generation LT device, in that laser milling is used to create physically isolated sensitive volumes for charge collection. The 1st generation LT device was limited in terms of microdosimetric applications by the size of the sensitive volumes, due to the substrate thickness (500 μm) and pixel size (606x606 μm^2). This device improves upon the previous design in three main ways:

1. Thin substrate (30 μm)
2. Smaller pixels (30x30 μm^2)
3. Mirrored contacts

Each improvement, has been purposefully made to create sensitive volumes truly representative of microdosimetry, along with an improved electric field structure. The placement of the electrical contacts, relative to the pixel are centralised and 'mirrored' top to back, so as to create a uniform field structure within the device as compared with the previous 1st generation LT device.

Due to equipment issues, this device was not completed at the time of submission, however

a test device which utilised the same fabrication procedure was completed. It should be noted that work on this project is ongoing and will be presented at a later date. Due to the unfinished nature of this work, this chapter will be dedicated to explaining the current status of the work at time of submission, as well as the rest of the processes required in order to complete the fabrication stage. Initial electrical characterisation of the test device is also included to verify the fabrication technology. This device represents the culmination of 3.5 years of work in developing diamond based microdosimeters.

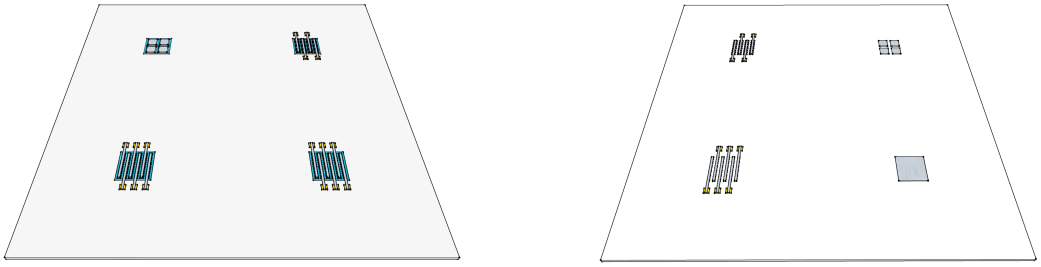

(a) Top view of diamond device design.

(b) Bottom view of diamond device design.

Figure 9.1

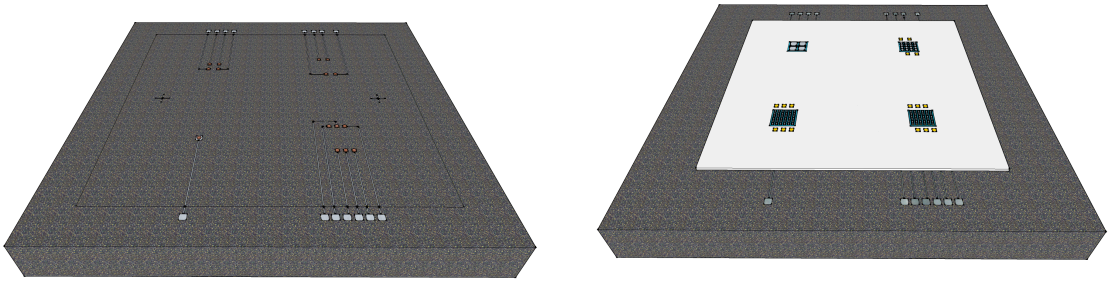

(a) Top view of the pcCVD base design.

(b) Top view of diamond device design mounted upon pcCVD base

Figure 9.2

9.1 Fabrication

As mentioned in the previous section, this device was not completed at the time of submission. For this reason, the discussion upon the fabrication techniques and process used

shall be divided into two subsections dealing with what has been done and what is currently underway. The fabrication procedure for this device is well known however, having already been tested upon a thick sample of diamond previously. The second section then is a description of the steps required to finish the device based upon previous work, added with the context of the necessary modifications required in moving from fabrication upon thick to thin substrates of diamond.

9.1.1 Steps completed

The 4th generation device was fabricated upon a wafer of ultra high purity single crystal diamond with dimensions, 4 x 4 x 0.03 mm^3 from Element6 via Diamond Delaware Knives. The first step in the fabrication process was sample preparation, where the device was cleaned with ethanol, isopropanol and deionised water and then dried in pure N_2. A layer of 50 nm gold was evaporated upon the surface of the diamond substrate using e-beam evaporator, to act as an absorbing layer for laser ablation. Prior to laser milling, the diamond substrate surface was rotated ($\approx 20\ ^\circ$) with respect to the CNC plane of the laser apparatus. This rotation was done with the crystal axis in mind. Previous work during the preparation phase, demonstrated the fragility of thin diamond, and the increased likelihood of cleavage along laser cuts made along the diamond crystal planes, during successive phases of the work. A slight rotation was hypothesised to decrease the probability of cleavage by maintaining the structural integrity of the diamond bulk.

Following the evaporation of a gold absorption layer, a nano second pulsed laser with wavelength $\lambda = 532\ \mathrm{nm}$, generated by the Oxford Laser-Alpha series, was used to mill trenches in the diamond substrate 5 $\mu\mathrm{m}$ wide and 15-20 $\mu\mathrm{m}$ deep. Three designs (D1, D2 and D3) have been built upon the wafer as detailed in Fig. 9.2b. D1 features a 2 by 2 array of pixels with size 120 x 120 $\mu\mathrm{m}^2$. D2 features a 4 by 4 array of pixels with size 60 x 60 $\mu\mathrm{m}^2$. D3 features a 6 by 6 array of pixels with size 30 x 30 $\mu\mathrm{m}^2$. The sample was then placed into an acid bath

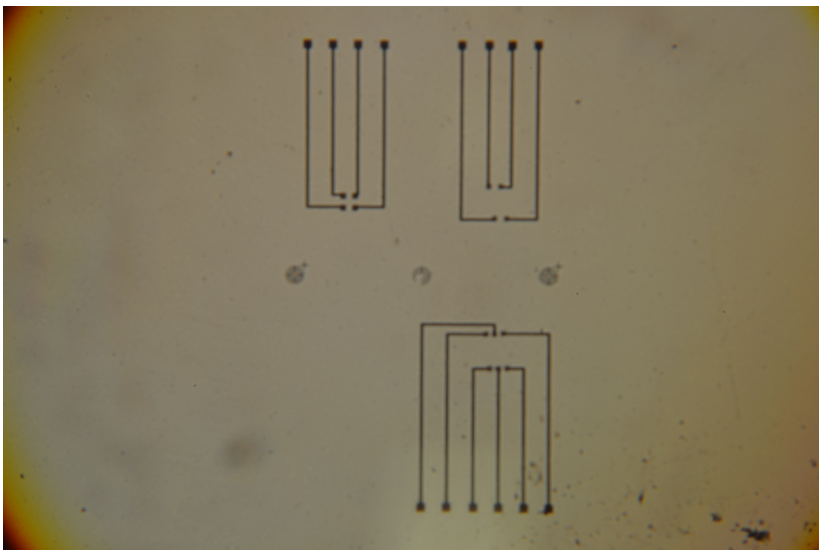

Figure 9.3: pcCVD base after laser milling, but before application of silver ABA. Three patterns corresponding to devices D1, D2 and D3 are seen.

($NaNO_3$ & H_2SO_4) for 60 min at approximately 225 $^{\circ}\mathrm{C}$ to remove the graphitic by-products of laser ablation and then cleaned in stages with ethanol, isopropanol and deionised water and then dried in pure N_2.

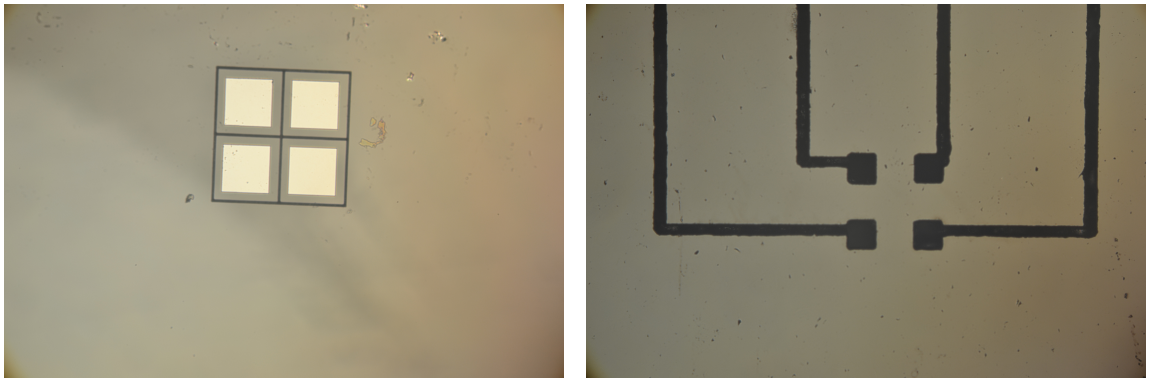

(a) D1: 2x2 pixel. (b) pcCVD base for D1.

Figure 9.4: 1st device design (D1: 2x2 pixel array) of the 2nd Generation LT prototype. The array (left) and trenched pattern (right) are created through laser ablation. Aluminium contacts (white squares) created through E-beam evaporation. Photos were taken before silver ABA was applied to fill patterned trenches (right).

Due to the reduced thickness and associated fragility of the diamond sample, a polycrys-

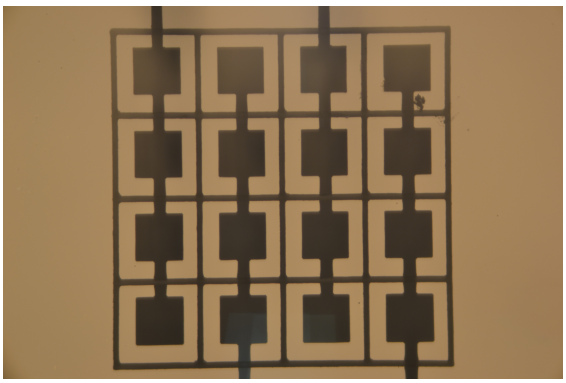

(a) D2: 4x4 pixel.

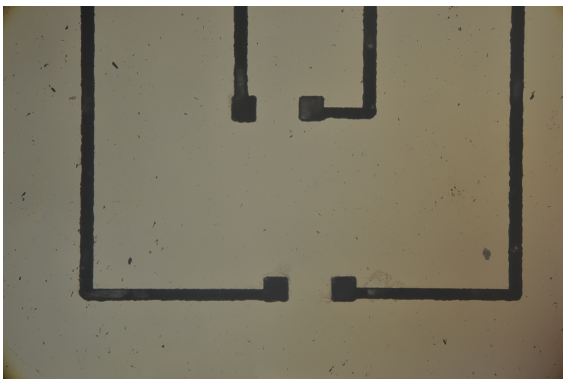

(b) pcCVD base for D2.

Figure 9.5: 1st device design (D2: 4x4 pixel array) of the 2nd Generation LT prototype. The array (left) and trenched pattern (right) are created through laser ablation. Aluminium contacts (white squares) created through E-beam evaporation. Photos were taken before silver ABA was applied to fill patterned trenches (right).

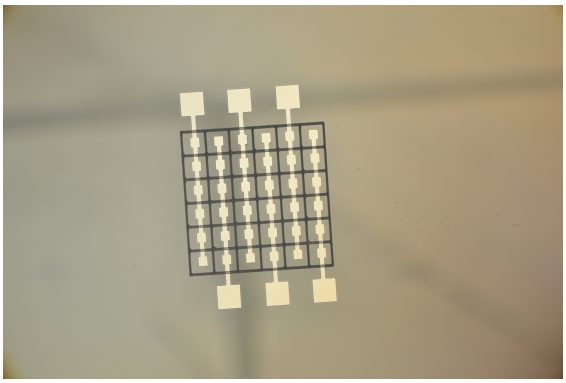

(a) D3: 6x6 pixel.

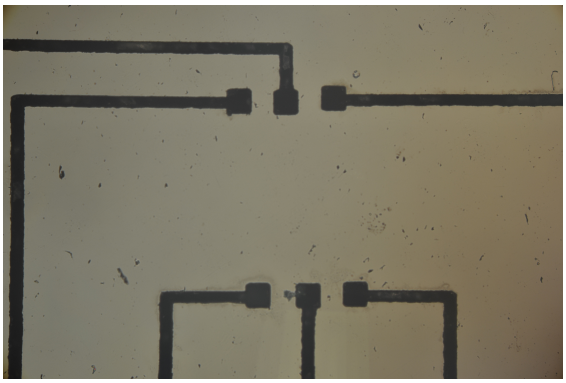

(b) pcCVD base for D3.

Figure 9.6: 1st device design (D3: 6x6 pixel array) of the 2nd Generation LT prototype. The array (left) and trenched pattern (right) are created through laser ablation. Aluminium contacts (white squares) created through E-beam evaporation. Photos were taken before silver ABA was applied to fill patterned trenches (right).

talline CVD diamond was acquired (5 x 5 x 0.5 mm^3) to serve as a base as well as to allow for electrical connection to the back contacts of the device. Laser ablation was also used in this work to create milled squares in the same positions as their back contact counterparts previously created upon the backside of the thin scCVD diamond. A second set of laser milled squares with size 80 x 80 $\mu\mathrm{m}^2$ were created outside the placement of the scCVD diamond. Laser milled trenches were created to connect the inner milled squares to their larger,

distant counterparts. These grooves were filled with a silver ABA, to provide an electrical contact and heated to above 900 ° under vacuum using an evaporation beam chamber to set the braze. The pcCVD diamond is then lapped to remove any braze from the surface, leaving only the silver braze filled trenches.

9.1.2 Steps in progress

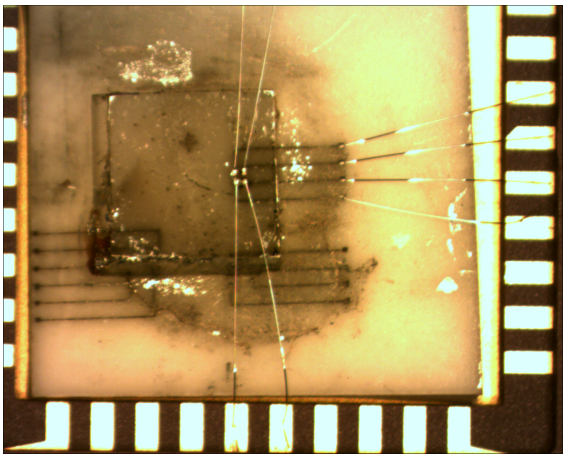

(a) Test device featuring 2x2 pixel array. An aluminium based ceramic is used in place of the pcCVD base that will be used on the final device.

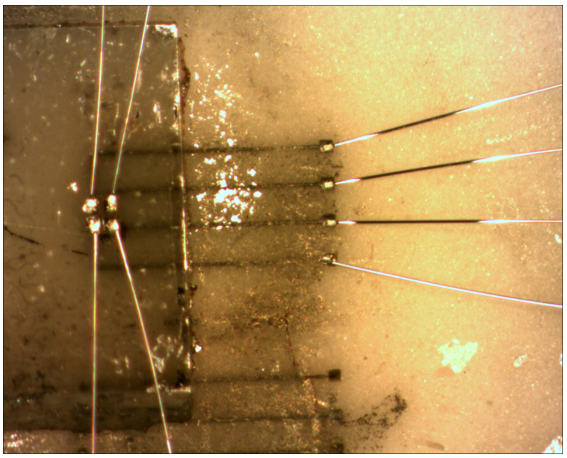

(b) Optically zoomed image of the test device. Wire bonding has been made directly to the top four contacts on the diamond surface as well as to the four silver filled trenches.

Figure 9.7

The 30 µm wafer was then mounted upon a glass slide (laser milled trenches down) in order to provide ease in handling and add robustness for succeeding steps in the fabrication process. Photoresist is then spun onto the mounted diamond sample and baked at 100 °C for 60 s. Previous devices utilised contact based photolithography as part of the process of creating electrical contacts upon diamond. It was found during the preparation phase that the pressure applied in contact photolithography was too high and caused cleavage along the weak points in the diamond bulk, either the lattice planes or laser cuts. Projection based photolithography was chosen to substitute the contact based alternative. This method utilised a lens to focus the UV light (see Section 3.6.2.3), rather than rely upon a lack of

separation as with contact based methods. The diamond sample was then exposed to UV light (λ = 350 nm) through a purpose made mask and then rinsed in a developer solution. The E-beam evaporator is used to create a patterned back contacts of 20 nm titanium, 50 nm of nickel and 50 nm of platinum.

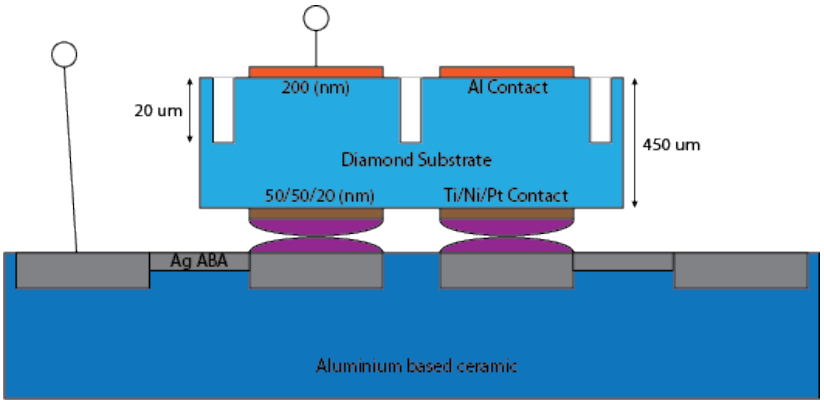

Figure 9.8: Simplified design cross-section of the entire device. The recycled diamond substrate on top (light blue) features laser milled trenches (clear) with aluminium contacts on top (orange) and Ti/Ni/Pt contacts (brown) on the bottom. The diamond is electrically and physical connected to an aluminium based ceramic via indium bumps (purple) and silver braze (grey). Not visible in this diagram is an epoxy layer filling the voids between the diamond and the ceramic.

The next stage in the fabrication process is indium bump bonding to join the pcCVD base and the 30 µm thick diamond substrate, see Fig. 9.8. The first step is to spin a thick photoresist upon the back side of the scCVD diamond ontop of the back contacts as well on to the top of the pcCVD diamond. Using contact based photolithography each sample was exposed to UV light through a duplicate and mirrored shadow masks and then developed. Indium bumps 10 µm high were deposited in the mirrored locations on both samples using the PVD75 thin film deposition system. These indium lumps were bump bonded together to create a continuous electrical contact. The device is sprayed with teflon, leaving only the area of separation between the two devices left uncoated. Epofix resin is then applied to the pcCVD diamond base in order to fill the gap between the pcCVD base and the scCVD substrate and provide structural integrity. Once the EpoFix has cured, the teflon is removed

by cleaning with methanol, isopropanol, water and dried with N_2. With the bump bonding complete and the EpoFix cured, the scCVD sample and pcCVD base now electrically and physically connected.

EpoFix (25 resin:3 hardener) was applied to entire top surface of the diamond substrate in order to fill the laser milled trenches and then left to cure within a desiccator for 24 h. The resin is then gently lapped until diamond pixels are revealed, but not so far that the EpoFix is removed from the laser milled trenches. The primary purpose of the resin is to provide a supporting structure for parallel aluminium contacts connecting rows of centrally placed aluminium contact squares for each pixel. Aluminium contacts were also deposited upon the bottom of the diamond sample to mirror those upon the top.

The device is then mounted upon a 20 pin DIL package using silver paste upon the pcCVD diamond base. Electrical connections from the top and bottom contacts of the device are made to the DIL package using gold ball point bonding.

9.2 Electrical Characterisation: Dummy Sample 2x2

The electrical characteristics of the test device were performed using a Keithley 6517A electrometer. The measurements were taken between mirrored sets of contacts with bias applied to the top contact and the corresponding back contact connected to a virtual ground corresponding to an input of electrometer. I-V measurements were taken in the range of -1000<V<1000, with bias applied to the front contacts individually and ramped in 20 V increments. A time delay of 2s was utilised to allow measured currents to stabilise after each step in applied bias. Lastly, a current threshold (1 μA) was used as a current limiter.

The IV characteristics presented in Fig. 9.9 depict IV curves for two of the four sets of contacts of a 2x2 pixel array of the Gen4 test device. The IV curves for both devices depict similar characteristics, with breakdown occurring at approximately -900 and -700 V. The IV curves depict asymmetric behaviour due to the different metals used to create electrical

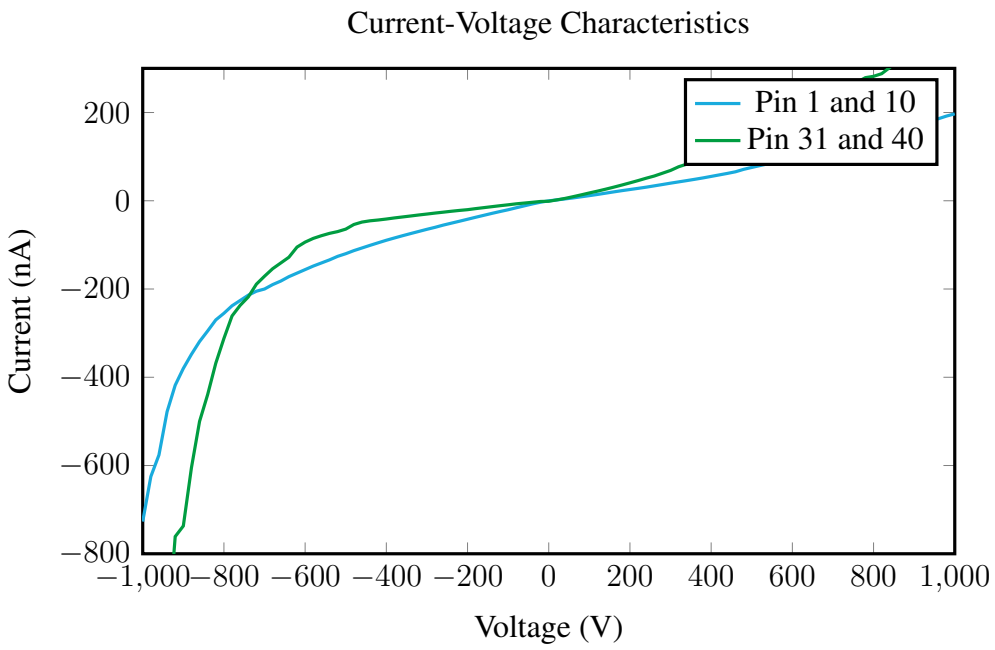

Figure 9.9: Electrical characteristics of the test device of the 2nd generation LT prototype.

contacts upon either side of the diamond substrate.

Capacitance measurements were also undertaken with a constant capacitance of approximately 0.5 pF was measured across each device. This is slightly higher than measured previously (0.2 pF), i.e., on the 2nd Generation device. The higher capacitance is hypothesised to be a result of changing geometry (Substrate thickness, Contact area), materials and the additional components of indium bump bonding etc.

9.3 Discussion

The fabrication of the 2nd generation diamond based microdosimeter prototype, utilising laser milled trenches on a thin diamond substrate is well under way. This device represents a significant step forward in the advancement of diamond based microdosimetry. A test device was produced as part of this work to validate the fabrication procedure given the complexity of processing stages required in order to create such a device. The IV curves

of the test device demonstrate the functionality of the device and serve as a preliminary validation of the fabrication process.

Chapter 10

Trenches, Buried contacts and Cylindrical SVs

10.1 Introduction

This chapter is dedicated to dealing with alternative devices, either that of the pixelated design using laser milled trenches (LT), lateral SV structure using buried contacts (BC) or a new cylindrical sensitive volume (CSV) structure combining different aspects of fabrication techniques used in the various devices produced thus far.

Each of the three types of devices are fabricated concurrently upon the same sample material. The fabrication method of each device are treated individually within each section. It should be noted that several fabrication steps listed for the individual devices are not unique to that particular device, i.e., sample preparation, laser ablation, acid bath etc and so are performed at the same time.

10.2 Sample production and the common contact

The sample of diamond used in this work, was produced at the Melbourne Centre for Nano-fabrication (MCN). The sample having a layered structure was grown in stages, as each layer has a slightly different composition. The base layer or seed High Pressure High Temperature (HPHT) diamond with dimensions 3x3x0.5 mm^3, with a 3 µm layer of boron doped single crystal synthetic diamond grown upon the top. Electronic grade diamond (Nitrogen content in the order of ppb) is then grown on top of this base layer to provide the detector grade diamond to be utilised for construction of sensitive volumes. The surface area of this layer is the same as that of the base and differs only in the thickness which is approximately 30 µm.

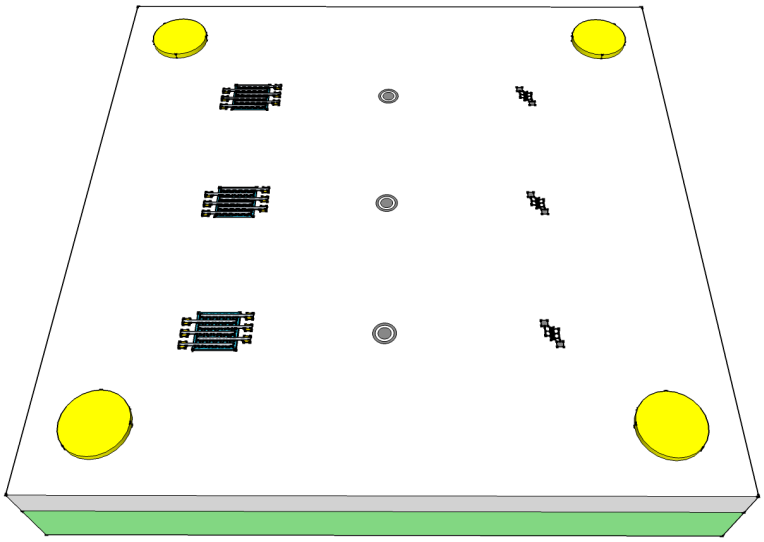

Figure 10.1: Tilted birds eye view of the entire device. A 3x3 array of the devices are fabricated to include three of every device. A gold cylindrical contact is present at each corner. These are the back contacts which connect to the boron doped layer (green) through use of laser milling and subsequent metallic brazing.

The sample structure provided unique opportunities in terms of fabrication and was a source of inspiration for the designs produced. The boron doped substrate provided a conductive layer of diamond that could be used as a common contact, provided a suitable means of creating an electrical connection. This was achieved by milling through the electronic

grade diamond with laser and filling the milled structure with gold ABA. This gold filled trench can then be wire bonded giving an electrical connection to the entire boron doped region, thus creating a common contact.

10.3 MIM pixelated: Gen3

This design features a 6x6 array of SV created using laser milled trenches and filled with an epoxy (EpoFix) to provide a supporting structure for the aluminium contacts evaporated through a shadow mask onto the top surface such that within each pixel there is a 10x10 μm^2 contact and with each row of pixels connected in parallel by a strip of aluminium. This design is for all practical purposes the same as that described in the previous chapter, with the notable difference that the back contact is the boron doped layer connected electrically via a laser milled trenched filled with silver ABA and connected via gold ball bonding. The top contacts are the same, as shown in Fig. 10.2a.

Following laser milling, the diamond is then subjected to an acid bath within ($NaNO_3$ & H_2SO_4) for 60 min at approximately 225 $^{\circ}\mathrm{C}$ to remove the graphitic by-products of laser ablation and then cleaned in stages with ethanol, isopropanol and deionised water and then dried in pure N_2. The sample is then wetted with EpoFix (25:3) and allowed to set within a desiccator for 24 hours. The surface of diamond is lapped down to remove any epoxy from the top but keeping trenched regions filled. The method involves careful abrasion using various grades of sandpaper and finally tissue paper to perform finer and finer smoothing to level epoxy within the trenched regions with the diamond surface.

Photoresist is then spun onto the mounted diamond sample and baked at 100 $^{\circ}\mathrm{C}$ for 60 s.The diamond sample was then exposed to UV light (λ = 350 nm) through a purpose made mask and then rinsed in a developer solution. The E-beam evaporator is used to create a patterned contacts of 200 nm aluminium. Lift-off of excess aluminium is performed by rinsing in methanol solution and drying with N_2 gas.

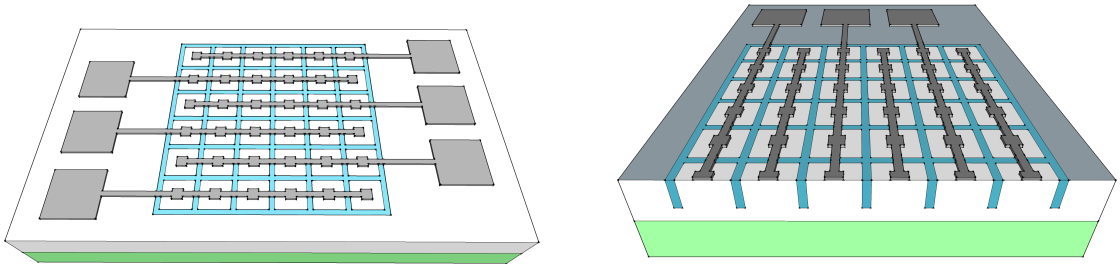

(a) Tilted birds eye viewpoint

(b) Tilted cross section viewpoint of device 1 design.

Figure 10.2: Device 1 design: The contacts (grey) are easily visible as well as the epoxy filled (blue) trenches used to create pixelated sensitive volumes along with the boron doped substrate (green) used to create a common ohmic contact upon the back side.

10.4 Buried Contacts: Gen2

This device is the next step in the evolution of lateral SV structure created via buried contacts. It is a natural extension of the previous device, in that it allows multiple SVs to be connected in parallel. The reduced contact size, diamond substrate thickness and proximity of laser milled boundary trenches provides the detector with improved SV definition. This device can also be used the more traditional vertical method by connecting only one of the contacts and using the common boron doped diamond as a back contact. This provides an advantage in terms of operating the devices in two modes with each having a different SV structure in terms of size and geometry.

The first stage of the fabrication process is sample preparation; where the device was cleaned with ethanol, isopropanol and deionised water and then dried in pure N_2. Next, 50 nm layer of gold is evaporated upon the surface of the diamond substrate using e-beam evaporator, to act as an absorbing layer for laser ablation. A program written in g-code was created specifically to control the laser milling according to the design specifications. Numerous tests were carried out prior in order to properly calibrate laser parameters so that trench width

were not so great so as to create overlaps or so deep to mill into boron doped region. The first stage of laser milling creates the milled squares (grey) 10x10x10 μm^3, black squares for wire bonding 50x50x10 μm^3 and the connecting trenches also marked in black in Fig. 10.3, to connect the two.

Following the first stage of laser milling, the diamond is then subjected to an acid bath within ($NaNO_3$ & H_2SO_4) for 60 min at approximately 225 $^{\circ}C$ to remove the graphitic by-products of laser ablation and then cleaned in stages with ethanol, isopropanol and deionised water and then dried in pure N_2. Following this, the diamond surface is 'wetted' with silver ABA in order to fill trenched regions with conductive metal to create contacts and heated to 800 $^{\circ}$ under vacuum using an evaporation beam chamber to set the braze. The second stage of laser milling is then implemented using the silver layer as an absorbing ablation layer. The second stage is used to create the boundary trenches (blue) as represented in Fig. 10.3. These trenches are left unfilled and serve the purpose of confining charge collection. Finally the entire surface of diamond is lapped down to remove any silver from the top but keeping trenched regions filled. The method involves various stages of lapping, first using the RotoPol system to perform a coarse removal of silver and then using various grades of sandpaper and finally tissue paper to perform finer and finer smoothing to level silver within the trenched regions with the diamond surface.

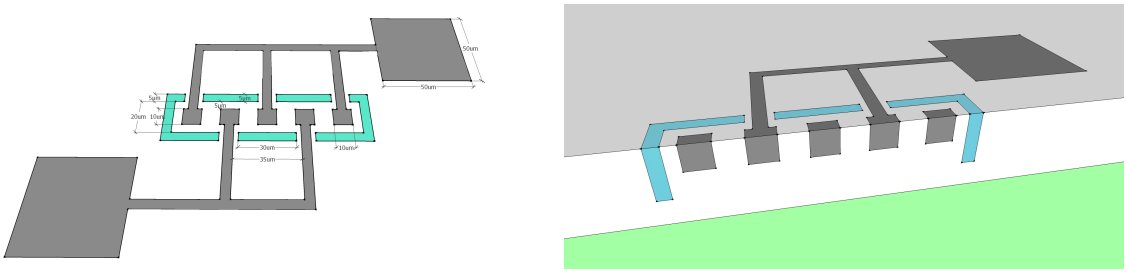

(a) Tilted birds eye viewpoint. (b) Tilted cross section viewpoint.

Figure 10.3: Device 2 design: The buried contacts and connecting strips (grey) are easily visible as well as the epoxy filled (blue) trenches used to help promote charge confinement.

10.5 Cylindrical SV: Gen1

The last of the devices fabricated upon the layered diamond sample is the first attempt in creating cylindrical SVs within diamond. The process used in the fabrication of this device is relatively simple with respect to some of the devices previously covered in this thesis. This device again makes use of the laser milling and active brazing alloy technologies previously used in alternative devices, like that of the buried contacts to produce a lateral SV structure. The first stage of the fabrication process is sample preparation; where the device was cleaned with ethanol, isopropanol and deionised water and then dried in pure N_2. Next, 50 nm layer of gold is evaporated upon the surface of the diamond substrate using e-beam evaporator, to act as an absorbing layer for laser ablation. Laser ablation is then used to create first a milled cylinder (depth = 20 $\mu\mathrm{m}$) and secondly a circular boundary trench (depth $\geq$ 20 $\mu\mathrm{m}$) surrounding the milled centre. Care must be taken prior to this stage to ensure that the operating parameters of the laser are correct, as the depth of each of the two patterns must be carefully governed. If the central milled cylinder is milled too deep, then an electrical short will be created and the device will be non functional.

Following laser milling, the diamond is then subjected to an acid bath within ($NaNO_3$ & H_2SO_4) for 60 min at approximately 225 $^{\circ}\mathrm{C}$ to remove the graphitic by-products of laser ablation and then cleaned in stages with ethanol, isopropanol and deionised water and then dried in pure N_2. Following this, the diamond surface is 'wetted' with silver ABA in order to fill trenched regions with conductive metal to create contacts and heated to 800 $^{\circ}$ under vacuum using an evaporation beam chamber to set the braze. Finally the entire surface of diamond is lapped down to remove any silver from the top but keeping trenched regions filled. The method involves various stages of lapping, first using the RotoPol system to perform a coarse removal of silver and then using various grades of sandpaper and finally tissue paper to perform finer and finer smoothing to level silver within the trenched regions with the diamond surface.

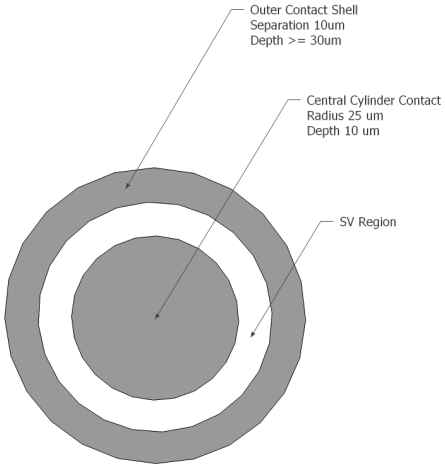

Figure 10.4: Birds eye view of device 3 design. The buried contacts, both inner and outer (grey) are easily visible.

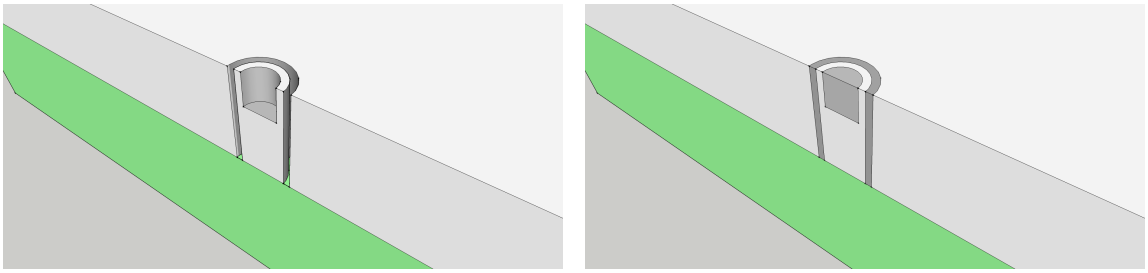

(a) After laser ablation.

(b) After silver ABA.

Figure 10.5: Device 3 design: The inner penetrates to a depth of 10 µm whilst the outer cylindrical shell penetrates to boron doped region below (µm). This figure shows the buried trenches filled with Silver ABA. The inner electrode can be wire bonded directly whilst the outer electrode will be connected via the boron layer.

10.6 Discussion

Three separate devices were designed and fabricated upon a 30 µm thick sample of electronic grade diamond grown upon a 500 µm thick base layer of boron doped single crystal diamond. These devices have not at the time of submission been set upon a DIL package and so no experimental characterisation has been carried out. Instead, each device has been modelled with a dedicated TCAD simulation so that a theoretical characterisation can be completed.

Part V

Theoretical Characterisation for Device Optimisation

Chapter 11

Geant4: CCE dependence upon contact thickness

11.1 Introduction

This chapter represents the first component of work carried out to theoretically characterise the devices produced in this thesis. This study was initiated to support the experimental element of the work carried out upon the 1st generation BID device (see Chapter 6). In the aforementioned study, observed charge collection underneath the aluminium contact pad of the device showed inconsistencies, which were not fully understood. The charge collection observed underneath the middle of the contact pad was uniform, but increased towards the edges of the contact pad. Two possible scenarios to explain this enhanced charge collection were hypothesised at the end of this study presented in Chapter 6, including:

- Increased aluminium contact thickness.
- Increasing electric field strength due to the geometry of the circular contact pad.

This study utilised GEANT4 to examine the effect of contact thickness upon the energy deposition and charge collection efficiency of the device. A second study utilising TCAD

was also commissioned to investigate the electric field structure of the circular contact pad in conjunction with a buried electrode structure. This TCAD study is addressed in Chapter 14. The results of this study were published in IEEE Transactions on Nuclear Science 2012[7] and the simulation study was used to create the new radioprotection example for the advanced examples released in Geant4 9.6.

11.2 Geant4 Simulation

A Geant4[91] application was developed to characterise the diamond based microdosimeter in terms of effect of aluminium front contact thickness in proximity of the SVs. The diamond microdosimeter was modelled in detail in the Geant4 9.3 application. A sketch of the device modelled in the experimental set-up of the simulation is shown in Fig. 11.1, 11.2 and 11.3. The device is set within a vacuum. The device has been modelled to have four sensitive volumes of pure diamond 150x150x1.38 μm^3; these are surrounded by a boron doped layer 480x480x1.38 μm^3. Underneath is a pure diamond layer of 480x480x300 μm^3. Above the sensitive volumes is aluminium pad 480x480xT_d μm^3, where T_d is a variable thickness from 0 to 1 μm.

The Geant4 General Particle Source (GPS) is used to model the different radiation fields adopted in the simulation study. Two different radiation fields were modelled during the course of this study. The first was a pencil beam normally incident upon the centre of a SV. The Geant4 Low Energy Physics Package, based on Livermore data libraries[92] was employed to describe all the electromagnetic interactions of particles, valid down to 250 eV. The energy threshold of production of secondary particles was fixed equal to a 10 nm cut in range corresponding to 250 eV, to describe the interactions of particles with adequate accuracy. The Geant4 QGSP BIC HP physics list was selected to model the hadronic physics processes because it has shown the best agreement with experimental results, in a proton radiation field of interest for our work[102]. Primary and secondary particles were tracked in

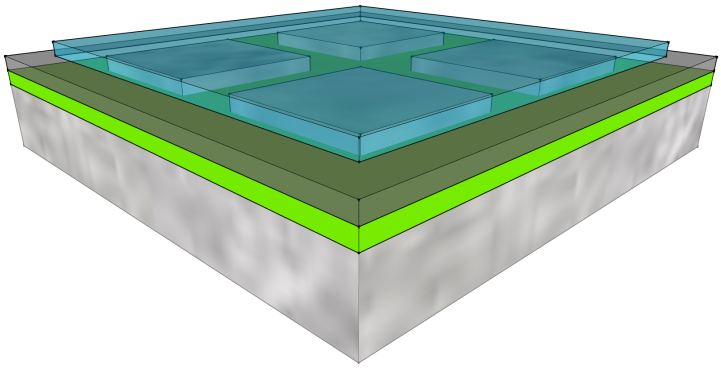

Figure 11.1: Tilted transparent viewpoint of the geometry to be modelled. The device features pure unaltered diamond substrate (solid grey) upon the bottom layer, then boron implanted diamond (Fluro green), another 1.38 μm thick layer of intrinsic diamond (transparent grey) within which 4 SV structures (solid grey prisms) are positioned and finally a layer of aluminium on top (0, 0.5 and 1 μm (blue))

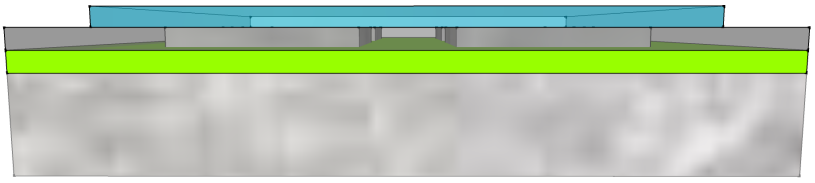

Figure 11.2: Cross sectional viewpoint of the geometry to be modelled. The device features pure unaltered diamond substrate (solid grey) upon the bottom layer, then boron implanted diamond (Fluro green), another 1.38 μm thick layer of intrinsic diamond (transparent grey) within which 4 SV structures (solid grey prisms) are positioned and finally a layer of aluminium on top (0, 0.5 and 1 μm (blue))

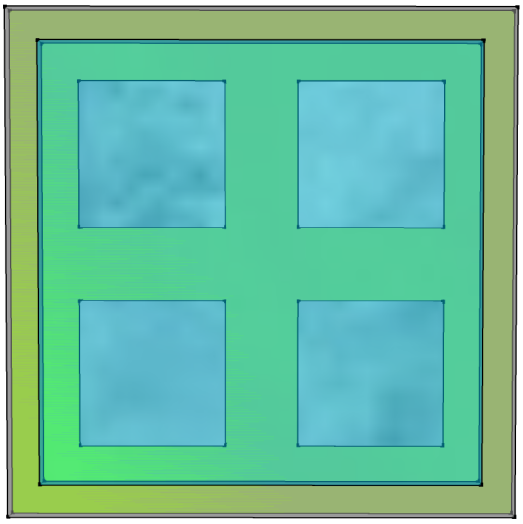

Figure 11.3: Top viewpoint of the geometry to be modelled. The device features pure unaltered diamond substrate (solid grey) upon the bottom layer, then boron implanted diamond (Fluro green), another 1.38 μm thick layer of intrinsic diamond (transparent grey) within which 4 SV structures (solid grey prisms) are positioned and finally a layer of aluminium on top (0, 0.5 and 1 μm (blue))

the experimental set-up and the output of the simulation was the energy deposition per event in the SVs, where one event corresponds to the generation of one primary particle.

11.3 Charge Collection Efficiency Study

The Geant4 application was used to verify if the non-uniform charge collection, documented in section IV, was due to a varying thickness of the aluminium pads. A pencil beam of stripped beryllium ions, with same energy of IBIC experiment, was normally incident on the microdosimeter device. The energy deposition per event was simulated for different thickness's of the aluminium pad, ranging between 0 and 1 μm. Fig. 11.4 shows the frequency of energy depositions deriving from 1×10^5 events within the SV's with 0μm, 0.5μm and 1μm thick Al contact, respectively. The area of the plots is normalised to 1. The peaks for 0μm, 0.5μm and 1μm thick Al contact are approximately 1.9, 1.95, and 2 MeV respectively.

Due to increased LET there is a shift in the energy deposition peak as the thickness

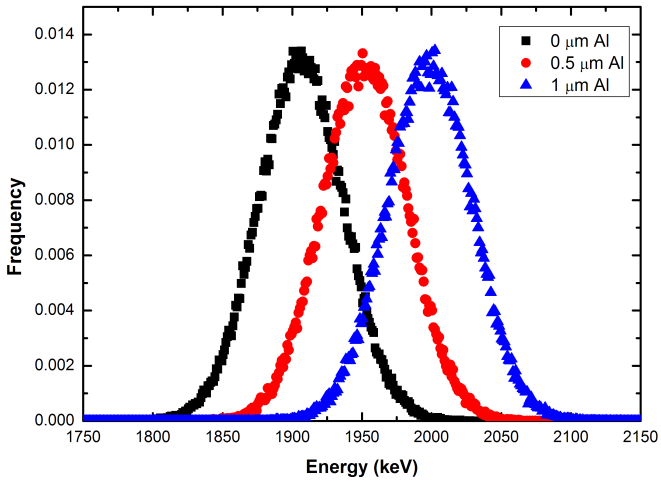

Figure 11.4: Energy deposition per event deriving from 5.9 MeV Be ions. The area of the curves is normalized to 1. Errors are shown but are small and fall within the symbol shapes.

of the aluminium pad is increased about 5% per 1 µm of deposited Al for 5.9 MeV Be ions. The effect of non uniformity of charge collection observed in SVs close to the edge of Al electrode demand much higher than 1 µm variation of Al thickness to explain charge enhancement almost twice for regions presented in a Fig. 6.18 in comparison with Fig. 6.16. Further understanding of this edge effect should be carried out.

11.4 Conclusion

To investigate the effect of a non-uniform aluminium overlayer, the BID microdosimeter structure has been studied by Geant4 simulations. Given the range of a 5.9 MeV beryllium ion in diamond and aluminium of 4.36 and 8.26 µm respectively, it has been hypothesised that the non uniformity in charge collection may be partially explained by a variance in the thickness of the overlaying aluminium layer[7].

A study using both Geant4 and SRIM based simulations has shown that while small variations in the Al overlayer can have a small effect upon the energy deposition within the

sensitive volume, it is not enough to account for the change in charge collection efficiency seen in the IBIC results. This has led to the conclusion that the increased charge collection efficiency of region III (Fig. 6.17 & 6.18) in comparison with region I (Fig. 6.17 & 6.14) may result from material and electric field non uniformity in the 3D SVs under the Al electrode as opposed to dimensional variations in the Al electrode itself.

Chapter 12

Geant4: Tissue Equivalence Study

12.1 Introduction

Tissue equivalence is an important consideration in microdosimetry. Tissue equivalent materials are designed to radio-graphically mimic human tissue. Without tissue equivalent materials, dose measurements become inherently inaccurate. To that end, the tissue equivalence of diamond is further investigated in this chapter with respect to protons and alpha particles. This work was published in IEEE Transactions on Nuclear Science[9].

It was shown by S. Guatelli et al[103], that a simple geometrical scaling factor ($\approx$0.56) of linear dimensions of the SV is adequate to convert experimentally obtained microdosimetric energy deposition spectra in silicon to equivalent microdosimetric energy deposition spectra in water, in a proton radiation field of energy ranging between few MeV and 250 MeV. Such a scaling factor C corresponds to the ratio of the stopping power (SP) of protons in water to silicon, as predicted by theory. In this work, a similar approach is adopted to study the tissue equivalence of diamond: we investigate the possibility of defining a scaling factor C to convert energy deposition spectra from diamond to water based upon the ratio of the stopping powers. The goal of the project is to identify the linear size of a cubic water SV that best approximates the energy deposition spectra in a cubic diamond SV with 10x10x10

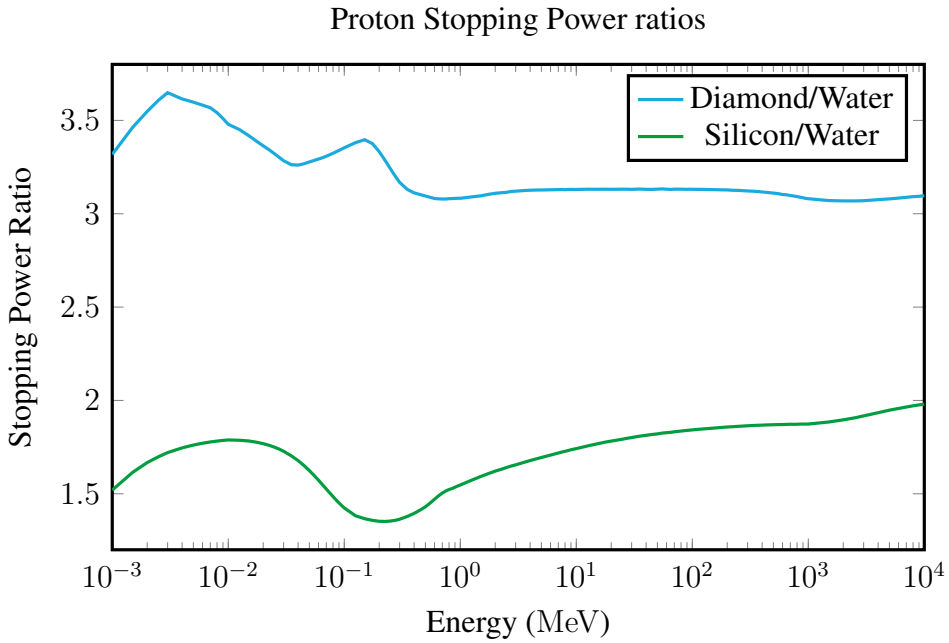

Figure 12.1: NIST PSTAR Database: Proton Stopping Power ratios[60]

μm^3 size, by means of Geant4 simulations. The release of Geant4 10.0 featured updates to the Geant4 built-in examples. The advanced example: radioprotection was derived from the Geant4 simulation used in this thesis. The SP ratios of diamond to water and silicon to water for protons and α particles respectively are presented in Fig. 12.1 and 12.2, in the energy range between 1 keV and 10 GeV. The data are derived from the National Institute of Standards and Technology (NIST) databases PSTAR and ASTAR[60]. The SP of diamond (S_D) was calculated by multiplying the known SP of graphite (S_G) with the ratio of densities of graphite (ρ_G) to diamond (ρ_D), as shown in the formula given below:

$$S_D = S_G \frac{\rho_D}{\rho_G} \tag{12.1}$$

In the energy range between 1 MeV and 10 GeV, corresponding to CREME96 GCR/SPE spectra under study, the average SP ratio of diamond to water is 3.1 and varies within 6% and 12%, for protons and α particles, respectively. Alternatively silicon within the same

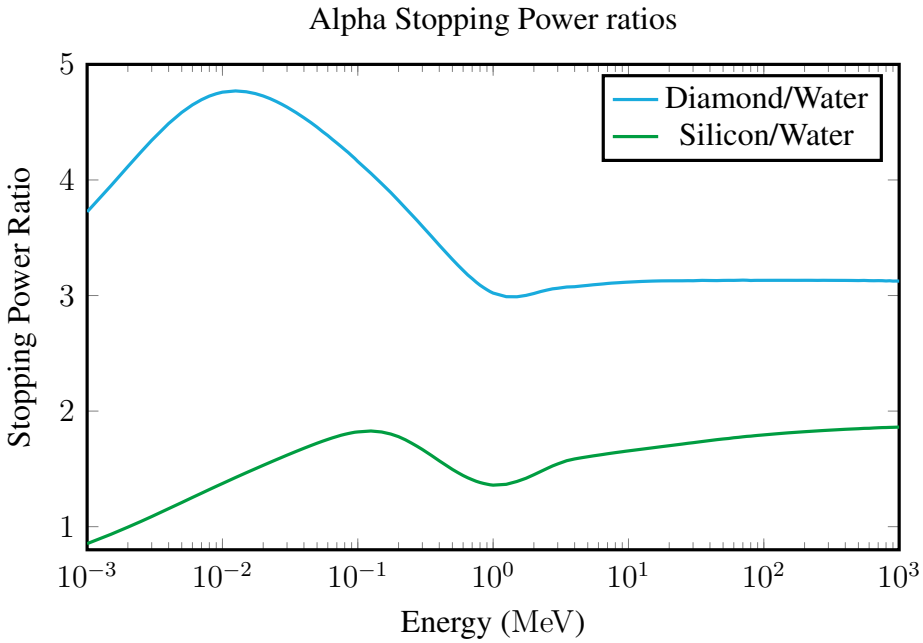

Figure 12.2: NIST ASTAR: Alpha Stopping Power ratios[60]

range has an average SP ratio of 1.8 and varies within 24% and 28%, for protons and α particles respectively. From the discussion above, it is clear that the SP ratio shows more constancy for the ratio $SP_{Diamond}/SP_{Water}$ than for $SP_{Silicon}/SP_{Water}$ within the energy range of interest. This means that, in case of a diamond SV, we expect to find a scaling factor C that is valid over a wide energy range of protons and α particles. The second observation is that the scaling factor C should provide more precise conversion from microdosimetric energy deposition from diamond to water than from silicon to water. A factor based upon scaling the linear dimensions of the water SV with respect to the dimensions of the diamond SV takes advantage of this relative constancy with the SP ratio of diamond to water. The scaling factor C is defined here as:

$$C = \frac{SP_{Diamond}}{SP_{Water}} = \frac{l_{Water}}{l_{Diamond}} \tag{12.2}$$

Where l_{Water} and $l_{Diamond}$, are the linear dimensional sizes of the water and diamond

SV, respectively, when the energy deposition is the same in the water and diamond SVs.

We expect a scaling factor C approximately equal to 0.32, corresponding to a SP ratio for diamond to water, equal to 3.1. This work is performed by means of Geant4 simulations as it allows for a detailed study of the effect of chord length distribution, of particle scattering and of hadronic interactions on the conversion factor C.

12.2 The Geant4 Simulation

A Geant4 application[91],[94] was developed for this study to calculate the energy deposition distributions deriving from protons and α particles with energies typical of interplanetary space, within diamond and water SVs. Both electromagnetic and hadronic interactions are modelled. Previous studies[103] demonstrated the adequacy of Geant4 to microdosimetric studies. In each simulation, incident particles are directed towards the SV within a vacuum. A cubic SV was chosen as it most closely represents the ideal SV structure in a diamond microdosimeter design. The size of the diamond SV is kept constant at 10 $\mu\mathrm{m}$, corresponding to what can be considered a realistic microdosimeter SV size. The SV can be either water or diamond. The water SV linear size, substituting the diamond SV, is then scaled using the stopping power ratio as a guide (see section 12.1), varying between 30 and 34 $\mu\mathrm{m}$. Water has been adopted in this study to represent tissue as it has an effective atomic number of 7.42, which is very close to that of tissue average and it represents approximately 70% of the human body composition. The Geant4 based study follows an iterative-incremental approach. At each development cycle the space radiation environment modelled in the Geant4 application is refined. This method allows to study in detail the effect of space radiation environment characteristics on the tissue equivalence of diamond. In a first stage, monoenergetic protons and α particles are directed normally upon the SV. The energies of the radiation field modelled can be 10, 50, 100, 250, and 500 $\mathrm{MeV\,u^{-1}}$ and $1\mathrm{GeV\,u^{-1}}$, representing a subset of energies of GCRs. This setup is illustrated in Fig. 5 and it allows the study of a factor

C for the conversion of microdosimetric energy deposition in diamond to water, when the chord length is kept fixed, corresponding to the size of the SV. The simulation application is then refined by substituting the pencil beam with an isotropic field typical of interplanetary space environment. Here, primary particles are generated inwards from a random point on a sphere with radius 1 m, centered with the SV, with cosine-law angular emission. This choice assures that if the generator surface is far enough away from the SV, the distribution is isotropic[?]. In order to reduce simulation times, without affecting the accuracy of the results deriving from the simulation study, the primary particle emission angle was limited to 0<ϕ<2π and 0<θ<θ_{max}. The angle, θ_{max}, was chosen such that the number of primary particle tracks not traversing the SV would be small. This setup, depicted in Fig. 5, permits to study the effect of isotropic incidence of particles upon the SV, as here the chord length has a distribution and this can influence the energy deposition spectra in the SV and therefore the correction factor C (see Section 12.1). The last cycle of refinement consists in the modelling of the radiation environment, isotropically, with energy spectra provided by CREME96. This set-up allows the study of the energy deposition spectra and therefore C in the most realistic scenario for space applications.

The Geant4 Low Energy Physics Package, based on Livermore data libraries[94] [93], was selected to describe all the electromagnetic interactions of particles, down to 250 eV, limit of validity of these physics models. The Geant4 QGSP BIC HP physics list was selected to model the hadronic physics processes because it has shown the best agreement with experimental results, in a proton radiation field of interest for our work[10]. The simulation-based study allows investigating the effect of nuclear recoils deriving from hadronic interactions and the effect of the chord length distribution upon the tissue equivalence of diamond. Primary and secondary particles were tracked in the experimental set-up and the output of the simulation was the energy deposition per event in the SVs, where one event corresponds to the generation of one primary particle. $10^4 - 10^8$ events were generated in each simulation to

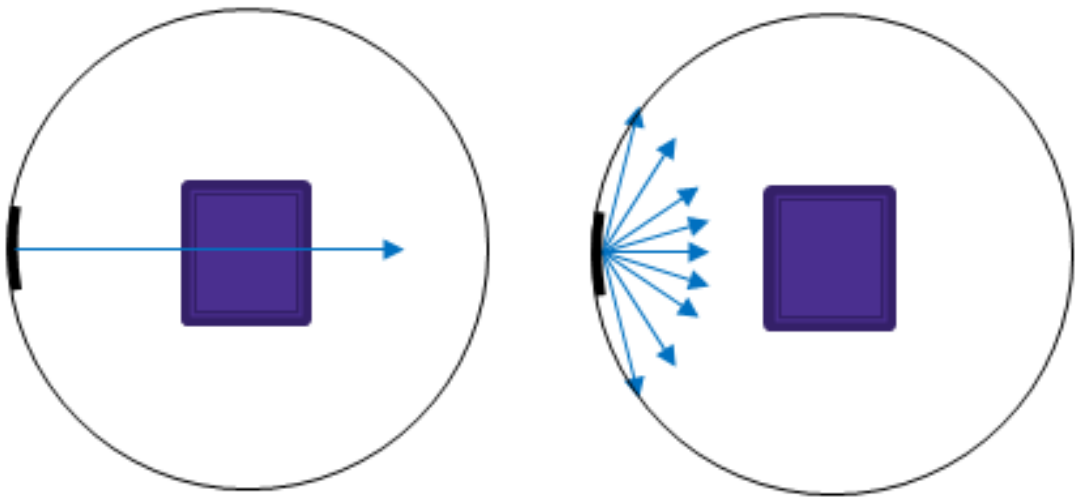

(a) Geant4 model of the TEQ simulation (pencil-beam field)

(b) Geant4 model of the TEQ simulation (isotropic field)

Figure 12.3

obtain statistically meaningful results. Geant4 9.3 was used. ROOT was adopted as analysis tool.

12.3 Statistical Analysis

A statistical method was utilized to verify the agreement between the response within the diamond SV and the water SV with varying size. The method used is the Kolmogorov-Smirnov (KS) test[27][?]. The KS test was used to evaluate quantitatively the best agreement in terms of the linear size of a water SV size to reproduce the response within diamond SV. The KS test is a Goodness-of-Fit (GoF) statistics test, designed to determine if two datasets differ significantly. The KS test statistics is based on the maximum vertical distance between the cumulative frequency distribution of each data-set F1 and F2:

$$Max(|F_1(x) - F_2(x)|) \tag{12.3}$$

The KS test output is known as a p-value, representing the test of the null hypothesis

that the two compared energy deposition distributions are compatible. A p-value higher than 0.05 corresponds to the acceptance of the null hypothesis. The KS test is used here to identify the linear size of the water SV corresponding to the best approximation of the energy deposition spectra in the diamond SV. This approach has been adopted as it demonstrated to be adequate in previous work[103]. The best agreement between energy deposition distributions in diamond and water SV is established using two criteria. Firstly, by comparing the position of the peak of the energy deposition distribution. Secondly, by identifying the highest p-value, resulting from the statistical comparison of the energy deposition spectra, in the diamond and in the water SV with varying linear size. In the analysis of the results, the histogram binning is reported for completeness. The KS test was used to determine the scaling factor C. The accuracy of the determined C was then verified with realistic GCR and SPE radiation fields, incident on the water and diamond SVs.

12.4 Results

12.4.1 Pencil beam of monoenergetic protons and alpha particles

This section summarises the results obtained with monoenergetic protons and alpha particles with energies spanning from 10 $\mathrm{MeV\,u^{-1}}$ up to 1 $\mathrm{GeV\,u^{-1}}$. Particles are generated as a pencil-beam as explained in Section IV as shown in Fig. 12.3a. Fig. 12.4a shows the energy deposition for an incident proton with energy 10 MeV on a water SV with size varying between 30 and 34 $\mu\mathrm{m}$. We can observe that the energy deposition increases with the size of the SV, due to the nature of energy loss of heavy charged particles. The more the proton penetrates in the SV, the more the energy deposition increases as it approaches the Bragg Peak. We can also notice that the energy deposition distribution tends to have a Gaussian behavior, with increasing SV size. This is due to the energy loss fluctuations of the incident particles. Fig. 12.4b shows the energy deposition per event within 10 $\mu\mathrm{m}$ diamond SV for

incident protons of different incident energies. We can observe that higher energy particles deposit less energy in the SV, as they are minimum ionizing particles. The energy deposition shifts to higher values with lower incident energies as the particles approach the Bragg peak when depositing energy in the SV. The energy deposition tends to pass from a Landau to a Gaussian distribution with lower energy of incident particle because of the energy loss fluctuations.

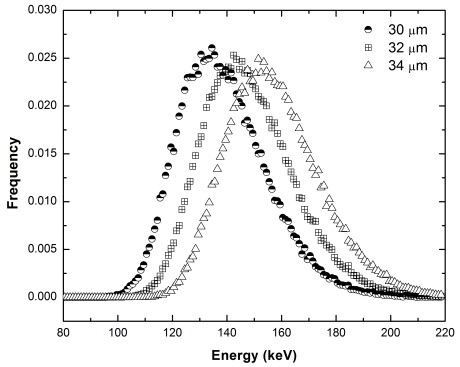

(a) Energy deposition per event from 10 MeV protons within three different sized water SVs. Left to right, 30, 32, and 34 $\mu\mathrm{m}$. The area under each curve is normalized to 1.

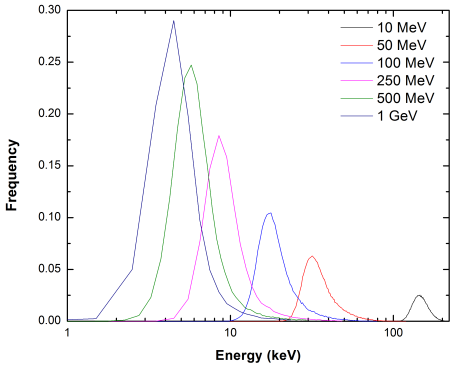

(b) Energy deposition per event within 10 $\mu\mathrm{m}$ diamond SV for incident protons of different incident energies. The area of the curves is normalized to 1.

Figure 12.4

Table 12.1 reports the summary of the analysis results when identifying the size of water SV which better approximates the energy deposition within the diamond SV, deriving from a pencil beam of protons and alpha particles with energies 10 $\mathrm{MeV\,u^{-1}}$, 250 $\mathrm{MeV\,u^{-1}}$ and 1 $\mathrm{GeV\,u^{-1}}$. The KS GoF test shows that water with SV with a linear Side Size (SS) between 31 and 32 $\mu\mathrm{m}$ shows the best agreement with the energy deposition spectra in a diamond SV with size 10 $\mu\mathrm{m}$. Fig. 12.5a, 12.6a and 12.7a show the plot of energy deposition spectra from protons in diamond SV and also within the water SV showing best agreement. similarly, Fig. 12.5b, 12.6b and 12.7b show the plot of energy deposition spectra from alpha particles in diamond SV and also within the water SV showing best agreement.

Particle	Energy	BinSize	P-value	Best agreement	Conversion Factor
Proton	10 $\mathrm{MeV\,u^{-1}}$	1 keV	1.0000	32 µm	0.313
Alpha	10 $\mathrm{MeV\,u^{-1}}$	1 keV	1.0000	31 µm	0.323
Proton	250 $\mathrm{MeV\,u^{-1}}$	0.5 keV	0.9855	31 µm	0.323
Alpha	250 $\mathrm{MeV\,u^{-1}}$	0.5 keV	0.9328	31 µm	0.323
Proton	1 $\mathrm{GeV\,u^{-1}}$	0.1 keV	0.9964	31 µm	0.323
Alpha	1 $\mathrm{GeV\,u^{-1}}$	0.1 keV	0.7148	31 µm	0.323

Table 12.1: Summary of the statistical analysis comparing energy deposition in a diamond SV wit SS of 10 µm sized and varying water SV, for incident monochromatic pencil beams of proton and alpha particles. The last column reports the conversion factor associated with the size of the water SV showing best agreement in terms of microdosimetric energy deposition distribution with the diamond SV.

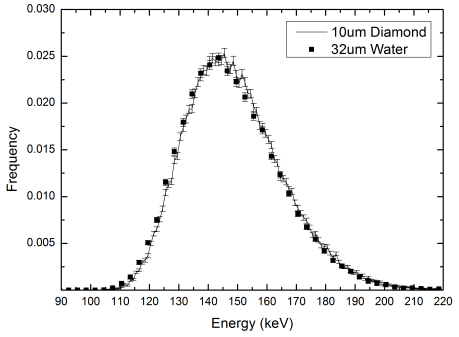

(a) Energy deposition spectra in water SV with SS of 32 µm and in a diamond SV with SS of 10 µm sized . The radiation field is a pencil beam of 10 $\mathrm{MeV\,u^{-1}}$ protons. The area under the curves is normalized to 1.

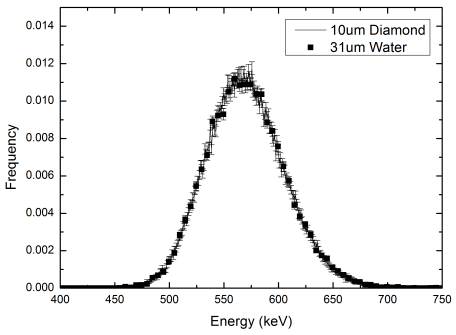

(b) Energy deposition spectra in water SV with SS of 31 µm and in a diamond SV with SS of 10 µm. The radiation field is a pencil beam of 10 $\mathrm{MeV\,u^{-1}}$ alpha particles. The area of the curves is normalized to 1.

Figure 12.5

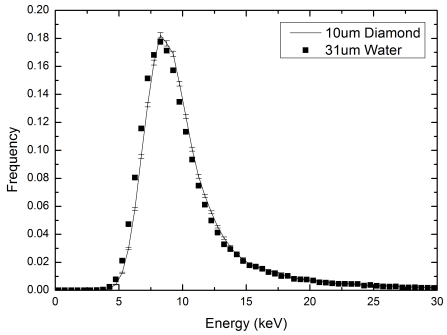

(a) Energy deposition spectra in water SV with SS of 31 µm and in a diamond SV with SS of 10 µm. The radiation field is a pencil beam of 250 $\mathrm{MeV\,u^{-1}}$ protons. The area under the curves is normalized to 1.

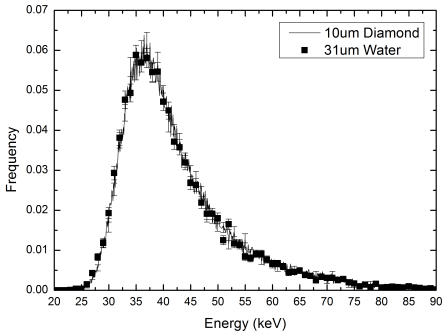

(b) Energy deposition spectra in water SV with SS of 31 µm and in a diamond SV with SS of 10 µm. The radiation field is a pencil beam of 250 $\mathrm{MeV\,u^{-1}}$ alpha particles. The area under the curves is normalized to 1.

Figure 12.6

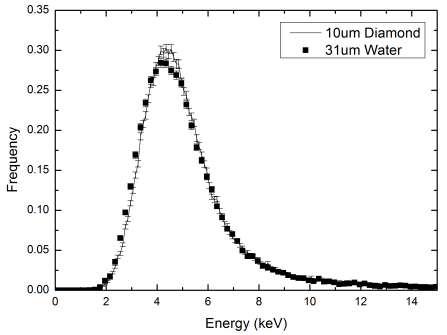

(a) Energy deposition spectra in a 31 µm sized water SV and in a 10 µm sized diamond SV. The radiation field is a pencil beam of 1 $\mathrm{GeV\,u^{-1}}$ protons. The area under the curves is normalized to 1.

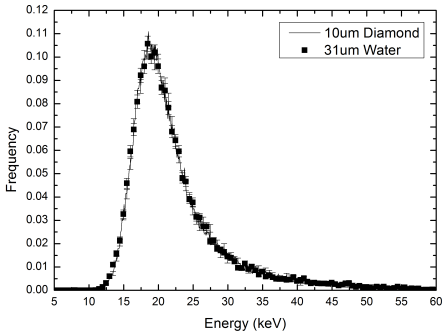

(b) Energy deposition spectra in water SV with SS of 31 µm and in a diamond SV with SS of 10 µm. The radiation field is a pencil beam of 1 $\mathrm{GeV\,u^{-1}}$ alpha particles. The area under the curves is normalized to 1.

Figure 12.7

12.4.2 Isotropic field of monoenergetic protons and alpha particles

This section summarises the results obtained with monoenergetic protons and alpha particles with energies spanning from 10 $\mathrm{MeV\,u^{-1}}$ to 1 $\mathrm{GeV\,u^{-1}}$, incident with an isotropic distribution on the SV, as shown in Fig. 12.3b. In this set-up, as mentioned in Section IV,

Particle	Energy	BinSize	P-value	Best agreement	Conversion Factor
Proton	10 $\mathrm{MeV\,u^{-1}}$	1 keV	0.9999	32 $\mu\mathrm{m}$	0.313
Alpha	10 $\mathrm{MeV\,u^{-1}}$	1 keV	0.7818	31 $\mu\mathrm{m}$	0.323
Proton	250 $\mathrm{MeV\,u^{-1}}$	0.5 keV	0.9154	32 $\mu\mathrm{m}$	0.313
Alpha	250 $\mathrm{MeV\,u^{-1}}$	0.5 keV	0.9973	32 $\mu\mathrm{m}$	0.313
Proton	1 $\mathrm{GeV\,u^{-1}}$	0.1 keV	0.9986	32 $\mu\mathrm{m}$	0.313
Alpha	1 $\mathrm{GeV\,u^{-1}}$	0.1 keV	0.9669	31 $\mu\mathrm{m}$	0.323

Table 12.2: Summary of the KS GoF test results, comparing the energy deposition in diamond SV of SS 10 $\mu\mathrm{m}$ with a varying water SV size, in an isotropic field of protons and alpha particles. The last two columns reports the size of the water SV showing best agreement in terms of microdosimetric energy deposition distribution with the diamond SV and the associated conversion or scaling factor.

we can study the effect of chord length distribution on the conversion factor C. Table 12.2 reports the summary of the KS GoF test results when identifying the size of water SV which better approximates the energy deposition within the diamond SV, when an isotropic field of protons and alpha particles with energies spanning between 10 $\mathrm{MeV\,u^{-1}}$ and 1 $\mathrm{GeV\,u^{-1}}$ is incident on the SV. The KS GoF test shows that water SV with SS of 32 $\mu\mathrm{m}$ shows the best agreement with the energy deposition spectra in a diamond SV with SS of 10 $\mu\mathrm{m}$. Fig. 12.8a, 12.9a and 12.10a show the plot of energy deposition spectra from protons in diamond SV and also within the water SV showing best agreement. similarly, Fig. 12.8b, 12.9b and 12.10b show the plot of energy deposition spectra from alpha particles in diamond SV and also within the water SV showing best agreement.

12.4.3 Isotropic field of GCR protons & alpha

This section reports the results of tissue equivalence of diamond when the radiation field is isotropic with energy spectra derived from CRÃĹME96 as shown in Fig. 2.2. Table 12.3

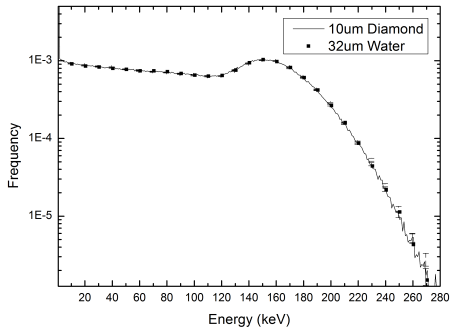

(a) Energy deposition spectra in water SV with SS of 32 µm sized and in a diamond SV of SS 10 µm. The radiation field is an isotropic field of 10 $\mathrm{MeV\,u^{-1}}$ protons. The area under the curves is normalized to 1.

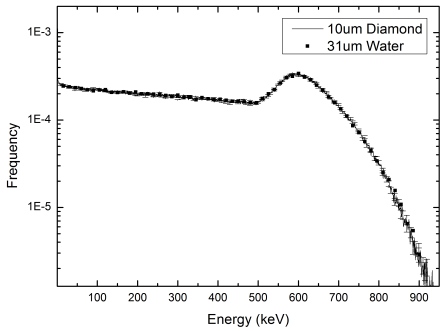

(b) Energy deposition spectra in water SV with SS of 31 µm sized and in a diamond SV of SS 10 µm. The radiation field is an isotropic field of 10 $\mathrm{MeV\,u^{-1}}$ alpha particles. The area under the curves is normalized to 1.

Figure 12.8

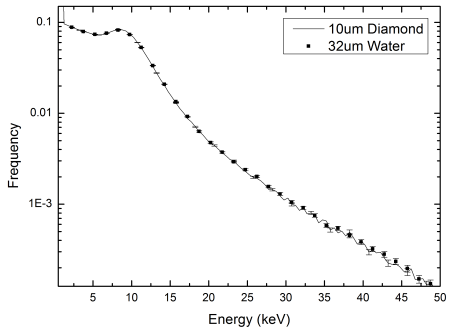

(a) Energy deposition spectra in water SV with SS of 32 µm sized and in a diamond SV of SS 10 µm. The radiation field is an isotropic field of 250 $\mathrm{MeV\,u^{-1}}$ protons. The area under the curves is normalized to 1.

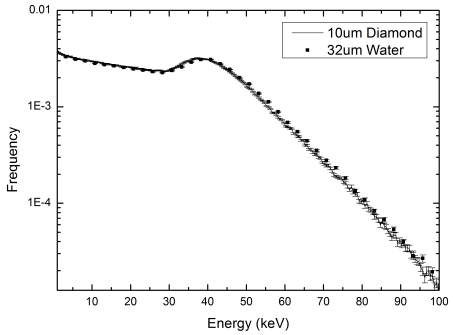

(b) Energy deposition spectra in water SV with SS of 32 µm sized and in a diamond SV of SS 10 µm. The radiation field is an isotropic field of 250 $\mathrm{MeV\,u^{-1}}$ alpha particles. The area under the curves is normalized to 1.

Figure 12.9

reports the summary of the analysis results when identifying the size of water SV which better approximates the energy deposition within the diamond SV. The radiation field of interest here is an isotropic field of GCR proton and alpha. The GoF test showed that water with SV SS between 30 and 31 µm shows best agreement with the energy deposition spectra

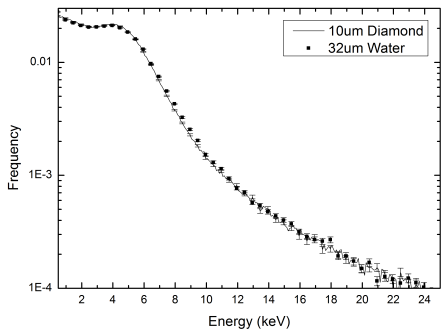

(a) Energy deposition spectra in water SV with SS of 32 µm sized and in a diamond SV of SS 10 µm. The radiation field is an isotropic field of 1 $\mathrm{GeV\,u^{-1}}$ protons. The area under the curves is normalized to 1.

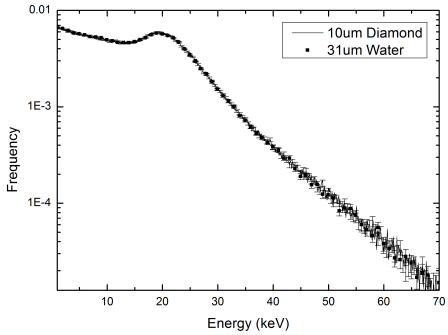

(b) Energy deposition spectra in water SV with SS of 31 µm sized and in a diamond SV of SS 10 µm. The radiation field is an isotropic field of 1 $\mathrm{GeV\,u^{-1}}$ alpha particles. The area under the curves is normalized to 1.

Figure 12.10

Particle	BinSize	P-value	K-value	Best agreement	Conversion Factor
Proton	1 keV	0.8316	0.0227	30 µm	0.334
Alpha	1 keV	0.2830	0.0180	31 µm	0.323

Table 12.3: Summary of the statistical analysis comparing energy deposition in 10 micrometer diamond and varying water SV, for GCR protons and alphas. The table gives a report of the size of the water SV showing best agreement in terms of energy deposition distribution with the diamond SV and the associated correction factor. .

in a diamond SV with size 10 µm. Fig. 12.11a and 12.11b show the plot of energy deposition spectra in diamond SV and in the water SV showing best agreement.

The Kolmogorov-Smirnov test was again applied for isotropic GCR protons and alpha to match the energy distributions within diamond to water. The KS test showed agreement for both cases, with GCR protons and alphas having p-values of 0.8316 and 0.2830 respectively. Discontinuities can be seen at distinct points within Figs. 12.11a and 12.11b. These are the result of high LET particles or 'stoppers' which have deposited all of their energy and have come to rest within the SV. Thus they are particles with range less or equal than that

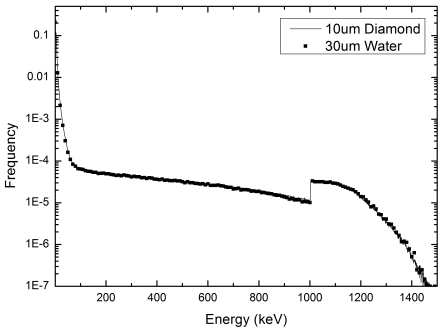

(a) Energy deposition within 30 μm of water and 10 μm of diamond for an isotropic field of GCR protons. The area under the curves is normalized to 1

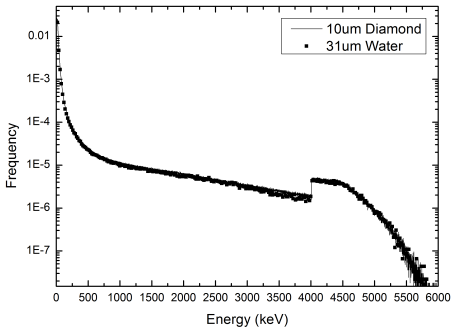

(b) Energy deposition within 31 μm of water and 10 μm of diamond for an isotropic field of GCR alpha. The area under the curves is normalized to 1.

Figure 12.11

of the chord length. In the case of an isotropic field, particles may traverse the SV from any direction, thus creating a probability distribution for the chord length. Whether or not a particle comes to rest is therefore dependent upon its energy and its path/chord length through the SV. For a 10 μm sized SV, the most probable chord length is 10 μm and the maximum is 17.32 μm. The maximum chord can be determined from the geometry of the SV structure itself and the probability distribution in Fig. 12.12 can be determined from Monte Carlo simulations via Geant4. It should be noted that these 'stoppers' make up a significant percentage of the GCR spectrum for both proton and alpha particles.

Particles with energies less than or equal to 1.1 MeV and 4.5 MeV for proton and alpha will have a range less than 10 μm in diamond. These particles are then associated with the highest probability of becoming 'stoppers'. Particles within this energy range make up approximately 0.7 percent of the GCR proton and alpha spectral fluence. As previously stated the maximum chord length for a 10 μm sized SV is 17.32 μm. This corresponds to stoppers with initial energies up to 1.6 MeV and 6.5 MeV for GCR proton and alpha. For particles crossing the along the path of the maximum chord of the SV, 2.6 percent of the GCR proton spectral fluence and 1.6 percent of the GCR alpha spectral fluence would be

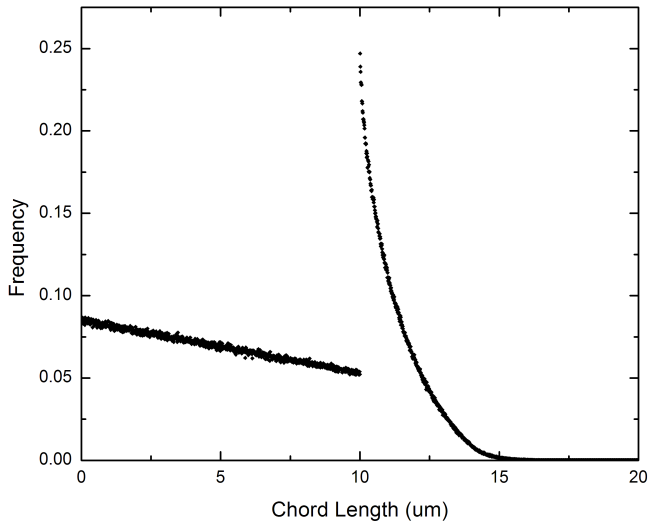

Figure 12.12: shows the chord length distribution for a 10 µm cube. The most probable chord is represented as a peak or discontinuity within the curve at a length of 10 µm.

'stoppers' and deposit all of their energy. Thus it is clear that particles of these relatively low energies can play a significant role.

12.4.4 Isotropic field of SPE protons & alpha

This section reports the results of tissue equivalence of diamond when the radiation field is isotropic with energy spectra derived from CREME96 as shown in Fig. 2.4. Table 12.4 reports the summary of the analysis results when identifying the size of water SV which better approximates the energy deposition within the diamond SV. The radiation field of interest here is an isotropic field of SPE proton and alphas. The KS GoF test showed that water with SV size of 31 µm shows the best agreement with the energy deposition spectra in a diamond SV with size 10 µm. Fig. 12.13a and 12.13b show the plot of energy deposition spectra in diamond SV and in the water SV showing best agreement.

Particle	BinSize	P-value	K-value	Best agreement	Conversion Factor
Proton	1 keV	0.8035	0.0245	31 µm	0.323
Alpha	1 keV	0.2018	0.0195	31 µm	0.323

Table 12.4: Summary of the statistical analysis comparing energy deposition in 10 µm diamond and varying water SV, for SPE protons and alphas. The table gives a report of the size of the water SV showing best agreement in terms of energy deposition distribution with the diamond SV and the associated correction factor.

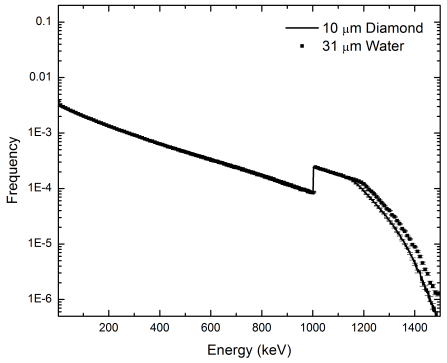

(a) Energy deposition within 31 µm of water and 10 µm of diamond for an isotropic field of SPE protons. The area under the curves is normalized to 1.

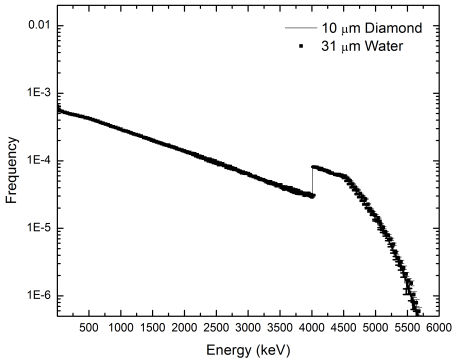

(b) Energy deposition within 31 µm of water and 10 µm of diamond for an isotropic field of SPE alpha. The area under the curves is normalized to 1.

Figure 12.13

The results derived from SPE protons and alphas as presented in Fig. 12.13a and 12.13b are similar as those derived from GCR particles in Fig. 12.11a and 12.11a. In each respective plot, the same discontinuities arising from the geometric configuration of the SVs can be seen as well as the agreement between scaled water SVs. The statistical results derived from the KS GoF test are also similar. Under the same specifications, the KS GoF test gives P-values for SPE protons and alphas respectively as 0.8035 and 0.2018, very closely matching the results from derived from GCR spectra.

12.5 Discussion and Conclusion

In this project a correction method was studied to convert diamond based microdosimetric energy deposition spectra to water by means of Geant4 simulations. The study concerned GCR and SPE proton and alpha particles. This study showed that a scaling factor C 0.32 is adequate to convert the microdosimetric energy deposition distribution from diamond to water, in a GCR protons and alpha particles radiation field. Fig. 12.14 and 12.15 show the correction factor from diamond and silicon respectively to water. The correction for silicon (≈ 0.56) was found in previous study[103]. It is clear that the correction factor applied to diamond stopping power is more constant with that of water than silicon for the range of energies of interest in terms of space applications. This correction factor is consistent with ratio of stopping powers of diamond and water depicted in Fig. 12.1 and 12.2. The corrected stopping power of diamond lays easily within a 5% agreement for protons and alpha within the energy range of interest. This is in comparison with the ratio of stopping powers for corrected silicon and water which show deviations up to 14% for protons and 24% for alpha.

The next stage of this study will be to continue a study of heavy charged particles typical of GCR (i.e carbon, oxygen and iron) and extend the study towards neutrons. Future studies will involve simulating the SV's within a microdosimeter structure in order to account for potential secondary particles including nuclear recoils created when incident radiation field traverses the detector.

Newer versions of Geant4 have been released in the time since this study was commenced. These new versions include physics models valid for an increased range of energies, and in addition now have the capability of modelling channelling effects. Since the effect of crystal structure can have a direct impact upon energy deposition, this study should be repeated with an emphasis upon crystalline orientation[104] [105].

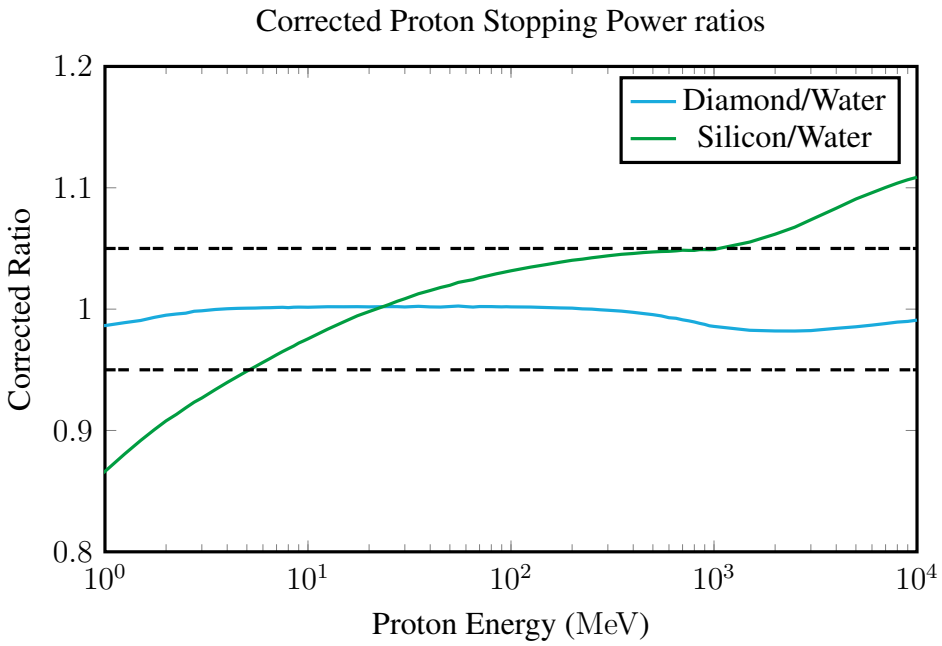

Figure 12.14: Comparison of the correct ratio of stopping powers for protons of diamond and silicon with water.

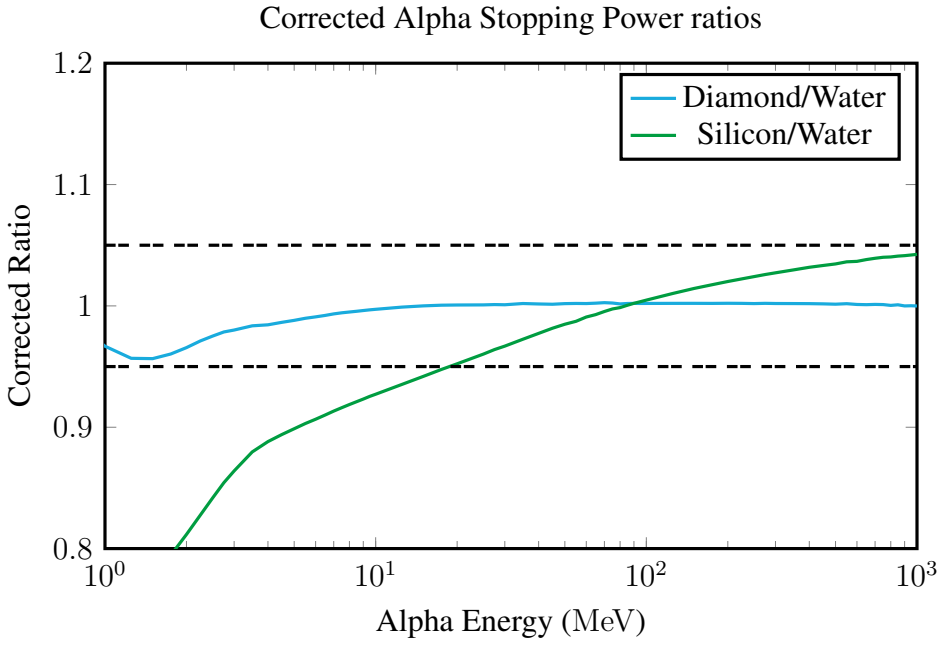

Figure 12.15: Comparison of the correct ratio of stopping powers for alphas of diamond and silicon with water.

Chapter 13

TCAD: Material Characterisation

13.1 Introduction

In this chapter, the TCAD simulations to be used throughout the rest of this work are initiated and the steps taken to validate the material defined and the basic simulation parameters itself. The device modelled, was a planar Metal-Insulator-Metal (MIM) device, in order to maintain simplicity in the simulation. The device modelled is a 2D diamond substrate 500 $\mu\mathrm{m}$ thick and 1100 $\mu\mathrm{m}$ wide with aluminium contacts centrally placed upon the top and back sides with dimensions 600 $\mu\mathrm{m}$ wide and 200 nm thick.

The material modelled utilised the one of the standard in-built Insulator files as a base, along with user defined parameters unique to diamond in order to create a new material (Diamond.par). Some of the key parameters are :

- **Dielectric Constant:** ϵ **= 5.7**
- **Bandgap:** E_g **5.5** eV **,** χ_0 **= 0.5** eV
- **Carrier Mobility:** μ_{max} **=** 2.8×10^3**,** $2.0 \times 10^3\ \mathrm{cm^2\,V^{-1}\,s}$

- **Lattice Heat Capacity = C_v = 3.0** $\mathrm{J\,K^{-1}\,cm^3}$
- **Thermal Conductivity: κ = 22.20** $\mathrm{W\,K^{-1}\,cm}$
- **Refractive Index: n = 2.42**

13.2 Meshing Optimisation

Meshing is a technique used in TCAD modelling to simplify equations through the subdivision of a large element or volume into many smaller and simpler discrete elements or volumes. There are three different mesh types: rectangular, cylindrical and triangular; with triangular meshing, only available in 3D modelling. In defining a mesh, there is a compromise between computational efficiency and time economy. If the meshing used is too fine, the time taken to produce a result may be too long or cause a simulation crash in the worst case scenario, conversely the coarseness of the meshing may reduce the accuracy of the results. The optimal meshing scenario will utilise coarse and fine meshing strategies where needed to ensure accuracy without prolonged simulation time. Priority in mesh refinement should be given to regions that incorporate material interfaces, doping gradients, trapping centers and any other region where interesting effects may occur. Applying the appropriate meshing strategy for a simulation case requires skill, experience and a deep understanding of the intricacies and nuances of the physics as well as that of the simulation package.

13.3 Results: DC simulation

A DC simulation in the context of this body of work, refer to any and all measurements of the device response to a fixed bias, i.e. current, electric field etc. These simulations are referred to as steady-state simulations, i.e. the partial derivative with respect to time is zero. The simulation parameters used in this work involve defining initial bias conditions

to a set of electrodes, and stepping the bias, whilst simultaneously measuring the device response for each bias condition. The initial bias conditions used in this work specify a set of electrodes to start at the same bias ($V_{Initial}$ = 0 V) or ground. The bias is then increased in small steps (V_{Step}) until it reaches a maximum (V_{Max}) so that the maximum electric field strength ($\vec{E}$ = 1 V µm^{-1}).

The result of these DC simulations is the production of JV curves were produced from the 2D structure described in the previous section for the same bias range. A correction factor was applied to the simulated data so that the current density (J) in A cm^{-1} was converted to current (I) in A to allow for a legitimate comparison with the experimental data. The comparison of the experimental and simulated IV data is shown in Fig. 13.1. In this figure, it can be easily seen that the two sets of data fall within the same order of magnitude indicating the diamond material modelled has satisfied the minimum requirements of agreement.

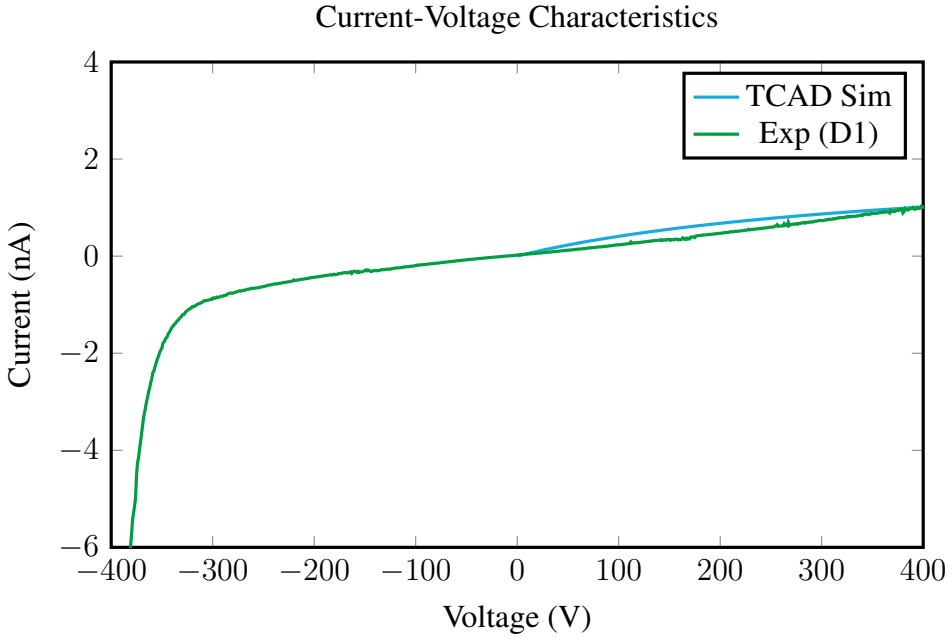

Figure 13.1: TCAD simulation IV curve versus Experimental IV curve for D1

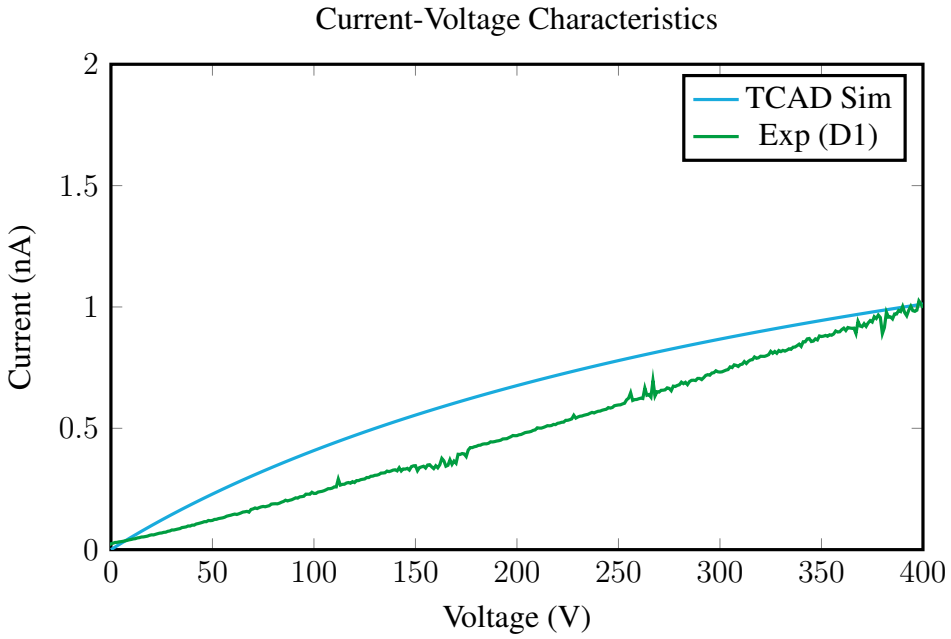

Figure 13.2: TCAD simulation IV curve versus Experimental IV curve for D1

13.4 Results: AC simulation

An AC simulation is a powerful tool that can be used to determine the intrinsic and extrinsic parasitic capacitance of a device and also enables the modelling of the device frequency performance (i.e. F_t). An AC simulation differs from its DC counterpart in that a sinusoidal signal is superimposed upon the DC solution. Sentaurus is used to compute the Y-Matrix, which is a description of the behaviour of currents within a circuit or device, with respect to small perturbations in applied bias (δV) at a contact node.

$$\delta i = Y.\delta v = (A + j.\omega.C).\delta V \tag{13.1}$$

The complex Y-matrix can be split into its real (A- Admittance matrix) and imaginary (C-Capacitance matrix) components. The Admittance and Capacitance matrices measure the in-phase and out of phase response of the current with the voltage respectively. An

example of a Y-matrix for a typical MIM device is presented below having two terminals; top (T) and bottom (B). The resulting A and C matrices have the following elements:

$$\begin{bmatrix} i(T) \\ i(B) \end{bmatrix} = \left(\begin{bmatrix} a(T,T) & a(B,T) \\ a(T,B) & a(B,B) \end{bmatrix} + j.\omega. \begin{bmatrix} c(T,T) & c(B,T) \\ c(T,B) & c(B,B) \end{bmatrix} \right) . \begin{bmatrix} v(T) \\ v(B) \end{bmatrix} \tag{13.2}$$

Given that diamond as a material is not included within the Sentaurus database, AC simulations were run in order to determine the capacitance of the material being modelled in order to ensure the appropriate modelling of a dielectric material. The capacitance of the device was measured up to a maximum bias of 500 V applied to the top contact. The capacitance measured for this range was equal to $(1.685 \pm 0.011)e^{-16}$ $\mathrm{F\,\mu m^{-1}}$, and can be considered for all practical purposed to be constant, confirming the dielectric nature of the material modelled.

13.5 Results: CCE simulation

Transient simulations are where the variable of time is introduced into the 'equation'. Simulations within the time domain, or transient simulations, allow for the study of non quasi-static detector behaviour. In this work, the heavy ion function was called upon the describe a 5.5 MeV alpha particle. Whilst an alpha particle function does already exist within the TCAD framework, the heavy ion function was chosen to describe the ion impact due to the differences in the way the particles are described.

The simple model of a MIM detector already described in previous sections, was again utilised; this time with the purpose of performing Charge Collection Efficiency (CCE) simulations. SRIM was used to create an LET versus depth profile for a 5.5 MeV stripped helium ion within diamond, see Fig. 13.3. Using the Sentaurus driven HeavyIon model capability, alpha particles were made to be normally incident upon the diamond surface. The

amount of charge (Q_0 = 0.0685 pC) produced by such an ion strike can be calculated by integrating under the curve. The charge collected by the modelled device, can be found by integrating under the I versus t curve following an ion strike (Q = 0.0376 pC), see Fig. 13.4 and 13.5. The Charge Collection Efficiency can then be estimated by comparing the charge collected (Q) with the theoretical maximum in charge produced (Q_0), see equation 13.3.

$$CCE = \frac{Q}{Q_0} = (3.76e-14/6.85e-14) * 100 = 55\% \tag{13.3}$$

It should be noted that the charge collection of the true device, with which this model has been compared with previously, had a CCE of approximately 100 %. The sudden drop in charge collection that occurs after the initial peak in Fig. 13.4 is an indication that the production of space charge is preventing full charge collection.The lower than expected CCE is suggestive that the material parameters in particular the recombination properties of the material, require further refinement. Thus the result obtained here, whilst promising in terms of providing qualitative description of diamond based device is not yet ready to provide quantitative data.

13.6 Conclusion

TCAD is a useful tool for modelling the behaviour of semiconductor devices. It is limited however, by the materials able to be modelled. New materials however, can be defined for use with TCAD, by detailing their physical and electrical characteristics. The modelling of a new material like diamond, requires validation with respect to experimental data. This chapter explains the initial work being done to validate a model of diamond for use in TCAD. A simple planar type device was modelled for this work.

Using an AC simulation, the capacitance per unit length of the device modelled, was determined to be $(1.685 \pm 0.011)e^{-16}$ $\mathrm{F\,\mu m^{-1}}$ and was for all practical purposes constant in

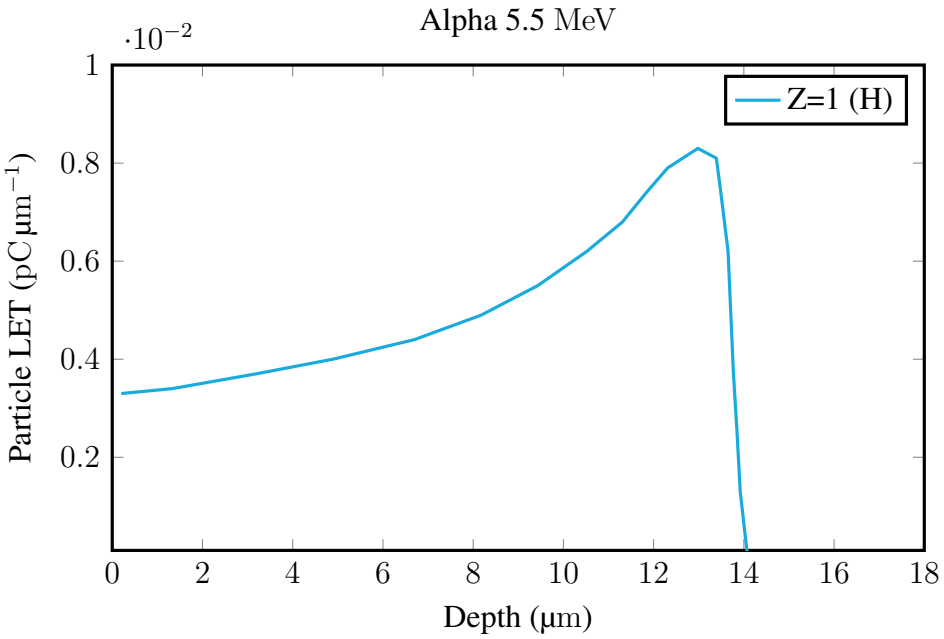

Figure 13.3: 5.5 MeV Alpha depth in diamond. The range is 13.6 µm with longitudinal and lateral straggling of 1742 and 2399 Å respectively

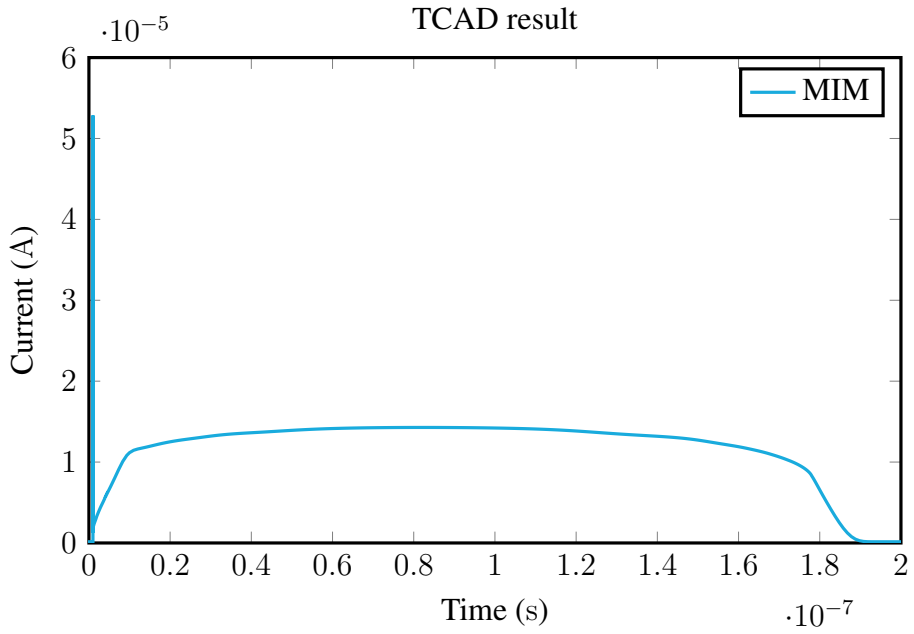

Figure 13.4: Transient Current Vs Time following heavy ion strike in simple MIM design.

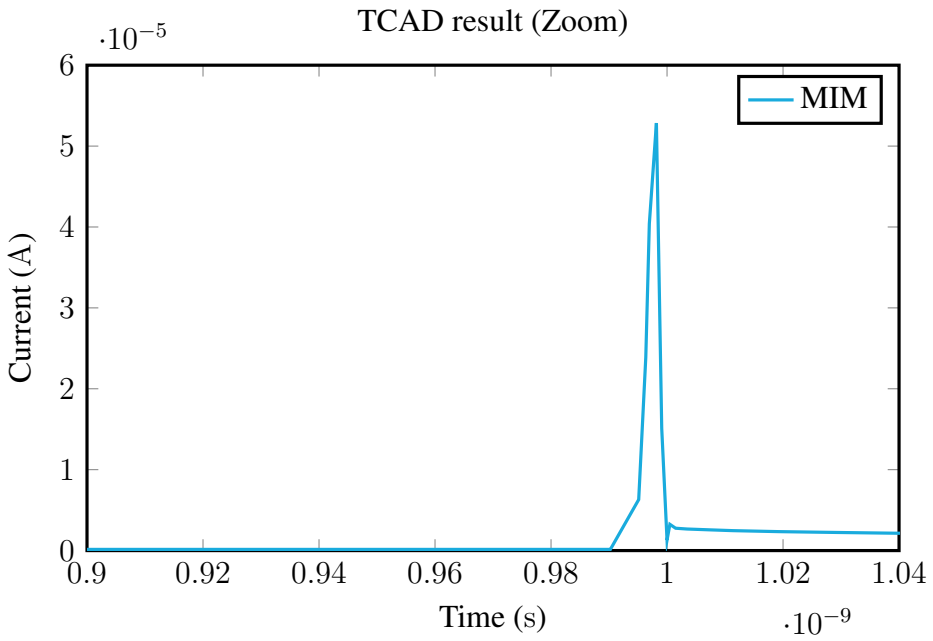

Figure 13.5: Transient Current Vs Time following heavy ion strike in simple MIM design.

the bias range tested ($0 < V < 500$ V). The constant capacitance is consistent with the dielectric nature of the material modelled. The IV curves produced from the DC simulations are consistent with experimental IV curves from the device characterised in Chapter 7. The CCE derived from the simulated heavy ion strike within the diamond material at 55 %, are evidence that the material modelled is not completely accurate. It can be concluded from this study, that the material modelled, whilst not to be considered to be completely representative of diamond used in experimental devices, is at the very least, a good first approximation, and it will take further work in order to become fully validated. It is for this reason, that the results derived from TCAD models presented in the following chapters will be used to provide only a qualitative as opposed to a quantitative analysis of the various microdosimeter designs under investigation in this thesis.

Chapter 14

TCAD: Boron Implanted Mesh

14.1 Introduction

In this chapter, the first, in a series of dedicated TCAD studies is introduced. TCAD studies are utilised to examine the electric field structure and charge collection properties of a device that has already been experimentally characterised, as is the case in this chapter, or one that is still in the design/fabrication stage. The purpose of these TCAD studies is twofold; firstly it can be used to help explain experimental results and secondly it can be used to optimise the current design of the device for future design consideration.

This first study was designed to answer questions raised in the experimental characterisation of the 1st generation microdosimeter prototype covered in Chapter 6. In Chapter 6, it was observed that charge collection while uniform towards the centre of the top electrode, was enhanced towards the edges. Two reasons were given that might independently or jointly cause such a result to occur. The first, being an increased thickness of contact material was addressed in Chapter 11.1. The second reason, which is concerned with increasing field strength due to the geometry of the contact pad itself will be addressed in this chapter. The goal of this work is two-fold; firstly to model geometry and visualise the resultant electric field under bias conditions and secondly using the HeavyIon transport package in DESSIS

to understand the overall reduced charge collection efficiency, obtained in experimentally results.

14.2 Device Modelling

Sentaurus device editor was used to model the device in 2D and 3D. The 2D models, were designed as if a cross-section was taken through the middle of the device structure. The 3D structure, was slightly more complex, however the extra dimension is necessary in order to understand the geometric effect of circular contact pads in terms of field structure and charge collection. As a balance between simulation time and accuracy, the device was modelled as simplistically as possible. The model as depicted in Fig. 14.1, shows a slab of diamond 100x100x10 μm^3, with a cylindrical contact pad of aluminium, with diameter 50 μm and height of 0.5 μm. A 100x100x0.5 μm^3 region of boron implanted diamond was defined at a depth of 1.5 μm and having a uniform concentration of boron of $1e^{15}/\,cm^{-3}$, see Fig. 14.1a. The circular aluminium pad was defined to be the 'top' electrode, whilst the boron doped region was designated as the 'bottom' electrode. This model presents a vastly simplified version of the real device, where the boron doped mesh, is replaced with a boron doped layer and the thickness of the underlying substrate is reduced from 500 μm to 10 μm, to optimise simulation time.

14.3 3D Results

A bias of 10 V was applied at the top aluminium electrode, with the boron doped layer acting as a grounded floating contact. The resulting electric field is uniform between the two electrodes with a strength 6.67 $V\,\mu m^{-1}$ with increasing field strength towards the sides of the top aluminium electrode due to edge effects. The increasing electric field at the contact edge, visible in Fig. 14.1b, offers up a possible explanation for the enhanced charge collection

observed with the 1st diamond based microdosimeter (BID) prototype characterised and discussed in Chapter 6.

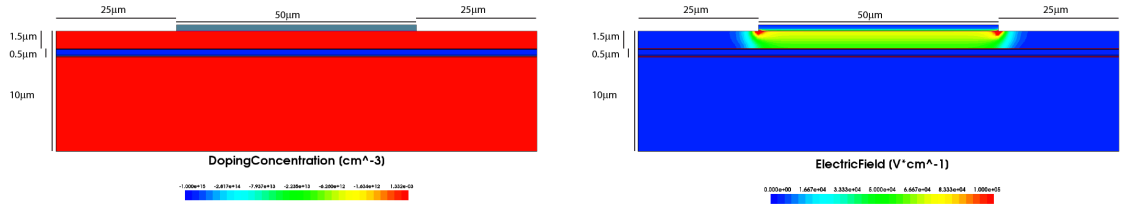

(a) Doping (Boron) Concentration (b) Electric Field Profile

Figure 14.1: 3D model of the BID detector modelled using TCAD. Simplified 3D model (cross section) of the BID microdosimeter prototype with the boron dopant concentration (blue) depicted clearly. The electric field is shown with red indicating regions of higher electric field strength.

3D modelling offers an increased capability to visualise the electrical behaviour that this device design offers. Fig. 14.2a and 14.2b present a tilted and top-down viewpoint of the electric field produced by the potential difference between the two electrodes.

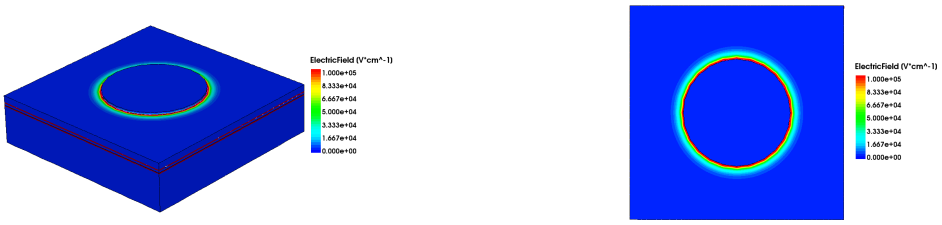

(a) Tilted viewpoint (b) Top-down viewpoint

Figure 14.2: 3D model of the BID detector modelled using TCAD. The electric field is shown with red indicating regions of higher electric field strength.

A 5.5 MeV alpha particle was modelled to be normally incident 5 µm to the side of the top aluminium electrode. The following sets of images show the electron density within the BID detector with respect to time (where: time of ion strike = 0.9 ns). Given the range of the particle, the majority of charge carriers are produced underneath the boron implanted

region. The effect of the electric field presence, in the region above the boron implantation is immediately obvious with equilibrium conditions quickly established as electrons drift towards electrodes under the influence of the strong and highly localised field or through diffusion into the surrounding medium.

Equilibrium conditions take far longer to occur in the bottom region, and indeed have not yet occurred, within the time frame presented here. Without the presence of an electric field, charge carries migrate through the medium through either diffusion or recombination (Shockley-Read-Hall SRH) based mechanisms. The presence of the boron doped region not only provides a means of creating a contact structure but also provides a barrier opposing charge migration. Boron impurities within diamond act as an acceptor dopant, meaning the hole can act as a charge trap for electrons. Whilst this acts to oppose migratory electrons from the underlying region, the build-up of charge affects the magnitude of the electric field which could result in a decreased CCE. If this is the case, then this would be a plausible explanation for the reduced CCE of the BID detector characterised in Chapter 6.

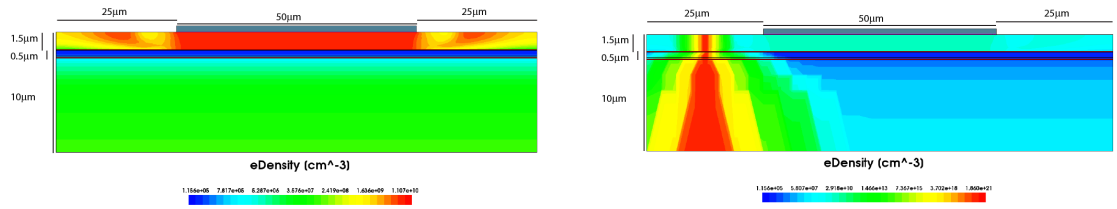

(a) Time = 0.9 ns (b) Time = 1 ns

Figure 14.3: Electron density within 3D model of BID detector at time = 0.9 and 1 ns

14.4 Conclusion

A qualitative examination of the electric field structure produced from a simplified model of the first diamond based microdosimeter prototype characterised and discussed in Chapter

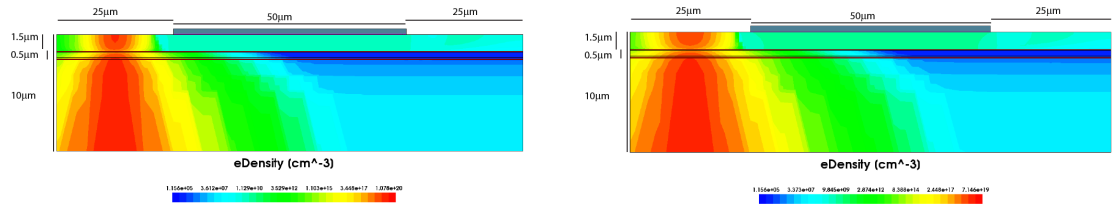

(a) Time = 1.1 ns (b) Time = 1.2 ns

Figure 14.4: Electron density within 3D model of BID detector at time = 1.1 and 1.2 ns

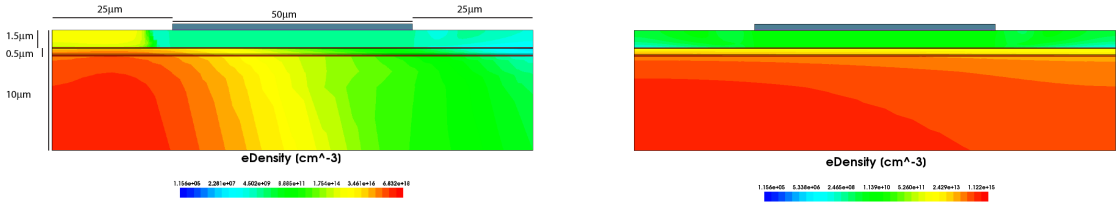

(a) Time = 4.1 ns (b) Time = 60 ns

Figure 14.5: Electron density within 3D model of BID detector at time = 4.1 and 60 ns

6 provides a possible explanation for the enhanced charge collection observed at the edges of the top aluminium electrode. The results produced from a study, involving the use heavy ions, is suggestive that the boron doped layer, whilst useful in terms of providing a conductive layer of diamond for the production of an electric field, also acts as a drain in terms of CCE. The next step in this work is to more accurately model the device and repeat the simulations. This will involve a more accurate modelling of the mesh structure of the boron implanted region, including the modelling of possible charge traps and defects caused by the implantation method. Once this and the model of diamond have been sufficiently validated against experimental work, TCAD will be able to be utilised to optimise the detector design and establish whether the charge collection properties can be improved enough to warrant boron implantation as method for creating diamond based microdosimeters.

Chapter 15

TCAD: Laser Milled Trenches

15.1 Introduction

In this chapter, the second in a series of four applied TCAD studies is presented. This study is concerned with investigating the field structure and charge collection properties within the device experimentally characterised in Chapter 7. The primary aim is to investigate the effect of the 20 μm deep Laser milled Trenches (LT) upon charge collection within sensitive volumes and charge sharing from without/adjacent volumes. This work will be used to support the experimental characterisation of the 1st generation LT device fabricated upon thick (500 μm) diamond. In addition, TCAD will be used to model the 2nd generation LT device, produced upon a thin (30 μm) wafer of electronic grade diamond. Given that this device, is only midway in the fabrication process, this TCAD model will be used as a a means of providing proof of concept behind the 2nd generation LT device fabricated upon thin diamond and featuring mirrored contact structure.

15.2 1st Generation LT Model

The second set of devices structures are modelled to be representative of that described in Chapter 7. The type of device is a metal-insulator-metal structure, with diamond being the insulator and aluminium (top/back) as the metal used to create electrical contacts. Four different structures (2D cross section) were modelled in this work, with the primary differences being the presence or lack of presence of laser milled trenches and the use of a common or mirrored back contact setup.

The diamond substrate was modelled to have dimensions 2160x500 μm^2. The size of the top contacts and in the case of the mirrored contact set-up are 600 μm wide and 0.2 μm thick, whilst the common contact used is 1620 μm wide and 0.2 μm thick. The laser milled trenches are 20 μm deep and 20 μm wide. The four devices described in this section were modelled in 2D only.

15.2.1 Results: LT 1st Generation

The next set of results are derived from the 2D modelling of the device experimentally characterised in Chapter 7. Two of the four devices fabricated on this device have been modelled and simulated, in order to examine the effect of laser milled trenches upon charge confinement. These models, like the real device make use of a common back contact which has been defined to be at 0 V, whilst the two top contacts are made to be at 500 V. Fig. 15.1 depicts the superimposed electric fields of the two diamond models with and without the presence of laser milled trenches.

The results, show that the physical presence of a trench alone, is not responsible for the charge confinement depicted in the experimental results presented in Chapter 7. Rather, charge confinement may be a result of the fabrication method itself inducing localised charge traps/defects in the regions surrounding the laser milled trenches. The inclusion of such defects will be included in future work.

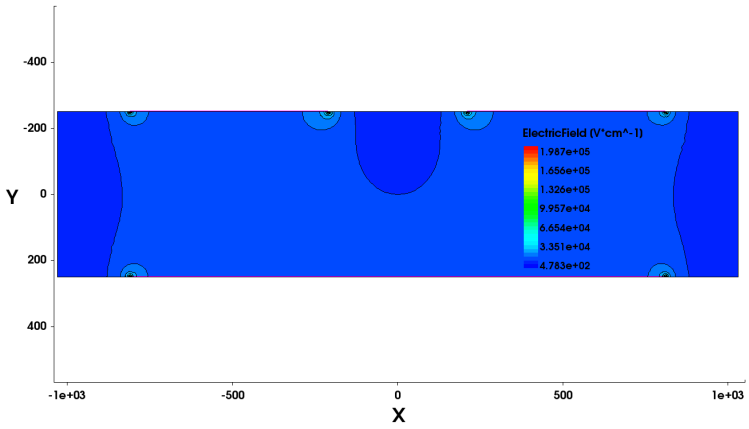

Figure 15.1: Superimposed 2D model of D2 and D3, featuring the electric field profile of the 2nd Generation diamond microdosimeter prototype. This model makes use of two top contacts 600 µm wide and 200 nm thick. The model for D3 is identical with one exception, being the inclusion of charge confining laser milled trenches 20 µm deep and 20 µm wide.

Whilst the exact mechanism for charge confinement has not been fully established and confirmed, methods for improving upon the confinement of the electric field were explored as part of this work. The simulation was repeated using the same structure with one notable difference. The common back contact was replaced with two contacts of equal dimension and placement with respect to the top contacts. The results from this simulation are presented in Fig. 15.2. The mirrored contact set-up, demonstrates a vast improvement of the confinement of electric field to the desired regions, using purely geometric based considerations of the detector construction. This effect can be further enhanced by decreasing the overall thickness of the diamond substrate and will be explored in the 2nd generation LT device.

15.3 2nd Generation LT Model

The second generation LT device utilises the same structure as that already discussed, with the main differences being the size of the sensitive volume modelled due to a decreased diamond substrate thickness (30 µm) and a decreased width of electrical contacts (10 µm). The

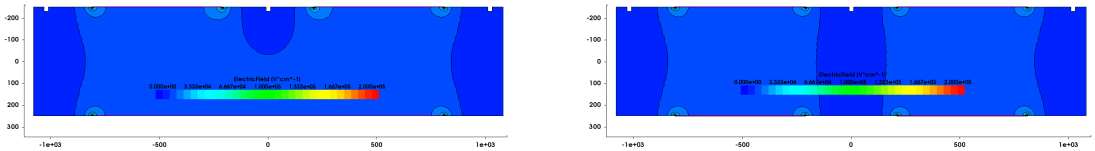

(a) Common Back Contact (b) Mirrored Contact

Figure 15.2: Electric field profiles for MIM structure. 500 V bias is applied at the the top two electrodes with the common and mirrored back contacts at ground (0 V). The mirrored contact model (right) improves upon the common contact model (left). It makes use of two sets of top/bottom contacts 600 µm wide and 200 nm thick and maintains the inclusion of charge confining laser milled trenches.

models used in this section is an simplified representation of D3 which present a 6x6 array of SVs with mirrored contacts. The diamond substrate modelled, is of the same thickness as the substrate upon which the real devices are being fabricated, i.e. 30 µm. The dimensions of the trench are 20 µm deep and 5 µm wide. The trench depth is then now almost equal to that of the substrate thickness when compared with previous designs based on 500 µm thick samples of diamond. Aluminium contacts 10x10x0.2 μm^3 placed centrally upon the top and bottom sides of each 'island' or SV, are also present. To save on simulation time, only one quadrant of the 6x6 device was modelled, i.e see Fig 15.3 is the 3D model of a 3x3 SV array with individual SVs having dimensions of 30x30x30 μm^3.

15.3.1 DC Results: LT 2nd Generation

The results from this section are derived from models based upon the unfinished 2nd generation diamond based microdosimeter prototype. A bias of 30 V is applied to the top "outside" electrodes centrally located upon each 'island' or SV, whilst their counterparts upon the bottom side have been grounded at 0 V. The central electrode, also has a bias of 30 V applied to the top electrode, on what may be considered effectively, as a "second channel". The following set of figures (Fig. 15.3 and 15.4) depict the electric field present within the device structure with the configuration just described.

These results show that the mirrored contact structure along with a decreased substrate thick-

ness produces an electric field structure well confined to the individual diamond 'islands' or SVs.

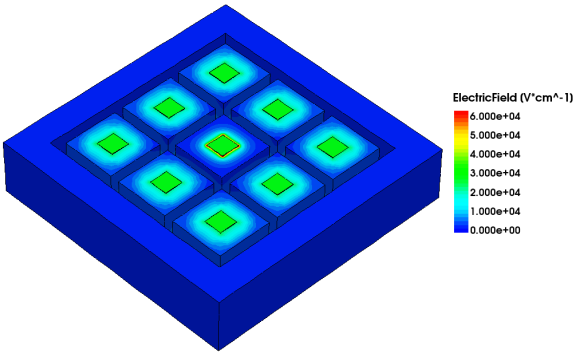

Figure 15.3: Tilted viewpoint of the 3D model featuring a 3x3 array of diamond SVs. 30 V is applied to the top electrodes centrally located upon each 'island' or SV. The resulting electric field is displayed.

(a) Top viewpoint.

(b) Bottom viewpoint.

Figure 15.4: Top and bottom viewpoint of the 3D model featuring a 3x3 array of diamond SVs with electric field shown.

15.3.2 CCE Results: LT 2nd Generation

A 5.5 MeV alpha particle was modelled to be normally incident underneath the central top aluminium electrode. The following sets of images show the electron current density within the 2nd generation LT detector with respect to time (where: time of ion strike = 0.9 ns).

The first result (see Fig. 15.5a) depicts the typical or reference conditions, portraying the current due to the movement of electrons under influence of an externally applied electric field. After the ion strike, which causes the generation of electron hole pairs, the electron current density as depicted in Fig. 15.5b shows some very obvious changes. The presence of the ion strike track is immediately obvious, depicting an electron current density greater than the surroundings by several orders of magnitude. The collapse of the electric field in the ion strike region due to the abundance of charge carriers, is evident in Fig. 15.6b and is shown to increase in Fig. 15.8a as charge carriers migrate through the medium. At 99 ns after the ion strike, the electric field shown in Fig. 15.8b shows initial signs of recovery, as the charge carriers continue to migrate towards the electrodes. As more of the ionised charge carriers are collected, there is an associated drop in the electron current density, which in turn corresponds to a slight recovery of the electric field.

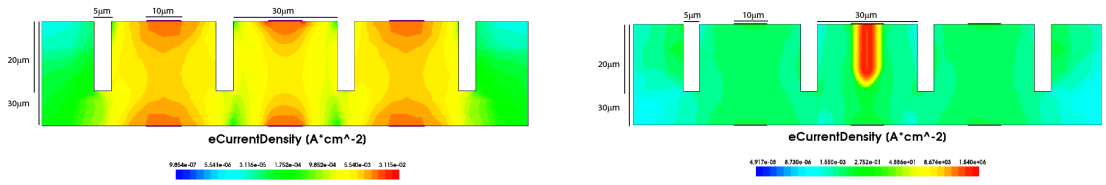

(a) time = 0.9 ns (b) time = 1.1 ns

Figure 15.5: Electron current density within 2nd generation LT device with respect to time.

Whilst these results appear promising, more work needs to be done. In particular, an extended analysis of charge collection with respect to time and bias conditions, should be performed.

15.3.3 Conclusions

2D and 3D models were created of the 1st and 2nd generation diamond based microdosimeter prototypes featuring laser milled trenches, a.k.a. LT device. The 2D models of the 1st

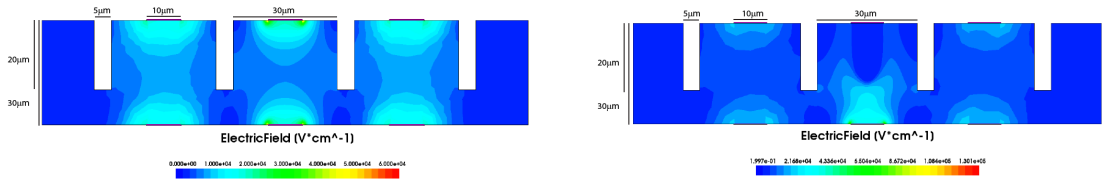

(a) time = 0.9 ns (b) time = 1.1 ns

Figure 15.6: Electric field (cross-section) within 2nd generation LT device with respect to time.

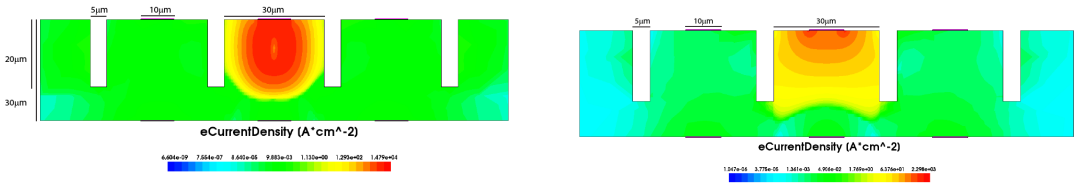

(a) time = 4.1 ns (b) time = 99 ns

Figure 15.7: Electron current density within 2nd generation LT device with respect to time.

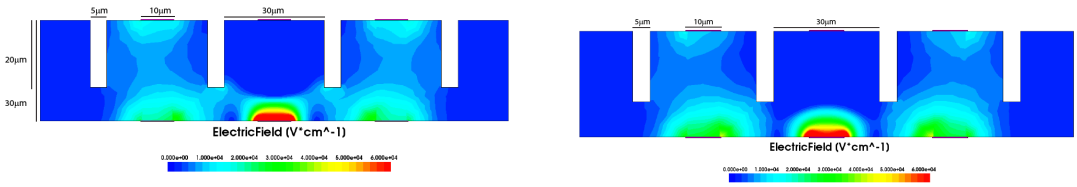

(a) time = 4.1 ns (b) time = 99 ns

Figure 15.8: Electric field (cross-section) within 2nd generation LT device with respect to time.

generation LT device with and without trenches are suggestive that the charge confinement observed in the experimental characterisation of the 1st generation LT device are not caused by physical isolation or pixelation of SV regions. Instead, it is more likely that the charge

confinement is a result of charge defects caused by the laser ablation process. Further studies incorporating different types and amounts of charge defects surrounding trenches will need to be included in further work in order to test this hypothesis. The addition of mirrored contact structure, firstly in the 2D models of the 1st gen LT device, and then again in the 2nd gen LT devices (3D 3x3) displayed improved electric field confinement with respect to SV definition. These results serve as a proof of concept behind the design of the 2nd generation LT device.

Chapter 16

TCAD: Buried Contacts

16.1 Introduction

The motivation behind the buried contacts device, was to investigate alternative means of creating isolated sensitive volumes within diamond. To that end, buried pairs of electrodes, created by filling laser milled trenches with silver active brazing alloys were fabricated so as to confine charge collection to region laying in between the electrode pairs. The primary aim of this study is to investigate the effect of bias upon the electric field structure and charge collection region underneath and surrounding the electrode structure.

16.2 BC Concept

The first design modelled was that of the ideal case. TCAD provides an advantage in that whilst this design was not able to be fabricated at the time with the equipment and materials on offer, it could still be modelled and analysed in terms of its potential merit as a micro-dosimeter. The device was modelled in 3D and features two buried contacts of identical size (10 μm wide and 10 μm deep) separated by distance of 10 μm embedded in a diamond substrate 30 μm thick with width and length of 20 and 30 μm respectively. A boundary trench

(vacuum) surrounded the contact pair, made to be a minimum of 5 μm separation from the closest electrode point.

16.2.1 DC Results: BC Concept

The results for the concept structure modelled in 3D are presented in this section. Fig. 16.1 depicts a tilted top down perspective of the device where the electric field structure can be clearly be seen to be heavily confined between the two buried electrodes with rapid degradation in electric field strength due to presence of boundary trench. Fig 16.2b and 16.2a depict a cross sectional and bird eye view of the electric field profile of the buried contact device concept. These results demonstrate the existence of strong electric fields in the immediate space laying between the two buried electrodes as expected. The cross sectional viewpoint of the electric field structure, which exemplifies a strong and homogeneous field in between the electrodes also demonstrates the electric field extending albeit to a weaker intensity all the way to the bottom of the device. This effect can be reduced if not eliminated through proper control of the bias conditions. Fig. 16.2a also shows an electric field profile, reminiscent of the IBIC results presented in Chapter 8.

16.3 1st Generation BC Detector

Three 2D models were created in this section to be consistent with the device described and experimentally in Chapter 8. Each device has been modelled as a cross section taken through the middle of the device, so that all important features of the device are described. Each model in this section features buried contacts of identical size (80 μm wide and 30 μm deep) separated by distance of either 10, 20 or 30 μm in 500 μm thick substrate of diamond. Each of the three models features trenches, to contain the buried electrode pair structure between and separated by 300 μm.

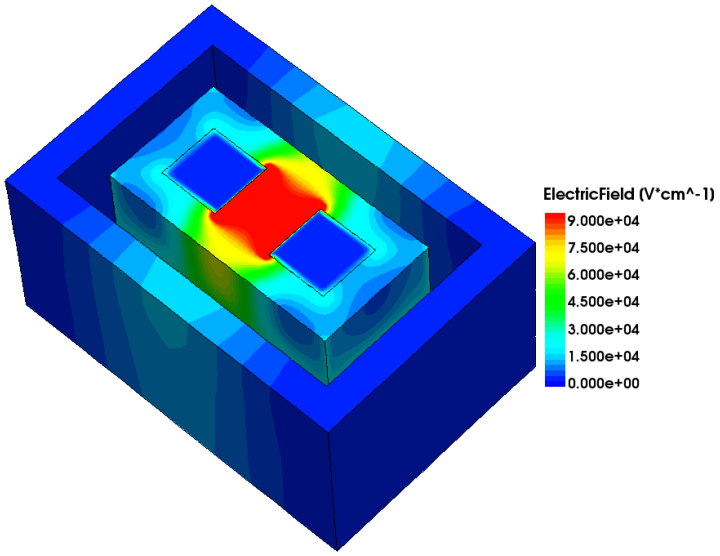

Figure 16.1: Tilted Viewpoint of the buried contact concept model

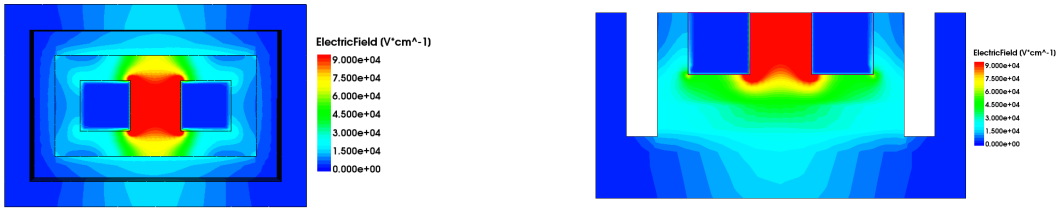

(a) Birds eye viewpoint

(b) Cross-sectional viewpoint

Figure 16.2

16.3.1 DC Results: 1st Generation

Fig. 16.3 and 16.4 depict the results which coincide with 10 and 30 V, applied to the right electrode (the contact separation for these two devices is 10 and 30 µm). The bias conditions were chosen specifically to give an electric field strength between the two electrodes of 1 $\mathrm{V\,\mu m^{-1}}$ (or equivalently 10000 $\mathrm{V\,cm^{-1}}$). Whilst the electric field within the vicinity of the contact separation region, i.e. the SV, is roughly equivalent, the increased bias in the case of Fig. 16.4 along with the contact geometries leads to an enlarged fields size, allowing for

potential to collect charge from an even greater volume. Given the need for an accurately defined collection region or SV, this increased collection region is not desirable.

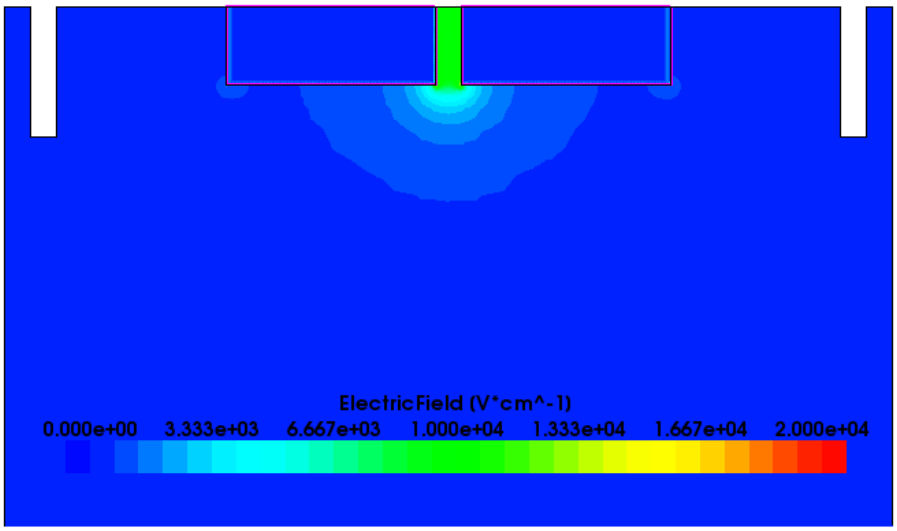

Figure 16.3: Cross-sectional viewpoint of the 1st Generation BC device (D1). Separation = 10 µm & Bias = 10 V

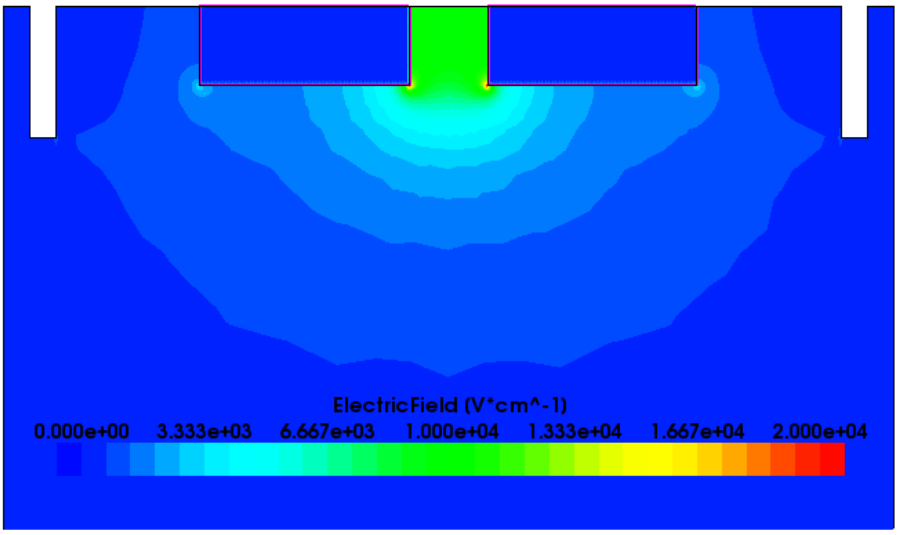

Figure 16.4: Cross-sectional viewpoint of the 1st Generation BC device (D3). Separation = 30 µm & Bias = 30 V

To examine the effect of bias, the electric field strength versus position in terms of depth and lateral distance was plotted. D1 which features a contact separation of 10 µm was

examined under different applied bias, i.e., 5, 10 and 20 V. Fig. 16.5, depicts the electric field profile between the two buried contacts at constant depth. As expected, the result shows a uniformity in the magnitude of the electric field strength corresponding the ratio of applied bias to the contact separation.

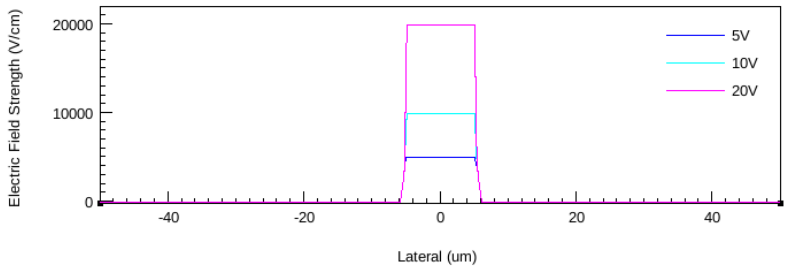

Figure 16.5: Electric field strength ($\mathrm{V\,cm^{-1}}$) versus lateral distance (μm) taken through the middle of contact structures, for BC device with 10 μm separation.

Fig. 16.6 depicts the electric field strength ($\mathrm{V\,cm^{-1}}$) versus depth (μm) for BC device with 10 μm separation for 5, 10 and 20 V applied bias and Fig. 16.7 depicts the electric field strength versus lateral distance at 5 μm depth underneath the buried electrodes. These two figures demonstrate, how the operating bias can be optimised, to help confine the electric field to a desired region, i.e., the decreased magnitude of the electric field strength with distance away from the SV region corresponds to decreased applied bias.

To examine the effect of separation distance, the electric field strength versus position in terms of depth and lateral distance was plotted. Three devices were modelled (D1, D2 and D3), each identical with the exception of having a different contact separation distance, i.e., 10, 20 and 30 μm. So that the magnitude of the electric field strength between the two electrodes would be equal, the applied bias for D1, D2 and D3 was defined to be 10, 20 and 30 V. This is depicted in Fig. 16.8, see below.

The next two results presented in Fig. 16.9 and 16.10, depict how slight changes in the geometry of electrical contacts can affect the resultant electric field structures. Fig. 16.9 clearly shows that the BC device with a 10 μm contact separation at an applied bias of 10

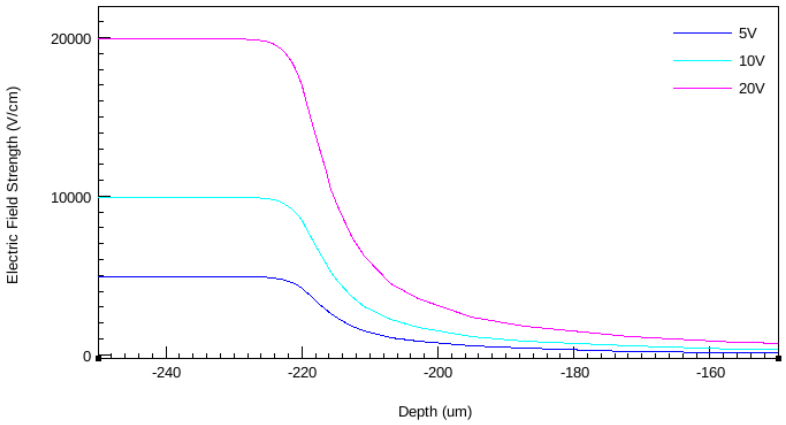

Figure 16.6: Electric field strength ($\mathrm{V\,cm^{-1}}$) versus depth ($\mu\mathrm{m}$) for BC device with 10 $\mu\mathrm{m}$ separation.

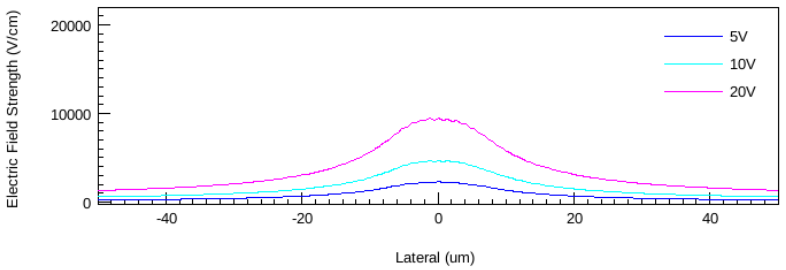

Figure 16.7: Electric field strength ($\mathrm{V\,cm^{-1}}$) versus lateral distance ($\mu\mathrm{m}$) taken 5 $\mu\mathrm{m}$ below contact structures, for BC device with 10 $\mu\mathrm{m}$ separation.

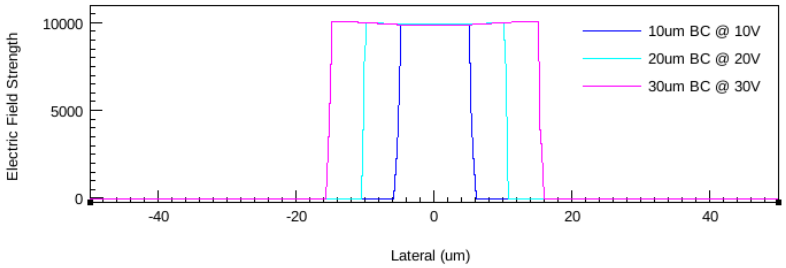

Figure 16.8: Electric field strength ($\mathrm{V\,cm^{-1}}$) versus lateral distance ($\mu\mathrm{m}$) taken through the middle of contact structures, for BC device with 10, 20 and 30 $\mu\mathrm{m}$ separation.

V has the best electric field structure in terms of uniformity and definition with respect to applicability to microdosimetry. Fig. 16.10 depict the electric field strength ($\mathrm{V\,cm^{-1}}$) versus lateral distance ($\mu\mathrm{m}$) taken midway through and 5 $\mu\mathrm{m}$ below contact structures respectively

and shows decreases "spillout" beneath the SV region. This result can be used as confirmation to show that given an appropriate combination of operating conditions (bias) and contact geometry, in this case the separation distance, the buried contact structure can be used to create a well defined SV region.

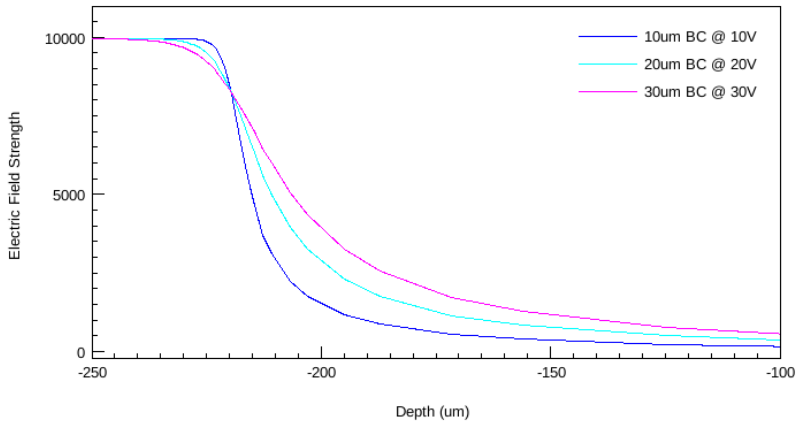

Figure 16.9: Electric field strength ($\mathrm{V\,cm^{-1}}$) versus depth ($\mu\mathrm{m}$) for BC devices with 10, 20 and 30 $\mu\mathrm{m}$ separation at 10, 20 and 30 V respectively.

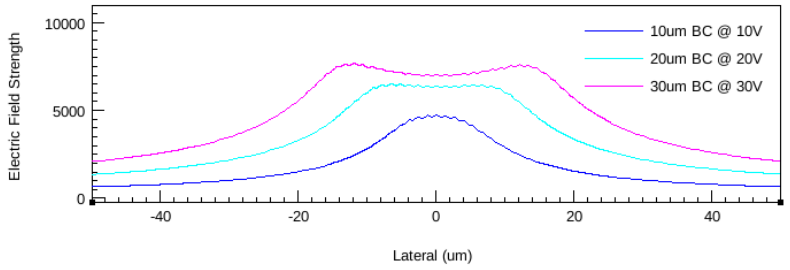

Figure 16.10: Electric field strength ($\mathrm{V\,cm^{-1}}$) versus lateral distance ($\mu\mathrm{m}$) taken 5 $\mu\mathrm{m}$ below contact structures, for BC device with 10, 20 and 30 $\mu\mathrm{m}$ separation.

16.3.2 CCE Results: 1st Generation

A 5.5 MeV alpha ion strike was simulated to be normally incident upon the diamond surface, centred between the two buried electrodes for the BC device with electrode separation of 10 $\mu\mathrm{m}$. The following sets of results show the electron density within the device structure

at different times after the ion strike has occurred. To illustrate the effect of an applied bias, results for 0 V and 10 V are presented for comparison. Without an applied bias, charge carriers created through the ionisation event diffuse throughout the medium gradually undergoing recombination. The application of 10 V bias is shown to cause drift mechanisms to dominate over diffusion with the result being that electrons are quickly drawn and fully collected at the right electrode in a short period of time.

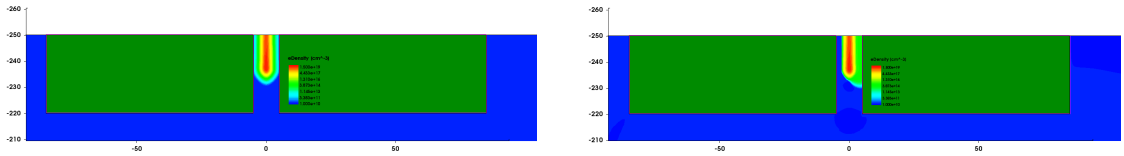

(a) Bias = 0 V (b) Bias = 10 V

Figure 16.11: Electron density for BC device with 10 µm separation at the time of the 5.5 MeV alpha ion strike (t = 0.9 ns). The effect of bias can be observed by comparing the two results.

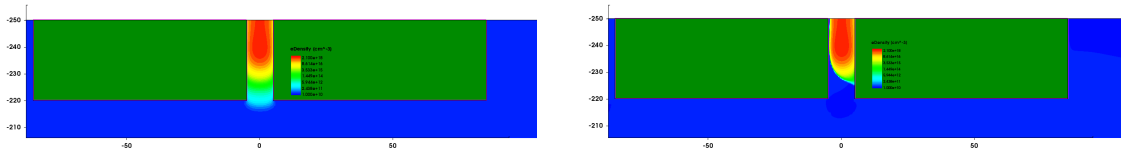

(a) Bias = 0 V (b) Bias = 10 V

Figure 16.12: Electron density for BC device with 10 µm separation at time = 1.1 ns after 5.5 MeV alpha ion strike. The effect of bias can be observed by comparing the two results.

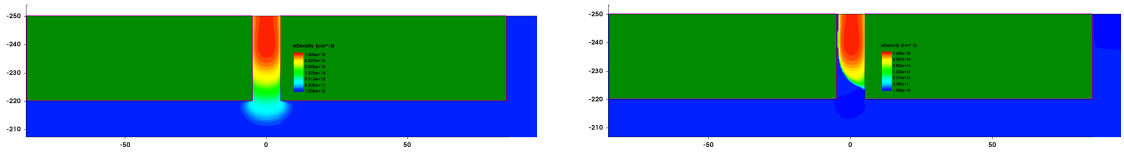

(a) Bias = 0V (b) Bias = 10 V

Figure 16.13: Electron density for BC device with 10 µm separation at time = 3 ns after 5.5 MeV alpha ion strike. The effect of bias can be observed by comparing the two results.

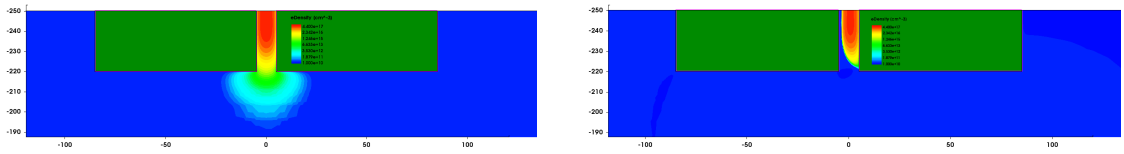

(a) Bias = 0 V (b) Bias = 10 V

Figure 16.14: Electron density for BC device with 10 µm separation at time = 4.1 ns after 5.5 MeV alpha ion strike. The effect of bias can be observed by comparing the two results.

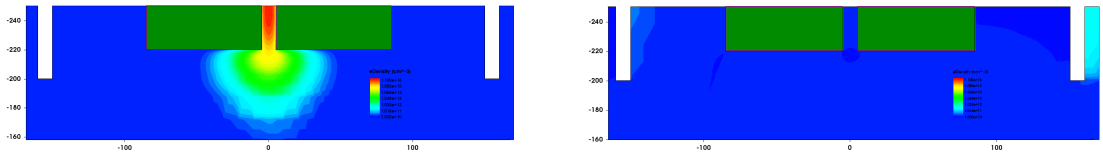

(a) Bias = 0 V (b) Bias = 10 V

Figure 16.15: Electron density for BC device with 10 µm separation at time = 1.0 ns after 5.5 MeV alpha ion strike. The effect of bias can be observed by comparing the two results.

16.4 2nd Generation BC Detector

The next set of models describe devices that are still within the fabrication stage and would represent the 2nd generation of buried electrode structure for diamond microdosimetry. The models implemented in this section closely represent the final product following completion of the fabrication stage. These models describe multiple sets of silver contacts (10x10x10 μm^3, separated by 10 µm). These buried contacts are set up, so that the contacts are biased and grounded in alternate order, to effectively 4 sensitive volumes for charge collection. This device was previously described in detail in Chapter 10. TCAD is invaluable in allowing the characterisation of a device that is unfinished in terms of fabrication.

16.4.1 DC Results: 2nd Generation

The results presented here refer to the improved designs of the buried contact structure which now include multiple SV's connected alternately in parallel. The five buried electrodes have been grouped into two set of contacts; inside and outside, with the outside referring to far left, central and far right buried electrodes and the inside referring the inner left and inner

right.

The first result presented in Fig. 16.16a depicts the electric field profile of the device with 10 V applied to the "outside" electrode, whilst the "inner" electrode is grounded. The result depicts good confinement of the field to the SV regions with only slight "spillage" of the electric field, which might be reduced through optimisation of the bias conditions.

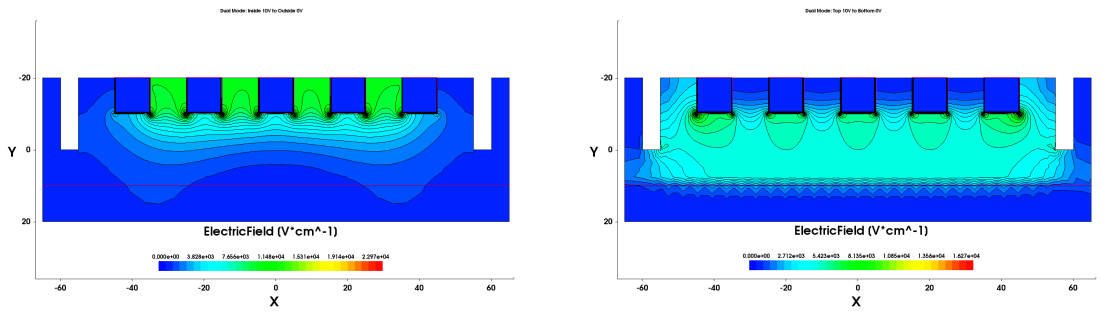

(a) Microdosimetry Mode (b) Minidosimetry Mode

Figure 16.16: Electric Field profile under different configurations.

The addition of a boron doped under-layer, provides additional modes of operation, as well as changing the electric field structure under normal operating parameters, i.e., those used previously. To explain the next set of results, it is necessary to explain the naming terminology used to describe contact sets. In addition to the "inside" and "outside" electrodes defined earlier, two additional sets are further defined. When all five electrodes are biased at the same potential, they are then referred to as the "top" electrodes and the boron doped under-layer is referred to as the "bottom" electrode. The following set of results presented here, refer to the device being operated in lateral (standard) and top/down mode. This second alternative mode of operation makes use of the boron doped layer as a common back contact and the buried electrodes either individually or collectively as the top contacts. This mode of operation, whilst not being the aim of this project, may potentially be useful for dosimetric applications, making this a device able to function as both a dosimeter and microdosimeter, depending upon the bias configuration. This alternate mode in which the

2nd Generation BC device can be operated, is presented in Fig. 16.16b. The configuration presented here, is with all of the buried electrodes, i.e., the "top" electrode, under a constant bias of 10 V and the "bottom" electrode (boron doped layer) grounded at 0 V. This mode of operation increases the effective SV size which may be desirable for applications outside of microdosimetry, with minidosimetry representing just one option.

16.5 Conclusions

Buried contacts for use in microdosimetric applications have been studied by way Sentaurus TCAD driven simulations in this chapter. Variations of the device geometries have been modelled in 2D and 3D. The devices have been modelled in terms of the electric field structures determined by device geometry and bias conditions, as well as the response to heavy ion strikes (5.5 MeV alpha (He^{2+}) particle). The initial results of the TCAD simulations provide positive input in terms of optimising the device design. To that effect, the device has been redesigned and remodelled. The optimised design features a thinned substrate,increased proximity of the boundary trenches and smaller buried contacts. The separation between the buried contacts and the boundary trenches has been decreased to be 5 $\mu\mathrm{m}$. The buried contacts have new dimensions of 10x10x10 $\mu\mathrm{m}^3$. Finally, the substrate thickness has been reduced from 500 $\mu\mathrm{m}$ to 30 $\mu\mathrm{m}$ and layered upon a boron doped substrate. By making use of the same milling and brazing technology previously used to create the buried contacts, an electrical path can be fabricated to connect to the boron doped diamond under-layer. This allows the device to be operated in multiple modes, i.e., potentially making it both a microdosimeter and a minidosimeter. The use of TCAD allows for an understanding of the alternate SV regions as defined through the biasing of optional contact sets.

Chapter 17

TCAD: Cylindrical Sensitive Volumes

17.1 Introduction

This device dubbed as the "cylindrical SV" (CSV) device is the last in a series of devices aimed at producing alternative means of creating SV structures for use in diamond based microdosimetry. The fabrication methodology of this device was outline in Chapter 10 and as yet remains unfinished and untested in terms of experimental characterisation at the time of submission. The method of fabrication as well as that of simulation results in a hollow CSV structure. The aim of this project is to determine the viability of this technology for use in microdosimetric applications.

17.2 1st Generation CSV Detector

Two versions of the CSV structure were modelled in this work. The first model was to simulate the original concept structure of a central electrical contact or pylon surrounded by a second contact shell with both contacts penetrating into the diamond substrate to equal depths. The second design was modelled to fit with the design discussed in Chapter 10. This design is almost identical to the first, but differs in that the boundary contact shell penetrates

further to create an electrical path to a buried boron doped region (Boron concentration= 1E15). These two different designs were modelled so as to portray the advantages and disadvantages of each.

17.2.1 Results: Model Comparison

The results from the two different structures modelled in 2D are presented here in Fig. 17.1a and 17.1b. The bias conditions are the same for each device modelled, with 10 V being applied to the central electrode and the outer electrode and boron doped region in the case of device 2 all grounded at 0 V. Fig. 17.1a depicts a uniform electric field between the inner and outer electrodes with "spillout" beneath. Fig. 17.1b shows the same uniformity between the inner and outer electrode but also adds the extra field from the region between the boron doped diamond and inner electrode. The results show that in the case of the "ideal" device, the confinement of field to the region directly between the electrodes can be improved or decreased through proper bias control. The results which include an additional boron doped layer underneath the device structure demonstrate a constant and knowable volume definition.

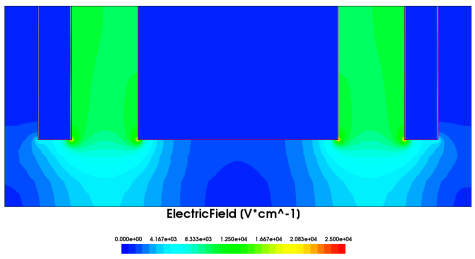

(a) Cross sectional viewpoint of electric field in 2D model of Cylindrical SV device without boron doped underlayer.

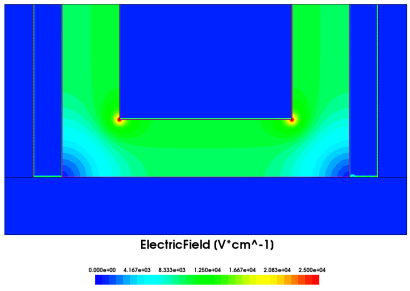

(b) Cross sectional viewpoint of electric field in 2D model of Cylindrical SV device with boron doped underlayer.

Figure 17.1: Comparison of the electric field distribution of CSV device with and without boron doped underlayer

17.2.2 Results: CCE of CSV

In this section, the initial results of the response of the CSV device with respect to a 5.5 MeV alpha particle, are presented. The ion strike was modelled to be normally incident midway between the inner and outer electrodes. As discussed previously, the outer electrode is electrically connected to a boron doped 'underlayer' as depicted in Fig. 17.2a. A bias of 10 V is applied to the inner electrode, whilst the outer electrode and boron doped layer are grounded at 0 V, see Fig. 17.2b.

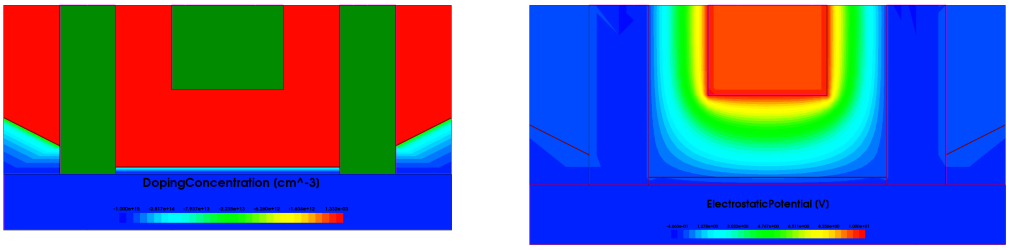

(a) Concentration of Boron dopant. (b) Potential difference.

Figure 17.2: Model of the 1st generation CSV device depicting boron dopants and applied bias.

The electron current density with respect to time is presented in Fig. 17.3. Fig. 17.3a, depicts the electron current density at 1.1 ns, or 0.2 ns after the ion strike. In this result, the electron current density is greatest in the ion strike region as expected, and shows an obvious migration toward the central or inner electrode. Fig. 17.3b, also depicts the electron current density within the CSV device, though at a much later time (99 ns). At this time, the response of the device appears to have stabilised, as evident by the symmetry of electron current density within the sensitive volume region. All of the ionised charge carriers have been collected, meaning that any current now measured, is a function of the electric field alone.

At this point, no quantitative analysis of the device response is on offer, however, it is clear from a qualitative standpoint that the device is functioning as expected. Charge carriers generated by the presence of an ionising particle are quickly swept up by the strong radial

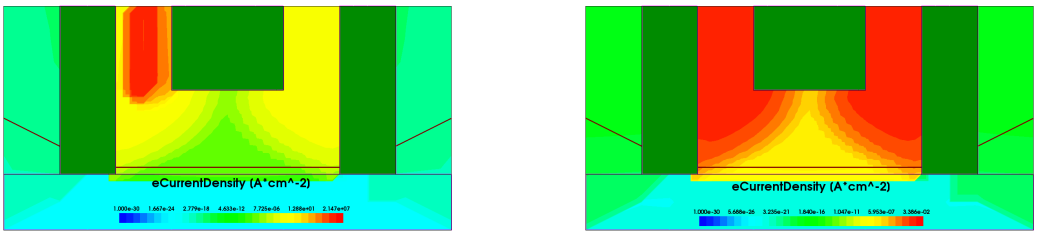

(a) time = 1.1 ns (b) time = 99 ns

Figure 17.3: Electron current density within 1st generation CSV device with respect to time.

field the cylindrical SV structure offers. Further modelling of this device will be required in the future in order to be fully understood.

17.3 Conclusions

A diamond device utilising buried contact structure to produce cylindrical SVs was modelled using TCAD. This design represents the last in a series of detector designs created in this thesis to explore alternative methods of creating diamond based microdosimeter. Two variations of the cylindrical SV device were modelled in this study. The first model depicts a 2D cross section of a central cylindrical silver electrode with radius 10 µm and depth of 10 µm. The central electrode is surrounded by a cylindrical shell with thickness 5 µm and depth 10 µm which in 2D is portrayed as three rectangles separated by 10 µm. TCAD was used to study the change in electric field profile produced by the structure just described. The cylindrical SV represents an improvement upon the alternate design configurations in terms of chord length variance as well as the production of a radial electric field distribution with uniformity that should hypothetically improves upon charge collection efficiency. Apart from some spill-out from the bottom of the SV leading to a slight lack of confinement, the improvements are readily recognisable in the electric field profiles presented. The second design features a boron doped layer underneath the electrode structure with the outer shell

structure now penetrating to a depth to reach the conductive boron doped layer. The effect of this design improves upon SV definition but has the added affect of increasing the volume size. The cylindrical sensitive volume design of this device represents a step forward to realistic diamond based microdosimetry, in that cylindrical volumes are a better approximation for human cells which may be considered spherical, than the cubic structures which have dominated much of the previous designs.

Part VI

This is the end!

Chapter 18

Discussion and Conclusions

The primary aim of this thesis was to design, fabricate and test alternate prototypes for diamond based microdosimetry, with secondary aims of improving upon the body of knowledge related to diamond. This was realised in three major parts. Firstly the experimental characterisation of three alternative designs. Secondly, the design and fabrication of next generations detectors. Thirdly, the optimisation/development of new designs using TCAD and correcting for tissue equivalence with protons and alphas with GEANT4. This chapter presentations a summary of the major contributions made in this work and presented in this thesis and offers some recommendations for future research and direction of the project.

18.1 Summary of Contributions

After the introduction, the second chapter of the thesis provides a review of the current literature in the field. It begins by providing a small summary of the various radiation environments the detector is being developed for. It then provides the basics of microdosimetry and the material qualities of diamond in terms of its potential use. Following Chapter 2, the next three chapters deal with the methods; fabrication, experimental and theoretical, that were used in this work.

In Chapter 6, the first in a series of alternate microdosimeter prototypes (Boron Implanted Diamond (BID) Device) was characterised by experimental means and was published in J. A. Davis, et al, IEEE TNS 2012. This detector featured aluminium contact pads (top) and utilised boron implantation to create a buried floating contact at depth within the diamond substrate. IBIC measurements with 5.5 MeV He^{2+} with bias applied between the top aluminium electrode and bottom buried electrode, showed isolated SV structures, well defined by the boron implanted mesh. Whilst the technology showed itself to be capable of creating tailor made SVs with dimensions determined by the original mesh and boron ion energy, it did have the drawback of a reduced charge collection efficiency (CCE). The reduced CCE was hypothesised to be the result of radiation damage induced charge defects, caused by the implantation method (see Section 18.2). Enhanced CCE also observed occurring towards the edges of the top aluminium contact pad and further studies utilising Geant4 and TCAD were commissioned in order to investigate the cause.

In Chapter 7, the second in a series of alternate microdosimeter prototypes (Laser-milled Trench (LT)) was characterised by experimental means and was published in J. A. Davis, et al, IEEE TNS 2014. The LT device is based upon a planar metal-insulator-metal (MIM) design using laser ablated/milled trenches to isolate sensitive volume regions thereby creating a pixelated detector. IBIC measurements with 5.5 MeV He^{2+} of this device showed that laser milled trenches, along with optimised biasing conditions could create fully isolated SVs with next to zero loss in CCE. Whilst the charge collection results produced using the heavy ion microprobe at ANSTO are promising, the current design requires further refinements in order to scale down the size of the SVs in order to be useful for microdosimetric applications.

In Chapter 8, the third in a series of alternate microdosimeter prototypes (Buried Contact BC) was characterised by experimental means. The BC detector was formed by laser ablating rectangular voids within diamond and filling with silver Active Brazing Alloy (ABA) to

create a buried lateral contact structure surrounded by a laser milled boundary trench to contain the electric field produced when biassed. The effectiveness of the boundary trench, like with the previous LT device was found to have an anti-correlation with the penetrative depth of energetic particles, which can be improved by reducing the thickness of the substrate itself. The peak in charge collection, as expected, was found to occur in the intermediary region between the two buried contact structures. It should be noted, however, that charge was collected from the surrounding regions demonstrating that the SV is not fully defined. In addition, the contact geometry itself, implies that the minimum SV size, by definition is as yet unsuitable for microdosimetry. The BC device has shown the potential in buried contact technology and this will be improved in successive generations.

In Chapter 9 and 10, the fabrication process and initial characterisation work for the next generation of LT and BC type devices is detailed. In addition, a new device, featuring buried cylindrical volumes based upon the technology used to create the BC device is introduced. These devices aimed at addressing the shortcomings of their predecessors, are the next step in diamond based microdosimetry, and although the technological complexity in terms of the fabrication process has increased dramatically, these devices look to take diamond based microdosimetry one step closer to becoming a commercial reality. In Chapter 11.1, the first of two explanations for the enhanced charge collection occurring in the BID device previously discussed was studied. A GEANT4 based investigation with the aim of determining the effect upon charge collection efficiency with respect to varied thickness of overlaying contact material. It was shown that the increasing thickness towards the edge of the contact pad could result in increased CCE due to loss of energy within the aluminium overlayer. This is unllikely though, from a fabrication standpoint, where it is more probable that that the thickness would decrease rather than increase, as would be necessary to explain the experimental results. In Chapter 12, another GEANT4 based investigation was discussed, this one, with the aim of determining a geometric scaling factor to convert the energy deposition

for protons and alpha particles within a diamond volume to water for the purpose of confirming the tissue equivalence of diamond. It was shown that due to relatively constant stopping power ratio of diamond and water for protons and alpha with energies in the range of 1 MeV to 10 GeV, a constant scaling factor of 0.31 could be used to correct for the difference in energy deposition response within diamond to water. This correction is a geometric scaling factor that means that the energy deposition repsonse in a 10x10x10 $\mu\mathrm{m}^3$ diamond volume is equal to that in corrected water volume of 31x31x31 $\mu\mathrm{m}^3$. Such a correction, allows for the tissue equivalence definition of diamond, to be extended for protons and alphas with energies typical of GCR and SPE, i.e., radiation specific to a space environment. Chapter 13 introduces the first of five TCAD based studies, implemented in this thesis. In this chapter, the initial steps to define a material (diamond), that is not part of the inbuilt material database is carried out. Whilst not completely successful, the model shows promise that with a few refinements of being able to correctly model intrinsic electronic grade diamond such as that used within the experimental devices discussed previously. The model defined in this work showed similar IV characteristics as that of the first generation LT device and a capacitance that was in accord with a dielectric material. The major failing of the model at present is the underestimation of charge collection efficiency; being almost half of that realised by the experimental device, upon which the simulation was modelled. It was concluded that the model in its present state while suitable for qualitative analysis of device structures and usable for device optimisation was unsuitable for quantitative analysis.

Chapter 14 which features the 2D and 3D modelling of the simplified BID device, showed an increased electric field strength at the contact edges defined which serves as a more probable explanation for the enhanced charge collection than that of increased contact thickness. Chapter 15 which modelled the 1st and 2nd generation LT devices, showed that contrary to the author's expectations, the physical separation of the laser milled trenches alone could not explain the charge confinement observed in the experimental characterisation of the 1st

generation LT device. It was concluded that instead, the charge confinement is a result of a change in electrical properties in the region surrounding the laser milled trenches, perhaps caused by laser induced charge defects. It was also shown that the mirrored contact set-up realised in the 2nd generation LT device offered up a better SV definition than that seen in its 1st generation counterpart. Chapter 16 modelled the 1st and 2nd generation BC devices. These models served to explain the charge collection results in terms of the effect of contact geometry and biasing conditions. The models of the 2nd generation device were also useful in showing alternative modes of operation, i.e. microdosimeter mode and minidosimeter mode. Chapter 17 showed what the expected electric field would be in the cylindrical SV device still in the fabrication stage. The device was modelled with and without a boron doped diamond underlayer. Without electrical connection to a boron doped underlayer, the electric field was shown to spill-out from the bottom of the device giving a SV whose definition is now dependent upon the magnitude of the bias conditions. Whereas, the electrical connection of the outer electrode shell to a boron doped underlayer, while increasing the size of the volume, produced a more definite and knowable volume shape and size. The SV of this device is shown to be easily definable through the thickness of the thin electronic grade diamond and the depth and radius of the central cylindrical electrode. To summarise the above; a variety of alternative microdosimeter designs were fabricated and tested, demonstrating varying degrees of success. Different computational methods were utilised to improve upon the body of knowledge of diamond as a material for microdosimetry and to optimise detector design. The main aims of this thesis have been addressed, yet more work still needs to be done.

18.2 Recommendations for Future Research

The recommendations for future research are in part to be made by considering the drawbacks of the various detector designs created in addition to effects observed that were not

completely understood/anticipated. These recommendations are made in the order that each occurred within this body of work.

The first recommendation is to validate a model of diamond in TCAD using existing experimental results, and extend this to duplicates the CCE response of the BID and LT detector. This model should include details of radiation induced defects caused by the boron implantation and the possible concentration of charge defects caused by laser ablation. In addition the model should investigate the effect of straggling upon the boron location within the diamond substrate and the associated effects with SV definition. Future optimisation of the BID device will depend upon an accurate and validated modelling of the device and understanding of boron implantation in diamond.

The second recommendation is to concentrate efforts related to current detector development upon LT, BC and Cylindrical SV based designs, as they represent the best hopes for diamond based microdosimetry in terms of considerations related to charge confinement and collection efficiency. These designs can be further improved through a substitution of high Z contact materials with more tissue equivalent alternatives like aluminium and more preferably graphite.

Thirdly, the TEQ study should be extended to include heavy ions (i.e., Z>2), neutrons and electrons. These simulations should also begin to take into account the effect of contact materials through weighted contribution of stopping powers etc.

References

[1] G. Reitz, R. Facius, and H. Sandler, "Radiation Protection in Space," *Acta astronautica*, vol. 13, no. 16, pp. 3661–3668, 1995.

[2] E. Normand, "Single event upset at ground level," *IEEE Transactions on Nuclear Science*, 1996.

[3] H. H. Rossi, "Microdosimetry and the effects of small doses of radiation," *IEEE Transactions on Nuclear Science*, vol. 23, no. 4, pp. 1417–1421, 1976.

[4] J. Cameron, "Radiation dosimetry." *Environmental health perspectives*, vol. 91, pp. 45–8, Mar. 1991.

[5] A. Allisy, W. A. Jennings, A. M. Kellerer *et al.*, "Quantities and Units for Use in Radiation Protection," *ICRU*, no. December 1991, pp. 5–9, 1991.

[6] J. A. Caffrey and D. M. Hamby, "Space Radiation Dosimetry : Overview and Recent Developments," vol. 3, no. 1, pp. 3–12, 2013.

[7] J. A. Davis, K. Ganesan, A. D. C. Alves *et al.*, "Characterization of a Novel Diamond-Based Microdosimeter Prototype for Radioprotection Applications in Space Environments," *IEEE Transactions on Nuclear Science*, vol. 59, no. 6, pp. 3110–3116, Dec. 2012.

[8] J. A. Davis, K. Ganesan, A. D. C. Alves *et al.*, "Characterization of an Alternative Diamond Based Microdosimeter Prototype," *IEEE Transactions on Nuclear Science*, vol. 61, no. 6, pp. 3479–3484, 2014.

[9] J. A. Davis, S. Guatelli, M. Petasecca *et al.*, "Tissue Equivalence Study of a Novel Diamond-Based Microdosimeter for Galactic Cosmic Rays and Solar Particle Events," *IEEE Transactions on Nuclear Science*, vol. 61, no. 4, pp. 1544–1551, 2014.

[10] A. J. Tylka, J. H. Adams, P. R. Boberg *et al.*, "CREME96 : A Revision of the Cosmic Ray Effects on Micro-Electronics Code," *IEEE Transactions on Nuclear Science*, vol. 44, no. 6, pp. 2150–2166, 1997.

[11] F. Spurný, "Space and Flights Radiation Protection," pp. 1–16.

[12] W. M. Yao, T. K. Gaisser, and T. S. Bartol, "Cosmic Rays," *Journal of Physics G*, vol. 33, no. 1, pp. 1–20, 2006.

[13] N. deGrasse Tyson, *Death by Black Hole: And Other Cosmic Quandaries*. W. W. Norton, 2007.

[14] L. W. Townsend, "Implications of the space radiation environment for human exploration in deep space," *Radiation Protection Dosimetry*, vol. 115, no. 1-4, pp. 44–50, Jan. 2005.

[15] I. Usoskin, L. Desorgher, P. Velinov *et al.*, "Solar and galactic cosmic rays in the Earth's atmosphere."

[16] M.-H. Y. Kim, F. a. Cucinotta, and J. W. Wilson, "A temporal forecast of radiation environments for future space exploration missions." *Radiation and environmental biophysics*, vol. 46, no. 2, pp. 95–100, Jun. 2007.

[17] D. F. Smart and M. A. Shea, "Galatic Cosmic Radiation and Solar Energetic Particles."

[18] D. Allard, E. Parizot, and a. Olinto, "On the transition from galactic to extragalactic cosmic-rays: Spectral and composition features from two opposite scenarios," *Astroparticle Physics*, vol. 27, no. 1, pp. 61–75, Feb. 2007.

[19] A. C. Cummings, E. C. Stone, and C. D. Steenberg, "Composition of Anomalous Cosmic Rays and Other Heliospheric Ions," *The Astrophysical Journal*, vol. 1, no. 1999, pp. 194–210, 2002.

[20] E. Benton and E. Benton, "Space radiation dosimetry in low-Earth orbit and beyond," *Nuclear Instruments and Methods in Physics Research B*, vol. 184, pp. 255–294, Sep. 2001.

[21] A. Papaioannou, H. Mavromichalaki, M. Gerontidou *et al.*, "Solar particle event analysis using the standard radiation environment monitors: applying the neutron monitor's experience," *Astrophysics and Space Sciences Transactions*, vol. 7, no. 1, pp. 1–5, Jan. 2011.

[22] "Radiation Protection 140: Cosmic Radiation Exposure of Aircraft Crew," Tech. Rep., 2004.

[23] H. Rossi and M. Zaider, *Microdosimetry and its applications*. Springer, 1996.

[24] A. Rosenfeld, P. Bradley, I. Cornelius *et al.*, "A new silicon detector for microdosimetry applications in proton therapy," *IEEE Transactions on Nuclear Science*, vol. 47, no. 4, pp. 1386–1394, 2000.

[25] "NCRP Report No. 098 - Guidance on Radiation Received in Space Activities," Tech. Rep.

[26] NASA, "The Radiation Challenge," p. 36, 2008.

[27] A. Y. Vlasov, "Extension of Dirac's chord method to the case of a nonconvex set by the use of quasi-probability distributions," *Journal of Mathematical Physics*, vol. 52, no. 5, pp. 1–13, 2011.

[28] R. S. Sussmann, Ed., *CVD Diamond for Electronic Devices and Sensors*. Wiley, 2009.

[29] W. Atwell, E. R. Beever, a. C. Hardy *et al.*, "Space radiation shielding analysis and dosimetry for the space shuttle program," *AIP Conference Proceedings*, vol. 186, pp. 289–296, 1989.

[30] J. V. Bailey, "Dosimetry During Space Missions," *IEEE Transactions on Nuclear Science*, vol. 23, no. 4, pp. 1379–1384, 1976.

[31] "ICRP Publication 60," Tech. Rep., 1990.

[32] J. W. Wilson, J. L. Shinn, R. K. Tripathi *et al.*, "Issues in deep space radiation protection." *Acta astronautica*, vol. 49, no. 3-10, pp. 289–312, 2001.

[33] D. T. Bartlett, "Radiation protection aspects of the cosmic radiation exposure of aircraft crew," *Radiation Protection Dosimetry*, vol. 109, no. 4, pp. 349–355, 2004.

[34] E. V. Benton, A. L. Frank, E. Benton *et al.*, "High LET, Passive Space Radiation Dosimetry and Spectrometry," Tech. Rep., 1995.

[35] A. D. Wrixon, "New ICRP recommendations." *Journal of radiological protection*, vol. 28, pp. 161–168, 2008.

[36] P. D. Bradley, A. B. Rosenfeld, and M. Zaider, "Solid state microdosimetry," pp. 135–157, 2001.

[37] I. M. Cornelius, I. Orlic, R. Siegele *et al.*, "Ion beam induced charge collection time imaging of a silicon microdosimeter," *Nuclear Instruments and Methods in Physics Research B:*, vol. 210, pp. 191–195, Sep. 2003.

[38] D. A. Prokopovich, M. I. Reinhard, G. C. Taylor *et al.*, "Comparison of SOI microdosimeter and tissue equivalent proportional counter measurements at the CERF facility," *IEEE Transactions on Nuclear Science*, vol. 59, no. 5 PART 3, pp. 2501–2505, 2012.

[39] A. Wroe, A. Rosenfeld, M. Reinhard *et al.*, "Solid State Microdosimetry With Heavy Ions for Space Applications," vol. 54, no. 6, pp. 2264–2271, 2007.

[40] W. Lim, a.L. Ziebell, I. Cornelius *et al.*, "Cylindrical silicon-on-insulator microdosimeter: Design, fabrication and TCAD modeling," *2007 IEEE Nuclear Science Symposium Conference Record*, pp. 1633–1636, 2007.

[41] A. L. Ziebell, N. S. Lai, W. H. Lim *et al.*, "The next step in cylindrical silicon-on insulator microdosimetry: Charge collection results," in *IEEE Nuclear Science Symposium Conference Record*, 2008, pp. 1088–1092.

[42] J. Livingstone, S. Member, D. A. Prokopovich *et al.*, "Charge Collection in n-SOI Planar Microdosimeters," *IEEE Transactions on Nuclear Science*, vol. 60, no. 6, pp. 4289–4296, 2013.

[43] J. Livingstone, D. A. Prokopovich, M. L. F. Lerch *et al.*, "Large area silicon microdosimeter for dosimetry in high LET space radiation fields: Charge collection study," *IEEE Transactions on Nuclear Science*, vol. 59, no. 6, pp. 3126–3132, 2012.

[44] L. T. Tran, S. Member, D. A. Prokopovich *et al.*, "Ultra-Thin 3-D Detector : Charge Collection Characterization and Application for Microdosimetry," *IEEE Transactions on Nuclear Science*, vol. 61, no. 6, pp. 3472–3478, 2014.

[45] L. T. Tran, L. Chartier, D. A. Prokopovich *et al.*, "3D-Mesa "Bridge" Silicon Microdosimeter: Charge Collection Study and Application to RBE Studies in Radiation Therapy," *IEEE Transactions on Nuclear Science*, vol. 62, no. 2, pp. 504–511, 2015.

[46] C. M. Breeding and J. E. Shigley, "The "Type" Classification System of Diamonds and its Importance in Gemology," *Gems & Gemology*, vol. 45, no. 2, pp. 96–111, 2009.

[47] "Diamond Properties," 2015. [Online]. Available: http://www.ioffe.rssi.ru/SVA/NSM/Semicond/Diamond/index.html

[48] E. A. Konorova and S. F. Koslov, "Diamond Detector for Nuclear Radiation," *Soviet Physics Uspekhi*, vol. 12, no. 4, pp. 583–583, 2007.

[49] F. Nava, C. Canali, C. Jacoboni *et al.*, "Electron effective masses and lattice scattering in natural diamond," *Solid State Communications*, vol. 33, pp. 475–477, 1980.

[50] S. F. Kozlov, R. Stuck, M. Hage-Ali *et al.*, "Preparation and characterisitics of natural diamond nuclear radiation detectors," *IEEE Transactions on Nuclear Science*, vol. 22, pp. 160–170, 1975.

[51] E. A. Burgemeister, "Dosimetry with a diamond operating as a resistor." *Physics in medicine and biology*, vol. 26, no. 2, pp. 269–275, 1981.

[52] R. J. Keddy, T. L. Nam, and R. C. Burns, "Synthetic diamonds as ionisation chamber radiation detectors in biological environments." *Physics in medicine and biology*, vol. 32, no. 6, pp. 751–9, Jun. 1987.

[53] V. D. Kovalchuk, V. I. Trotsik, and V. D. Kovalchuk, "Letter to the Editor Diamond detector as a fast neutron spectrometer," *Nuclear Instruments and Methods in Physics Research A*, vol. 351, pp. 590–591, 1994.

[54] G. F. Knoll, *Radiation detection and measurement*, 2nd ed. New York: Wiley, 1989.

[55] C. Canali, E. Gatti, S. Kozlov *et al.*, "Electrical properties and performances of natural diamond nuclear radiation detectors," pp. 73–77, 1979.

[56] M. Bucciolini, F. Banci Buonamici, S. Mazzocchi *et al.*, "Diamond detector versus silicon diode and ion chamber in photon beams of different energy and field size," *Medical Physics*, vol. 30, no. 8, pp. 2149–2154, 2003.

[57] M. Bucciolini, E. Borchi, M. Bruzzi *et al.*, "Diamond dosimetry: Outcomes of the CANDIDO and CONRAD INFN projects," *Nuclear Instruments and Methods in Physics Research Section A: Accelerators, Spectrometers, Detectors and Associated Equipment*, vol. 552, no. 1-2, pp. 189–196, Oct. 2005.

[58] G. Cirrone, G. Cuttone, S. Lo Nigro *et al.*, "Dosimetric characterization of CVD diamonds in photon, electron and proton beams," *Nuclear Physics B - Proceedings Supplements*, vol. 150, pp. 330–333, Jan. 2006.

[59] S. Almaviva, M. Marinelli, E. Milani *et al.*, "Chemical vapor deposition diamond based multilayered radiation detector: Physical analysis of detection properties," *Journal of Applied Physics*, vol. 107, 2010.

[60] "National Institutes of Standards and Technology." [Online]. Available: http://www.nist.gov/

[61] M. Bruzzi, M. Bucciolini, G. a. P. Cirrone *et al.*, "Characterisation of CVD diamond dosimeters in on-line configuration," *Nuclear Instruments and Methods in Physics Research A*, vol. 454, pp. 142–146, 2000.

[62] A. J. Whitehead, R. Airey, C. M. Buttar *et al.*, "CVD diamond for medical dosimetry applications," *Nuclear Instruments and Methods in Physics Research, Section A*, vol. 460, pp. 20–26, 2001.

[63] I. Ciancaglioni, R. Consorti, M. Rossi *et al.*, "Polycrystalline diamond detectors compared with silicon X-ray dosimeters for clinical use," *IEEE Symposium Conference Record Nuclear Science 2004.*, vol. 7, no. C, pp. 8700–8702, 2004.

[64] S. Ramkumar, C. M. Buttar, J. Conway *et al.*, "Assessment of radiotherapy dosimeters based on CVD grown diamond," *Nuclear Instruments and Methods in Physics Research, Section A: Accelerators, Spectrometers, Detectors and Associated Equipment*, vol. 460, no. 2-3, pp. 401–411, 2001.

[65] M. Assiamah, T. L. Nam, and R. J. Keddy, "A synthetic diamond probe for low-energy X-ray dose measurements." *Applied radiation and isotopes : including data, instrumentation and methods for use in agriculture, industry and medicine*, vol. 65, no. 5, pp. 545–52, May 2007.

[66] R. J. Tapper, "Diamond detectors in particle physics," *Reports on Progress in Physics*, vol. 63, no. 8, pp. 1273–1316, Aug. 2000.

[67] B. Planskoy, "Evaluation of diamond radiation dosemeters," *Physics in medicine and biology*, vol. 25, no. 3, pp. 519–532, 1980.

[68] Y. P. Kozlov, S P and Bachurin, A V and Petrusev, S S and Pedorovsky, "Research of beta/gamma ratio for diamond nuclear radiation detectors," *IEEE Transactions on Nuclear Science*, vol. 24, no. 1, pp. 240–241, 1977.

[69] D. Kania, M. Landstrass, and M. Plano, "Diamond radiation detectors," *Diamond and Related ...*, vol. 2, pp. 1012–1019, 1993.

[70] C. Bauer, I. Baumann, and C. Colledani, "Radiation hardness studies of CVD diamond detectors," *Nuclear Instruments and Methods in Physics Research Section A*, vol. 367, pp. 207–211, 1995.

[71] J. Hassard, "The neutron radiation hardness of diamond detectors for future particle physics experiments," *Nuclear Instruments and Methods in Physics Research Section A: Accelerators, Spectrometers, Detectors and Associated Equipment*, vol. 368, no. 1, pp. 217–219, Dec. 1995.

[72] G. Betzel, S. Lansley, F. Baluti *et al.*, "Operating parameters of CVD diamond detectors for radiation dosimetry," *Nuclear Instruments and Methods in Physics Research A*, vol. 614, pp. 130–136, Feb. 2010.

[73] M. Pomorski, E. Berdermann, M. Ciobanu *et al.*, "Characterisation of single crystal CVD diamond particle detectors for hadron physics experiments," *Physica Status Solidi (a)*, vol. 202, no. 11, pp. 2199–2205, Sep. 2005.

[74] H. Bjorkman, P. Rangsten, U. Simu *et al.*, "Diamond microstructure replicas from silicon masters," in *Proceedings MEMS 98. IEEE. Eleventh Annual International Workshop on Micro Electro Mechanical Systems. An Investigation of Micro Structures, Sensors, Actuators, Machines and Systems (Cat. No.98CH36176)*. IEEE, 1998, pp. 34–39.

[75] I. Aharonovich, J. C. Lee, A. P. Magyar *et al.*, "Bottom-up engineering of diamond micro- and nano-structures," *Laser & Photonics Reviews*, vol. 7, no. 5, pp. L61–L65, Sep. 2013.

[76] M. J. Burek, B. J. Shields, N. P. de Leon *et al.*, "Angle-etched free-standing photonic crystal nanobeam cavities in single-crystal diamond," *Conference on Lasers and Electro-Optics 2012*, p. CM1M.2, 2012.

[77] W. Adam, C. Bauer, and E. Berdermann, "The first bump-bonded pixel detectors on CVD diamond," *Nuclear Instruments and Methods in Physics Research Section A*, vol. 436, pp. 326–335, 1999.

[78] L. Pan, S. Han, D. Kania *et al.*, "Electrical properties of high quality diamond films," *Diamond and Related Materials*, vol. 2, no. 5-7, pp. 820–824, Apr. 1993.

[79] F. Borchelt, W. Dulinski, and K. Gan, "First measurements with a diamond microstrip detector," *Nuclear Instruments and Methods in Physics Research A*, vol. 354, pp. 318–327, 1995.

[80] J. Isberg, J. Hammersberg, and E. Johansson, "High carrier mobility in single-crystal plasma-deposited diamond," *Science*, vol. 297, no. September, pp. 1670–1672, 2002.

[81] J. Isberg, J. Hammersberg, H. Bernhoff *et al.*, "Charge collection distance measurements in single and polycrystalline CVD diamond," *Diamond and Related Materials*, vol. 13, no. 4-8, pp. 872–875, Apr. 2004.

[82] H. Pernegger, "High mobility diamonds and particle detectors," *Physica Status Solidi (a)*, vol. 203, no. 13, pp. 3299–3314, Oct. 2006.

[83] A. Lohstroh, P. J. Sellin, S. G. Wang *et al.*, "Effect of dislocations on charge carrier mobilityâĂŞlifetime product in synthetic single crystal diamond," *Applied Physics Letters*, vol. 90, no. 10, 2007.

[84] D. Menasce, L. Moroni, J. Ngadiuba *et al.*, "Tracking performance of a single-crystal and a polycrystalline diamond pixel-detector," *Journal of Instrumentation*, vol. 8, no. 06, pp. 1–14, Jun. 2013.

[85] Y. A. Mankelevich and P. W. May, "New insights into the mechanism of CVD diamond growth: Single crystal diamond in MW PECVD reactors," *Diamond and Related Materials*, vol. 17, no. 7-10, pp. 1021–1028, 2008.

[86] J. D. Getty, "How Plasma-Enhanced Surface Modification Imporves the production of Microelectronics and Optoelectronics," Tech. Rep., 2002.

[87] P. Mehta, "Studies on Application of Single Crystal Diamond for Charge Particle Detection: Design, TCAD Simulations, Technology Development, & Dc Characterization," *Global Journal of Researches in Engineering: F Electrical and Electronics Engineering*, vol. 14, no. 6, 2014.

[88] M. Werner, "Diamond metallization for device applications," *Semiconductor Science and Technology*, vol. 18, no. 3, pp. S41–S46, 2003.

[89] R. Siegele, D. D. Cohen, and N. Dytlewski, "The ANSTO high energy heavy ion microprobe," *Nuclear Instruments and Methods in Physics Research*, vol. 158, pp. 31–38, 1999.

[90] T. Kashiwagi, K. Hibino, H. Kitamura *et al.*, "Investigation of basic characteristics of synthetic diamond radiation detectors," *IEEE Transactions on Nuclear Science*, vol. 53, no. 2, pp. 630–635, Apr. 2006.

[91] J. Allison, K. Amako, J. Apostolakis *et al.*, "Geant4 Developments and Applications," *IEEE Transactions on Nuclear Science*, vol. 53, no. 1, pp. 270–278, 2006.

[92] S. Chauvie, Z. Francis, S. Guatelli *et al.*, "Geant4 Physics Processes for Microdosimetry Simulation : Design Foundation and Implementation of the First Set of Models," vol. 54, no. 6, pp. 2619–2628, 2007.

[93] V. N. Ivanchenko, S. Incerti, J. Allison *et al.*, "Geant4 electromagnetic physics : improving simulation performance and accuracy," *Joint Internation Conference on Superconducting in Nuclear Applications and Monte Carlo*, 2013.

[94] K. Amako, S. Guatelli, V. Ivanchencko *et al.*, "Validation of Geant4 electromagnetic physics versus protocol data," *IEEE Symposium Conference Record Nuclear Science 2004.*, vol. 4, pp. 2115–2119, 2004.

[95] R. Minixhofer, "TCAD As an Integral Part of the Semiconductor Manufacturing Environment," in *International Conference on Simulation of Semiconductor Processes and Devices*, 2006, pp. 9–16.

[96] W. Fichtner, D. Rose, and R. Bank, "Semiconductor device simulation," *IEEE Transactions on Electron Devices*, vol. 30, no. 9, pp. 1018–1030, 1983.

[97] "Element 6: Synthetic Industrial Diamonds." [Online]. Available: http://www.e6.com/

[98] J. F. Ziegler, "The Stopping of Energetic Light Ions in Elemental Matter," vol. 85, pp. 1249–1272, 1999.

[99] J. F. Ziegler, M. D. Ziegler, and J. P. Biersack, "SRIM: The stopping and range of ions in matter," vol. 268, 2010.

[100] S. Ramo, "Currents Induced by Electron Motion*," *Proceedings of the I.R.E*, no. 11, pp. 584–585, 1939.

[101] T. Behnke, P. Hüntemeyer, A. Oh *et al.*, "The charge collection properties of CVD diamond," *Nuclear Instruments and Methods in Physics Research Section A: Accelerators, Spectrometers, Detectors and Associated Equipment*, vol. 414, no. 2-3, pp. 340–356, Sep. 1998.

[102] C. Z. Jarlskog and H. Paganetti, "Physics settings for using the Geant4 toolkit in proton therapy," *IEEE Transactions on Nuclear Science*, vol. 55, no. 3, pp. 1018–1025, 2008.

[103] S. Guatelli, M. I. Reinhard, B. Mascialino *et al.*, "Tissue Equivalence Correction in Silicon Microdosimetry for Protons Characteristic of the LEO Space Environment," vol. 55, no. 6, pp. 3407–3413, 2008.

[104] J. H. Lee, G. B. Kim, I. S. Seong *et al.*, "Measurement of the quenching and channeling effects in a CsI crystal used for a WIMP search," pp. 1–31, 2015.

[105] E. Bagli, M. Asai, D. Brandt *et al.*, "A model for the interaction of high-energy particles in straight and bent crystals implemented in Geant4," *The European Physical Journal C*, vol. 74, no. 8, p. 2996, 2014.